Physical Mechanisms of the Therapeutic Effect of Ultrasound (A Review)[1]

M. R. Bailey*, V. A. Khokhlova**, O. A. Sapozhnikov**, S. G. Kargl*, and L. A. Crum*

* *Center for Industrial and Medical Ultrasound, Applied Physics Laboratory, College of Ocean and Fishery Science,*
University of Washington, Seattle, Washington, 981056–6698 USA
e-mail: bailey@apl.washington.edu
** *Department of Acoustics, Physics Faculty, Moscow State University,*
Moscow, 119992 Russia
Received November 16, 2002

Abstract—Therapeutic ultrasound is an emerging field with many medical applications. High intensity focused ultrasound (HIFU) provides the ability to localize the deposition of acoustic energy within the body, which can cause tissue necrosis and hemostasis. Similarly, shock waves from a lithotripter penetrate the body to comminute kidney stones, and transcutaneous ultrasound enhances the transport of chemotherapy agents. New medical applications have required advances in transducer design and advances in numerical and experimental studies of the interaction of sound with biological tissues and fluids. The primary physical mechanism in HIFU is the conversion of acoustic energy into heat, which is often enhanced by nonlinear acoustic propagation and nonlinear scattering from bubbles. Other mechanical effects from ultrasound appear to stimulate an immune response, and bubble dynamics play an important role in lithotripsy and ultrasound-enhanced drug delivery. A dramatic shift to understand and exploit these nonlinear and mechanical mechanisms has occurred over the last few years. Specific challenges remain, such as treatment protocol planning and real-time treatment monitoring. An improved understanding of the physical mechanisms is essential to meet these challenges and to further advance therapeutic ultrasound. © *2003 MAIK "Nauka/Interperiodica".*

INTRODUCTION

The core promise of therapeutic ultrasound is the creation of clinical effects within the body without damaging intervening tissue. Broad and diverse therapies have been demonstrated experimentally and, in some applications, utilized clinically. High intensity focused ultrasound (HIFU) is one example. Figure 1 shows the fundamental concept of HIFU applications. In the focused ultrasound field, the acoustic intensity is sufficiently low near the transducer so that tissue is unharmed. In the focal volume, the intensity is much higher and absorption of the acoustic field is significant enough to thermally denature tissue proteins. A hand-held transducer positioned on the skin can therefore noninvasively cauterize bleeding or necrose tumors at specific sites deep inside the human body. This article concentrates on HIFU therapy, which includes hemostasis, surgery, and stimulation of the immune response, but also describes the physical mechanisms of two other ultrasound therapies—shock wave lithotripsy (SWL) and ultrasound-enhanced drug delivery. Recent research and development have brought therapeutic ultrasound to the doorstep of widespread clinical application. Further understanding of ultrasound propagation and physical mechanisms of its interaction with tissue provides the key to fulfilling this potential. The goal of this article is to describe the physical mechanisms that both enable and restrict clinical implementation of therapeutic ultrasound. Background is given; treatment limitations are identified; devices are introduced; numerical and experimental research tools are discussed.

BACKGROUND AND MOTIVATION

Pioneering Work

Ultrasound therapy has a long history, and several review articles describes this field [1–9]. Pioneering work in ultrasound therapy was international [7, 8]. In France, in 1917, Langevin observed the death of fish during the development of sonar [9]. In the United States (US), in 1926 and 1927, Woods and Loomis studied the lethal effect of ultrasound on cells, tissues, fish, and frogs. In Germany, in 1938, Ziess first studied the effects of ultrasound on the eye. Lynn *et al.* are generally credited with the invention of focused ultrasound therapy. They built and tested a high-power, focused, ultrasound transducer and identified localized damage without injury to intervening tissue. In the 1940s, Wall *et al.* in the US, 1950s Fry and Fry in the US, and 1960s Oka *et al.* in Japan, developed focused ultrasound for *in vivo* application to the central nervous system. Fry and coworkers began clinical trials in 1956. Simultaneously, in Russia, Burov and Andreevskaya [10] at the

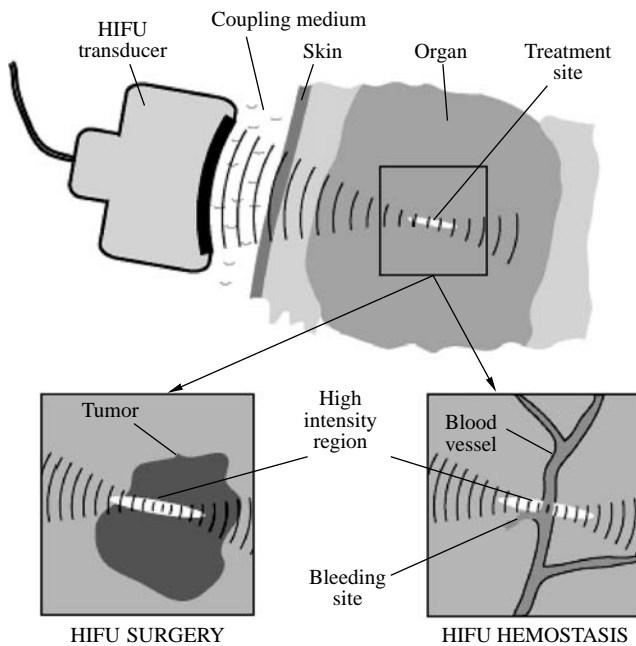[1] This article was submitted by the authors in English.

Fig. 1. The high intensity focused ultrasound (HIFU) beam is focused to necrose a localized tumor region or cauterize a specific bleed without injuring intervening tissue. Acoustic energy distributed over the face of the transducer is concentrated into a volume roughly the size of a grain of rice.

Laboratory of Anisotropic Structures, Academy of Sciences of the USSR were testing somewhat lower intensity, unfocused ultrasound on cancer tumors and found an increased immunological effect. Only recently has much of this work been made public [11]. From these pioneering works, ultrasound has branched into many different treatment areas and types.

Therapeutic Applications of Ultrasound

The clinical applications of ultrasound therapy are broad [2]; however, here, three main categories are defined: (1) high intensity focused ultrasound (HIFU) therapy, which includes tumor necrosis, hemostasis (stopping bleeding caused by trauma or surgical procedure), and immunotherapy; (2) ultrasound-enhanced drug delivery, (3) shock wave lithotripsy (SWL).

The main idea of HIFU therapy, which follows directly from the work of Lynn *et al.* and Fry and Fry, is the use of focused acoustic fields to coagulatively necrose or cauterize tissue [8]. HIFU necrosis has been applied to the brain [12], soft tissue cancers [13–15], benign prostatic hypertrophy (BPH) [16], prostate cancer [17, 18], glaucoma [19], ocular melanoma [20], uterine fibroids [1], fetal surgery [21], myocardial ischemia [3], and many other maladies.

In tumor necrosis, it was found that ultrasound could occlude blood vessels [22] and, subsequently, it has been applied to hemostasis for emergency medical care [23], fetal blood sharing [21], and tumor blood

supply [24]. Likewise, as the direct goal of the work of Burov and Andreevskaya [10] or as a beneficial side effect of HIFU therapy, ultrasound has been shown to induce an enhanced immune response that necroses tumors and protects against new tumor growth [25: Wu *et al*., pp. 34–43; Marberger *et al.*, pp. 146–153]. It has been shown that ultrasound can enhance the transport of chemicals and genes across biological barriers, such as cells, tissues, and blood clots [2].

Lithotripsy is the use of shock waves to break kidney stones [26–30] or gall stones [31]. In addition, lithotripters are finding new applications in orthopedic medicine [32], such as comminuting calcifications in joints [33].

Although the specific fields of hyperthermia and physical therapy can be classified as therapeutic ultrasound, these fields are not considered in this article because of the low-acoustic intensities typically employed. Ultrasound is commonly used in physical therapy to warm tissues about 1°C. For physical therapy, ultrasound intensities are on the order of 1 W/cm^2, and treatment times are about 10 min. In hyperthermia, ultrasound is generally not focused; the temperature of a tissue is elevated and held at the level of a threshold temperature (42–43°C) that necroses cancer but not normal cells. The intensities for hyperthermia are on the order of 10 W/cm^2, and treatment times are 1–2 h. The intensities applied for HIFU are ~1000 W/cm^2, and tissue is heated to >70°C in 1–3 s. However, the physical mechanism of tissue heating in physical therapy and hyperthermia is the same as in HIFU therapy; hence, as more is learned about HIFU, both of these treatments may benefit. In particular, hyperthermia, which has practically declined due to the problems of temperature control, may undergo a resurgence because of HIFU temperature-monitoring and transducer technology as well as synergistic effects with other treatments such as radiation [3].

Clinical Practice

HIFU. Although much basic research remains to be done, it should be underscored that high intensity therapeutic ultrasound is already in clinical use. Representative clinical applications are summarized here. Currently, the world leader in the clinical application of HIFU is China, where at least three companies exist that manufacture HIFU machines and over 1400 patients have been treated for cancerous tumors in bone and soft tissue [15; 25: Wu *et al.*, pp. 34–43]. Chinese machines have been exported and are being used in liver and kidney cancer treatments in Oxford, England. Prostate cancer is treated in Europe [25: Chaussy *et al.*, pp. 1–7] and Japan [18; 25: Uchida *et al.*, pp. 8–16], and BPH is also treated in the US by HIFU [16]. Two companies produce and sell machines for prostate therapy [25: Chaussy *et al.,* pp. 1–7; Uchida *et al.,* pp. 8–16]. An MRI-guided HIFU machine is produced in

Israel, and MRI-guided HIFU trials are underway for breast cancer [14]. Clinical trials for the treatment of soft tissues continue in Sutton, England without the need for patient anesthetic [13; 25: Allen *et al.*, pp. 17–25]. Ten patients with pancreatic cancer have been treated by an interstitial HIFU device in France [25: Lafon *et al.*, pp. 26–33]. A catheter-based device is used in the US to heat vascular stents to prevent restenosis [34]. Since 1985, HIFU has been used in the US to reduce intraocular pressure produced by glaucoma [8, 35]. In hemostasis, trials are underway for catheter wound closure by HIFU.

Ultrasound-enhanced drug delivery. Human trials are underway in the US for catheter-based ultrasound in conjunction with thrombolytic drugs to accelerate the dissolution of blood clots in the heart. At least two US companies are developing thrombolytic ultrasound devices. In Russia devices are commercially available for intraocular drug delivery [36, 37].

Lithotripsy. Since the early 1980s, lithotripsy has been the most common treatment for kidney stones and continues to be the favored method for uncomplicated, upper urinary tract calculi, even with the advent of percutaneous surgical techniques. Over 40 models of lithotripter models are available. Modified lithotripters are used in the US and Europe to treat plantars fasciitis and epicondylitis.

This list is intended to show that ultrasound therapy is not solely a scientific exercise but it is in expanding clinical use. However, aside from a recent burgeoning in HIFU cancer therapy in China, the treatment of kidney stones is the only therapeutic ultrasound that is in significant use. Nevertheless, by targeting specific injuries or ailments, therapeutic ultrasound is finding increasing clinical application.

Challenges and Pitfalls

Five major challenges to successful clinical implementation of HIFU are discussed here.

Focal gain and acoustic windows. One specific challenge is obtaining large focal gains of acoustic pressure through acoustic windows available in the body to transmit ultrasound. Large gain is needed to insure high intensities only at the focus and to spare intervening tissue. Skin burn is the most common side effect of transcutaneous HIFU treatment, because absorption in the skin is several times higher than internal soft tissue. Acoustic intensities, therefore, must be particularly low when crossing the skin [8]. In addition, efficient acoustic coupling to the skin and cooling of the transducer can eliminate skin burns and are important areas of research engineering. For example, flat transducers are more difficult to focus than curved ones but can be easily coupled by direct contact with the skin. Bones are even more absorptive than skin, so it is important to minimize their exposure to ultrasound and is usually avoided during treatment. Wu *et al.*

[25: p. 34–43] have removed ribs to open acoustic windows for HIFU treatment of the liver, and Fry and Fry [7] removed portions of the skull to access the brain. Clement and Hynynen [12] use high aperture transducers with very large gain to focus through the skull, but must correct for refraction of the acoustic beam. Such a need for correction requires the use of phased arrays for electronic focusing and steering the HIFU beam.

Real-time imaging is a second challenge for diagnosis of the disease, targeting, and monitoring the HIFU. Clinical trials for HIFU treatment of Parkinson's disease had successful outcomes but were stopped because of the difficulty of diagnosing the area to be treated and in monitoring the treatment [8]. In contrast, the HIFU treatment of glaucoma has been accepted clinically because of the simplicity of imaging and targeting, as the treatment site is optically transparent [19]. It should be noted that imaging is the area that has advanced most significantly since the early HIFU experiments. Current researchers can leverage emerging imaging modalities in MRI and ultrasound. However, the following challenges remain: real-time compensation for patient motion, localization of tumors or bleeding sites, and determination of therapy end point such as complete tumor necrosis or kidney stone comminution.

Treatment planning, the choice of optimal parameters of HIFU-transducer and treatment protocol, based on the acoustic parameters for each specific case is a third challenge. Consider, for example, the process of treating a tumor. To set the parameters of treatment for ablation of the tumor and only the tumor, it is necessary to perform theoretical modeling of acoustic and temperature fields in tissue for given amplitude, frequency, and geometry of the HIFU transducer and with account of absorption and refraction of ultrasound and heat diffusion. On the other hand, for modeling, it is necessary to know tissue parameters, which cannot be measured or predicted with high enough accuracy in all situations. Furthermore, the typical lateral size of the beam focal spot is about 1 mm, which is substantially smaller than the size of many tumors, so a method to treat the whole tumor is needed. The process of creating a discrete sequence of small lesions to necrose a large tumor has been used until recent time. However, in some cases, this protocol appeared to be prohibitively long, because without sufficient cooling time between exposures, the lesions become unpredictably distorted in their shape due to the change in acoustic parameters of heated tissue and cavitation [38, 39]. Wu *et al.* [15; 25: p. 34–43] introduced another scheme in order to accelerate HIFU therapy. Instead of a series of individual thermal lesions, Wu *et al.* paint a stripe of lesion as the transducer of much higher intensity is continuously moved. Control of the HIFU treatment in this case is to adjust the ultrasound intensity level based on real-time ultrasound imaging feedback—a hyperecho, a bright spot, which is observed during HIFU treatment at such high intensities. This is the current trend in HIFU tumor

necrosis: to emphasize real-time imaging, not relying only on precise prediction of treatment but on the ability to react to the image as well.

Calibration and optimization. Fundamental study and understanding of the physical mechanisms involved in ultrasound therapy enable optimization of HIFU instrumentation and standardization of protocols for treatment in new therapies. Standards have been developed for calibration of transducers by force balance or hydrophone [40], for cavitation detection [41], ultrasound bioeffects [42], and correction for artifact in temperature measurement by thermocouples [43]. However, further standardization and dosimetry of HIFU is needed [25: ter Haar *et al.*, pp. 307–313]. For example, one of the main characteristic values for HIFU transducers is spatial average intensity I_{SAL} defined as $I_{SAL} = W_*/\pi r_*^2$, where W_* is the acoustic power transmitted through the circle area of radius r_*, which is the lateral beam radius measured in the focal plane at half-maximum pressure level at low intensity in water [44]. However, treatments with the same time-averaged I_{SAL} but different duty cycles yield very different lesions. In some cases, another measure, such as maximum peak pressure, is needed as well to calibrate the treatment. Frequency and F-number (focal length/aperture diameter) are also both necessary to characterize an HIFU source.

Consider, as another example, lithotripsy. One of the standard calibration measures of the lithotripter shock field is the peak positive pressure that should define the maximum mechanical stress on a kidney stone. However, it appears that peak positive pressure does not correlate with effectiveness among different types of machines. Hence, other mechanisms must be considered, such as cavitation, which depends not on the positive but on the negative pressure. It appears also that lithotripsy is an effective treatment for kidney stones but it is not successful to comminute more common gallstones. The reason is that conditions in the gallbladder inhibit the physical mechanisms of shock wave impact on stones. Gallstones are more resistant to brittle failure than kidney stones; the fluid surrounding the stone is more viscous, which suppresses cavitation erosion of the stone; and lastly, the mechanism for removal of stone particles is not as efficient as in the kidney. Hence, although the clinical extension of lithotripsy to gallstones is possible, the same mechanisms are not as effective, and calibration and optimization are specific to this particular application.

Indirect technical influences. Clinical trials and targeted engineering are expensive; therefore, the perceived financial payback must be clear. The following considerations influence the investment in HIFU application and have a strong impact on its development: ease of use, reliability, portability, efficiency and sterilability, competing technologies, money/marketability. Ultrasound for intraoperative hemostasis has some distinct advantages over the current clinical treatment of electrocautery. Electrocautery is restricted to the tissue surface, and surface bleeding reduces the effectiveness of electrocautery. Conversely, ultrasound penetrates beneath the surface, and blood improves the ultrasound coupling. However, water filled coupling housings for the ultrasound transducers are difficult, and, thus, more expensive, to keep sterile than the simple metal spatula electrocautery transducers. These facts drive the engineering of new coupling for HIFU hemostasis [45]. In another example, the number of lithotripsy procedures increased significantly with a small technological advance—the advent of mobile lithotripters—that delivered the treatment to the patients in a way that conventional surgery could not.

Complexity and high cost of the new methods become unimportant when the existing methods are not successful. For example, although it may seem that a tumor can be removed surgically if it can be imaged and localized, this is not always the case. There are inoperable tumors (e.g., many liver metastases and pancreatic tumors) for which HIFU may offer the only treatment option, because it is bloodless, it has low risk of infection, and the procedure can be repeated.

METHODS

Transducer Technology

HIFU. An excellent review of current transducer technology can be found in a recent paper by Cathignol [9]. The transducers used in surgery and hemostasis generally are piezoceramic and operate in the 1−10 MHz frequency range, with 2–4 MHz being the most common, and up to 20 MHz for some applications in the eye. Intensities (I_{SAL}) at the focus range from 1000–10000 W/cm^2. The most common intensities are around 1500–3000 W /cm^2, in interstitial applications, intensities are typically lower, but the new clinical Chinese devices operate on the order of 10 000 W/cm^2. Transducers receive 100–500 W of electrical power with the acoustic output generally limited to a maximum pressure of 2–4 MPa sustainable by simple, unmodified ceramics. F-numbers are approximately one but can be as high as 1.5. Treatment depths are up to 15 cm. Transducers usually operate in periodic pulse regimes being on for seconds and off for tens of seconds. If an HIFU transducer works simultaneously with an ultrasound imaging system, the intense signal introduces a strong noise into the image. To synchronize with the video frame rate of an ultrasound imager, the HIFU driving signal can be gated at about 20 Hz.

Transducers are generally manufactured in the shape of a spherical segment, either as a single curved element or several elements on a curved backing. Figure 2 shows some single element transducers for hemostasis. Elements are made of piezoceramic or piezocomposite material. The piezoceramic can be machined into curved shapes, and the entire surface area is active.

However the characteristic acoustic impedance (33 MRayl) is not well matched to water (1.5 MRayl), so special matching layers are generally used to improve transmission. Parasitic vibration modes are common [46]. Adding backing material behind the element reduces the parasitic modes and increases the bandwidth but decreases the efficiency of the transducer. To make arrays, a piezoceramic must be sectioned.

A piezo-composite is a diced ceramic, where the spaces are filled with a polymer [46]. The composite material can be designed for heat dissipation or structural support. The material can be formed, vibrations are naturally damped, and the structure is inherently designed to be implemented as an array. Compared to piezoceramic, the characteristic acoustic impedance of piezo-composite (10 MRayl) is much closer to that of water, so transmission is more efficient. The piezo-composite also has a high electromechanical coupling factor (0.7); for piezoceramic it is normally less than 0.5. Efficiencies of both piezoceramic and piezo-composite transducers used in HIFU are often 70%. Liquid cooling is often required for interstitial devices but neglected in transcutaneous devices. To treat larger tissue volumes in a minimum treatment time, two approaches have been taken in transducer design: focus aberration and arrays. The focus has been blurred to broaden the treatment area by mechanical vibration of the transducer [47], electrode strips [20], and a split focus design [48]. Arrays offer the ability to steer the HIFU focus or to create simultaneously multiple HIFU foci in order to increase the treatment volume [3, 49, 50]. An HIFU array or a mechanically scanned single-element source [18] can be used for imaging as well as for treatment; however, a separate imaging array is commonly used [1, 17]. Precise manufacturing of the HIFU system is required to isolate each element electrically and acoustically, to prevent overheating, and to integrate a large number of linear amplifiers to properly and finely phase the signals.

Ultrasound-enhanced drug delivery. Frequencies used for ultrasound-enhanced drug delivery are usually around 20 kHz, although 1–2 MHz are also used. Typical intensities are lower, but treatment is longer than in HIFU. Transducers are generally unfocused and less taxed than in HIFU, although miniaturization of catheter devices to target small vessels responsible for strokes presents an engineering challenge. Lithotripters are also used for gene and drug transport [27]. A unique design developed by Kawabata *et al.* for extracorporeal drug delivery is two confocal transducers with two frequencies 0.5 and 1 MHz [25: p. 539–543]. The mixing of these frequencies properly shifted in phase substantially decreases the cavitation threshold and enhances cavitation, which is a primary mechanism in enhancement of drug delivery. Similar results have been recently obtained with mixing high frequency bursts and continuous low frequency ultrasound [25: Bailey *et al.*, pp. 472–480]. Cavitation can be localized in this
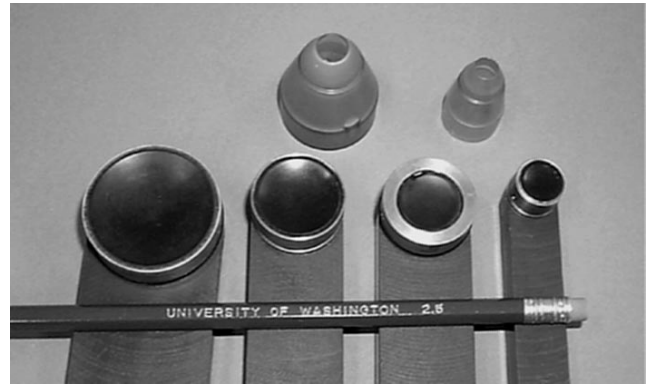

Fig. 2. Single element piezoceramic transducers (3–10 MHz) designed for acoustic hemostasis. The circular matching layer and element connect to a 10-cm handle. A detachable water-filled cone provides the acoustic coupling. [Figure courtesy of P.J. Kaczkowski, CIMU, University of Washington.]
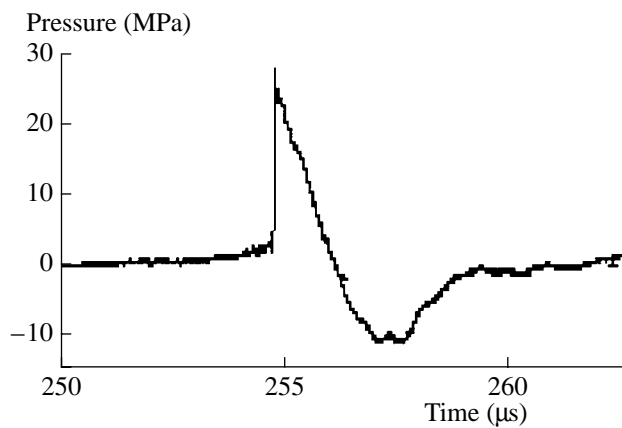

Fig. 3. Waveform measured with a PVDF membrane hydrophone at the focus of an electrohydraulic lithotripter. Characteristically, a positive-pressure spike leads a slightly longer negative pressure trough. Treatment commonly requires about 2000 pulses administered at 1–2 Hz.

case if the higher frequency transducer is focused. The field of manipulating the waveform to control cavitation in therapeutic ultrasound is an emerging one with great potential.

Lithotripsy. Lithotripters produce short focused microsecond pulses as opposed to a burst of many cycles at a characteristic frequency in HIFU. A common lithotripter waveform at focus is shown in Fig. 3. Peak positive pressure is 20–140 MPa and peak negative pressure is –8 to –15 MPa. Thousands of pulses are delivered in a treatment at rates of 1–2 Hz. Electrohydraulic lithotripters are commonly gated to the cardiac cycle because the electrical output can cause arrhythmia. Higher rates would accelerate treatment but cause more tissue injury. Lithotripters are typically tens of centimeters in aperture with F-numbers around one. Acoustic coupling with the patient is achieved through
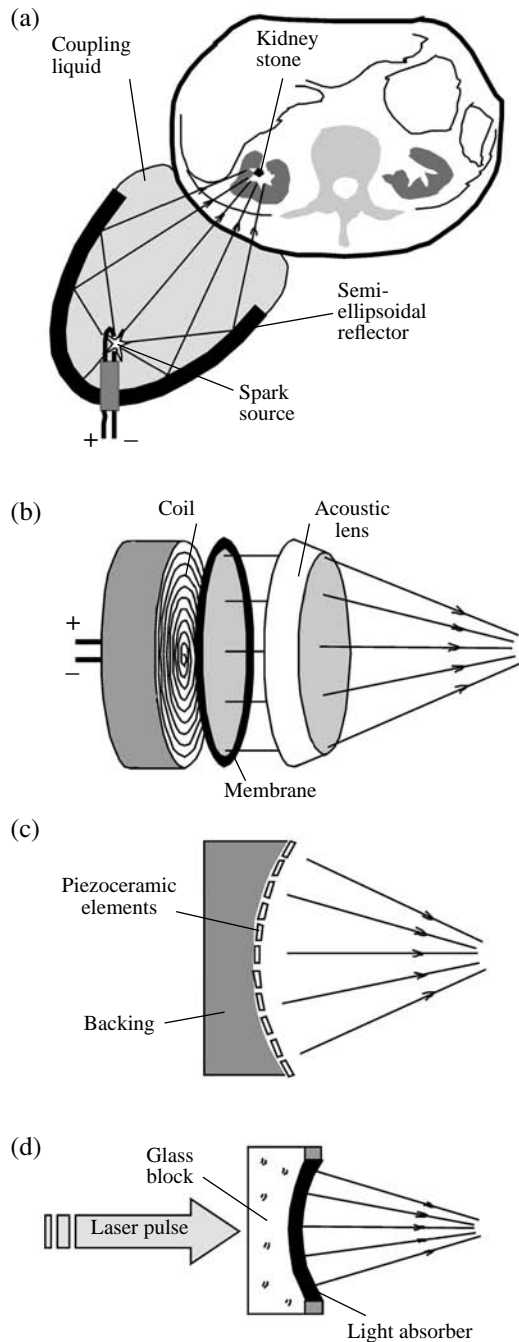
Fig. 4. Three clinical and one research lithotripter designs. Electrohydraulic machines (a) use an ellipsoidal reflector to focus the shock wave generated by an underwater spark. Electromagnetic devices (b) employ impulsive displacement of a plate to generate the wave, which is focused by a lens or reflector. Piezoceramic lithotripters (c) utilize the waves generated by piezoelectric elements. The laser lithotripter (d) relies on the conversion of an optical wave to an acoustic one in a thin spherical layer of a light-absorbing liquid.

water baths or liquid-filled pillows. Finally, orthopedic applications are driving the development of compact designs.

There exist three fundamental types of clinical extracorporeal shock wave lithotripters—electrohydraulic, electromagnetic, and piezoceramic (see Fig. 4). In electrohydraulic lithotripters, an underwater spark generates a shock wave that is focused on the kidney stone by an ellipsoidal reflector. The first and most common lithotripter, the Dornier HM3, is considered the gold standard because of its high long-term stone-free rates (67–90%) for a wide range of stones. New electrohydraulic lithotripters incorporate longer lasting electrodes, which provide repeatable waveforms. Electromagnetic lithotripters conduct high current through a coil, which then repulses a parallel plate. Lenses or reflectors focus the wave created by the displacement of the plate. Piezoceramic lithotripters are generally arrays built on a spherical segment. Array technology allows steering of the beam and even image tracking of the stone. Sufficiently powerful compact devices are being developed with stacked composite elements [51] or electrically prestressed piezoelectric material [9]. Lithotripters are commonly compared on the basis of the product of the peak pressure at the focus and the −6-dB pressure volume, which ranges from 0.2 to 10 cm^3. Since peak pressures are so varied, it might be more logical to compare the volume in which a super-threshold pressure is produced. However, this threshold value has not been determined yet, and a higher product correlates with improved clinical efficacy. Electrohydraulic lithotripters, particularly the HM3, produce low peak pressures (30–40 MPa) but the largest focal volume and the largest product. Newer electromagnetic and piezoceramic lithotripters generally produce more tightly focused beams and higher peak pressures, with the notable exception of the low-amplitude, broad-focused lithotripter developed by Eisenmenger [52]. A fourth type of extracorporeal lithotripter uses a laser source and optoacoustic transduction to generate shock waves (see Fig. 4). A prototype of the laser lithotripter has been built but is not yet used clinically [53]. Sparks, mechanical drills, and lasers are also used intracorporeally to break stones.

New lithotripter research focuses on controlling cavitation. Corresponding methods are to manipulate the timing between pulses [54, 55] or to modify the lithotripter waveform by altering the reflector material in electrohydraulic [56] or electromagnetic devices or reversing the polarity in piezoceramic devices [57].

Numerical Techniques

The goals of theoretical modeling are to better understand ultrasound propagation in tissue, to quantify the interaction of the acoustic field and tissue, and to plan and optimize treatment protocols. Analytical methods yield qualitative estimations, trends, and guides for numerical simulations, which are necessary in most cases. An ideal numerical code must include a model for the nonlinear acoustic field produced by an ultrasound source coupled with models of the main

ultrasound induced phenomena: tissue heating and cavitation. Inclusion of models for streaming, acoustic radiation pressure, shear stresses, reflection, inhomogeneous structure of tissue, and refraction across a liquid–tissue interface may also be necessary; however, calculation time and computational memory place limitations on the complexity of the model. The goal of this section is to describe how each of these effects is simulated and to show their contribution to the acoustic impact on tissue, which will be discussed in more detail in the next section.

Ultrasound field. The Khokhlov–Zabolotskaya–Kuznetsov (KZK) nonlinear evolution equation is widely used to model numerically high intensity acoustic beams [58]. The KZK model has been successfully applied to simulate the acoustic field generated by HIFU [59–61] and lithotripsy sources [62]:

$$\frac{\partial p}{\partial z} - \frac{\beta}{c_0^3 \rho_0} p \frac{\partial p}{\partial \tau} - \frac{b}{2c_0^3 \rho_0} \frac{\partial^2 p}{\partial \tau^2} = \frac{c_0}{2} \int_{-\infty}^{\tau} \Delta_\perp p(\tau') d\tau'. \quad (1)$$

Here, p is the acoustic pressure, z is the coordinate along the beam axis, c_0 is the small-signal sound speed, ρ_0 is the ambient density, $\tau = t - z/c_0$ is the retarded time, β is the coefficient of nonlinearity, b is the dissipative parameter, and $\Delta_\perp$ is the Laplacian operator with transverse coordinates $\mathbf{r} = (x, y)$. The boundary condition $p_0(\tau, \mathbf{r})$ is given at $z = 0$. Equation (1) is the simplest model that provides an adequate description of nonlinear and diffraction phenomena in focused ultrasound beams. The equation accounts for diffraction within a parabolic approximation, while thermoviscous absorption and acoustic nonlinearity are considered within a plane wave approximation. Acoustic nonlinearity is necessary in the model because, at high-pressure levels (typical for HIFU and lithotripsy), it affects thermal and mechanical changes within the tissue. Several modifications of Eq. (1) have been proposed to better fit the frequency power law of absorption found in tissue [59–61, 63, 64] or to more accurately model the diffraction effects [65, 66]. More comprehensive models, based on the solution of Navier–Stokes equations or full wave equations, have been developed recently for lithotripsy and HIFU [67; 25: Curra *et al.*, pp. 275–282].

Various finite-difference algorithms for the solution of Eq. (1) have been developed based on the method of fractional steps with an operator-splitting procedure [68]. The solution is calculated plane by plane along the beam axis z, and, at each Δz step, the diffraction, nonlinearity, and absorption effects are applied sequentially. The algorithms are implemented either in the time domain [62, 69] or in the frequency domain [59–61, 69–73].

In the frequency-domain schemes, the solution to Eq. (1) is represented in the form of a Fourier series expansion

$$p(z, \mathbf{r}, \tau) = \sum_{n=-\infty}^{\infty} C_n(z, \mathbf{r}) \exp(-in\omega_0 \tau). \quad (2)$$

Substitution of Eq. (2) into Eq. (1) yields a set of nonlinear, coupled differential equations for the harmonics C_n of the initial signal. Frequency-domain schemes are better suited for modeling cw ultrasound (cancer treatment, hemostasis, drug delivery) and easier to account for frequency dependent absorption in tissue. Time-domain schemes are better for modeling pulsed regimes used in lithotripsy and nonlinear imaging [62, 69]. Specific transformations of the spatial coordinate system are introduced in some algorithms to follow the focused geometry of an acoustic beam [60, 71, 73]. All models can be implemented in two or three dimensions; however, most results have been obtained for two-dimensional axisymmetric beams. Some simulations are available for rectangular ultrasound sources, but these simulations are much more time consuming and have larger memory requirements and, therefore, are still difficult for modeling [74, 75].

The diffraction term, which is on the right-hand side of Eq. (1), is usually solved by either implicit backward or Crank–Nicholson finite difference methods in both the time and the frequency domain [68]. For frequency-domain schemes, implemented not in the form of the complex series of Eq. (2) but in real series, an additional iterative procedure is necessary to obtain the solution [58, 59, 71]. A particular requirement is to perform simulations within reasonably small spatial windows, which results in nonphysical reflections from the transverse boundaries. To avoid this numerical effect, an artificial absorption is introduced within a layer at the edge spatial grids [61, 71]. Some algorithms employ more accurate diffraction operators without the parabolic approximation [65, 66]. In this case, the numerical solution at each z is obtained by the Rayleigh integral. These algorithms are more time consuming; however, they provide more accurate results for strongly focused ultrasound beams.

The absorption term is calculated in the frequency domain based on the exact solution for the amplitude of each harmonic propagating over the distance Δz:

$$C_n(z + \Delta z) = C_n(z) \exp(-\alpha_n \Delta z). \quad (3)$$

Here, $\alpha_n = (n\omega_0)^2 b/2 c_0^3 \rho_0$ is the attenuation coefficient, which exhibits quadratic frequency dependence according to Eq. (1). Attenuation in tissue is nearly linearly dependent on frequency, because relaxation processes dominate thermoviscous heating. In most tissues, attenuation is on the order of 0.1 Np/cm/MHz. The absorption can be easily modified in the frequency domain (3) as $\alpha_n = \alpha_0 (\omega/\omega_0)^\eta$ with $1 < \eta < 1.4$. The dispersion is then calculated from local dispersion relationships [64] or minimum phase digital filters [65]. In time-domain algorithms, a finite-difference method is

applied to the absorption term in Eq. (1), as it is proportional to the second derivative [62]. For an arbitrary frequency power law of absorption, this method cannot be used and a convolution is often applied [109]. FFT methods are also used to obtain a solution in the frequency domain and then return to the time-domain formulation at each step [58].

Nonlinear acoustic propagation, the second term in Eq. (1), is implemented in the frequency domain by solving a set of coupled nonlinear equations for harmonics using Runge–Kutta methods. The number of harmonics is up to 1000 for high intensities and shock regimes [61, 76], which makes the algorithms very time consuming even for two-dimensional axisymmetric beams. To decrease the number of harmonics, an artificial viscosity rapidly increasing with frequency is introduced for the last few harmonics [59, 63]. Artificial or numerical absorption of high frequencies and the corresponding smoothing of the shock front may result in an underestimation of the enhanced heating. To avoid the smoothing of the solution, an asymptotic spectral method has been developed to govern shock waves. In this method a relatively small number of the first harmonics is calculated numerically and the higher harmonics are included in the algorithm using a high frequency asymptote of a shock wave spectrum [60, 64]. The asymptote is also employed in the reconstruction of an acoustic waveform from the finite spectrum, calculation of intensity, and heating. Various methods of solving the nonlinear term in Eq. (1) are used in the time-domain schemes. One method uses an exact solution that distorts a uniform time grid and then interpolates the solution back to the initial grid [62, 69]. This method is very stable but introduces an artificial absorption of the solution. An absorption term is also necessary to correctly govern the movement of the shock front. Other finite-differences schemes have been developed that use the method of characteristics [58] or conservation laws [63].

The results of modeling the acoustic field are used to model the thermal and mechanical impact of ultrasound on tissue. Heat sources are calculated from the time-averaged intensity vector $Q = -\nabla \cdot \mathbf{I}$ as $\mathbf{I} = \langle p\mathbf{v} \rangle$ in full-wave equation models or strongly focused beams. In the quasi-plane wave approximation of Eq. (1), the intensity and the heat sources can be written in terms of the harmonic amplitudes, Eq. (3), as

$$I = \langle p^2 \rangle / c_0 \rho_0 = 2 \sum_{n=0}^{\infty} |C_n|^2 / c_0 \rho_0$$

$$\text{and } Q = 4 \sum_{n=0}^{\infty} \alpha_n |C_n|^2 / c_0 \rho_0. \qquad (4)$$

In designing an HIFU source, a useful estimate for Q can be obtained from the case of linear plane-wave propagation. The acoustic power absorbed per unit volume at the depth L in tissue is

$$Q = -dI/dz = 2\alpha I_0 \exp(-2\alpha L), \qquad (5)$$

where I_0 is the initial wave intensity at the entrance to the tissue. This simple expression yields an estimate of an appropriate HIFU frequency for penetration to various treatment depths in the tissue. The maximum heat deposition at the distance L in tissue corresponds to the frequency f with absorption length $\alpha^{-1} = 2L$, which satisfies $\partial Q / \partial \alpha = 2I_0(1 - 2\alpha L)\exp(-2\alpha L) = 0$. This estimate is also valid in the quasi-plane wave approximation for weakly focused acoustic beams.

Various generalizations of the presented modeling scheme and complications should be listed here. The KZK equation is an evolution-type equation; i.e., only one-way wave propagation is assumed. A full-wave formulation is computationally intensive but accurately calculates forward and backward propagation caused by reflection from tissue boundaries, bones, or bubbles (i.e., multiple scattering paths). Multiple reflections can be important for skin overheating. A two-dimensional axisymmetric calculation of heating uniform tissue is on the order of minutes to hours with Eq. (1), and a three-dimensional calculation of heating in layered media with a blood vessel or bubble formation takes on the order of a week with a full-wave code [25: Curra *et al.*, pp. 275–282]. The accuracy depends largely on the accuracy of tissue parameters, which must be obtained from experiments, and on the influence of cavitation bubbles. However, a threshold can be determined below which cavitation is unlikely to occur and, thus, will not complicate the calculation or therapy. Another problem is that heat deposition in tissue is proportional to absorption. However, an experimentally measured attenuation includes both absorption and scattering losses with only approximately known relative contribution of scattering. This uncertainty also decreases the accuracy of modeling.

Temperature field. The mathematical model for temperature elevation in tissue is based on the BioHeat Transfer Equation (BHTE) in which the effects of heat diffusion, blood perfusion, and heat deposition are taken into account [77]:

$$\frac{\partial T}{\partial t} = k\Delta T - \frac{T - T_0}{\tau} + \frac{Q}{c_v}. \qquad (6)$$

Here, t is the time, $T(\mathbf{r}, t)$ is the tissue temperature, T_0 is the equilibrium temperature, $k = K/c_v$ is the local tissue temperature conductivity, K is the heat conductivity, c_v is the heat capacity of a unit volume, and Δ is the Laplacian operator. The absorbed ultrasound energy, Q, is calculated from the KZK equation, a full-wave model, or a bubble dynamics equation. The perfusion time, τ, is of the order of hundreds of seconds and can often be neglected in short (~10 s) HIFU treatments. Figure 5 shows good agreement between measured temperature induced in excised liver and the temperature calculated for liver with Eqs. (1) and (6) [78]. Figure 6 shows the
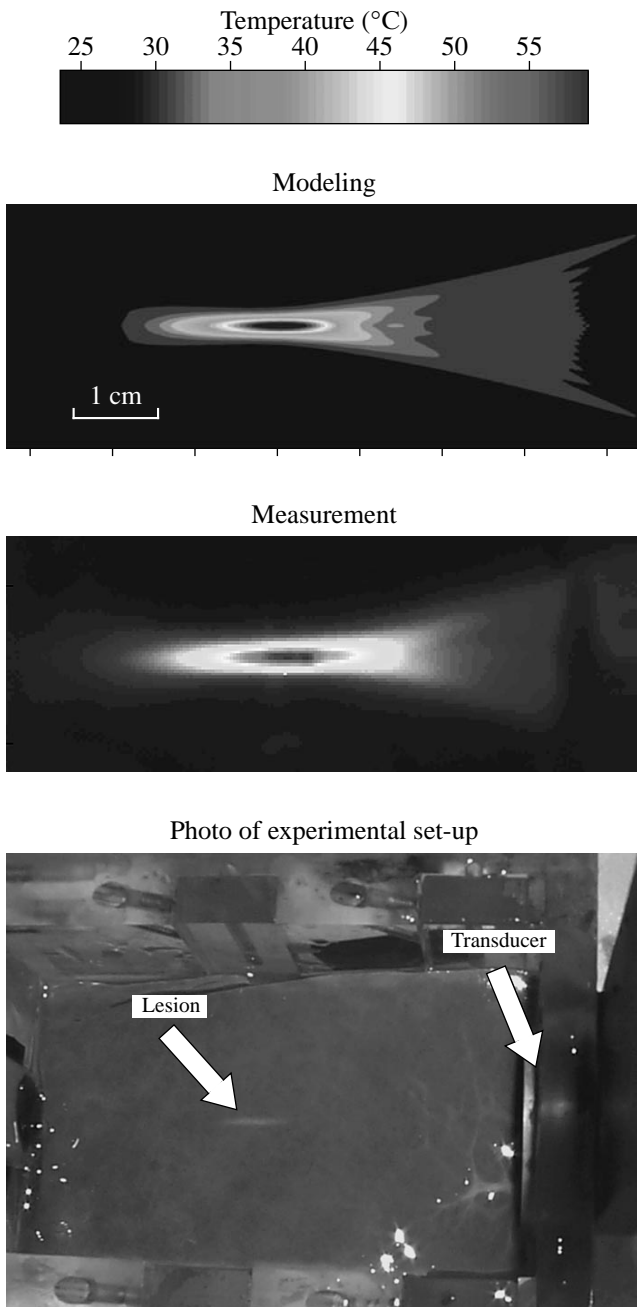
Temperature (°C)
25   30   35   40   45   50   55

Modeling

1 cm

Measurement

Photo of experimental set-up

Transducer

Lesion

Fig. 5. Calculated (top) and measured (center) by infrared camera HIFU-induced temperature rise in tissue. 2-MHz transducer with a 60-W acoustic power, 55-mm focal length, and 35-mm diameter (F-number 1.57) is on the right. For experiment, two layers of bovine liver were stacked along the beam axis. The top layer was immediately removed after 10 s of HIFU exposure, and the thermal image was recorded [78]. The photo of the corresponding lesion is shown at the bottom (white spot).

results of a 3D code to calculate heating near a blood vessel [25: Curra *et al.*, pp. 275–282].

A threshold for thermal necrosis, the denaturing of tissue protein, is calculated according to the thermal
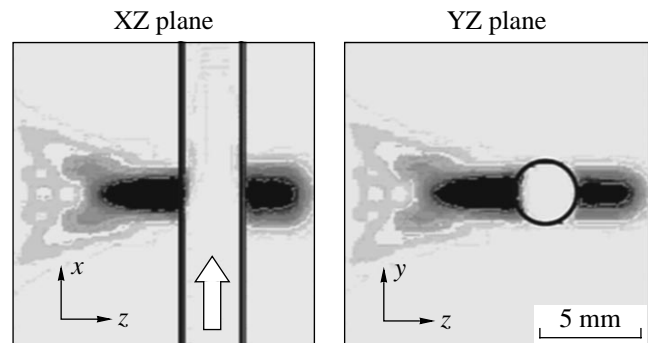
XZ plane   YZ plane

5 mm

Fig. 6. Numerically simulated tissue temperature near a blood vessel shows that HIFU heating is significant in tissue but advective cooling by blood flow and low absorption in blood keep the interior of the vessel cool. Hence, ruptured vessels can be sealed but remain patent. [Figure courtesy of F. Curra, CIMU, University of Washington.]

dose (*TD*) formulation

$$TD_{43°C}(t) = \int_0^t R^{43 - T(t')} dt',$$ (7)

with $R = 0.25$ if $T(t) < 43°C$ and 0.5 otherwise [79]. The thermal dose required to create a thermal lesion is equivalent to the thermal dose of a 240-min exposure at 43°C. This definition originated from the hyperthermia protocol, when the tissue was heated to a temperature of 43–45°C in the range during a long exposure of several hours. However, it has been shown that this model gives good estimations of the thermal lesion for the higher temperatures caused by HIFU, which include 10 s at 53°C, 1 s at 57°C, and 0.1 s at 60°C. In HIFU treatments, the temperature commonly exceeds 70°C in about 1–4 s. Thus, tissue necrosis occurs almost immediately.

Cavitation bubble dynamics. In lithotripsy and HIFU, it is common to use cavitation models based on the behavior of a single spherical bubble. These models predict the radial oscillations of a single spherical bubble smaller than the acoustic wavelength and, despite the narrow restrictions of the model, capture the general physics of clusters of bubbles *in vivo* quite well. Most of the single bubble models represent various modifications of the Rayleigh model [80]. For brevity, only the RPNNT (Rayleigh–Plesset–Noltingk–Neppiras–Poritsky) equation is presented here for the radius $R(t)$ of the bubble exposed to ultrasound with an angular frequency ω and peak pressure p_a [80]:

$$R\ddot{R} + \frac{3}{2}\dot{R}^2$$
$$= \frac{1}{\rho}\left[\left(p_0 + \frac{2\sigma}{R_0}\right)\left(\frac{R_0}{R}\right)^{3\gamma} - \frac{4\mu\dot{R}}{R} - \frac{2\sigma}{R} - (p_0 - p_a\sin\omega t)\right].$$ (8)
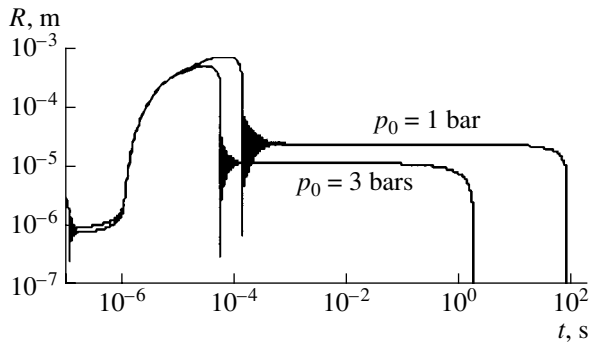
Fig. 7. Calculated radial response of a bubble to a lithotripter pulse for various hydrostatic pressure $p_0 = 1$ and 3 bars. The positive pressure spike (see Fig. 3) of the lithotripter pulse collapses the bubble. The ensuing negative pressure trough initiates growth that continues long after the passage of the lithotripter pulse. Eventually, the pressure difference across the water–bubble interface initiates implosion with strong rebounds. The inertia of the in-rushing fluid that collapses the bubble is sufficiently strong to create shock waves, microjets, and free radicals. Elevated hydrostatic pressure significantly accelerates further dissolution of the bubble.

Here, R, $\dot{R}$, and $\ddot{R}$ are the bubble wall radius, velocity, and acceleration, respectively. The density of the liquid is ρ, p_0 is the external hydrostatic pressure, R_0 is the equilibrium bubble radius, σ is the surface tension, μ is the shear viscosity of the liquid, and γ is the adiabatic exponent of the gas. Equation (8) accounts for the acoustic pressure field that drives the bubble, viscous stresses at the bubble–liquid boundary, and the presence of the gas in the bubble. The Gilmore–Akulichev model is an extension of the RPNNT model, which accounts for the compressibility of the fluid and acoustic radiation [81]. The model has been further modified to include gas diffusion into the bubble [81, 82], evaporation and condensation in the bubble [83], and tissue constraint on the bubble [84]. The numerical solutions to the bubble dynamics equations are obtained with fourth or fifth order Runge–Kutta algorithms with adaptive time steps [68]. Figure 7 shows typical calculated radius-versus-time curves for a 1-μm bubble excited by a lithotripter pulse [82]. The bubble dissolves more quickly at higher hydrostatic pressure.

Coupling of acoustics, temperature, and cavitation. Recent developments in theoretical and numerical models include the interaction of cavitation–temperature–sound effects, complicated structure of acoustic transducers, and the tissue. Bubbles contribute to tissue through the reflection of the acoustic field [59], through nonlinear reradiation [85, 86], and through their motion in a viscous fluid [86, 25: Holt *et al.*, pp. 120–131]. More complicated models have been designed to calculate jet formation [87, 88] or to consider bubble cloud behavior [25: Matsumoto *et al.*, pp. 290–299]. Bubbles can superfocus the acoustic wave by forming a lens and, on the contrary, temperature rise affects sound
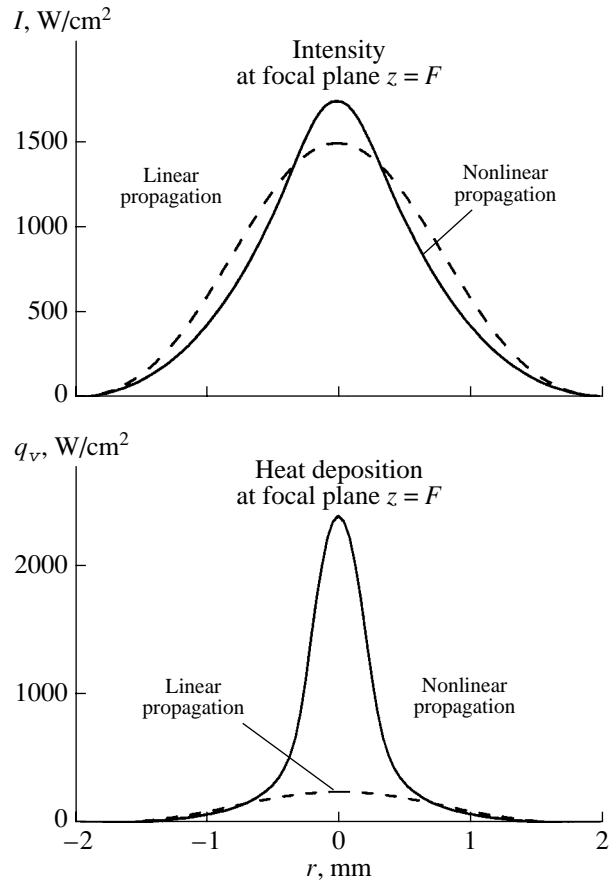

Fig. 8. Focal intensity I and heat deposition q_v versus transverse dimension calculated in liver for a 1.7-MHz transducer with a 15-cm focal length, and 8.4-cm diameter assuming linear and nonlinear propagation [61]. Nonlinear effects predict slightly higher intensities in a slightly narrower focus due to tighter focusing of generated higher harmonic frequencies but predict greatly enhanced heating due to stronger absorption of higher frequencies. Elevated heating efficiency can be achieved through nonlinear acoustic propagation and a judicious selection of peak acoustic amplitude, transducer gain, and duty cycle.

propagation by self-defocusing due to increase of the sound velocity with temperature up to 37–60°C in many soft tissues [89]. In other words, the acoustic parameters of the tissue are temperature and bubble dependent. To compensate for self-defocusing, models of acoustic arrays permit investigation of phase and absorption corrections to predict better locality of the focal spot [90]. Effects of shear can be calculated from the acoustic field and bubble dynamics calculations but as yet are not generally coupled into a dynamic model [91].

Numerical results. Some specific results of numerical modeling are listed here. Nonlinear acoustic models predict a highly localized region of enhanced heating close to the focus. The locally enhanced heat deposition is shown in Fig. 8. An outcome of this result could be lower average power requirements for the same heating predicted linearly by reducing the duty

cycle. Modeling has also described the mechanisms of lesion distortion and migration, specifically, the distortion to a tadpole shape and migration toward the transducer. The following factors are listed in order of increasing contribution to this distortion: nonlinear acoustics, temperature-dependent absorption, and bubbles. The dominant role of bubbles was confirmed by experiment [92, 93]. In SWL, self-refraction, a nonlinear acoustic effect whereby the highest amplitude wave on the axis travels faster and acts to defocus the wave explains why the highest peak pressures are postfocal and the highest peak negative are prefocal [94]. Since negative pressure drives cavitation, and cavitation appears to be an important mechanism in stone comminution, this result might direct where a stone should be positioned in the field [95]. The models also underscore the need for careful determination of tissue parameters and for description of bubble sizes, number of bubbles, vapor or gas content, and effect of tissue constraint on bubble dynamics.

PHYSICAL MECHANISMS

The corner stones of engineering development, numerical simulation, and clinical implementation are the physical mechanisms of the therapeutic effect of ultrasound on biological tissue. The mechanism is critical to design: to increase the likelihood of one mechanism, cavitation, the ultrasound frequency should be lowered; to increase another mechanism, ultrasound absorption, the frequency, in general, should be raised. In addition, the mechanism is crucial to obtaining the desired effect: therapeutic ultrasound is used, in one instance, to stop bleeding and, in another, to reestablish blood flow in clotted arteries. Here, we review some major mechanisms of ultrasound action in different therapeutic procedures.

High Intensity Focused Ultrasound

Absorption. The fundamental physical mechanism of HIFU, ultrasound absorption and conversion to heat, was described by Lele and Pierce in 1972 [96]. Thermal injury is consistent with the coagulative necrosis seen in histology of HIFU treatments [1]. As ultrasound propagates, some energy is absorbed through relaxation and thermoviscous processes and converted to heat [97]. An intrinsic tissue property is that absorption increases nearly linearly with ultrasound frequency; hence, more heating occurs at higher frequencies. However, for transducers with the same F-number, the focus is smaller with higher frequency [98] and penetration depth is also limited by the higher absorption. Equation (5), $\alpha^{-1} = 2L$, defines an optimum frequency for a specific depth. In addition, tissue absorption tends to increase with temperature, especially when the temperature is sufficient to denature proteins. Although complicated by absorption's dependence on temperature, HIFU frequency, and tissue type, we refer to this process as lin-

ear absorption, because the heating rate is linearly proportional to the sound intensity (see Eqs. (5) and (6)).

Finite-amplitude acoustics. At high intensity levels, typical for HIFU, ultrasound propagates nonlinearly: the waveform distorts and steep shock fronts develop in the profile. The waveform distortion is synonymous with the production of more rapidly absorbed higher harmonics, which reduces the HIFU intensity and increases the tissue heating [99]. In the case of strong nonlinearity, when shocks are formed close to the transducer, ultrasound can be absorbed before it reaches the focus, leading to overheating of undesirable areas and less focal heating. However, for typical HIFU parameters, nonlinearity is strongly pronounced close to the focus only, which results in enhanced focal heating as strong harmonic production is concentrated and localized [59–61, 72, 99]. The results of numerical simulation of the enhanced temperature rise are shown in Fig. 9. The heating rate is nonlinearly proportional to the HIFU intensity [100]. In fact, waves of the same time-average intensity but different peak pressures and duty cycles produce different heating rates (see Fig. 10).

The amplified heating due to nonlinear absorption is superfocused, which may mean that nonlinear effects play a more significant role during the initial phase, when the thermal lesion is initiated, resulting in a fast excess of the threshold of thermal necrosis in a very small volume, much less than the desired volume of lesion. Later, when the size of the lesion expands over
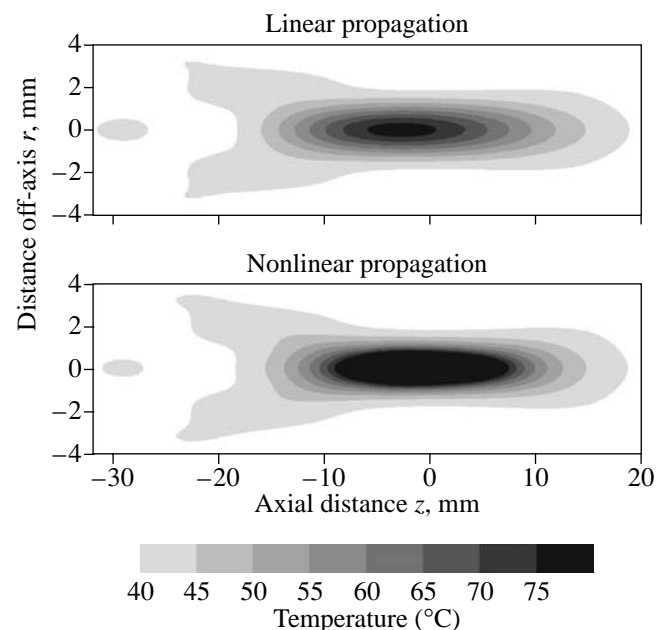

Fig. 9. Numerical simulations of temperature elevation in liver enhanced due to nonlinear acoustics for the same transducer parameters as in Fig. 8. The total volume heated is roughly the same, but the superheating (dark) in the superfocus initiates necrosis sooner and can lead to production of a bubble through boiling.
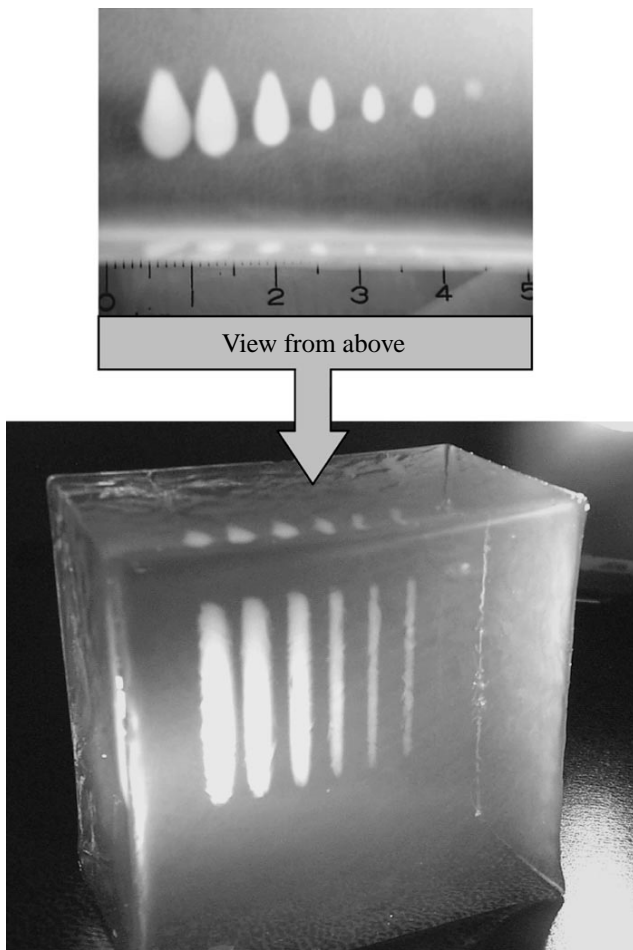
Fig. 10. Top and side view of lesion stripes made by linearly scanning the transducer. The time average intensity is constant, but the duty cycle decreases, the pressure increases, and the lesion increases from right to left due to nonlinear acoustics and cavitation.

the superheated area, nonlinear absorption is less important if only the thermal mechanism is taken into account. However, if the amplified nonlinear heating is significant, it can accelerate the formation of bubbles and, therefore, initiation of another mechanism of tissue damage—cavitation.

Cavitation damage by HIFU was reported as early as 1930 [101], and a long history makes the case that cavitation (bubble activity) occurs in many HIFU treatments [5, 92]. Bubbles may form from boiling of fluid in blood or tissue or by the growth of tiny cavitation nuclei within the body due to the negative pressure of the acoustic wave. Once initiated, cavitation bubbles oscillate in the acoustic field either noninertially, where the bubbles almost linearly track the pressure changes of the sound field, or inertially, where the bubble dynamics is nonlinear. The change from the negative acoustic pressure to the positive initiates the bubble implosion, and the inertia imparted into the surrounding in-rushing liquid results in bubble collapse. The

timing and degree of collapse is determined by the inertial properties of the surrounding liquid. Inertial collapse is often followed by bubble rebounds.

Bubble formation from nuclei occurs above a threshold that is dependent on pressure (acoustic cavitation), absorbed energy (boiling), and ultrasound frequency. Although formed as primarily vapor cavities, bubbles evolve to contain both gas and vapor, the amount of which varies as the bubble oscillates in the acoustic field. Over large inertial bubble oscillations, such as shown for lithotripsy in Fig. 7, gas diffuses into the bubble and vapor forms by evaporation. In repeated oscillations, bubbles absorb gas and grow by a process of rectified diffusion [102]. When the bubble is large, the gas concentration in the bubble is low and gas diffuses in through a large area and across a thin diffusion skin with rapid change of the dissolved gas concentration. When the bubble is small, the concentration is high and gas diffuses out but through a small area with a thicker diffusion skin. Simulations show that the bubbles grow to a resonant size in the order tens of milliseconds or longer.

Resonant bubble radius depends on the ultrasound frequency. In water, it is approximately $3/f$ μm where the frequency is measured in MHz [80]. In tissue, the resonant radius can be an order of magnitude larger, because tissue constraint makes the bubble stiffer.

Gas softens the bubble collapse by providing stiffness to stop the mass of rushing in water. On the contrary, vapor generally condenses and does not soften collapse by damping the liquid in-rushing to the center of the bubble. However, in lithotripsy, the bubble collapses too quickly for vapor to completely condense, and chemical reactions in the trapped vapor may be significant damping mechanisms [83]. Although bubbles tend toward a resonant size, smaller bubbles are continuously created by bubble fragmentation and dissolution, and larger bubbles may be created by agglomeration.

Bubbles are strong scatterers of ultrasound and, thus, significantly influence HIFU therapy. Bubbles scatter acoustic waves shielding tissue behind a bubble cluster from HIFU energy. Sanghvi *et al.* [5] and others observed that once bubbles form little HIFU penetrates the focus. Bubbles backscatter acoustic waves, causing more energy to be absorbed in the prefocal region before a bubble cluster than that occurring without bubbles. The effect, observed by Watkin *et al.* [39], is the lesion grows wider and toward the transducer as shown in Fig. 11. In practice, the scattering can inhibit therapy if, for example, precisely sized and positioned lesions are planned to completely necrose a tumor volume. On the other hand, scattering from bubbles may enable therapy, in a different HIFU protocol. For example, hemostasis in a tissue volume can be achieved as the lesion propagates toward the transducer in what has been termed a "wall of cautery" [47].
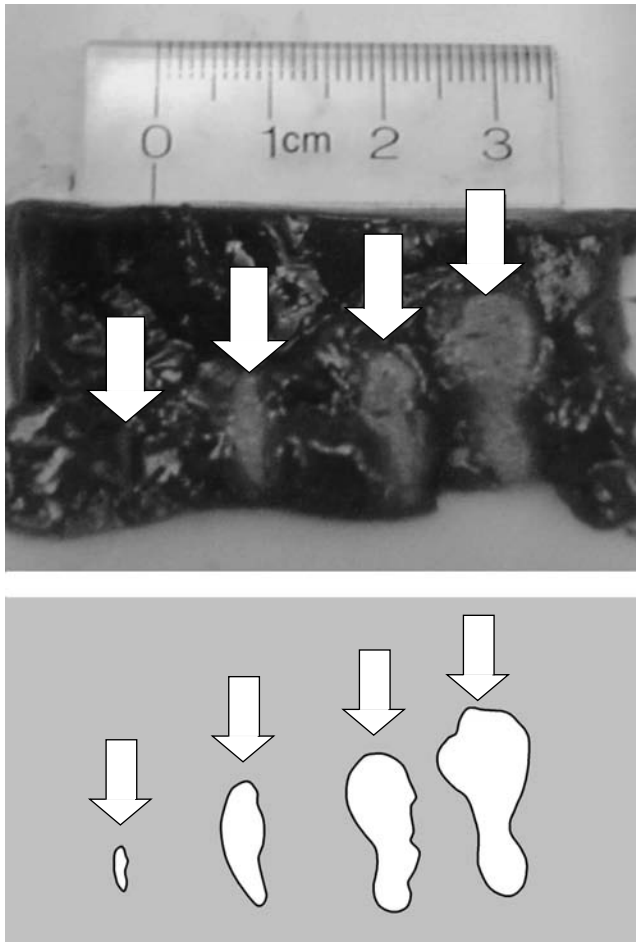
Fig. 11. Increasing HIFU intensity (left to right) creates tissue lesions that grow toward the transducer and distort from a symmetric cigar shape to an asymmetric tadpole shape because of scattering from bubbles. Arrows indicate the direction of the axis of the acoustic beam. For better viewing, the lesions are drawn separately in the bottom picture.

Fig. 12. HIFU lesions (left) in transparent gel phantom and B-mode ultrasound images (right) at 1 bar (top) and 100 bars (bottom) static pressure. The lesion is smaller and no hyperecho (arrow) is seen at 100 bar, a sufficiently elevated static pressure to suppress cavitation.

In addition, scattering from bubbles formed in the focal region can be used to image the treatment volume. On B-mode ultrasound, the bubbles appear hyperechoic. Note that overpressure suppresses both the enhanced heating and the hyperecho as shown in Fig. 12 [25: Bailey *et al*., pp. 472–480]. In fact, it has been observed *in vivo* that hyperecho can occur prior to creation of an observable thermal lesion. Thus, at least for some subset of HIFU parameters, the bubbles may precede thermal injury.

It has been observed *in vitro* that a dramatic increase in heating occurs with the appearance of bubbles [86, 25: Holt *et al.*, pp. 120–131]. The bubbles themselves cause increased heating due to several mechanisms. First, the energy absorbed by bubbles converts to heat by damping of their oscillation due to viscosity and thermal conductivity inside and close to the bubbles. Second, scattering from bubbles is nonlinear: in addi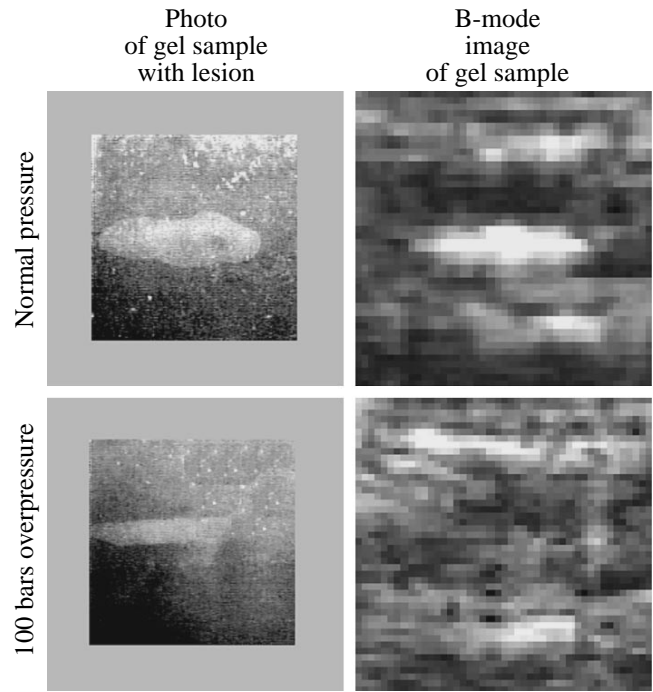tion to the fundamental frequency, the acoustic wave scattered from the bubbles contains higher harmonics that are readily absorbed by the tissue at small distances from bubbles. Bubbles can also be driven to a violent inertial collapse that creates mechanical effects by expansion [104, 105], shock waves [85, 106], microjets [107], and free radicals [108]. Figure 13 shows mechanical tissue disruption at the core of an HIFU lesion in liver.

It has been observed that, in hemostasis, mechanical effects of cavitation emulsify blood and tissue into paste. Radiation force on bubbles slows the bleed (as the transducer axis is commonly opposite the direction of the flow) and drives the paste into the vessel [47]. HIFU heat then cauterizes the paste in place to cover the damage in the vessel. The coagulation cascade can be exited by HIFU when cavitation is present [109].

In tumor treatment, the mechanical effects of cavitation alone, without absorptive heating, can destroy tumor tissue [101]. More recent reports [111] contradict early reports [112] that mechanical effects increase metastasis. In fact, there appears to be an increased resistance to metastasis due to HIFU. It has been proposed that this noninvasive immunotherapy is due to dispersing fragmented antigens into the blood stream that then train the immune system to recognize and attack cancer cells.

Nonthermal, noncavitational mechanisms. Thermal and cavitational mechanisms appear to dominate
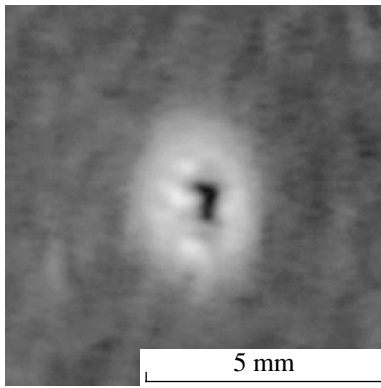
5 mm

Fig. 13. Mechanical disruption and cavities can be seen at the core of a HIFU-induced lesion in excised liver for sufficiently high exposure intensities or times. Hyperecho, audible acoustic emission, and migration of the lesion often accompany mechanical damage. Cavitation of predominantly vapor bubbles, especially arising in the localized axial region where nonlinear acoustics enhance heating, likely causes the disruption. [Figure courtesy of P.J. Kaczkowski and B.W. Cunitz, CIMU, University of Washington.]

HIFU hemostasis and tumor treatment; however, the mechanisms of a different nature also contribute to HIFU impact on tissue. There is clear documentation of a noncavitational, nonthermal effect on increased immunity to cancer following the treatment. A.K. Burov and coworkers found that, at intensities too low to create thermal lesions ($200 \ W/cm^2$, small duty cycle), tumors, grown in rabbits from injection of metastatic Brown–Pearce tumor cells, shrunk and even disappeared and that new tumors did not grow following subsequent injection of tumor cells into the vasculature. The same results were seen when animals were treated under elevated hydrostatic pressure to suppress cavitation [10, 11]. Late-stage melanoma tumors were reduced in humans as well. Wu *et al.* have seen a similar immunological effect in shrinkage of tumors not treated directly by HIFU but elsewhere in the body [25: p. 34–43].

It was described above that cavitation fragments cancer cells, releasing material that triggers the immune response. Along with cavitation, pressure gradients resulting directly from the ultrasonic waves may also fragment cells. Although the wavelength of the acoustic waves (usually on the order of 1 mm) is much larger than a cell (8 μm), the shock wave thickness in an ultrasonic wave can be much smaller. In lithotripsy, the shock thickness measured *in vivo* was 150 nm [113]. Hence, a pressure difference on the order of 10 MPa can exist inside a cell and, in addition, the individual components of the cell with differing acoustic impedances are subject to differing forces. These forces can break the cell [11]. Sturtevant and coauthors [29] proposed a mechanism only slightly different for tissue damage by a lithotripter shock wave. The very narrow shock front of the focused wave in fact could be superfocused by inhomogeneities in tissue (what is called

wave front folding in the case of sonic booms propagating in a turbulent atmosphere). This superfocusing creates pressure gradients and shear within cells, tissues, and, in particular, blood vessels. Sturtevant proposed that the shear broke cells. Overpressure experiments in cell suspensions confirm a minimal level of lysis attributed to shear when thermal (in lithotripsy, the pulses are sufficiently short that absorptive heating is negligible) and cavitation effects are suppressed [114]. Ultrasound thus creates shear that yields a nonthermal, noncavitational bioeffect. Note that shear damage *in vivo* may yield pools of blood where cavitation then acts.

Summary of HIFU mechanisms. Chinese clinical success and other evidence establish a number of reasons for working at very high amplitude: faster treatment, increased heating efficiency, and imaging usefulness of bubbles. In fact, in many treatment regimes, bubbles appear unavoidable and may dominate the therapy. Cavitation has been detected at fairly low HIFU amplitudes by harmonic reradiation *in vivo* [115]. Significant heating was measured after cavitation bubbles appeared *in vitro* [86] and *in vivo* [115]. Hyperecho, attributed to bubbles, in some HIFU protocols always accompanies therapy [25: Ebbini p. 280–287] and may precede appearance of a lesion [103]. Numerical simulations show that nonlinear propagation, which results in distortion of waveforms and amplified heating, is inherent in most HIFU protocols [59–61, 72]. According to all these revealed phenomena, the early HIFU paradigm that tissue absorption warms the tissue, the temperature becomes sufficient to denature proteins, the lesion grows through thermal diffusion, and treatment is ceased before increased absorption and heating cause boiling is less accepted now. Instead, it appears more typical that mechanical effects or superheating in a superfocused region due to finite-amplitude propagation of the acoustic wave yields bubbles. Reradiation from the bubbles is a significant mechanism of tissue heating, and the lesion forms after the bubbles. The focus is quickly moved once the lesion has formed to avoid complication caused by bubble scattering. A raster scan pattern of necrotic stripes is painted from the far side of the tumor towards the transducer. The bubbles shield against acoustic penetration and heating beyond the tumor. Throughout, linear and nonlinear mechanisms of absorption are involved simultaneously in heating the tissue.

Lithotripsy

Five stone comminution mechanisms have been studied in lithotripsy. They are erosion [116], spallation [117], dynamic fatigue [29], shear [114], and circumferential compression [52]. These mechanisms may all be activated to differing degrees by either the lithotripter shock pulse or the subsequent collapse of cavitation bubbles excited by the pulse.

Erosion results particularly when bubbles collapse against a surface. In-rushing water is not balanced by

in-rushing water from the direction of the surface, and as a result, a jet of water burrows through the bubble and impinges on the surface. Individual bubbles and bubble clusters create jets, as shown in Fig. 14. Clusters occur in SWL, because the stone exists in a pool of liquid (urine) in the collecting system. It has been calculated that collapses of outer bubbles generate shock waves that force the collapse of the next layer of the cluster, which produces another shock wave, which builds and amplifies toward the cluster center [88].

The shock wave transmitted into the stone when the jet impinges on the stone or the acoustic transmission into the stone of the lithotripter pulse can lead to spallation in the following way. Powerful compression pulse from a lithotripter penetrates into the stone and, after passing to the back surface, reflects from the acoustically soft interface of stone to fluid (the specific acoustic impedance of stones is roughly three to five times higher than that of water or urine). The reflected pulse has an invert polarity; i.e., the powerful compression pulse transforms into a rarefaction pulse of almost the same amplitude. This negative-pressure reflected pulse superimposes with the negative-pressure tail of the incident pulse, creating a high tensile stress and resulting in spallation at some distance close to the back surface of the stone (see Fig. 15). Evidence exists that, without cavitation, spall is reduced or even negated.

Dynamic fatigue is a failure process whereby cracks grow under the repeated compressive and tensile cycles. Commonly, over 1000 lithotripter pulses are used in a treatment, and it is reasonable to expect dynamic fatigue contributes to comminution. The shear mechanism is that described for tissue injury in SWL. Focusing the shock wave can create pressure gradients and, therefore, shear forces within the stone.

Circumferential compression or "squeezing" is the result of the compressive shock pulse traveling faster in the stone than in the surrounding fluid. Hence, at some point, the pulse has traveled through the stone, but ringing the stone is the high pressure of the shock pulse in water, as is seen in Fig. 15. The compressive ring at the equator of the stone produces tensile stress and cracks at its poles.

Compression and spall contribute noticeably when the stone is large. The stones typically are 2–10 mm, bubble clusters reach ~10 mm, the lithotripter pulse is 1–10 mm, bubbles and jets are 1 μm to 1 mm, and the shock front is 150 nm. Research indicates that cavitation is an important factor in lithotripsy [31, 56]: stones initially break by spall, and erosion grinds the fragments into a size suitable for the patient to pass [30]. Simply breaking the stone into pieces is a negative outcome: fragments must be 2 mm or smaller. All these mechanisms may act to varying degrees with different lithotripter and stone types.
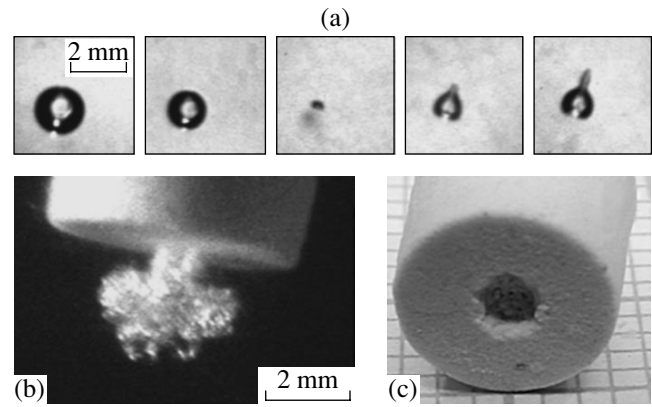
Fig. 14. Jet formation in a single bubble (a) and a bubble cluster (b) due to a lithotripter shock wave. The single bubble (a) excited to 1-mm radius collapses in the third frame and, on rebound, creates a jet of fluid. Frame rate is 20 μs. The cloud that grew to engulf the proximal end of the stone collapses to a mushroom shape (b) as a fluid jet erodes the stone surface (c).
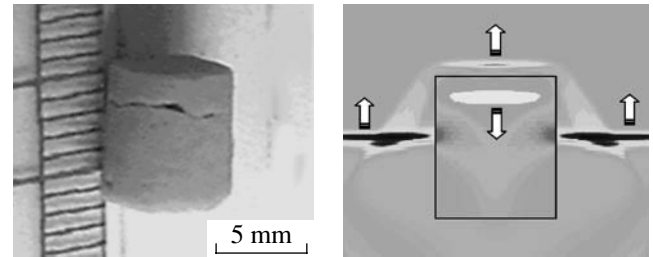

Fig. 15. Calculation of a lithotripter shock wave (pressure shown in dark) traveling up through and around a stone. The pulse moves faster in the stone and reflects and inverts at the distal end. The superposition of the reflection and the trailing negative-pressure trough maximizes the tensile stress at the distal end where the crack is seen in the stone (left). Positive pressure ringing the stone can also cause distal cracking. [Figure courtesy of R.O. Cleveland, Boston University.]

Drug Delivery and Gene Transfection

The primary mechanism of ultrasound-enhanced drug delivery and gene transfection is cavitation [2]. Cavitation microjets puncture holes in cell membranes and convect drugs into cells, tissues, and blood clots. In addition, flow around the oscillating bubble creates compressive, tensile, and shear stress on the biological interface. The flow aids in diffusion through mixing and opens channels by straining membranes.

Control of the cavitation threshold is therefore necessary for drug delivery procedure. It is known that this threshold is lower at lower frequencies because the liquid is under continuous negative pressure for a longer period. A Mechanical Index (peak negative pressure in MPa divided by the square root of frequency in MHz) has been established as the threshold for transient cavitation in diagnostic ultrasound [118]. It is considered
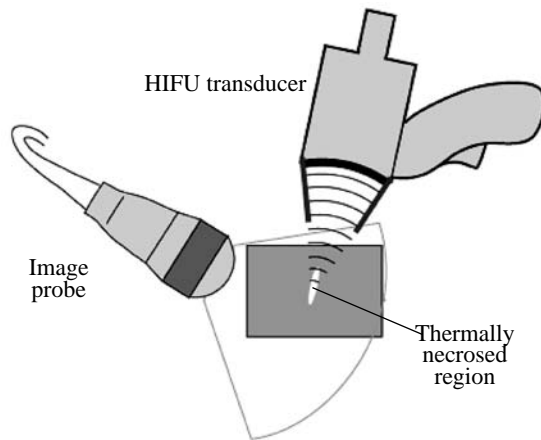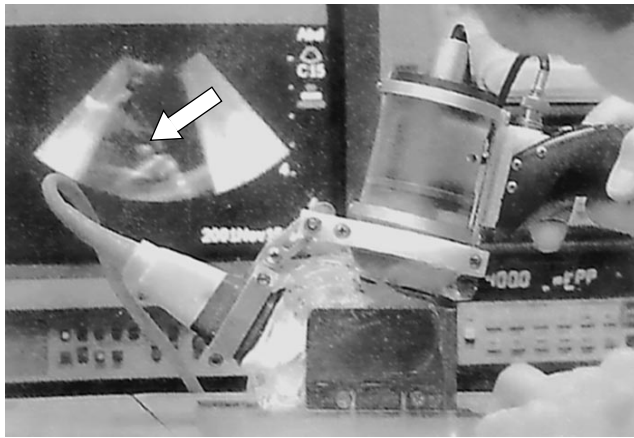
Fig. 16. Acoustic image-guided therapy. The photo of the system is shown on the top, the basic components are repeated at the bottom picture. An HIFU transducer can be translated within a water-filled cylindrical housing to alter the treatment depth. A trigger initiates treatment. Simultaneously, an image probe (left) affixed to the HIFU transducer guides treatment. A bright region (arrow) in the image shown behind corresponds to the thermally necrosed region in the protein/gel phantom.

that the threshold for nonstationary cavitation corresponds to MI = 1, but this is an approximate value. For example, according to MI = 1, 1.6 MPa at 2.5 MHz is the threshold, but measured thresholds in whole blood at 2.5 MHz exceed $p_- = 5$ MPa [119]. The addition of encapsulated microbubbles greatly reduces the cavitation threshold and increases the cavitation activity [2]. Much of current technology development focuses on developing microbubbles to transport the drug, attach preferentially to the target tissue for example a tumor, and facilitate drug delivery with acoustic cavitation.

Acoustic Image Guidance

The goals of image guidance are diagnosis, targeting, and monitoring of HIFU treatment. The requirement of the real-time imaging in order to target into tissue volume and monitor that bleeding is completely stopped or tissue is coagulated in the target site (and

only there) is unique to HIFU. In particular, compensation must be made for patient motion to avoid treatment of the surrounding tissue.

Fortunately, HIFU produces physical changes of tissue that can be exploited in ultrasound imaging. The fact that these changes take place over the course of the treatment makes reference-frame imaging, where subsequent images are compared to an initial image, and differential imaging, where consecutive frames are compared, useful tools. Changes that can be imaged are bubbles, nonlinear parameter, attenuation, temperature, shear modulus, and displacement of the tissue.

Cavitation/bubbles. The appearance of bubbles in the focal region produces a strong backscatter in the ultrasound imaging signal (see Fig. 12). Figure 16 shows an integrated imaging and treatment system. A hyperechoic region is seen immediately following treatment. It is also possible to image the scattering site during the treatment if HIFU and imaging are synchronized and interlaced in time [103]. The bright spot fades with time (~60 s) as bubbles dissolve and dissipate. If HIFU is ceased at first appearance of the hyperechoic region, no gross tissue injury is observed [103]. This result means that this hyperechoic region can be used to target the treatment area before necrosing tissue.

Nonlinearity. The nonlinear scattering of bubbles can be exploited by imaging techniques developed for microbubble echo contrast agents—second harmonic imaging and pulse inversion. Volterra filtering method has been developed specifically for HIFU [25: Ebbini *et al.*, pp. 280–287]. These methods suppress the linear scattering, which is dominant in tissue, and display other frequencies reradiated by the bubbles. In a slightly different use of nonlinear scattering from bubbles, microbubble contrast agents can be injected into the blood stream following treatment. Areas with blood perfusion become hyperechoic; unperfused regions with lesions give a negative return. Doppler imaging, which displays frequency as color, shows the perfused areas where bubbles produce strong nonlinear scattering. Figure 17 shows (b) B-mode image of the lesion (hyperechoic), (c) power, and (d) directional Doppler images as a contrast agent is injected into the portal vein, and (e) gross histology of the porcine liver lesion. The picture (a) is drawn on the base of (e) and shows the lesion position and size. All modes give a good assessment of the size and shape of the treated region.

Absorption. The absorption coefficient changes under HIFU treatment and this change is particularly large once tissue proteins have denatured. The absorption coefficient can be measured from the backscattered (or transmitted) amplitude versus time. This imaging technique is being developed for clinical implementation.

Temperature. Temperature rise in tissue (even before a lesion has formed) can be measured indirectly by a change of sound speed (travel time) in the tissue [120–122]. With sufficient scatterers in tissue, in either
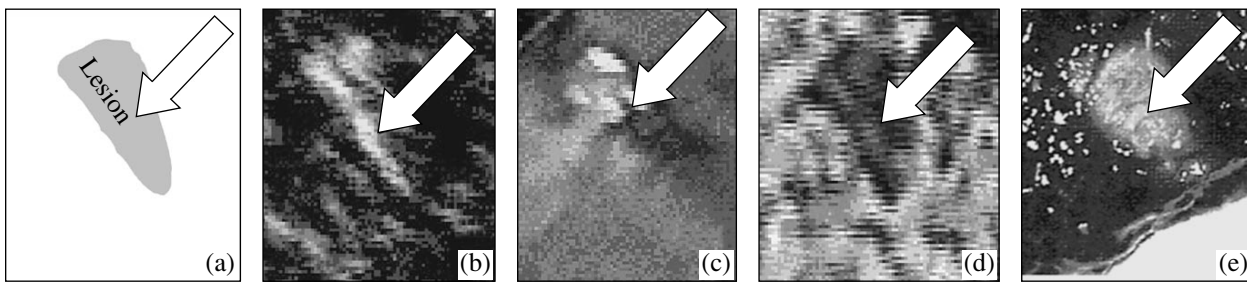
Fig. 17. Three ultrasound images and a gross-histology image of an HIFU lesion in bovine liver. Arrows indicate the lesion. The lesion position and shape are shown in the left picture (a). Hyperecho on B-mode (b) reveals the lesion but fades with time as bubbles dissolve from the lesion. Injection of echo contrast and Doppler mode imaging (c and d) reveal bright colorful signal in areas of healthy blood perfusion and show the necrosed tissue by negative contrast. All images correlated well with the size and shape of the lesion (a and e).

the frequency or time domain, the time between backscattered signals can be tracked and correlated with local sound speed. This technique has shown excellent research results but is not yet used clinically. The challenge appears to be obtaining sufficient scatters and image frames to maintain correlation between frames, especially during rapid heating. The weakness of the method results from the fact that sound speed may increase with temperature until denaturing and then decrease, which gives two values of temperature for a measured sound speed [89].

Shear. The dramatic increase in shear modulus of the lesion due to cross-linked proteins makes the lesion clear in elastography [123, 124] or vibro-acoustography [125, 126]. However, these techniques require modified equipment for applying displacements and detecting the change in backscatter under these displacements. The method is to resolve small displacements in stiff regions, such as the lesion, from large displacements in less stiff tissue by differential imaging with and without an applied force. The skill in elastography is in balancing displacement with imaging frame rate to maintain sufficient coherence between differential frames. Out-of-plane motion is particularly difficult to correct. Displacement can be produced by the HIFU itself and used in imaging [127]. Especially with bubbles in the lesion and the high absorption in necrosed tissue, radiation force is great on the lesion and displacements can be high [25: Lizzi *et al.,* pp. 267–274].

DISCUSSION AND CONCLUSIONS

Therapeutic ultrasound uniquely can treat a specific region in the body without harming surrounding or intervening tissue. Through ultrasound thermal and mechanical effects, activated by specific selections of frequency, amplitude, or waveform, an array of therapies can be affected. In addition, ultrasound can simultaneously provide real-time imaging for diagnosis, targeting, and monitoring of therapy. By targeting specific ailments, therapeutic ultrasound has established a clinical presence, and it has the potential for broad clinical application.

Five technical challenges were identified in order to fulfill the potential of therapeutic ultrasound: acoustic access, real-time imaging, treatment planning, dosimetry, and marketability. Transducer development, such as arrays, is making it possible to obtain high focal gains from existing acoustic windows. Transducers are becoming more powerful, smaller, and more efficient. Numerical modeling is guiding treatment planning. Novel methods of real-time imaging, calibration, and optimization of HIFU devices are being developed.

We suggest that understanding physical mechanisms is an integral to clinical success. The revealing example is the evolution of the concepts on the role of cavitation in lithotripsy and HIFU. Since the mid-1980s, shock wave lithotripsy (SWL) has been a common and effective clinical method to comminute kidney stones. Manufacturers have steadily increased the amplitude of the focus of devices and reduced the focal size in an effort to reduce the required number of shocks and to avoid tissue damage by restricting high acoustic pressures to the stone [28]. However, by many clinical measures, lithotripsy is becoming neither more efficacious nor safer [128, 129], because the designs neglect the mechanism of cavitation. On the other hand, the role of cavitation in HIFU was realized and efforts were made to avoid it. This fear of cavitation and an incomplete understanding of how to work with it have perhaps hindered clinical implementation of HIFU. Until recently, many machines and protocols were designed to heat tissue slowly and avoid cavitation pressure thresholds. Clinical machines currently treating patients in China operate quickly and utilize cavitation for effective tissue necrosis as well as real-time visualization and control of HIFU treatment.

We hope that this paper has given scientists in the other fields the background to apply their expertise to some of the challenges of therapeutic ultrasound.

ACKNOWLEDGMENTS

REFERENCES

1. S. Vaezy, M. Andrew, P. Kaczkowski, and L. Crum, Annu. Rev. Biomed. Eng. **3**, 375 (2001).

2. Echocardiography **18** (4), 309 (2001).

3. C. J. Diederich and K. Hynynen, Ultrasound Med. Biol. **25** (6), 871 (1999).

4. D. J. Coleman, F. L. Lizzi, R. H. Silverman, *et al.*, Ultrasound Med. Biol. **12** (8), 633 (1986).

5. F. J. Fry, N. T. Sanghvi, R. S. Foster, *et al.*, Ultrasound Med. Biol. **21** (9), 1227 (1995).

6. G. ter Haar, Ultrasound Med. Biol. **21** (9), 1089 (1995).

7. K. R. Erikson, F. J. Fry, and J. P. Jones, IEEE Trans. Sonics Ultrason. **21** (3), 144 (1974).

8. N. T. Sanghvi and R. H. Hawes, Exp. Invest. Endosc. **4** (2), 383 (1994).

9. D. Cathignol, in *Nonlinear Acoustics at the Beginning of the 21st Century: Proceedings of 16th ISNA, Moscow, 2002*, Ed. by O. V. Rudenko and O. A. Sapozhnikov (2003), Vol. 1, pp. 371–378.

10. A. K. Burov and G. D. Andreevskaya, Dokl. Akad. Nauk SSSR **106** (3), 445 (1956).

11. V. A. Burov, N. P. Dmitrieva, and O. V. Rudenko, Dokl. Akad. Nauk **383** (3), 101 (2002).

12. G. T. Clement and K. Hynynen, Phys. Med. Biol. **47** (8), 1219 (2002).

13. A. G. Visioli, I. H. Rivens, G. R. ter Haar, *et al.*, Eur. J. Ultrasound **9** (1), 11 (1999).

14. K. Hynynen, O. Pomeroy, D. N. Smith, *et al.*, Radiology **219** (1), 176 (2001).

15. F. Wu, W.-Z. Chen, J. Bai, *et al.*, Ultrasound Med. Biol. **27** (8), 1099 (2001).

16. N. T. Sanghvi, R. S. Foster, R. Bihrle, *et al.*, Eur. J. Ultrasound **9** (1), 19 (1999).

17. A. Gelet, J. Y. Chapelon, R. Bouvier, *et al.*, Eur. Urol. **40** (2), 124 (2001).

18. T. Uchida, N. T. Sanghvi, T. A. Gardner, *et al.*, Urology **59** (3), 394 (2002).

19. P. J. Polack, T. Iwamoto, R. H. Silverman, *et al.*, Invest. Ophthalmol. Visual Sci. **32** (7), 2136 (1991).

20. F. L. Lizzi, C. X. Deng, P. Lee, *et al.*, Eur. J. Ultrasound **9** (1), 71 (1999).

21. M. L. Denbow, I. H. Rivens, I. J. Rowland, *et al.*, Am. J. Obstet. Gynecol. **182** (2), 387 (2000).

22. C. Delon-Martin, C. Vogt, E. Chignier, *et al.*, Ultrasound Med. Biol. **21** (1), 113 (1995).

23. S. Vaezy, R. Martin, G. Keilman, *et al.*, J. Trauma **47** (3), 521 (1999).

24. K. Hynynen, V. Colucci, A. Chung, and F. Jolesz, Ultrasound Med. Biol. **22**, 1071 (1996).

25. *Proceedings of 2nd International Symposium on Therapeutic Ultrasound, Seattle, 2002*, Ed. by M. A. Andrew, L. A. Crum, and S. Vaezy (2003).

26. A. J. Coleman and J. E. Saunders, Ultrasonics **31**, 75 (1993).

27. M. Delius, Eur. Surg. Res. **34** (1–2), 30 (2002).

28. J. A. Moody, A. P. Evan, and J. E. Lingeman, in *Comprehensive Urology*, Ed. by R. M. Weiss, N. J. R. George, and P. H. O'Reilly (Mosby, New York, 2001), pp. 623–636.

29. B. Sturtevant, in *Smith's Textbook of Endourology*, Ed. by A. D. Smith, G. H. Badlani, D. H. Bagley, R. V. Clayman, G. H. Jordan, L. R. Kavoussi, J. E. Lingeman, G. M. Preminger, and J. W. Segura (Quality Medical, St. Louis, MO, 1996), Chap. 39, pp. 529–552.

30. S. Zhu, F. H. Cocks, G. M. Preminger, and P. Zhong, Ultrasound Med. Biol. **28** (5), 661 (2002).

31. M. Delius, F. Ueberle, and S. Gambihler, Ultrasound Med. Biol. **20** (3), 251 (1994).

32. M. Thiel, Clin. Orthop. Relat. Res. **387**, 18 (2001).

33. M. Maier, T. Saisu, J. Beckmann, *et al.*, Ultrasound Med. Biol. **27** (5), 665 (2001).

34. P. J. Fitzgerald, A. Takagi, M. P. Moore, *et al.*, Circulation **103** (14), 1828 (2001).

35. D. J. Coleman, F. L. Lizzi, J. Driller, *et al.*, Ophthalmology **92**, 347 (1985).

36. V. I. Filippenko and V. V. Tret'yak, Voen.–Med. Zh. **8**, 30 (1989).

37. E. I. Sidorenko, V. V. Filatov, and Yu. M. Alimova, Vestn. Oftalmol. **115** (2), 31 (1999).

38. A. L. Malcolm and G. R. ter Haar, Ultrasound Med. Biol. **22**, 659 (1996).

39. N. A. Watkin, G. R. ter Haar, and I. Rivens, Ultrasound Med. Biol. **22**, 483 (1996).

40. *IEEE Guide for Medical Ultrasound Field Parameter Measurements* (IEEE, New York, 1990), IEEE Std 790-1989.

41. ANSI S1.24 TR-2002 American National Standard Technical Report—Bubble Detection and Cavitation Monitoring (2002).

42. J. Ultrasound Med. **19**, 68 (2000).

43. R. L. Clarke and G. R. ter Haar, Ultrasound Med. Biol. **23** (2), 299 (1997).

44. C. R. Hill, Phys. Med. Biol. **15**, 241 (1970).

45. M. Brentnall, R. Martin, S. Vaezy, *et al.*, IEEE Trans. Ultrason. Ferroelectr. Freq. Control **48** (1), 53 (2001).

46. J. Y. Chapelon, D. Cathignol, C. Cain, *et al.*, Ultrasound Med. Biol. **26** (1), 153 (2000).

47. S. Vaezy, R. Martin, P. Kaczkowski, *et al.*, J. Vasc. Surg. **29** (3), 533 (1999).

48. S. Umemura, K. Sasaki, K. Kawabata, *et al.*, in *Proceedings of 1999 International IEEE Ultrasonics Symposium* (IEEE, 1999), Vol. 2, No. 99CH37027, p. 1439.

49. C. A. Cain and S. Umemura, IEEE Trans. Microwave Theory Tech. **34** (5), 542 (1986).

50. L. R. Gavrilov and J. W. Hand, IEEE Trans. Ultrason. Ferroelectr. Freq. Control **47** (1), 125 (2000).

51. J. P. Sferruzza, A. Birer, and D. Cathignol, Ultrasonics **38** (10), 965 (2000).

52. W. Eisenmenger, Ultrasound Med. Biol. **27**, 683 (2001).

53. O. V. Rudenko and O. A. Sapozhnikov, Moscow Univ. Phys. Bull. **46** (1), 5 (1991).

54. P. Zhong and Y. Zhou, J. Acoust. Soc. Am. **110**, 3283 (2001).

55. D. L. Sokolov, M. R. Bailey, and L. A. Crum, J. Acoust. Soc. Am. **110**, 1685 (2001).

56. A. P. Evan, L. R. Willis, B. A. Connors, *et al.*, J. Urol. **168** (4), 1556 (2002).

57. D. Cathignol, J. Tavakkoli, A. Birer, and A. Arefiev, IEEE Trans. Ultrason. Ferroelectr. Freq. Control **45** (5), 788 (1998).

58. N. S. Bakhvalov, Ya. M. Zhileikin, and E. A. Zabolotskaya, *Nonlinear Theory of Sound Beams* (Nauka, Moscow, 1982; AIP, New York, 1987).

59. P. Meaney, M. D. Cahill, and G. R. ter Haar, Ultrasound Med. Biol. **26**, 441 (2000).

60. F. P. Curra, P. D. Mourad, V. A. Khokhlova, *et al.*, IEEE Trans. Ultrason. Ferroelectr. Freq. Control **47**, 1077 (2000).

61. E. A. Filonenko and V. A. Khokhlova, Akust. Zh. **47**, 541 (2001) [Acoust. Phys. **47**, 468 (2001)].

62. M. A. Averkiou and R. O. Cleveland, J. Acoust. Soc. Am. **106**, 102 (1999).

63. T. Christopher, J. Comput. Acoust. **1**, 371 (1993).

64. S. S. Kashcheeva, O. A. Sapozhnikov, V. A. Khokhlova, *et al.*, Akust. Zh. **46**, 211 (2000) [Acoust. Phys. **46**, 170 (2000)].

65. J. Tavakkoli, D. Cathignol, R. Souchon, and O. A. Sapozhnikov, J. Acoust. Soc. Am. **104**, 2061 (1998).

66. P. T. Christopher and K. J. Parker, J. Acoust. Soc. Am. **90**, 488 (1991).

67. S. Ginter, M. Liebler, E. Steiger, *et al.*, J. Acoust. Soc. Am. **111**, 2049 (2002).

68. W. H. Press, S. A. Teukolsky, W. T. Vetterling, and B. P. Flannery, *Numerical Recipes in FORTRAN*, 2nd ed. (Cambridge Univ. Press, New York, 1992).

69. *Nonlinear Acoustics*, Ed. by M. F. Hamilton and D. T. Blackstock (Academic, San Diego, 1998), pp. 66–106.

70. J. Naze Tjotta, S. Tjotta, and E. H. Vefring, J. Acoust. Soc. Am. **89**, 1017 (1991).

71. B. Ystad and J. Bernsten, Acta Acust. (China) **3**, 323 (1995).

72. G. Wojcik, J. Mould, Jr., F. L. Lizzi, *et al.*, in *Proceedings of 1995 Ultrasonics Symposium* (IEEE, 1995), p. 1617.

73. T. Kamakura, T. Ishivata, and K. Matsuda, J. Acoust. Soc. Am. **107**, 3035 (2000).

74. A. C. Baker, A. M. Berg, A. Sahin, and J. Naze Tjotta, J. Acoust. Soc. Am. **97**, 3510 (1995).

75. T. Kamakura, M. Tani, Y. Kumamoto, and K. Ueda, J. Acoust. Soc. Am. **91**, 3144 (1992).

76. V. A. Khokhlova, R. Souchon, J. Tavakkoli, *et al.*, J. Acoust. Soc. Am. **110**, 95 (2001).

77. H. H. Pennes, J. Appl. Physiol. **1**, 93 (1948).

78. V. A. Khokhlova, N. Miller, R. Ollos, *et al.*, in *Proceedings of 17th International Congress on Acoustics* (Rome, 2001), p. 186.

79. S. Sapareto and W. Dewey, J. Radiat. Oncol. Biol. Phys. **10** (6), 787 (1984).

80. V. A. Akulichev, in *High-Intensity Ultrasonic Fields*, Ed. by L. D. Rozenberg (Nauka, Moscow, 1968; Plenum, New York, 1971).

81. C. C. Church, J. Acoust. Soc. Am. **86**, 215 (1989).

82. O. A. Sapozhnikov, V. A. Khokhlova, M. R. Bailey, *et al.*, J. Acoust. Soc. Am. **112**, 1183 (2002).

83. T. J. Matula, P. R. Hilmo, B. D. Storey, and A. J. Szeri, Phys. Fluids **14** (3), 913 (2002).

84. Z. Ding and S. M. Gracewski, J. Acoust. Soc. Am. **96** (6), 3636 (1994).

85. F. Chavrier, J. Y. Chapelon, A. Gelet, and D. Cathignol, J. Acoust. Soc. Am. **108**, 432 (2000).

86. R. G. Holt and R. A. Roy, Ultrasound Med. Biol. **27** (10), 1399 (2001).

87. J. E. Field, Phys. Med. Biol. **36**, 1475 (1991).

88. A. Philipp, M. Delius, C. Scheffczyk, *et al.*, J. Acoust. Soc. Am. **93**, 2496 (1993).

89. J. C. Bamber and F. Dunn, in *Encyclopedia of Acoustics*, Ed. by M. J. Crocker (Wiley, New York, 1997), Vol. 3, pp. 1699–1726.

90. Y. Y. Botros, J. L. Volakis, P. VanBaren, and E. S. Ebbini, IEEE Trans. Biomed. Eng. **44** (11), 1039 (1997).

91. M. Lokhandwalla and B. Sturtevant, Phys. Med. Biol. **46** (2), 413 (2001).

92. P. P. Lele, in *Ultrasound: Medical Applications, Biological Effects and Hazard Potential*, Ed. by M. H. Repacholi, M. Grandolfo, and A. Rindi (Plenum, New York, 1986), pp. 275–306.

93. M. R. Bailey, L. N. Couret, O. A. Sapozhnikov, *et al.*, Ultrasound Med. Biol. **27**, 696 (2000).

94. O. A. Sapozhnikov, Akust. Zh. **37**, 760 (1991) [Sov. Phys. Acoust. **37**, 395 (1991)].

95. D. L. Sokolov, M. R. Bailey, L. A. Crum, *et al.*, J. Endourol. **16** (10), 709 (2002).

96. P. Lele and A. Pierce, in *Proceedings of Workshop on Interaction of Ultrasound and Biological Tissues, Seattle* (DHEW, Washington, 1972), No. 73-8008, p. 121.

97. W. J. Fry, J. Acoust. Soc. Am. **22**, 867 (1950).

98. H. T. O'Neil, J. Acoust. Soc. Am. **21**, 516 (1949).

99. O. V. Rudenko, Moscow Univ. Phys. Bull., No. 6, 18 (1996).

100. O. A. Sapozhnikov, T. V. Sinilo, and Yu. A. Pishchalnikov, in *Nonlinear Acoustics at the Turn of the Millennium: Proceedings of 15th International Symposium on Nonlinear Acoustics, Goettingen, Germany, 1999*, Ed. by W. Lauterborn and T. Kurz (Am. Inst. of Physics, 2000), pp. 483–486.

101. F. O. Schmitt and B. Uhlemeyer, Proc. Soc. Exp. Biol. Med. **27**, 626 (1930).

102. L. A. Crum and G. M. Hansen, Phys. Med. Biol. **27**, 413 (1982).

103. S. Vaezy, X. Shi, R. W. Martin, *et al.*, Ultrasound Med. Biol. **27**, 33 (2000).

104. E. L. Carstensen, D. S. Campbell, D. Hoffman, *et al.*, Ultrasound Med. Biol. **16**, 687 (1990).

105. P. Zhong, Y. Zhou, and S. Zhu, Ultrasound Med. Biol. **27**, 119 (2001).

106. A. Vogel and W. Lauterborn, J. Acoust. Soc. Am. **84**, 719 (1988).

107. L. A. Crum, in *Proceedings of Ultrasonics Symposium* (1982), Vol. 1, p. 1.

108. T. R. Morgan, V. P. Laudone, W. D. Heston, *et al.*, J. Urol. **139**, 186 (1988).

109. S. L. Poliachik, W. L. Chandler, P. D. Mourad, *et al.*, Ultrasound Med. Biol. **27** (11), 1567 (2001).

110. J. Tavakkoli, A. Birer, A. Arefiev, *et al.*, Ultrasound Med. Biol. **23** (1), 107 (1997).

111. J.-Y. Chapelon, J. Margonari, F. Vernier, *et al.*, Cancer Res. **52**, 6353 (1992).

112. F. J. Fry and L. K. Johnson, Ultrasound Med. Biol. **4**, 337 (1978).

113. R. O. Cleveland, D. A. Lifshitz, B. A. Connors, *et al.*, Ultrasound Med. Biol. **24**, 293 (1998).

114. M. Lokhandwalla, J. A. McAteer, J. C. Williams, Jr., and B. Sturtevant, Phys. Med. Biol. **46** (4), 1245 (2001).

115. K. Hynynen, Ultrasound Med. Biol. **17** (2), 157 (1991).

116. A. J. Coleman, J. E. Saunders, L. A. Crum, and M. Dyson, Ultrasound Med. Biol. **13**, 69 (1987).

117. C. Chaussy, W. Brendel, and E. Schmiedt, Lancet **2** (8207), 1265 (1980).

118. R. E. Apfel and C. K. Holland, Ultrasound Med. Biol. **17** (2), 179 (1991).

119. C. X. Deng, Q. Xu, R. E. Apfel, and C. K. Holland, Ultrasound Med. Biol. **22** (7), 939 (1996).

120. R. Seip and E. S. Ebbini, IEEE Trans. Biomed. Eng. **42** (8), 828 (1995).

121. R. Maass-Moreno, C. A. Damianou, and N. T. Sanghvi, J. Acoust. Soc. Am. **100**, 2522 (1996).

122. M. Ribault, J.-Y. Chapelon, D. Cathignol, and A. Gelet, Ultrason. Imaging **20** (3), 160 (1998).

123. R. Souchon, L. Soualmi, M. Bertrand, *et al.*, Ultrasonics **40**, 867 (2001).

124. X. Shi, R. W. Martin, D. Rouseff, *et al.*, Ultrason. Imaging **21** (2), 107 (1999).

125. M. Fatemi and J. F. Greenleaf, Proc. Natl. Acad. Sci. USA **96** (12), 6603 (1999).

126. E. E. Konofagou, J. Thierman, T. Karjalainen, and K. Hynynen, Ultrasound Med. Biol. **28** (3), 331 (2002).

127. O. V. Rudenko and A. P. Sarvazyan, Crit. Rev. Biomed. Eng., No. 3, 6 (2000).

128. J. E. Lingeman, Urol. Clin. North Am. **24**, 185 (1997).

129. J. J. Rassweiler, C. Renner, C. Chaussy, and S. Thuroff, Eur. Urol. **39** (2), 187 (2001).

Physical and Technical Aspects of Ultrasonic Brain Imaging through Thick Skull Bones:
2. Experimental Studies

S. V. Baykov*, L. V. Babin**, A. M. Molotilov***, S. I. Neĭman**, V. V. Riman**, V. D. Svet*, and A. I. Selyanin**

* Andreev Acoustics Institute, Russian Academy of Sciences, ul. Shvernika 4, Moscow, 117036 Russia
** State Research Institute of Instrument Making, Yurlovskiĭ proezd 1, Moscow, 127490 Russia
*** OOO AMM-2000, Spasskiĭ tupik 6, Moscow, 129090 Russia
e-mail: vsvet@akin.ru
Received August 20, 2002

Abstract—Experimental results of the ultrasonic imaging of brain structures through thick skull bones are presented. The model imaging system and the ultrasonic images of blood vessel models and images obtained *in vivo* for some brain structures are described. © 2003 MAIK "Nauka/Interperiodica".

The first part of this paper [1] described the methods of ultrasonic imaging of brain structures through thick skull bones [2]. Our numerical and physical simulations showed that, with the use of broadband signals and the subsequent correlation compression combined with matched spatial filtering, these methods are capable of providing ultrasonic images with transverse and longitudinal resolutions of 1–1.5 mm and 0.5–1 mm, respectively, in the frequency band from 1.7 to 2 MHz. Below, we present some experimental results.

THE MODEL SYSTEM

The model imaging system was only intended for the experimental validation of the approach proposed by us. Therefore, the main requirements imposed on the system were as follows: first, it should have a simple design, and, second, it should provide an operating environment that allows the user to view and analyze the signals at every stage of the processing procedure and change the necessary parameters and even the algorithms in the course of the operation. Operation of the system in real time was not required.

Figure 1 shows a generalized structural diagram of the model system. It consists of four main functional units: a multielement piezoelectric sensor (*1*); a transmitter–receiver module; a signal processor; a personal computer; and a cell (*3*), which contained a phantom of the skull bone or a fragment of a real skull bone (*2*), nylon strings (*4*), and silicon pipes of various diameters to imitate blood vessels. The cell (*3*) was filled with a liquid whose acoustic parameters were close to those of brain tissue (see table, composition 7, see below).

As a transmitting–receiving antenna, we used one of the commercially available 128-element piezoelectric sensors operating at a center frequency of $F = 1.7$ MHz. The antenna was additionally damped on its rear side to increase the half-power bandwidth to 700 kHz. The reception sensitivity was 2 μV/Pa. The sensor dimensions were 85×20 mm. Like other similar sensors for ultrasonic diagnostics, it contained a silicon cylindrical lens whose focal line was parallel to the larger dimension. The transmitter–receiver module was used to amplify the signals (on transmitting and receiving) and to switch the elements of the piezoelectric matrix in a specified order.

The main component of the signal processing system was a TMS320C40 signal processor, which was supplied with a 14-bit A/D–D/A converter and a num-
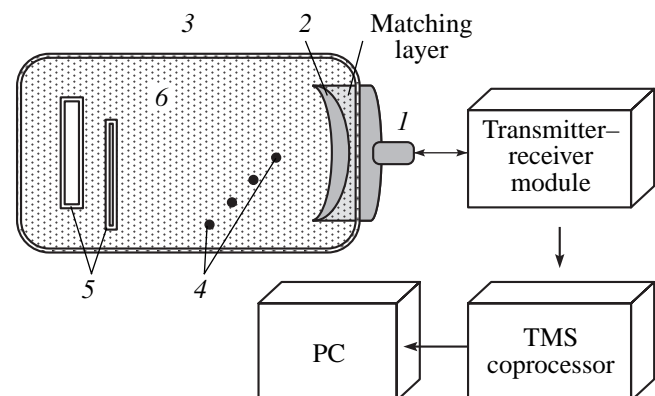

Fig. 1. Functional diagram of the model system: (*1*) multielement piezoelectric sensor; (*2*) bone phantom or a real skull bone fragment; (*3*) cell; (*4*) nylon strings; (*5*) silicon simulators of blood vessels; (*6*) liquid.

ber of additional service circuits. A personal computer (PC) controlled the processor and processed the images. As the operating environment, we chose the Labview software package running on the Windows operating system.

The TMS320C40 signal processor performed the following operations:

—generated simple 0.5- to 1-μs-long radio pulses;

—generated complex (up to 60-μs-long) broadband signals modulated in a special manner;

—redistorted the frequency spectrum of the transmitted signals in a prescribed manner;

—received echo signals from the transmitter–receiver module and preamplified them by up to 85 dB;

—quantized the signals received;

—generated inphase and quadrature signals;

—correlated and compressed the signals with a compression ratio of 80;

—stored the compressed signals in the random-access memory; and

—transmitted all signals via a common bus to the personal computer.

Let us briefly explain the signal processing principle. Since the equipment should be most simple and no real-time operation is required, the system generates images by the aperture synthesis method, which is used in synthetic aperture radars whose platform moves. Of course, in our case, the sensor did not move, but this principle was used to create the antenna pattern for both transmission and reception.

Simplistically, the principle may be represented as follows. At the initial time moment, a signal is emitted by either one element of the sensor or by several elements (we could enable no more than eight elements simultaneously). The echo signals are received by all sensor elements and are stored in the processor's memory, accurate to phase distortions. Then, the same signal is emitted by the second element of the sensor (or by the next few elements), and the whole procedure is repeated. As a result of this sequential operation of transmission and reception, a 128×128 matrix is created in the signal processor's memory, each element of this matrix containing 160 inphase and quadrature signals represented by 32-bit numbers. Here, it should be noted that, in this sequential operation, signals fed to the sensors have the same amplitudes but different phases. Therefore, in the subsequent aperture synthesis, we can form the required wave front of the emitted wave, in particular, by focusing it in angle and range at a given observation region. The aperture synthesis is thus performed twice, on transmission and reception. The process of recording the field and reconstructing the image from it is similar to the holographic technique, in which the signal recording, the formation of the hologram, and its reconstruction are separated in time.

THE PHANTOM SKULL BONE

The quality of ultrasonic diagnostic instruments is usually tested by special phantom biological tissues, for instance, the 530ATC Labs or 515ATC Labs samples [3, 4].

For our study, it was necessary to develop and fabricate a phantom bone tissue whose geometric and acoustic parameters are close to those of the skull bone. To test the main parameters of the phantom bone, we used fragments of real thick skull bones.

From the viewpoint of physics, the synthesis of tissuelike materials for given acoustic parameters can be reduced to finding the concentrations of various substances whose combination gives the required properties. The effective density of such a material can be represented as a linear combination of partial densities D_k of the component materials:

$$D_0 = D_1 N_1 + D_2 N_2 + \ldots + D_k N_k, \tag{1}$$

where N_k is the volume concentration.

A similar expression can be written for the effective absorption:

$$A_0 = A_1 N_1 + A_2 N_2 + \ldots + A_k N_k. \tag{2}$$

The effective compressibility can also be written as

$$K_0 = K_1 N_1 + K_2 N_2 + \ldots + K_k N_k, \tag{3}$$

where the adiabatic compression is related to the density and the velocity of sound as

$$K_k = D_k^{-1} C_k^{-1}.$$

By solving the system of these equations under the mass conservation condition

$$N_1 + N_2 + \ldots + N_k = 1, \tag{4}$$

one can in principle find the unknown concentrations of the component materials. Without going into a detailed analysis of these equations, let us formulate the main conclusions:

(i) To fabricate a phantom whose parameters (velocity of sound, density, and sound attenuation) are close to those of a real bone, one should use at least four substances, because the system of equations (1)–(4) contains four unknown concentration parameters N_{1-4}.

(ii) In general, a combination of the component substances cannot guarantee the required acoustic parameters, because, for arbitrary D_k, A_k, and K_k, the system of equations (1)–(4) may have no solution at all or yield a physically meaningless solution ($N_k < 0$ or $N_k > 1$).

Although the material can be synthesized by the above technique, it is rather laborious in practice, because the number of real substances suitable for fabricating a bone tissue simulator is quite limited. Therefore, we synthesized the bone phantom using a different approach that requires no accurate calculation of the

component substance concentrations. This approach relies on the least-squares technique and searching for values of $(N_1, N_2, \ldots N_k)$ such that the parameters D, A, and K be closest to D_0, A_0, and K_0.

Consider the function F,

$$
\begin{aligned}
F = {} & (d_1 N_1 + d_2 N_2 + \ldots + d_k N_k - 1)^2 \\
& + (a_1 N_1 + a_2 N_2 + \ldots + a_k N_k - 1)^2 \\
& + (k_1 N_1 + k_2 N_2 + \ldots + k_k N_k - 1)^2 \\
& + (N_1 + N_2 + \ldots + N_k - 1)^2,
\end{aligned}
\tag{5}
$$

where $d_i = D_i/D_0$, $a_i = A_i/A_0$, and $k_i = K_i/K_0$. In this case, N_i can be found by solving the system of equations

$$
dF/dN_i = 0. \tag{6}
$$

This method allows one to effectively and rather quickly calculate the appropriate substance concentrations, although the accuracy of these calculations is not very high. After this, the acoustic parameters are fitted experimentally by varying the concentrations of the substances. The experimental results obtained at a frequency of 1.7 MHz with various compositions are summarized in the table. Note that the velocity of sound was measured to within 3%; the absorption, within 2%; and the density, within less than 3%. As can be seen from these data, the parameters of compositions 1 and 6 are closest to those of the bone tissue. These compositions were chosen for fabricating the phantom.

Note that composition 7 is widely used in phantom biological tissues. Composition 6 was chosen as a basis for the phantom skull bone. It was used to fabricate a 10.3-mm-thick fragment whose curvature was close to that of a real 9.5-mm-thick skull bone. Both fragments were mounted in a cell made of transparent plastic. The cell itself was asymmetric, and its edges were bent so as to minimize the field reflected by the cell walls. No special absorbers were mounted on the cell walls. Above the cell, a positioner was installed, which was used to manipulate the simulators of blood vessels and other objects. To minimize multiple reflections between the surface of the matrix and the surface of the bone and to better match the sensor, an additional slightly absorbing liner was placed between the sensor and the outer surface of the bone phantom.

A photograph of the cell with the phantom skull bone and a real bone fragment is shown in Fig. 2.

EXPERIMENTAL RESULTS

First of all, we will demonstrate the main effects produced by a thick skull bone and how they manifest themselves in the reconstructed images. Figure 3a shows the time distribution of intensity of the signal received in the central angular spatial channel without
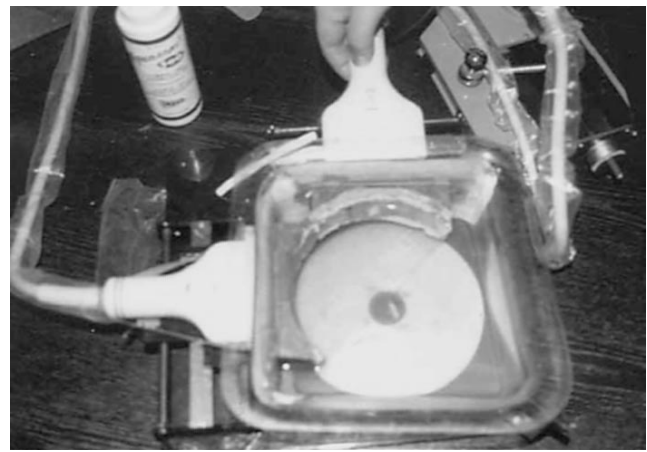
Fig. 2. Photograph of the cell with the piezoelectric sensors, the phantom bone, and the skull bone fragment.

the matched processing, and Fig. 3b shows the same distribution with the matched processing.

As can be seen from Fig. 3a, initially, intense multiple reflections from the bone predominate over the useful signal, which is almost unrecognizable, because it is two orders of magnitude smaller than the multiple

Compositions for the bone and brain tissue phantoms

| Composition	Acoustic parameters		
	density, g/cm^3	velocity, m/s $\times 10^5$	absorption, dB/cm
Skull bone	1.2–1.8	2.7–4.1	14–19
Brain tissue	0.95	1.52	1.5
1. Bone meal, 70% Joiner's glue, 30%	1.83	2.41	17
2. Bone meal, 65% Casein, 35%	1.32	2.21	9.1
3. Bone meal, 65% Epoxy resin, 35%	1.37	2.21	7.3
4. Tungsten powder, 20% Epoxy resin, 80%	1.65	3.15	9.5
5. Tungsten powder, 25% Epoxy resin, 75%	1.90	3.05	12.8
6. Tungsten powder, 30% Epoxy resin, 70%	2.15	2.95	16.5
7. Glycerol, 60% Alcohol, 30% Water, 10%	0.95	1.55	1.4

Magnitude $s(t)$
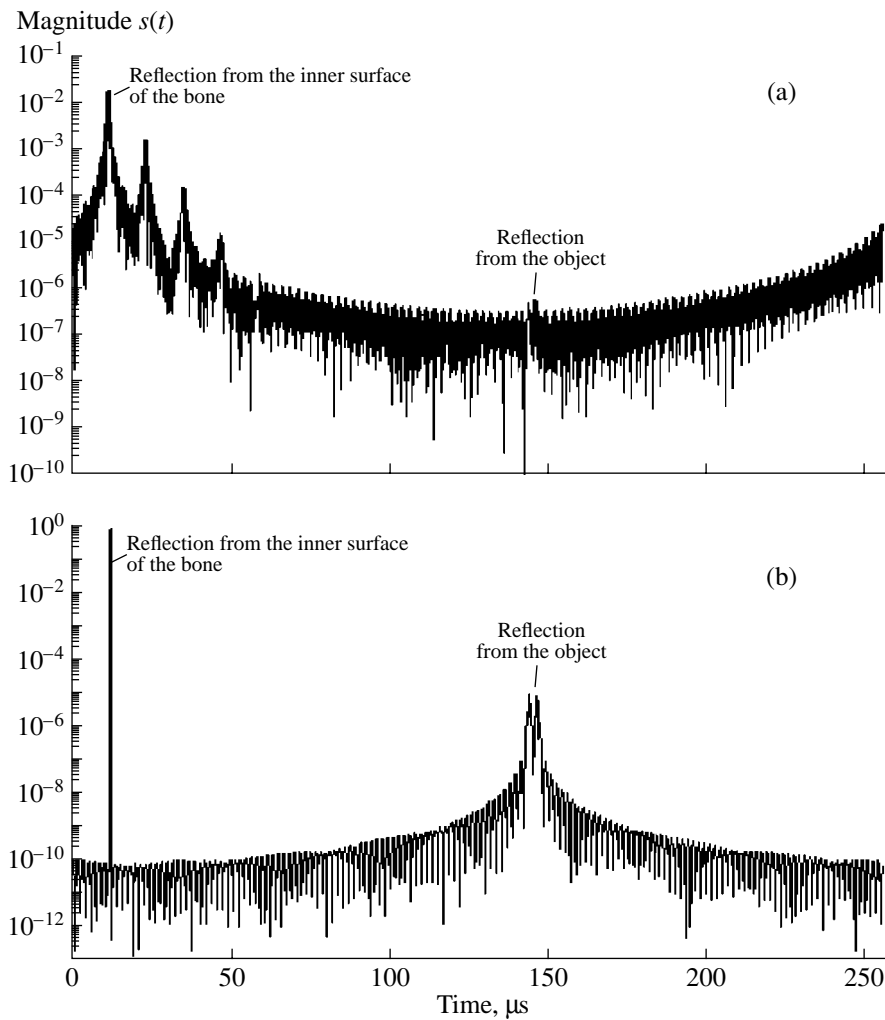
Fig. 3. Signal intensity distribution in the central angular channel obtained (a) without matched processing and (b) with matched processing.

reflections. Figure 3b demonstrates the effect of matched filtering: the multiple reflections are compressed into one signal at the beginning of the time sequence, and the signal produced by the point source is reliably extracted against the noise.

Figures 4a and 4b show ultrasonic images of point reflectors obtained in two modes. Five such reflectors (0.5-mm-diameter nylon strings) were placed in an angular sector of 0°–30° at various distances from the sensor. Since the angle of total internal reflection in the bone is within 27°–32°, this reflector arrangement occupies almost the entire angular field of the sensor.

The image in Fig. 4a was obtained in the usual *B*-scan mode, which does not use processing matched with the bone. The image clearly shows the main distortions introduced by the thick skull bone. The upper part of the picture contains bright stripes caused by multiple reflections of the ultrasonic signal in the bone. Since the photograph cannot reproduce the entire dynamic range of brightness and this range is strongly compressed, the

stripes occupy a small area in the figure, although they actually cover a much greater depth. In the other part of the figure, acoustic images of the point reflectors are observed. These images are seen to be greatly distorted and defocused.

The photograph in Fig. 4b shows the same images obtained with the use of matched filtering. The processing algorithms only used information about the bone's shape. The spread in transfer factors (local attenuation coefficients) proved to be small (no more than 15%). Note that the image in Fig. 4b was obtained with a complex 40-μs-long phase shift keyed signal. The local thickness values of the skull bone fragment were obtained with a simple 0.5-μs-long pulsed signal. The ultrasonic field intensity was no higher than 150 mW/cm^2. It is clearly seen that, first, the matched filtering effectively (although not completely) compresses the multiple reflection signals and, second, the images of the point reflectors prove to be focused and their linear dimensions almost coincide with the theo-
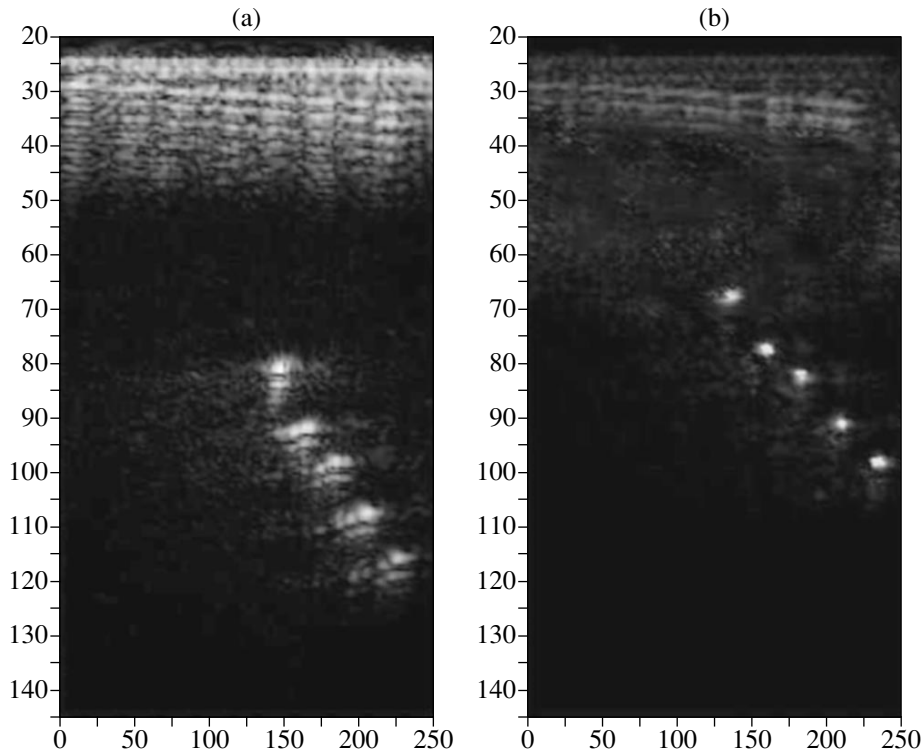
Fig. 4. Images of five point reflectors obtained through the fragment of a thick skull bone (a) without matched processing and (b) with matched processing.
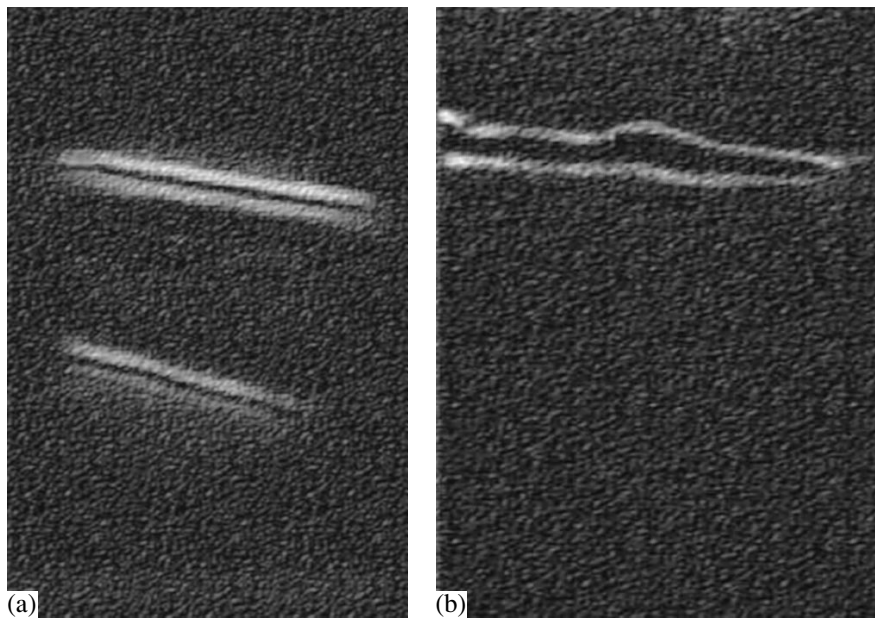
Fig. 5. Acoustic images of blood vessel models: (a) two 3- and 2-mm-diameter vessels placed at distances of 50 and 105 mm, respectively, from the inner surface of the skull bone fragment and (b) a model of a blood vessel with a progressive aneurysm placed at a distance of 45 mm from the bone (the average diameter is 3.5 mm).

retical dimensions of the spatial resolution element for the particular sensor aperture, frequency, and signal bandwidth.

The next photographs (Figs. 5a, 5b) show the acoustic images obtained for the blood vessel models made of silicon rubber tubes of various diameters and thick-

(a)　　　　　　　　　　(b)　　　　　　　　　　(c)

Fig. 6. Images of the venous sinus (cross section): (a) figure from an atlas; (b) X-ray angiography image, blood flow alone is seen; and (c) *in vivo* ultrasonic image, skull bones and walls of the venous sinus are seen.

(a)　　　　　　　　　　(b)　　　　　　　　　　(c)

Venous
sinus

Fig. 7. Image of the venous sinus (longitudinal section): (a) figure from an atlas; (b) X-ray angiography image, the venous sinus is seen as a white arc in the upper part of the figure; (c) ultrasonic image of the sinus, a curved venous channel is clearly seen.

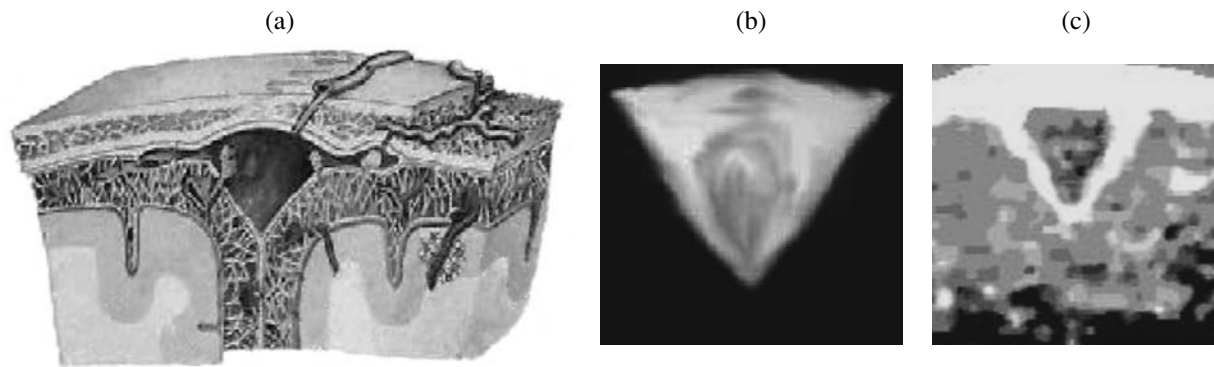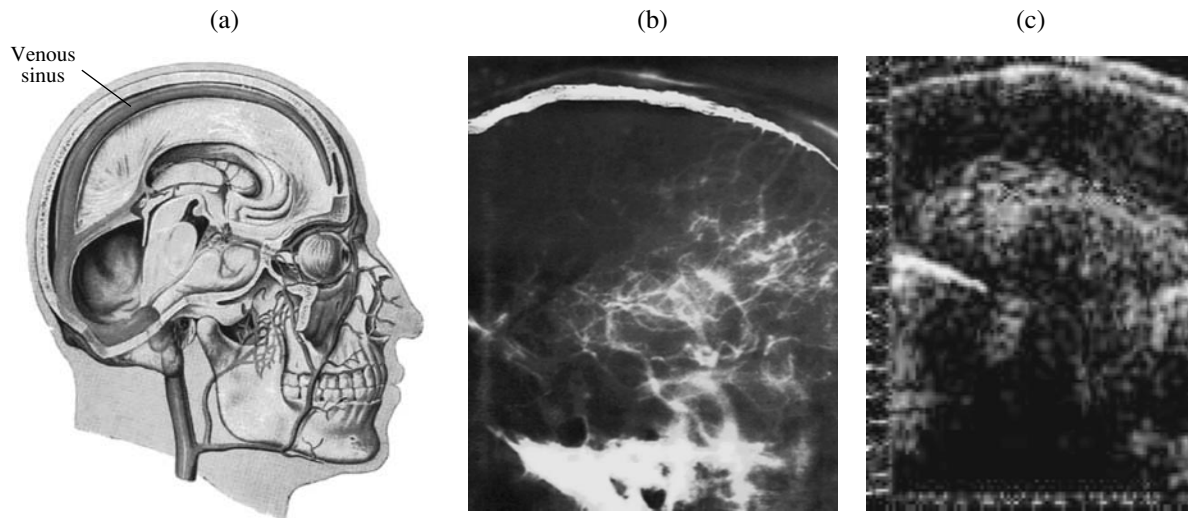nesses by echo-sounding through a thick bone and the subsequent processing with the use of matched filtering. One of the tubes modeled a vessel with a progressive aneurysm.

Our experiments corroborated the possibility of the acoustic imaging of brain structures through thick skull bones with a spatial resolution close to the theoretically predicted value. It was therefore of interest to obtain an *in vivo* acoustic image of a brain structure. Because the model system itself did not provide real-time images, we first recorded ultrasonic holograms with different positions of the sensor on the head and then used them to reconstruct the image. In these experiments, we could not use the techniques used previously for matching the sensor to the phantom skull bone. Therefore, the sensor was applied to the head through a special gel-like liner (bolus), which was actually lossless at the operating frequency, and the velocity of ultrasonic waves in it was close to the velocity of sound in water.

By applying the sensor in this way, it is impossible to avoid multiple reflections between the sensor and the bone. Therefore, to reduce the distortions of the image by these reflections, the liner was chosen to be rather thick (2.8 cm).

An unexpected result was the possibility of operation at a low intensity of about 100 mW/cm^2. This signal intensity was found to be sufficient for receiving echo signals reflected from depths of up to 110 mm with the actual average thickness of the skull bone under the sensor being approximately 12 mm. The length of the sounding signal was varied within 35 to 60 μs. As the object of observation, we chose the venous sinus, which is a bony mass located in the central part of the skull containing a major vessel that collects the brain's venous blood. Simplistically, the venous sinus can be viewed as a prolate triangular groove. Therefore, an acoustic image of its cross section must be close to a triangle. In the course of the *in*

vivo experiment, we faced additional problems caused by the irregularity of the inner boundary of the skull bone. One of them (the most difficult one) was that the real bone may have a double curvature, while the ultrasonic sensor is supplied with a silicon cylindrical lens, which forms a knife-edge beam pattern. Therefore, if the sensor is placed on a double-curved part of the bone, the narrow beam may leave the observation plane due to the additional lateral refraction, which makes it impossible to receive the echo signals. Since the second curvature also cannot be compensated for in the linear sensor, the beam deflection cannot be removed from or taken into account in the given model system instrumentally. Therefore, we had to choose places for the sensor such that the reflected beam remained in the observation plane. For this purpose, the sensor may be inclined within a small range to minimize the aforementioned effect.

Figure 6a shows an image of the venous sinus borrowed from an atlas; Fig. 6b, its X-ray angiography image; and Fig. 6c, an ultrasonic image obtained from a volunteer. Even though the imaging arrangement and the technique were far from optimal (see remarks above), the images are very similar, except that the angiography only shows the blood flow while the ultrasonic image pictures the vessel walls. Figures 7a, 7b, and 7c show similar longitudinal sections of the venous sinus. The X-ray image looks like a thick line, while the ultrasonic image resembles a longitudinal section of a bent pipe.

CONCLUSIONS

Our experiments corroborated that the technology for ultrasonic imaging of brain structures [1, 2] through thick skull bones is valid and can be used as a basis for ultrasonic transcranial diagnostic systems. The use of matched signal processing, complex signals, and signal compression allows one to overcome the problems associated with high ultrasonic attenuation in skull bones and with the wave front distortions caused by the irregular shape of thick bones. The range and azimuth resolution attained in the experiment was close to the system's hardware resolution.

The study has also revealed additional problems. It was found that the design of ultrasonic sensors must be changed to allow them to be used on double-curved solid surfaces. The best solution is a two-dimensional matrix sensor (matrix) similar to the one used in the ultrasonic imaging camera [5]. However other designs are possible, for example, a linear sensor with a different passive focusing system and different size of receiving elements. The receiving elements themselves must have a broad enough bandwidth. Experiments showed that the relative bandwidth must be no less than 07–0.8. An important problem is to measure the bone profile with the highest accuracy. These measurements should use higher sounding frequencies in order to better estimate the local delays (phases), because the phase errors in the antenna elements on the order of $\lambda/4$ (where λ is the wavelength) reduce the concentration factor by 2 to 3 dB. In addition, due to the double curvature, the bone profile should be measured in several closely located sections in order to decrease the measurement error.

An important element of the system is the device that matches the sensor to the head's surface (bone). Its design must minimize the unwanted multiple reflections between the sensor's surface and the bone. As for the signal processing system, it must be digital and allow parallel processing. As was noted in [2], the best structure is the "elementary channel–A/D converter" circuit. Although this solution leads to a more complex and expensive system, it is capable of supporting all additional image processing programs: three-dimensional imaging, Doppler mapping, and blood flow visualization by the speckle interferometry method [6].

REFERENCES

1. S. V. Baĭkov, A. M. Molotilov, and V. D. Svet, Akust. Zh. **49**, 332 (2003) [Acoust. Phys. **49**, 276 (2003)].

2. A. M. Molotilov, V. D. Svet, and S. V. Baykov, in *Proceedings of World Congress on Cerebral Embolism, New Orleans, LA, USA* (1998).

3. L. V. Osipov, *Ultrasonic Diagnostic Instruments* (VIDAR, Moscow, 1999).

4. *Physical Principles of Medical Ultrasonics*, Ed. by C. R. Hill (Ellis Horwood, Chichester, 1986; Mir, Moscow, 1989).

5. S. V. Baykov, V. D. Svet, and V. I. Sizov, in *Acoustical Imaging* (Plenum, New York, 1998), pp. 122–131.

6. N. V. Zuĭkova, T. V. Kondrat'eva, and V. D. Svet, Akust. Zh. **47**, 664 (2001) [Acoust. Phys. **47**, 578 (2001)].

Translated by A. Khzmalyan

Standard Source Method in Passive Acoustic Thermal Tomography

K. M. Bograchev and V. I. Passechnik[†]

ELDIS Research Center, Institute of Radio Engineering and Electronics,
Russian Academy of Sciences, Starosadskiĭ per. 8, Moscow, 101000 Russia
e-mail: laboratory@userline.ru
Received March 27, 2002

Abstract—Potentialities of passive acoustic thermal tomography in reconstructing the 2D temperature distribution in a human body are studied. Special attention is given to the estimation of the maximal temperature value. A method for its exact reconstruction is proposed. The method uses the assumption that the temperature distribution is formed by a local heat source and is based on the selection of the parameters of such a source by the minimization of the residual of the measured and hypothetical values of the acoustic brightness temperature. The accuracy of the determination of the maximal in-depth temperature by different methods is analyzed by numerical simulation. It is demonstrated that the proposed method provides a higher accuracy than Tikhonov's methods of global and local regularization, especially with a heat source at great depth. The proposed method is shown to cause no systematic error in the reconstruction of temperature peaks at great depth. The possibility of reconstructing a two-peak temperature distribution by the proposed method is demonstrated. © *2003 MAIK "Nauka/Interperiodica".*

One of the important areas of research in modern acoustics is the utilization of intrinsic thermal acoustic radiation of objects for monitoring the in-depth distribution of the temperature T of a human body in hyperthermia used in oncology [1, 2] and in thermal ablation [3]. As is well known, in the case of hyperthermia, it is necessary, within 30–40 min, to monitor the slowly varying temperature in a tissue, which is 42 to 43°C; i.e., it differs from the temperature at the body surface by 5–6°C. In the case of thermal ablation, the procedure lasts for about ten minutes, and the tissue temperature rises up to ~100°C. The precise measurement of the maximal temperature value in the region under study is especially important. The measurements by the method of passive acoustic thermal tomography encounter certain difficulties.

As is well known, a line of piezoelectric transducers positioned on the body surface is used to measure the temperature distribution within a human body. Their spread functions lie in a single plane. The quantity measured is the intensity of thermal acoustic radiation emitted from different points of the body at different angles. Since the signal source is thermal noise, the intensity values obtained by averaging the signal over a time of about 30 s, i.e., the so-called acoustic brightness temperatures, are measured to a certain accuracy $\delta T \sim$ 0.1 K, which cannot be reduced further. The resulting data set (about 300–400 measurements) is the initial information for solving the inverse problem of reconstructing the distribution of the temperature *T*.

The procedure of temperature reconstruction in passive acoustic thermal tomography is the key element of this kind of tomography. From the mathematical point of view, it is the solution of a 2D ill-posed inverse problem. The inaccuracy of this solution can exceed the measurement error [4]. It is possible to improve the solution by using *a priori* information on the processes of heat transfer (the so-called biothermal equation) [1, 2], and this possibility was confirmed by subsequent studies [2, 5, 6].

Several methods were used to solve the inverse problem: (1) Tikhonov's global and local regularizations (*a priori* information on the processes of heat transfer was taken into account in this case, and the efficiency of algorithms in a wide range of variation of the problem parameters was investigated [5, 6]) and (2) quadratic programming with the minimization of the functional including the *a priori* information on the equation of heat transfer [7]. The general formulation of the problem of temperature reconstruction with allowance for the *a priori* information on the heat sources is given in [8]. The numerical simulation [2, 5, 6] showed that, despite the small root-mean-square error, the maximal temperature value is reconstructed with a large systematic error.

The purpose of this study is to develop a new algorithm for solving the inverse problem with allowance for the information on the possible parameters of the heat source and, with its help, to clarify the ability of a passive acoustic thermal tomograph to reconstruct the maximal temperature value.

[†] Deceased.

We consider the problem of reconstructing the thermodynamic temperature $T(x, y)$ within a square region with the dimensions $l_x \times l_y$, $0 \le x \le l_x$; $0 \le y \le l_y$, where $l_x = 10$ cm and $l_y = 10$ cm. The measurements of the acoustic brightness temperature, which are necessary to solve the inverse problem, are conducted by scanning the region with a set of piezoelectric transducers. These transducers are positioned equidistantly on the body surface, and each of them can scan several angles.

As is well known, the acoustic brightness temperature b^δ determined with an error δ ($\delta \sim 0.1$ K) is described by the equation

$$\int_0^\infty \gamma(l)T(l)\exp\left(-\int_0^l \gamma(\xi)d\xi\right)dl = b^\delta, \qquad (1)$$

where l is the coordinate along the acoustic axis of a piezoelectric transducer. The components of the two-dimensional Fourier transform $u = F(T(x, y))$ of the thermodynamic temperature are related to the measured acoustic brightness temperatures by the formula

$$Au = b^\delta, \qquad (2)$$

where the matrix A is determined by the geometry of scanning over the region of interest and by the distribution of the absorption coefficient γ.

The problem is solved with allowance for the equation of thermal diffusivity (the biothermal equation) for the thermodynamic temperature:

$$-x_D^2\Delta T + T = q_T, \qquad (3)$$

where x_D is the characteristic distance determined by the thermodynamic properties of the medium and by the volume blood circulation [2], Δ is the two-dimensional Laplacian, and q_T is the density of linear temperature sources. Equation (3) for the Fourier components can be written in the form

$$Lu = q, \qquad (4)$$

where L is the operator depending on the number of harmonic n_x, n_y:

$$L = 1 + (2\pi x_D)^2[(n_x/l_x)^2 + (n_y/l_y)^2]. \qquad (5)$$

Here, the total number of harmonics is $N_H = \text{Max}(n_x \times n_y) = 256$ if the region under study is divided into 16×16 subregions.

The general problem of reconstructing the temperature distribution by the minimization of the functional

$$\Phi^\alpha = \left\|Au - b^\delta\right\|^2 + \alpha\|Lu - q\|^2 \qquad (6)$$

was formulated in [7] (the solution stabilizer is omitted in the latter expression). The main difficulty in using Eq. (6) consists in the fact that, in the general case, the source described by the quantity q is unknown. Therefore, only approximate methods were used until now.

Two methods of reconstructing $T(x, y)$ were proposed in [2, 5]: the methods of Tikhonov's global and local regularization. The functional

$$\Phi^\alpha = \left\|Au - b^\delta\right\|^2 + \alpha\|Lu\|^2 \qquad (7)$$

was minimized. It differs from Eq. (6) in that only part of the biothermal equation (4) was taken into account, while the effect of sources was ignored by setting

$$q = 0. \qquad (8)$$

In the case of local regularization, the operator L was used. In the case of global regularization, in addition to the above assumption, the characteristic length in the operator L was assumed to be equal to zero: $x_D = 0$, and, as a result, it was turned into a unit operator.

These methods provide an opportunity to determine with a sufficient accuracy the coordinates of a heat source. Unfortunately, a specific feature of these methods is the considerable distortion of the height and shape of the temperature peak. As the distance from the surface grows, the peak becomes flatter, the deeper its position is, and the reconstructed value of the maximal temperature T_{MAX} may be underestimated by ~50%.

It is possible to demonstrate that the poor reconstruction of the maximal temperature by the local algorithm is not connected with the approximation given by Eq. (8). For this purpose, it is sufficient to introduce two independent variables into functional (6): the vector u of the Fourier components of the temperature and the vector q of the Fourier components of the source density. (In this case, it is necessary to have the total number of measurements exceeding the total number of unknowns $2N_H$.) It is easy to show that, in this case, the problem of Eq. (6) is reduced to the problem of Eq. (7), and the solution coincides with that for the case of the local regularization with the same number of measurements and, therefore, has the same disadvantages. In other words, the validity of the biothermal equation for the object under investigation in itself contains insufficient information for a considerable improvement of the solution. Hence, it is necessary to include more detailed information on the heat source.

The "standard source" is proposed in [9] for a more accurate determination of the maximal temperature. Its essence lies in the fact that, by virtue of the validity of the biothermal equation, the temperature maximum in the region under study can be formed only due to the existence of heat sources, and their shape can be preset on physical grounds. This method is close to the method of taking into account *a priori* physical information about the desired solution, which is expressed in the form of preset functions. An essential difference is the fact that the corresponding functions do not directly describe the temperature distribution but are involved indirectly through the right-hand side, i.e., the sources of the biothermal equation. Taking into account this feature, this method was called the standard source method.
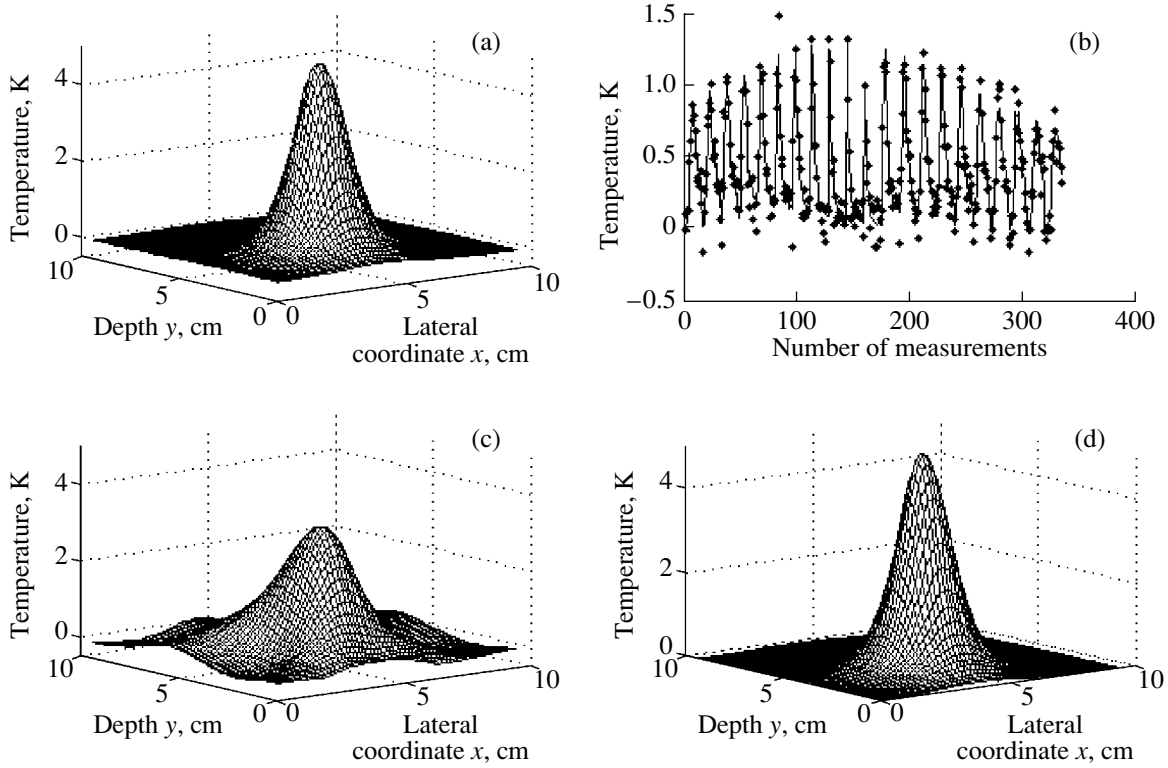
Fig. 1. Examples of reconstructing the temperature distribution $T(x, y)$ by different methods with one of the distributions of the random measurement error (the rms error is $\delta T = 0.1$ K). The heat source has one peak at a depth of 3 cm with a coordinate along the body surface (the lateral coordinate) of 4 cm. The temperature value at the maximum is equal to 5 K. (a) The initial temperature distribution $T(x, y)$; (b) the dependence of the "measured" acoustic temperature on the number of measurements: the solid line shows the dependence in the absence of noise and the dots correspond to the dependence with superimposed noise; (c) reconstruction of this distribution by Tikhonov's local regularization (the reconstructed temperature value at the maximum is $T_{MAX} \approx 3.7$ K); and (d) reconstruction by the standard source method, $T_{MAX} \approx 5.2$ K. $x_D = 0.8$ cm.

In the standard source method, the functional for the Fourier components of temperature $u^{\alpha, \varepsilon}$ is minimized. It includes in explicit form the Fourier components q^{ε} of the heat source Q_S^{ε} characterized by the set of parameters ε:

$$\Phi^{\alpha, \varepsilon} = \left\| Au^{\alpha, \varepsilon} - b^{\delta} \right\|^2 + \alpha^{\varepsilon} \left\| Lu^{\alpha, \varepsilon} - q^{\varepsilon} \right\|^2. \quad (9)$$

Here, α^{ε} is the regularization parameter depending on the parameters ε.

Using a standard minimization scheme, it is easy to demonstrate that, for each set of parameters ε, the minimum of functional (9) can be determined within the framework of the algorithm of Tikhonov's local regularization. Correspondingly, the Fourier components of temperature $u^{\alpha, \varepsilon}$ have the form

$$u^{\alpha, \varepsilon} = \left(A^T A + \alpha^{\varepsilon} L^T L\right)^{-1} \left(A^T b^{\delta} + \alpha^{\varepsilon} L^T q^{\varepsilon}\right). \quad (10)$$

Here, the upper index T denotes transposition, and the minimal value of the regularization parameter α^{ε} at the given values of the source parameters ε is determined from the condition that the residual of the measured

acoustic brightness temperature becomes equal to the rms error of measurements: $\sqrt{\left\| b^{\delta} - Au^{\alpha, \varepsilon} \right\|^2} = \delta T$.

After determining the solution at the given set of parameters ε and corresponding value of α^{ε}, the total residual of functional (9) is calculated:

$$\Delta^{\varepsilon} = \sqrt{\left\| Au^{\alpha, \varepsilon} - b^{\delta} \right\|^2 + \alpha^{\varepsilon} \left\| Lu^{\alpha, \varepsilon} - q^{\varepsilon} \right\|^2}. \quad (11)$$

In the general case, the problem of minimizing the functionals of the type of Eq. (11) is solved, and the values of the parameters ε and α^{ε} that deliver its minimal value are determined.

The method of numerical simulation involved setting the initial heat source, estimating the distribution of the thermodynamic temperatures in an object, and interpolating these data to obtain smooth functions of coordinates. Then, the calculation of the matrix A and the acoustic brightness temperatures was performed, and the inverse problem was solved with the help of local regularization (see [5] for details).

In this paper, we chose two models of a standard source with one and two peaks, respectively. In the first
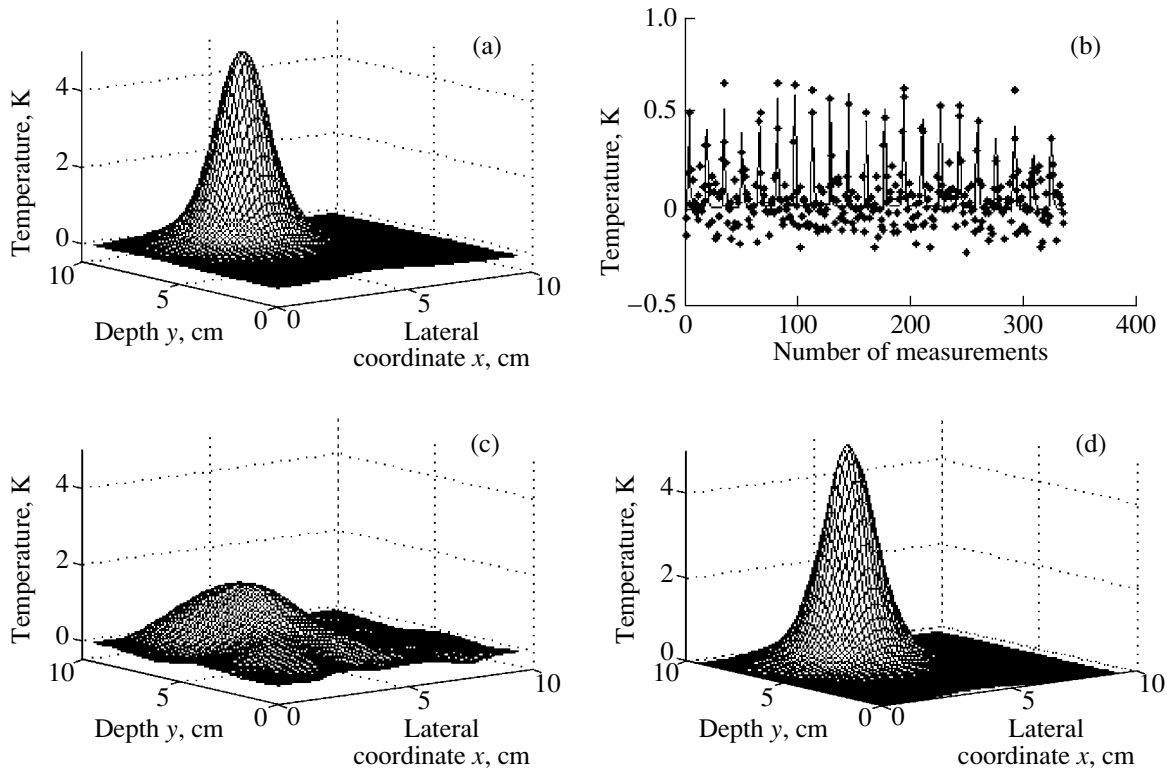
Fig. 2. The same as in Fig. 1 for a source depth of 7 cm.

case, we used the source approximation by the Gaussian function

$$Q_S = \varepsilon_1 K(\varepsilon_2) \exp\{-[(x-\varepsilon_3)^2 + (y-\varepsilon_4)^2]/\varepsilon_2^2\}, \quad (12)$$

which was characterized by four parameters: the intensity ε_1, the width (the characteristic spatial dimension) ε_2, and two coordinates, namely, the lateral position ε_3 (the x axis) and the depth ε_4 (the y axis). The correction factor was $K(\varepsilon_2) = K_0/\varepsilon_2^2$, where K_0 is a constant. Such a function $K(\varepsilon_2)$ was introduced to improve the process of minimization for functional (9). The point is that both parameters ε_1 and ε_2 affect the solution of the two-dimensional biothermal equation (3), which can be easily demonstrated. The maximal temperature value T_{MAX} is proportional to the source intensity ε_1, and, at the same time, an increase in the characteristic spatial dimension ε_2 of small-size heat sources also leads to an increase in T_{MAX} in proportion with ε_2^2. The factor $K(\varepsilon_2) = K_0/\varepsilon_2^2$ compensating the latter effect provides an opportunity to reduce the influence of the two parameters on one another and improves the convergence of the iteration process in the minimization of functional (9).

The initial source was specified by the same Eq. (12) for a single selected set of parameter values. The normalization used for the initial source was such that the maximal temperature value in the temperature distribution corresponding to this source was 5 K (the height of the temperature peak was determined from the interpolated function). The Fourier components of the source q were obtained from the distribution given by Eq. (12) with the help of conventional programs. A standard

Characteristics of the initial and reconstructed temperature distributions and the parameters of the standard source (mean values and standard errors for ten numerical experiments). The source of heating is at a depth of 7 cm

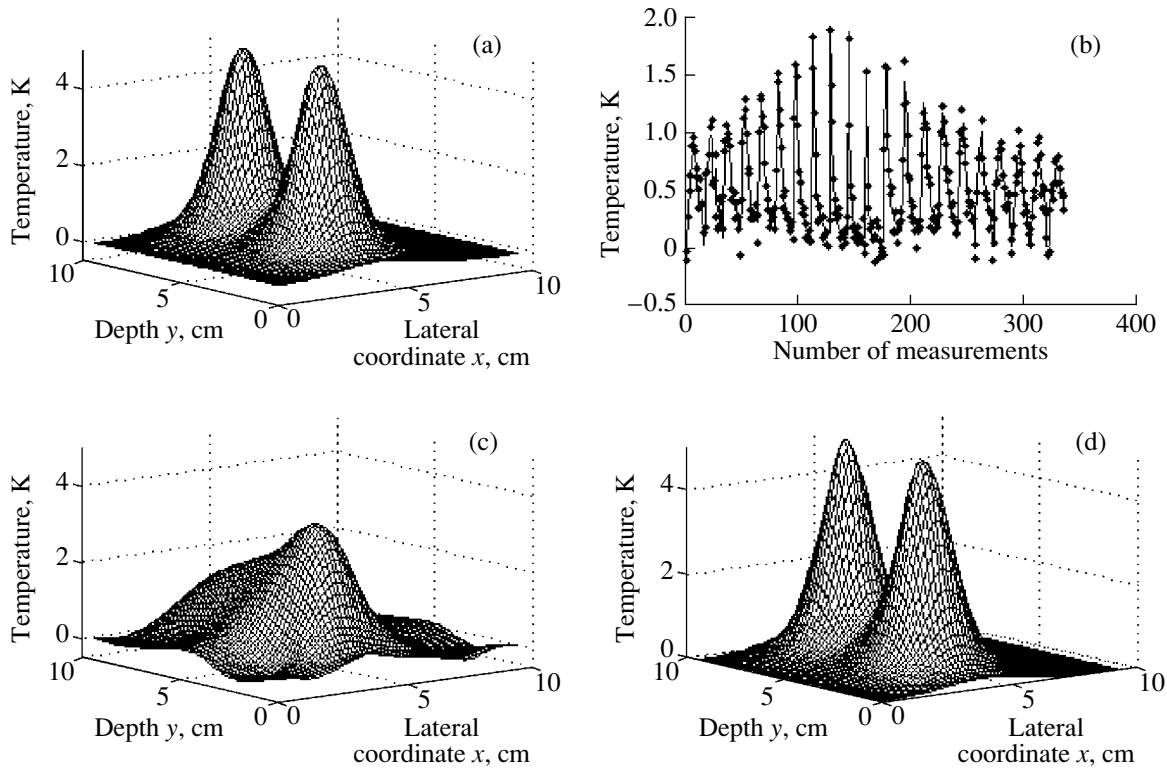| Initial $T(x, y)$ and reconstructed $T_R(x, y)$ temperature distributions		T_{MAX}, K	Parameters of the standard source			
			intensity ε_1, rel. units	width ε_2, cm	lateral position ε_3, cm	depth ε_4, cm
$T(x, y)$	Reconstruction method	5	1	0.8	4	7
$T_R(x, y)$	Standard source	5.32 ± 0.59	0.86 ± 0.16	0.6 ± 0.22	4.1 ± 0.21	6.69 ± 0.24
	Local regularization	1.83 ± 0.24				

Fig. 3. Reconstruction of the temperature field produced by a complex source characterized by two equal temperature peaks with heights of 5 K at the depths of 3 and 7 cm.

(and initial) source with two peaks was preset in the second model. It was characterized by eight parameters, ε_1–ε_8, respectively. The corresponding optimization programs were written using MatLab 5.3 software.

The proposed standard source method was used to reconstruct the temperature distribution with the peak value $T_{MAX} = 5$ K, which was produced by a Gaussian heat source with a width of 0.8 cm. The source was positioned at two distances: 3 and 7 cm from the surface (Fig. 1). The initial temperature distribution $T(x, y)$ produced by the source in the shallow position, i.e., at a depth of 3 cm, has one peak (Fig. 1a). Figure 1b demonstrates the dependence of the "measured" acoustic brightness temperatures on the number of measurements: the solid line shows the dependence in the absence of noise, and the dots, the dependence with the superimposed measurement error $\delta T = 0.1$ K. In the reconstruction of this distribution by the method of Tikhonov's local regularization, the maximal temperature value is $T_{MAX} \approx 3.7$ K (Fig. 1c). In the reconstruction of the distribution $T(x, y)$ by the standard source method (Fig. 1d), the value $T_{MAX} \approx 5.2$ K is almost the same as for the initial distribution.

Figure 2 presents the corresponding results of calculations for a source positioned at the greater depth of 7 cm. Comparing Fig. 1b and Fig. 2b, one can see that the reconstruction problem becomes much more difficult when the source is farther from the surface,
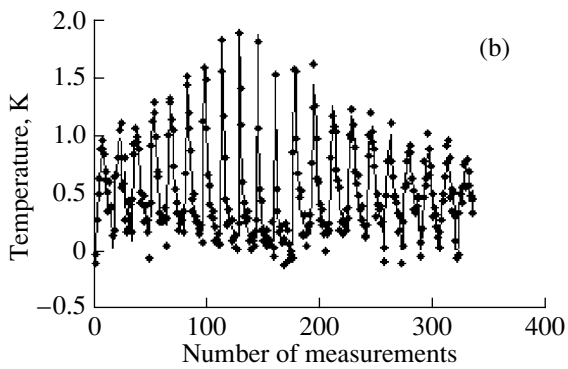
because the signal-to-noise ratio strongly decreases. The data shown in Fig. 1c and Fig. 2c illustrate the result that is well known from [2, 5]: the method of Tikhonov's local regularization considerably underestimates the maximal temperature values, the values of T_{MAX} decreasing fast as the source is shifted away from the body surface. At the same time, this disadvantage is absent in the standard source method, and the maximal temperature values are reconstructed to a high accuracy (Fig. 2d).

The reconstruction error depends on the specific realization of noise in the course of measurement. The table shows the corresponding data for the reconstruction of the temperature distribution produced by the source lying deep inside the object (at a depth of 7 cm). One can see that the maximal temperature value is adequately reconstructed with a small systematic error by the standard source method. In this case, the random scatter of temperature is ~0.6 K. At the same time, the method of Tikhonov's local regularization leads to a very large systematic error (~60%). It is necessary to note that the reconstructed parameters of a standard source are also close to the initial ones: the source coordinates are reconstructed well, but its intensity and width are reconstructed worse.

The standard source method provides an opportunity to obtain a good spatial resolution. Figure 3 shows the temperature reconstruction for the case when the

heat source is double and produces two temperature peaks that occur at the depths 3 and 7 cm below the body surface (Fig. 3a). The method of local regularization does not resolve these two peaks (Fig. 3c). At the same time, the standard source method reconstructs both peaks with correct heights (Fig. 3d).

The standard source method was also tested by simulating various situations arising in the reconstruction of temperature distributions in hyperthermia and thermal ablation. It turned out that it is possible to successfully reconstruct the temperature distributions produced by an asymmetric source with different dimensions along the x and y axes. Large temperature peaks corresponding to a temperature difference of ~70 K, which are characteristic of thermal ablation, can also be adequately reconstructed. The reconstruction quality is reasonable even when the measurement error is increased up to $\delta T = 0.4$ K (a considerable possible increase in δT is caused by the necessity to reduce the time of measurements in the dynamic process of thermal ablation).

Thus, the utilization of the standard source method as an algorithm for the image reconstruction provides a reliable determination of the shape of any temperature distribution with one or two peaks. Moreover, it allows a fairly accurate calculation of the maximal temperature value, including the case when the heat source is relatively far from the object's surface (~7 cm). The results of this study allow one to expect that the standard source method will provide efficient and accurate measurements of the peak values of in-depth temperature in hyperthermia and thermal ablation. However, it should be noted that the question of how much it is possible to increase the resolution of passive acoustic tomography with the help of this more advanced method of reconstruction in comparison with the well-known estimates [6] needs special investigation.

REFERENCES

1. V. I. Passechnik, A. A. Anosov, and K. M. Bograchev, Biomed. Radioélektron., No. 2, 3 (1999).
2. Yu. V. Gulyaev, K. M. Bograchev, I. P. Borovikov, *et al.*, Radiotekh. Élektron. (Moscow) **43** (9), 1140 (1998).
3. G. S. Gazelle, S. N. Goldberg, L. Solbiati, and T. Livraghi, Radiology **217** (3), 633 (2000).
4. V. I. Passechnik, A. A. Anosov, and M. G. Isrefilov, Int. J. Hyperthermia **15** (2), 123 (1999).
5. K. M. Bograchev and V. I. Pasechnik, Akust. Zh. **45**, 742 (1999) [Acoust. Phys. **45**, 667 (1999)].
6. K. M. Bograchev and V. I. Passechnik, Akust. Zh. **48**, 467 (2002) [Acoust. Phys. **48**, 406 (2002)].
7. M. S. Bosnyakov and Yu. V. Obukhov, Pattern Recogn. Image Anal. **12** (1), 57 (2002).
8. I. P. Borovikov, Yu. V. Obukhov, V. P. Borovikov, and V. I. Passechnik, Radiotekh. Élektron. (Moscow) **44** (6), 1 (1999).
9. K. M. Bograchev, I. P. Borovikov, M. S. Bosnyakov, *et al.*, in *Proceedings of XI Session of the Russian Acoustical Society* (GEOS, Moscow, 2001), pp. 169–172.

Translated by M. Lyamshev

Correlation Characteristics and Travel Time Differences for Hydroacoustic Signals under Directional Reception at Different Depths

O. P. Galkin and S. D. Pankova

Andreev Acoustics Institute, Russian Academy of Sciences, ul. Shvernika 4, Moscow, 117096 Russia
e-mail: bvp@akin.ru
Received December 25, 2001

Abstract—Experimental data are presented for the cross-correlation coefficients and travel time differences of audible signals measured at distances of ~60 and ~120 km in an oceanic waveguide. The signals are received simultaneously by two highly directional vertical arrays (with a main lobe width of ~2°) whose centers are at depths of 200 and 450 m. The radiation depths of the pseudonoise signals were 200 and 400 m. The high correlation coefficients (0.75–0.94) obtained for the signals received at different depths suggest that the changes in the frequency spectra of signals arriving over different paths are almost identical. The small fluctuations of the travel time differences (≤0.43 ms for the "water" signals and ≤0.63 ms for the signals reflected from the sea surface) testify to their high stability. © 2003 MAIK "Nauka/Interperiodica".

Information on the stability of the time differences between signals propagating over different rays and on their variability with varying distance in real conditions of an oceanic waveguide is becoming increasingly important. In applied problems, data on the time differences between signals propagating over different rays are often used, for example, for determining the sound source locations [1, 2]. Different algorithms [3–6] were suggested for solving acoustic oceanological problems on the basis of data on the time differences between signal arrivals at spatially separated receivers. In most publications, the preference is given to signals with frequencies of several tens or hundreds of hertz. Such signals propagate with minimal losses, which is particularly important for operating at distances of 1000 km or more. In several works, the problems of improving the accuracy of the source localization with small signal-to-noise ratios are considered. To increase this ratio, in our opinion, one should use directional arrays, which allow one to increase not only the signal-to-ambient noise ratio but also the signal-to-signal interference ratio. The signal interference arises because of the multipath sound propagation in the waveguide, which leads to a nonsimultaneous arrival of signals at the reception point. To obtain a sufficiently narrow directional pattern in the vertical plane with an acceptable size of the arrays, it is necessary to operate at higher frequencies. In particular, when operating at distances of ten to several hundred kilometers, it is expedient to use the signals in a frequency range of 1–3 kHz. These frequencies are close to the optimal ones and allow one to arrange a directional reception of the arriving signals in the vertical plane with relatively small arrays.

When signals propagate over refracted (water) rays, i.e., without reflections from the waveguide boundaries, the correlation and spectral characteristics of the received signals depend on the sound attenuation in the water column. The attenuation factor is determined by the absorption of sound and its scattering by random inhomogeneities. A theoretical estimate [7] of the effect of inhomogeneities of the environmental refractive index on the rms fluctuation of the signal travel time gives the values $\sigma_\tau < 0.3$ ms for the distances $r = 55$–70 km and $\sigma_\tau < 0.48$ ms for $r = 115$–130 km. We must keep in mind that these values of σ_τ are obtained on the assumption that the whole signal propagation track is filled with large inhomogeneities whose size is within 110–115 m. Since smaller inhomogeneities are also present in the real medium and, because of vertical refraction, inhomogeneities may be absent in some portions of the total propagation track, these values of σ_τ should be considered as the upper bound. For signals propagating with reflections from the ocean surface, the estimate of the fluctuations of the propagation time [8] yields $\sigma_\tau < 1.0$–1.5 ms for distances $r \cong 55$–60 km with a surface roughness of Beaufort 3.

Experimental data often differ from theoretical data, which, naturally, cannot take into account the effect of all oceanic factors. Therefore, it is important to carry out investigations in field conditions to obtain reliable data on the parameters that affect the results and to compare the experimental characteristics with the theoretical estimates.

The aim of this study is the experimental investigation of the variability of travel time differences and the cross-correlation of the signals simultaneously received

at different depths by highly directional arrays in the vertical plane (with a main lobe width of ~2°) in the first and second convergence zones. The results of such experiments on estimating the effect of the inhomogeneities of the water column on the characteristics of the received signals not only allow one to test the physical models of real waveguides but also may be useful for constructing space-developed arrays.

Note that the application of directional receiving systems and a source of intense pseudonoise omnidirectional radiation allows one to study the correlation characteristics of signals with their resolution in both angle and arrival time and, in addition, with a high signal-to-noise ratio.

The experiments were carried out in a deepwater region of the Atlantic Ocean (the sea depth was $H \sim$ 5100–5200 m). The receiving RV, *Sergey Vavilov*, drifted with two arrays lowered from the stern and foremost bathyposts. The horizontal separation of the bathyposts was ~45 m. The transmitting RV, *Petr Lebedev*, either lay to or was held in place by slowly moving against the drift in the electromotion regime. In the first case, the transmit–receive distance varied slowly due to the difference in the ship drift speeds; in the second case, the distance varied faster.

An omnidirectional sound source located at depths of 200 or 400 m emitted a continuous pseudonoise signal in a frequency range of 0.8–1.3 kHz. Vertically extended flexible receiving arrays, whose centers were at depths of 200 and 450 m, simultaneously received the arriving signals. The arrays had an external diameter of 5 cm and a length of 40 m, and each one consisted of 296 nonequidistant receivers. The receivers were combined in 74 phase centers, which served for the formation of the directional pattern. At the lower end of each array, a 700-kg load was suspended. The large weight of the end loads and the small diameter of the flexible arrays provided the necessary vertical orientation of the receiving arrays. The experimentally measured deviation from the vertical did not exceed ~1°–1.5°.

The investigations were carried out in the first and second convergence zones with a high signal-to-noise ratio (no less than 20 dB). The surface roughness was about Beaufort 3. The signals were received simultaneously by three directional patterns, which could be used in both the scanning mode and the guidance mode at chosen arrival angles. The distance between the source and the receiving arrays was measured by special signals received by one of the patterns. The signal resolution in the arrival angles in the vertical plane at a mean frequency of 1 kHz was ~2°, and the resolution in arrival time was ~2 ms. To measure the time spectra, continuous records from 2 to 10 min long were made. In the intervals between the time spectrum measurements, the angular structure of the sound field was recorded at both depths of the array locations. In this case, two patterns were operated in the scanning mode

in an angular range of ±20° (the plus sign means the signal arrival at the array from above and the minus sign, from below). For example, Fig. 1 exhibits a photograph taken from the indicator screen when the signals were received simultaneously at two depths (200 and 450 m). As is known, in the convergence zones, except for regions near caustics, the curvature of the wave fronts is small and the angular structure slowly and smoothly changes with distance. Therefore, the array response to the signals arriving at angles that differ from each other by more than the angular width of the main lobe of the directional pattern is similar to its response to a plane wave. Thus, when the field is scanned along the vertical, the array response in the direction of each signal arrival will repeat the form of the directional pattern. To obtain this result with a 40-m-long vertical array, one has to move away from the caustic by only ~1 km. In Fig. 1, it is seen that the angular width of the response of each array to signals received at angles of –12°, –2.5°, +2°, and +10° for the external scanning and –14.5°, –6.5°, +5.5°, and +10.5° for the internal scanning almost coincide with the main lobe width (~2°) of the directional patterns of the arrays. This fact suggests that the signals that arrived at both reception depths under the above-mentioned angles traveled over separate rays.

Figures 2a and 2b represent the changes in the distance r between the points of emission and reception during the experiments. Figure 2a refers to the first convergence zone, and Fig. 2b, to the second zone. In these plots, the points indicate the instants of distance measurement, and the circles, the instants of measuring the correlation characteristics and travel time differences between the signals received from different directions in the vertical plane, i. e., between the signals with different arrival angles. The numbers next to the circles mean the numbers of the figures in which the results of the corresponding measurements will later be presented. By the curve slopes in Figs. 2a and 2b, one can judge the rate of change of the distance in these experiments. A small slope of the curves corresponds to the measurements with both ships drifting, while a large slope, to the motion of the transmitting ship. In each experiment, the transmitting ship returned close to its initial distance within several hours. When operating in the first zone, it returned in 13 hours, lay to, and then started moving to provide a faster increase in the distance. During the experiments in the second convergence zone, the transmitting ship returned only in 17 hours, and then, for a period of three hours, it was in motion mode, after which it lay to. Figure 2c exhibits the typical sound velocity profile $c(z)$ that was multiply measured during the experiments. The calculated values of the grazing angles of the rays touching the ocean surface are ±8° for a depth of 200 m and ±11° for a depth of 450 m.

The set of arrival time differences for the same signal traveling over different rays, which below will be called the time spectrum of the received signals, was
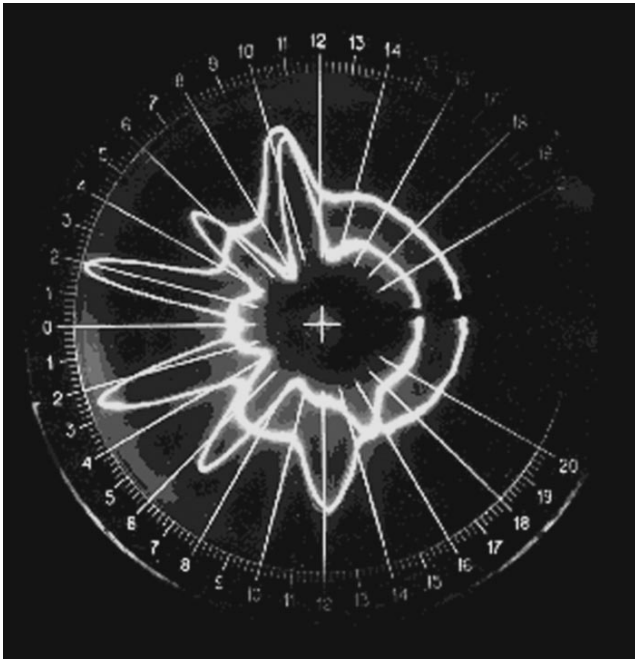
Fig. 1. Angular structure of the sound field for vertical arrival angles within ±20° for signals simultaneously received at depths of 200 and 450 m by 40-m-long vertical arrays.

measured by the correlation method. The cross-correlation functions between signals received at different depths were calculated by averaging over 1.024 s every 12 s; i.e., 10–49 independent measurements (N) of the correlation function were taken. The values of the time differences between the signal propagation over different rays were determined from the position of the correlation peaks $|R|$ on the delay axis τ. The set of the measured values of τ within the observation time t is precisely the time spectrum. Fluctuations of the time

spectra were estimated by the rms deviations σ_τ from the mean value $\bar{\tau}$ over N independent readings. In determining σ_τ, the trend of the mean values $\bar{\tau}$ with varying distance was excluded by the least squares method with a linear approximation.

Consider now the results of the measurements. Figures 3a and 3b present the time spectra for the signals received at different depths in the first convergence zone: Fig. 3a corresponds to a slow change in the distance between the points of emission and reception, and Fig. 3b, to a faster change. In Fig. 2a, the numbers 3a and 3b indicate the instants of performing these experiments. Figure 3a refers to the case when both ships drifted. Because of the small difference in the drift speed, the distance was changed by only 60 m during a 15-min observation. Figure 3b refers to the instant when the transmitting ship got on course to provide a faster increase in the distance. Here, the total change in distance was 190 m within the same observation time. Each of the plots exhibits two time spectra denoted by numbers *1* and *2* for two pairs of arrival angles. The values of the arrival angles and the depth of reception are also denoted in the figures: the grazing angle and its sign, in the numerator of the fraction; the depth of the array center, in the denominator. Thus, during the experiments, one of the three directional patterns was guided to the signal with an arrival angle equal to –6° (at a depth of 200 m); the other two arrays were guided to the signals with angles –(7.5°–8°) and –(11°–11.5°) (at a depth of 450 m). The correlation coefficients for both spectra (*1* and *2*) were within 0.84–0.87. Such large values of the cross-correlation coefficients $|R|$, or, more precisely, those lying in the interval $0.8 < |R| < 1$, in Fig. 3 and all subsequent figures are denoted by an asterisk. The plot in Fig. 3b is, in fact, a continuation of the plot shown in Fig. 3a. The time interval between the symbols, as noted above, is 12 s. The calculations
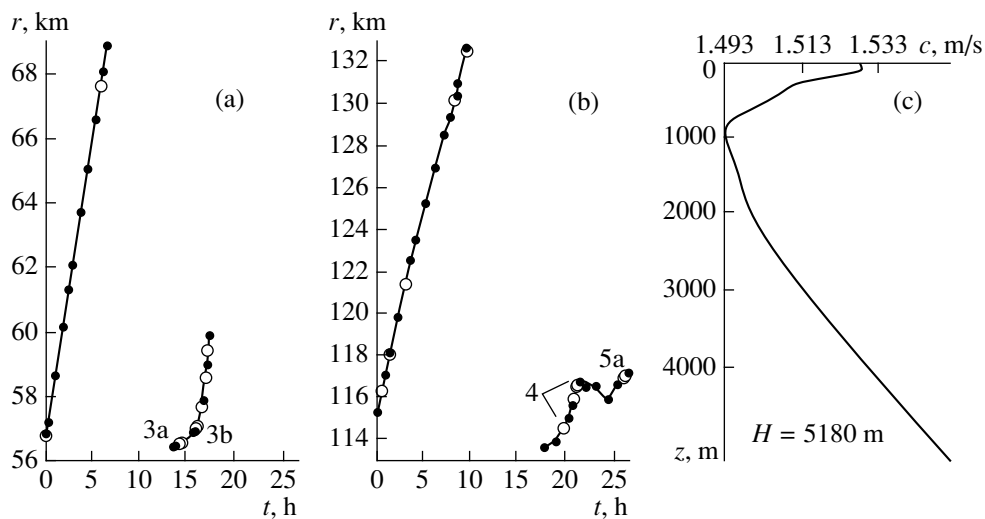

Fig. 2. Change in distance and the sound velocity profile $c(z)$ during the experiments: (a) change in distance in the first convergence zone; (b) change in distance in the second convergence zone; (c) $c(z)$ in the first and second zones during the experiments.
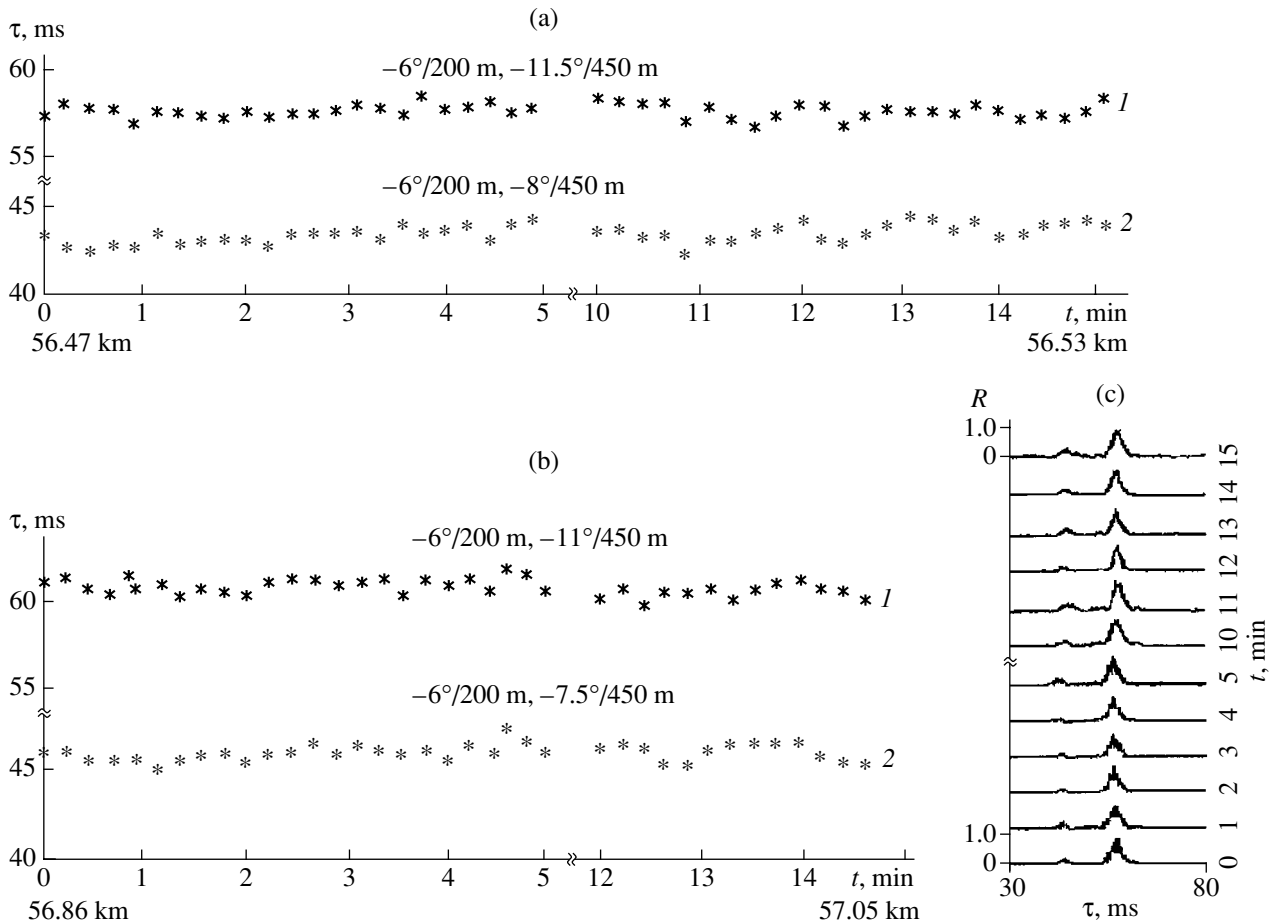
Fig. 3. Variability of the time spectra and cross-correlation functions for signals received at depths of 200 and 450 m in the first convergence zone; the source is at a depth of 200 m. (a) The transmitting and receiving ships are drifting; (b) the transmitting ship begins to move; (c) the cross-correlation functions for signals with the arrival angles $\alpha_1 = -6°$ and $\alpha_2 \cong -8°$ (the data correspond to curve 2 in Fig. 3a).

showed that, in the case under study, the measurements were carried out between the signals propagating over the rays of different congruencies. These signals arrived without reflections from the waveguide boundaries, i.e., over the rays refracted in the water column. The large values of the cross-correlation coefficients are caused by the good angular resolution of the signals in the vertical plane. Such situations correspond to so-called single ray reception of signals, when using each of the arrays we managed to single out only one ray from the arriving multiray signal. That is why only one correlation peak is observed in Fig. 3c, where several plots of the moduli of the cross-correlation functions are presented for spectrum 2 of Fig. 3a. The plots show the high stability of the travel time differences of the signals. In Figs. 3a and 3b, the rms fluctuation time spectrum 1 is $\sigma_\tau \cong 0.33$ ms, and for time spectrum 2, it is $\sigma_\tau \cong 0.40$ ms.

The mean values of the correlation coefficients at a single ray reception are usually much higher than at a multiray reception, when a complete angular resolution

of the signals cannot be achieved. In the latter case, the correlation coefficient decreases because of the interaction of the signals arriving at different times over the rays that are not resolved by the array. If the signals arrive outside the correlation interval of the emitted signal, they are perceived as additional additive noise.
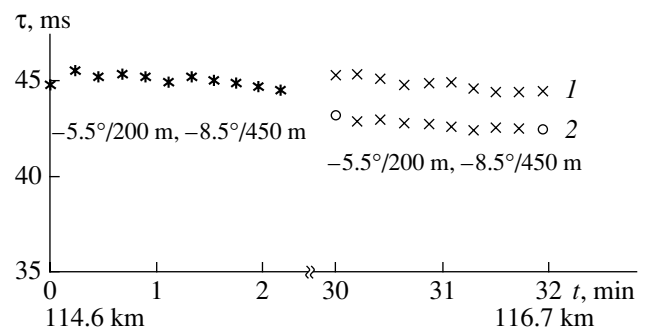

Fig. 4. Variability of the time spectra in the second convergence zone when the transmitting ship moves; the source is at a depth of 200 m.
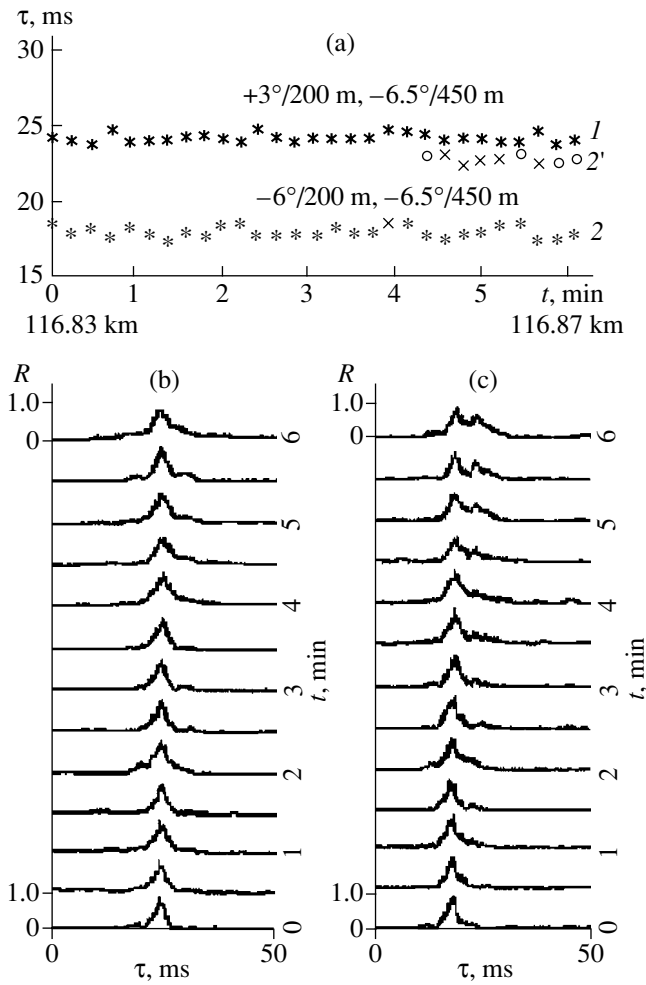
Fig. 5. The time spectra and the cross-correlation functions of signals received in the second convergence zone when the transmitting ship drifts and the source is at a depth of 400 m. (a) The time spectra of signals; (b) the cross-correlation functions between signals with the arrival angles $\alpha_1 = +3°$ and $\alpha_2 \cong -6.5°$ (curve I in Fig. 5a); (c) the cross-correlation functions between signals with the arrival angles $\alpha_1 = -6°$ and $\alpha_2 \cong -6.5°$ (curves 2 and $2'$ in Fig. 5a).

Figure 4 shows the variability of the time spectra in the second convergence zone in the case of a relatively fast increase in the distance, when the transmitting ship retained its position and the receiving ship continued to drift. The change in distance was ~21 km within a 32-min observation. Two 2-min segments of measurements of the time differences between the signal arrivals are also presented. Number 4 in Fig. 2b shows the instants of the measurements corresponding to Fig. 4.

The spectra were measured between the signals with an arrival angle of $-5.5°$ at a depth of 200 m and with an angle of $-8.5°$ at a depth of 450 m. In the first convergence zone, for each pair of arrival angles, only one component was observed in the time spectrum, which testified to a good spatial resolution of the signals by the arrays. In the second zone, two components appear

(I and 2) between the 30th and 32nd minutes, which points to the incomplete resolution of the signals by one of the arrays. Therefore, in the time spectrum, two signal components appear with arrival time differences of ~43 and ~45 ms. In this case, the correlation coefficients, naturally, decrease, which is shown in Fig. 4 by the signs "×" for $0.6 \leq |R| < 0.8$ and "o" for $0.4 \leq |R| < 0.6$. The mean values of the cross-correlation coefficients $|R|$ are within 0.80–0.86 for the first segment of the plot (a single ray reception of the signals). For the second segment of the plot (a multiray reception), $|R| \sim 0.51$–0.66. In the last case, the corrected correlation coefficient was calculated from formula $|R_\Sigma| = \sqrt{\sum_i |R_i|^2}$, which allows one to take into account the interfering effect of the signals arriving within the directional pattern over each (ith) ray. In the calculation, the arriving signals were assumed to have the same levels. The mean value $|\bar{R}_\Sigma|$ in this record is equal to 0.80. The rms fluctuation of the signal arrival time differences is $\sigma_\tau \cong 0.20$ ms. The calculations showed that the measurements, as in the first zone, were carried out between the signals belonging to different ray congruences.

Figure 5 exhibits the time spectra (Fig. 5a) and the cross-correlation functions (Figs. 5b, 5c) in the second convergence zone with an altered depth of the source. Instead of the 200-m depth, the source was lowered to a depth of 400 m. The transmitting and receiving ships were drifting. The instant of measurement is indicated by the number 5a in Fig. 2b. The time spectra were measured between the signals that arrived at a depth of 200 m at angles of $+3°$ or $-6°$ and the signal that arrived at a depth of 450 m at an angle of $-6.5°$. The signal with the arrival angle of $+3°$ propagated over a single ray during a 6-min-long interval, as well as the signal received at a depth of 450 m. Therefore, the time spectrum for this pair has only one component (curve I). The single-ray character of signal reception is confirmed by the changes that occur in the cross-correlation functions between these signals. Only one clearly defined correlation peak is present in the correlation functions (Fig. 5b). The mean value of the correlation coefficient is 0.88, while $\sigma_\tau = 0.36$ ms. The signal with an arrival angle of $-6°$ (at a depth of 200 m) arrived along two rays that were unresolved by the array at the end of the observation time. As a result, in addition to component 2, the second component $2'$ appears in the spectrum. This is confirmed by the character of the changes in the cross-correlation functions between these signals (Fig. 5c), where, beginning from the 4th minute of observation, the second correlation peak appears. The mean value of the correlation coefficient is -0.82 for component 2 and -0.41 for component $2'$ (the corrected correlation coefficient for spectrum 2 is $|\bar{R}_\Sigma| = 0.92$). The rms fluctuation of the arrival time difference is $\sigma_\tau = 0.34$ and 0.32 ms for components 2 and $2'$, respectively.

Table 1

r, km	t, h	$h_1 = 200$ m α_1, deg	$h_2 = 450$ m α_2, deg	$|\overline{R}_{max}|$	n	$|\overline{R}_{\Sigma}|$	$\overline{\tau}$, ms	σ_τ, ms
56.8	0	~−4.5	~−7	0.84	1	0.84	43.1	0.29
67.6	6	~+7	~+9	0.74	2	0.84	1.1	0.41
				0.47			4.6	0.25
56.5–56.9	14–16	~−6	~−11	0.85	1	0.85	57.6–60.8	0.33
56.5–56.9	14–16	~−6	~−8	0.86	1	0.86	43.5–46.1	0.39
57.7	16.5	~−8	~−6.5	0.90	1	0.90	41.9	0.40
57.7–59.8	16.5–17.2	~−3	~−6.5	0.88	1	0.88	44.8	0.22
58.6	17	~+1.5	~−13.5*	0.85	1	0.85	77.3	0.30
58.6–59.8	17–17.2	~+1.5	~−6.5	0.89	1	0.89	40.7–43.2	0.36

* The signals were reflected from a rough surface.

Table 2

r, km	t, h	$h_1 = 200$ m α_1, deg	$h_2 = 450$ m α_2, deg	$|\overline{R}_{max}|$	n	$|\overline{R}_{\Sigma}|$	$\overline{\tau}$, ms	σ_τ, ms
116.4	0	~−6.5	~−7	0.89	1	0.89	46.1	0.42
118.1	1	~−2.5	~−12*	0.79	1	0.79	56.5	0.34
121.3	2.5	~+1	−11.5–12*	0.57	3	0.78	65.0	0.63
				0.44			53.2	0.63
				0.34			81.7	0.53
121.3	2.5	~+1	~+7.5	0.94	1	0.94	13.8	0.35
130.1–132.6	8.2–9.3	~−7	~+10.5	0.52	3	0.66	11.5–17.9	0.37
				0.33			6.8–15.3	0.42
				0.27			21.3	0.33
114.5–116.5	19.3–21.4	~−1.5	~−8.5	0.81	2	0.97	45.7–47.8	0.41
				0.55			40.2–44.6	0.33
115.9	20.3	~−5	~−7.5	0.86	1	0.86	45.3	0.20
116.5	20.8	~−3.5	~−7.5	0.75	1	0.75	45.7	0.12
116.5–116.6	20.9–21.4	~−5.5	~−8.5	0.78	2	0.93	43.7–46.8	0.47
				0.52			43.2	0.31

* The signals were reflected from a rough surface.

Figures 3–5 present part of the results of measuring the time spectra and the correlation characteristics. The main data are summarized in Tables 1–3. The latter contain the information necessary for an analysis of the material presented above. In the tables, the following notations are used: r is the distance between the points of emission and reception; t is the time interval between the experiments; h_1 and h_2 are the depths of the centers of receiving arrays; α_1 and α_2 are the signal arrival angles at which the directional patterns of the arrays were guided; $|\overline{R}_{max}|$ are the values of the maximum correlation coefficients averaged over N measurements; n is the number of correlation peaks in the time spectra; $\overline{R}_{\Sigma}$ are the mean values of the corrected correlation coefficients for $n > 1$; $\overline{\tau}$ is the mean value of the arrival time difference between the signals; and σ_τ is the rms fluctuation of the arrival time difference, which was calculated by averaging over $10 \leq N \leq 49$ measurements.

The generalized data for the first convergence zone obtained for the source depth of 200 m are presented in Table 1. Considering the data of this table, one can draw the following conclusions for the distances within 56.5–67.6 km: the cross-correlation coefficients between the signals received simultaneously by two directional arrays at depths of 200 and 450 m with a single ray reception are within 0.84–0.90; the mean values of the arrival time differences between signals with almost identical pairs of arrival angles are stable in time, i.e., differ little even after an interval of 14–16 h

Table 3

r, km	t, h	$h_1 = 200$ m α_1, deg	$h_2 = 450$ m α_2, deg	$|\bar{R}_{max}|$	n	$|\bar{R}_\Sigma|$	$\bar{\tau}$, ms	σ_τ, ms
116.8	25.2	~+3	~−6.5	0.88	1	0.88	24.5	0.36
116.8	25.2	~−6	~−6.5	0.82 0.41	2	0.92	17.9 22.6	0.34 0.32
116.9	25.4	~+4	~−11	0.86	1	0.86	59.0	0.27
116.9	25.4	~+4	~−4.5	0.90	1	0.90	24.3	0.46

in the measurements; the fluctuations of the travel time differences do not exceed 0.41 ms.

Similar generalized data for the second convergence zone for the source at a depth of 200 m are summarized in Table 2.

From Table 2 for the distances 114.5 to 132.6 km, it follows that the correlation coefficients vary from 0.75 to 0.94 for a single ray reception, while for a multiray reception, the corrected correlation coefficients $|\bar{R}_\Sigma|$ lie within 0.66 to 0.97; the mean values of the travel time differences between the signals with almost identical pairs of arrival angles at different reception depths appear quite stable in time (that is, they vary only slightly at the same distance (~116 km) even after 20 hours); and the fluctuations of the time spectra do not exceed 0.63 ms for both purely water signals and signals reflected from the sea surface.

The results of measurements with the source at a depth of 400 m are summarized in Table 3.

At distances of 116.8–116.9 km, the mean values of the corrected correlation coefficients were 0.86–0.92 and the fluctuations of the arrival time differences between the signals were 0.27–0.46 ms.

Note that the aforementioned fluctuation values are determined not only by the inhomogeneities of the medium and the surface roughness, but also include instrumental errors of measurements, the effect of the ship's drift, the effect of the mutual displacement of the arrays, and other factors. The small fluctuation values obtained for the arrival time differences between the signals reflected from the surface are explained by the fact that, in our experimental conditions, the scattering pattern had a maximum in the specular direction. This occurred because the grazing angles near the surface were small, so that the relationship $k\rho \gg 1$ was satisfied, where k is the sound wave number and ρ is the correlation radius of the sea surface roughness. Remember that, according to our calculations, the fluctuations of the signal travel times at distances of 60–130 km should be insignificant in our experiments (smaller than 0.48 ms when they are caused by the inhomogeneities of the medium and not exceeding 1.0–1.5 ms when they are caused by the reflections from the ocean surface).

The data presented above show that the experimental results obtained in the first and second convergence zones for the signals in the frequency range 0.8–1.3 kHz with a simultaneous highly directional reception at different depths (200 and 450 m) almost coincide with the theoretical estimates. The rms fluctuations in the arrival time differences between the signals (fluctuations of the time spectra) are almost equal for the signals propagating over purely water rays (<0.48 ms) and for those reflected once or twice from a rough ocean surface (<0.63 ms). With a highly directional reception in the vertical plane, large values of the cross-correlation coefficients (>0.7–0.8) can be obtained when the depths of reception are separated even by several hundreds of meters. Note that this conclusion applies to signals arriving at points of reception over different rays rather than to signals arriving at different depths by the same path (which would be no surprise).

REFERENCES

1. A. M. Thode, J. Acoust. Soc. Am. **108**, 1582 (2000).
2. B. Berdugo, M. A. Doron, J. Rosenhouse, and H. Azhari, J. Acoust. Soc. Am. **105**, 3355 (1999).
3. S. R. Khosla and D. R. Dowling, J. Acoust. Soc. Am. **109**, 538 (2001).
4. J. S. Gerber and S. M. Flatte, J. Acoust. Soc. Am. **109**, 528 (2001).
5. M. Snellen, D. G. Simons, M. Siderius, *et al.*, J. Acoust. Soc. Am. **109**, 514 (2001).
6. G. J. Orris, M. Nicolas, and J. S. Perkins, J. Acoust. Soc. Am. **107**, 2563 (2000).
7. N. G. Kuznetsova and L. A. Chernov, Vopr. Sudostr., Ser. Akust., No. 15, 5 (1982).
8. V. P. Akulicheva and V. M. Frolov, Akust. Zh. **32**, 742 (1986) [Sov. Phys. Acoust. **32**, 465 (1986)].
9. O. P. Galkin and S. D. Pankova, Akust. Zh. **44**, 57 (1998) [Acoust. Phys. **44**, 44 (1998)].
10. O. P. Galkin and S. D. Pankova, Akust. Zh. **45**, 59 (1999) [Acoust. Phys. **45**, 52 (1999)].
11. O. P. Galkin and S. D. Pankova, Akust. Zh. **45**, 479 (1999) [Acoust. Phys. **45**, 426 (1999)].

Translated by Yu. Lysanov

Generation and Reception of Short Acoustic Pulses by Multilayer Piezoelectric Transducers

M. A. Grigor'ev, A. V. Tolstikov, and Yu. N. Navrotskaya

Chernyshevsky State University, ul. Astrakhanskaya 83, Saratov, 410026 Russia

e-mail: magrig@sgu.ssu.runnet.ru

Received June 17, 2002

Abstract—By means of the Fourier transformation, a formula is obtained for calculating the pulse response of a transducer when a square pulse of a given duration is supplied to its input and the excited "sound" is reflected from the free flat end of the acoustic line and returns to the transducer. For a frequency of 100 MHz, real lithium niobate transducers that are connected through intermediate layers to the acoustic line made of fused quartz and to a rear load with a given acoustic impedance are considered. The pulse response is calculated for the transducers with different values of the sublayer thickness, rear acoustic load, transmission line impedance, and original pulse duration. The results of the calculations are compared with the experiment. © *2003 MAIK "Nauka/Interperiodica".*

To form the optimal pulse response characteristic of a piezoelectric transducer that operates in the mode of generation and subsequent reception of short pulses, for example, in acoustic pulse microscopes [1], it is important to know how this characteristic can be controlled. For this purpose, one can use intermediate layers inserted in the transducer between the piezoelectric, acoustic line, and rear acoustic load. The rear load can also be used to affect the aforementioned characteristic. Intermediate layers are necessary in manufacturing transducers based on piezoelectric plates in order to connect the piezoelectric with the acoustic line and with the rear load. It is useful to analyze their effect on the pulse properties of the transducer. In our previous paper [2], we proposed algorithms for calculating the transfer constants of a multilayer piezoelectric transducer at the direct and inverse transformation. With the help of these algorithms and the programs developed on their basis, we obtained the amplitude–frequency and phase–frequency characteristics of a real multilayer piezoelectric element. The aforementioned transfer constants are necessary to analyze the pulse properties of the transducer. Therefore, the present paper should be considered as a continuation of the previous paper [2]. As far as we know, the solution of such a problem in application to a multilayer transducer is absent in the literature.

1. THE MODEL UNDER ANALYSIS AND THE ASSUMPTIONS

Figure 1 schematically represents the transducer under investigation. Between the piezoelectric layer *1* and the acoustic line *2*, intermediate layers (sublayers) are present. Between the piezoelectric and the rear load *3*, other intermediate layers (superlayers) are positioned.

We assume that the acoustic line has a finite length *l*, while the rear load has an infinite length. The sublayer and the superlayer immediately adjacent to the piezoelectric are metallic electrodes. In the diagram, they are connected to the *bb* terminals, which are connected to the stray shunt capacitance C_{sh}. The twin-wire transmission line matched with the voltage pulse source has an impedance Z_0 and is connected to the *aa* terminals. The latter, in their turn, are connected to the *bb* terminals through the inductance *L* and the loss resistance R_{los}. A single square voltage pulse $u(t)$ with an amplitude u_0 and duration τ is fed to the *aa* terminals of the transducer along the transmission line. The piezoelectric element generates an acoustic pulse in the acoustic line, which travels through the line, reflects from its free end, returns to the transducer, and is again transformed into an electric signal usually called the first echo pulse.

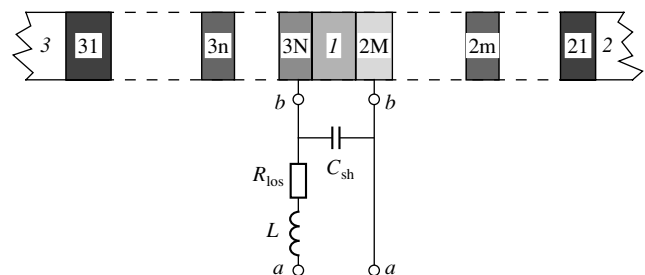**Fig. 1.** Model of the transducer under consideration: (*1*) piezoelectric; (*2*) acoustic line; (*3*) rear acoustic load; the indices 2*m* and 3*n* represent the sublayer with number *m* and the superlayer with number *n*, respectively; C_{sh} is stray shunt capacitance; R_{los} and *L* are loss resistance and inductance of the conductor connecting the transducer with the transmission line.

The problem is to determine the time dependence of this signal and the dependence of its amplitude and shape on the geometric and material parameters of the transducer. The aforementioned time dependence for the first echo pulse at the *aa* terminals is the pulse response to be found.

We seek the solution in the one-dimensional approximation ($\partial/\partial x = \partial/\partial y = 0$), neglecting the diffraction divergence and the acoustic damping in the layers of the piezoelectric element. The acoustic damping is taken into account only in the acoustic line. For this purpose, we introduce the complex propagation constant

$$\Gamma = \beta - j\alpha,$$

where $\beta = \omega/v$ is the wave number; v is sound velocity in the acoustic line; and α is the damping factor, which depends on frequency by square law

$$\alpha = A\omega^2/4\pi^2.$$

Here, A is the specific damping expressed in the [s²/m] units.

2. PULSE RESPONSE

The input pulse across the *aa* terminals can be represented in the form of a continuous frequency spectrum by means of the Fourier integral:

$$u(t) = \int_{-\infty}^{\infty} g(\omega)e^{j\omega t}d\omega,$$

where $g(\omega)d\omega$ is the complex amplitude of the voltage with the spectral frequency component ω and $g(\omega)$ is the spectral density obtained by the direct Fourier transformation

$$g(\omega) = \frac{1}{2\pi}\int_{-\infty}^{\infty} u(t)e^{-j\omega t}dt.$$

For the square pulse, with the time axis origin at its center, we have

$$g(\omega) = \frac{u_0\tau}{2\pi}\frac{\sin(\omega\tau/2)}{(\omega\tau/2)}. \tag{1}$$

As a result of the transducer operation, the spectral component of frequency ω gives rise to a forward wave of acoustic stress in the acoustic line, and this wave has the complex amplitude

$$T_+(x = 0) = g(\omega)k_+(\omega)d\omega, \tag{2}$$

where $k_+(\omega)$ is the complex transfer constant at the direct electroacoustic (EA) transformation, which is calculated by the program taken from [2].

The excited wave arrives at the free end of the acoustic line with a somewhat diminished amplitude

due to the acoustic damping. After the reflection from the end, its amplitude changes its sign, because the reflection factor of the acoustic stress wave is in this case equal to –1, and then the wave returns to the transducer. As a result of the inverse EA transformation, the voltage (the first echo pulse) with the amplitude

$$u_{aa}(\omega) = T_-(x = 0)k_-(\omega) \tag{3}$$

appears across the *aa* terminals. Here, $k_-(\omega)$ is the transfer constant at the inverse EA transformation.

From [2], it follows that $k_+(\omega)$ and $k_-(\omega)$ are equal, accurate to sign. On this basis, taking into account Eqs. (1) and (2), one can easily obtain from Eq. (3) the complex voltage amplitude of the spectral component of the echo pulse at the *aa* terminals. Applying then the inverse Fourier transformation, we determine the time dependence of the voltage at the *aa* terminals, i.e., the desired pulse response:

$$u_{aa}(t)$$
$$= \frac{u_0\tau}{2\pi}\int_{-\infty}^{\infty}\frac{\sin(\omega\tau/2)}{(\omega\tau/2)}e^{-2\alpha l}|k_+|^2 e^{j2\varphi}e^{-j(\omega/v)2l}e^{j\omega t}d\omega, \tag{4}$$

where φ is the phase of the transfer constant and l is the length of the acoustic line.

If now, in this integral, we divide the exponents of the imaginary arguments by the real and imaginary parts and take into account that $|k_+|^2$ is an even function of the frequency ω and the phase φ is an odd function, we finally obtain from Eq. (4) the formula for calculating the pulse response:

$$u_{aa}(t) = \frac{u_0\tau}{\pi}\int_{0}^{\infty}\frac{\sin(\omega\tau/2)}{(\omega\tau/2)}e^{-2\alpha l}$$
$$\times \{[(\text{Re}(k_+))^2 - (\text{Im}(k_+))^2]\cos[\omega(t - 2l/v)] \tag{5}$$
$$- 2\text{Im}(k_+)\text{Re}(k_+)\sin[\omega(t - 2l/v)]\}d\omega.$$

3. REAL TRANSDUCERS

When the pulse properties of real transducers were analyzed, the numerical integration in Eq. (5) was performed at different time points t, from the initial one $t_b \approx (\tau_{\text{del}} - 2\tau)$ to the end point $t_e = (t_b + 100 \text{ ns})$, where $\tau_{\text{del}} = 2l/v$ is the delay time. The time step was chosen to be $\leq 0.05\tau$. The desired transfer constant k_+ was calculated by the program taken from [2]. Owing to the rapid decrease in the integrand with ω, it was possible to lower the upper integration limit to 30 times the central frequency of the transducer.

Below, we consider multilayer piezoelectric transducers designed to operate in the range with a central frequency of ~100 MHz. An $(Y + 36°)$-cut LiNbO₃ plate is fixed on the acoustic line made of fused quartz by means of five metal layers (Cr, Cu, In, Cu, Cr). Over it,

two metal layers (Cr, Cu) and the rear acoustic load (epoxy resin with or without filling agent) are placed.

The geometric and electric parameters of the transducers are shown in the caption of Fig. 2. In Figs. 2 and 3 of [2], the theoretical frequency dependences of the conversion factor η and the phase shift φ are presented in the range from 10 to 450 MHz for two variants of transducers differing in thickness of the In layer. In the first transducer, the In layer was 1 μm thick, and in the second transducer, it was 6.5 μm thick. As follows from the aforementioned plots presented in [2], the second variant has a wider frequency band within which the factor $\eta(f)$ is approximately constant.

Figures 2a and 2b demonstrate the pulse responses calculated by Eq. (5) for the two transducer variants specified above. The amplitude of the input pulse was taken to be 1 V. The pulse duration τ determined according to the maximum in the amplitude of the first wave of the pulse response was taken to be 5 ns. It can be seen that the "tail" length of the curve $u(t)$ in Fig. 2b is noticeably smaller than that in Fig. 2a. As could be expected, the more wideband transducer with the In layer thickness of 6.5 μm provides a shorter pulse response. Figure 2c demonstrates one of the experimental curves obtained with the help of an electron pulse oscillograph for transducers with an indium layer of 1 μm. The duration of the square pulse fed to the transducer was chosen each time according to the maximum of the amplitude of the first response wave within 4–6 ns. The comparison of the calculated curve of Fig. 2a with the experimental one shows a good agreement. The smaller oscillation amplitude of the experimental curve can be explained by the fact that the probing pulse was fed to the transducer, as well as the echo pulse recorded, by means of a coaxial tee-joint. The central conductors were connected to each other by a "star" scheme through three resistors of 30 Ω each. As a result, a considerably smaller amplitude of the pulse response was observed in the experiment even at a greater amplitude of the generator pulse (1.6 V instead of 1 V in the theory).

It is interesting to know how the rear acoustic load affects the pulse characteristic. For this purpose, we specified different values of the acoustic impedance of the load Z_{0ac}. It was found that, at $Z_{0ac} \approx 30$ kg/mm²/s, the pulse response has the minimal tail and minimal amplitude. The material that has approximately the same acoustic impedance for the longitudinal wave is $(Y + 36°)$-cut lithium niobate. To illustrate the rear load effect, Fig. 3a shows the response for a transducer with an indium layer thickness of 6.5 μm and a load impedance of $Z_{0ac} = 20$ kg/mm²/s. Such a load may be epoxy resin with a proper filler. The comparison of the curves depicted in Figs. 2b and 3a shows that the tail length considerably decreases with increasing Z_{0ac}, and the amplitude of the pulse response also noticeably decreases.
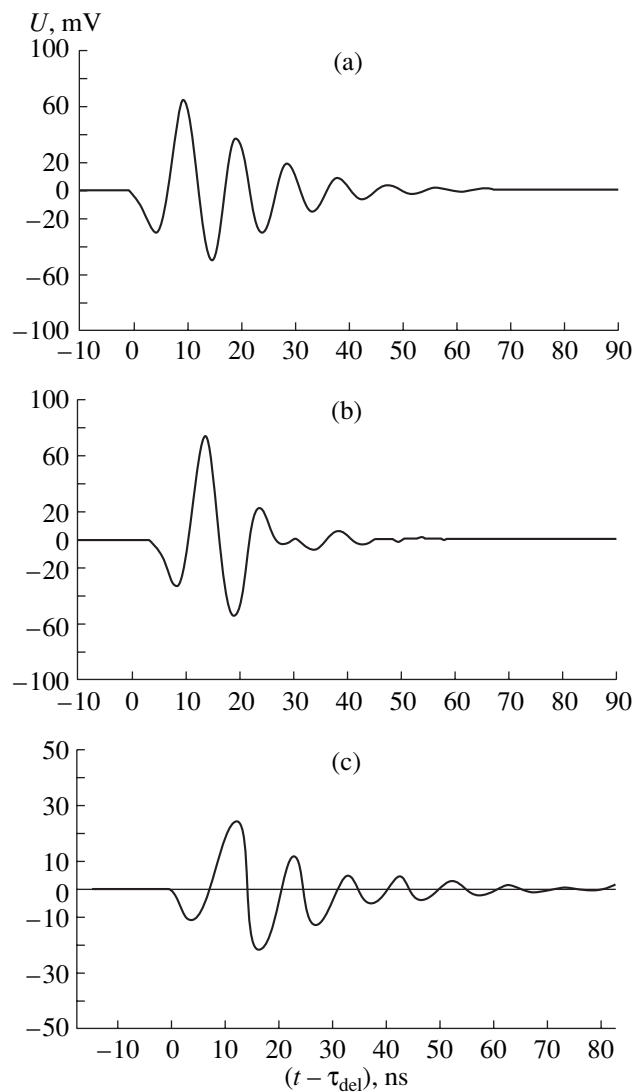

Fig. 2. Pulse responses of the transducers. Piezoelectric: $(Y + 36°)$-cut lithium niobate (32 μm). The acoustic line is made of fused quartz. The sublayers (counting from the piezoelectric): Cr (0.04 μm), Cu (0.2 μm), In (various thickness), Cu (0.2 μm), and Cr (0.04 μm). Superlayers (in the same order): Cr (0.04 μm) and Cu (0.2 μm). Other parameters are $L = 6$ nH, $R_{los} = 0.5$ Ω, $C_{sh} = 0$, and $Z_0 = 50$ Ω; the transducer diameter is 4 mm; $Z_{0ac} = 2.9$ kg/(mm²/s); $\tau = 5$ ns. (a) Theory: the In layer thickness is $h_{33} = 1$ μm; (b) theory: $h_{33} = 6.5$ μm; (c) experiment: $h_{33} = 1$ μm.

Formula (5) obtained above involves the transfer constant, which, in its turn, depends on the transmission line impedance Z_0. It is well known [3] that, when the transducer represents the load of a twin-wire line, the EA conversion factor reaches its maximum at $Z_0 = |Z|$, where Z is the electric impedance of the piezoelectric element. This value of Z_0, when applied to the piezoelectric transducer, is usually called the optimal transmission line impedance $Z_{0, opt}$. The calculation shows that, in the case of the transducers under consideration, we have $Z_{0, opt} \approx 3–4$ Ω. Thus, to obtain the maximal
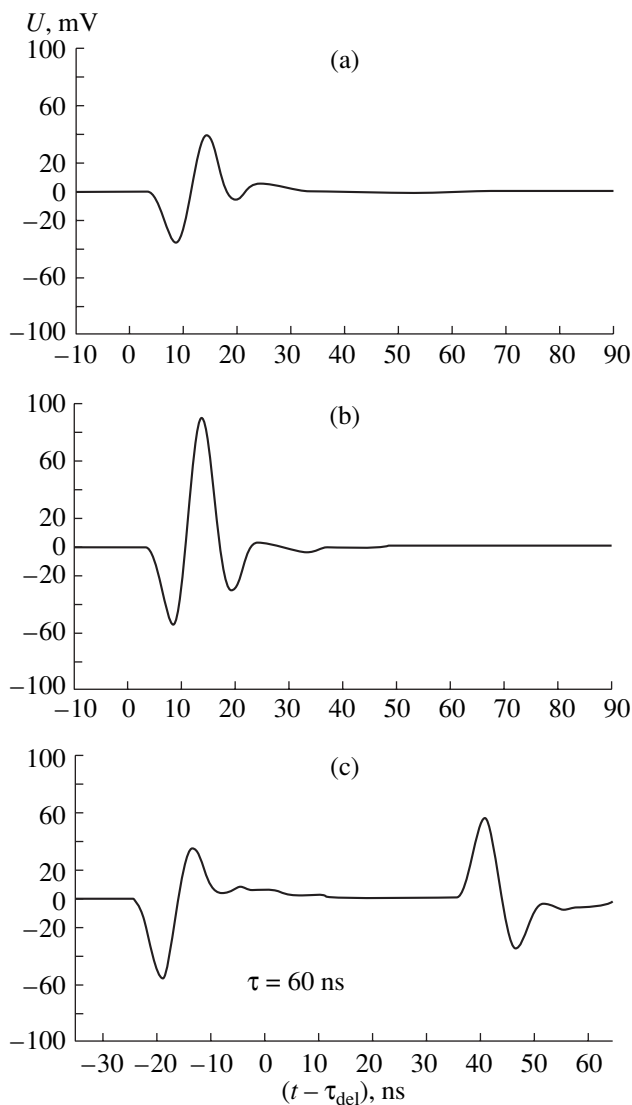
Fig. 3. Calculated pulse responses of transducers. The material, the layer thickness, and the electric circuit parameters are the same as in Fig. 2a, except for Z_{0ac}, Z_0, and τ: $Z_{0ac} =$ (a–c) 20 kg/(mm^2/s); $Z_0 =$ (a) 50 and (b, c) 20 Ω; and $\tau =$ (a, b) 5 and (c) 60 ns.

efficiency of the transducer, one should match the standard 50 Ω line with a lower impedance line. The realization of such a matching in a wide frequency band with the difference in impedances being greater than tenfold presents a difficult problem. Figu-re 3b demonstrates the change that occurs in the pulse response of a transducer when the impedance decreases to only $Z_0 =$ 20 Ω. It can be seen that the amplitude of the pulse response becomes noticeably greater.

Finally, we consider the pulse of a long duration. This case can serve as a test problem for the calculation program developed in this study. Figure 3c demonstrates the curve obtained for $\tau = 60$ ns. It can be easily seen that the leading and the trailing edges of the pulse separately generate the pulse responses.

4. CONCLUSION

In the present paper, we analyzed the pulse properties of multilayer transducers. The analysis is based on the results of the previous study [2] devoted to the calculation of the transfer constants of such transducers at the direct and inverse conversion. A formula is obtained for calculating the time dependence of the pulse response of the transducer when the pulse is reflected from the free flat end of the acoustic line while a square pulse of a given duration is fed to the transducer. Using $(Y + 36°)$-cut lithium niobate transducers based on an acoustic line of fused quartz with the central frequency of the operating range ~100 MHz as an example, we demonstrated how the pulse response is affected by the sublayer thickness, the acoustic impedance of the rear acoustic load, the transmission line impedance, and the pulse duration. The results are compared with experiment. The information obtained can be used, in particular, in the design of acoustic pulse microscopes.

REFERENCES

1. D. A. Knapik, B. Starcoski, C. J. Pavlin, and F. S. Foster, IEEE Trans. Ultrason. Ferroelectr. Freq. Control **47** (6), 1540 (2000).

2. M. A. Grigor'ev, A. V. Tolstikov, and Yu. N. Navrotskaya, Akust. Zh. **48**, 187 (2002) [Acoust. Phys. **48**, 155 (2002)].

3. M. A. Grigor'ev, V. Yu. Ushakov, A. V. Tolstikov, *et al.*, Radiotekh. Élektron. (Moscow) **25**, 1597 (1980).

Translated by A. Kruglov

A Method for Calculating the Speed of Sound in Seawater

D. A. Denisov, A. V. Abramov, and E. P. Abramova

Mendeleev University of Chemical Technology, Miusskaya pl. 9, Moscow, 125047 Russia

e-mail: smi@logic.ru

Received May 22, 2002

Abstract—A method of calculating the salt concentrations in seawater from known ion concentrations is proposed. Data on the salt concentrations allow one to determine the values of the solvent activity a_s and the concentrations of binary solutions, each of which consists of the solvent and one of the dissolved components, as well as the properties of binary solutions corresponding to the value of a_s of a mixed solution. The use of the concentrations of binary solutions and their corresponding properties makes it possible to calculate the speed of sound in seawater by the formula for the speed of sound in a mixed solution. The deviation of the calculated sound speed value from the experimental one is relatively small. © 2003 MAIK "Nauka/Interperiodica".

At present, the effect of the composition on some thermodynamic and acoustic properties of seawater is taken into account by using the only variable, namely, the salinity [1]. The use of this variable implies that the concentration ratios of some of the dissolved components are constant.

For inland seas, such as the Caspian, Azov, Aral, and Dead seas, and seas connected to oceans or neighboring seas by narrow straits, such as the Black and Red seas, the values of the concentration ratios of the dissolved components may differ from the values of the corresponding ratios for ocean water.

A more detailed analysis of the composition of seawater is possible with the use of the data on the ion concentrations, which can be found in the literature [1, 2].

The computation of the thermodynamic and acoustic properties of solutions containing electrolytes and nonelectrolytes can be performed using a model of ideal isopiestic solutions [3, 4], according to which a mixed solution is considered as an ideal mixture of binary subsystems consisting of a solvent and one of the dissolved components characterized by the same value of the thermodynamic solvent activity a_s equal to its value in the mixed solution.

To calculate the properties of mixed solutions, i.e., solutions with several dissolved components, it is necessary to know the concentrations of the neutral dissolved components [3–5].

The data on the composition of seawater include the values of the ion concentrations [1, 2]. Since seawater contains several types of cations and several anions, the salt concentrations, or, in other words, the distribution of anions between cations, cannot be easily calculated.

As a very rough approximation, we consider seawater to be an ideal isopiestic solution of four salts formed by four ions, Na^+, Mg^{2+}, Cl^-, and SO_4^{2-}, whose concentrations, according to [1], considerably exceed the concentrations of other ions. Neglecting the presence of any kind of ions in the aforementioned ideal isopiestic solution containing four or more salts, it is necessary, generally speaking, to change the mass ratio of one of the ions to other ions to satisfy the condition of the electric neutrality of the system. In this paper the mass of Cl^- is changed. The cited manual [1] presents the values of the ion masses expressed in grams per 1 kg of seawater.

To determine the molalities of the ions specified above, it is necessary to divide the number of ion moles per 1 kg of seawater N_i by the mass of pure water per 1 kg of seawater L_s. Then, the values of the masses of three out of four ions per L_s kg of pure water are equal to the masses of these ions per 1 kg of seawater.

To satisfy the condition of electric neutrality, it is necessary, in the general case, to change the mass of the fourth ion per L_s kg of pure water.

Since in the ideal isopiestic solution under consideration, which contains four ions and four salts, not all ions that occur in seawater are present, with allowance for the above comment concerning the mass of the fourth ion, the salinity S of the system will be determined by the ratio of the sum of the masses (in grams) of four ions per 1 kg of seawater, G_i, to the quantity $10^3 L_s + \sum_{i=1}^{4} G_i$. Obviously, the salinity of the ideal isopiestic solution, generally speaking, differs from the salinity of the seawater.

We determine the molalities of the ions by dividing the numbers of ion moles per 1 kg of seawater to L_s. The total mass of ions per 1 kg of seawater is 35.1755 g. Then, $L_s = 0.9648245$ kg. The values of G_i, N_i, and m_i are presented in Table 1.

Table 1. Masses of the Na^+, Mg^{2+}, and SO_4^{2-} ions and the corresponding numbers of moles of these ions per 1 kg of seawater for $S = 35.043‰$. The mass of Cl^- and the number of moles of Cl^- in 1 kg of seawater that are determined from the electric neutrality condition for the solution with four ions and the corresponding ion molalities. The values of the ion masses, the numbers of ion moles per 1 kg of seawater, and the values of the ion molalities used for describing the mixed solution of four salts

Ions	Masses of ions (in grams) per 1 kg of seawater, G_i, taken from [1] (except for G_{Cl})	Numbers of ion moles per 1 kg of seawater, N_i, taken from [1] (except for N_{Cl})	Molalities of ions in an ideal isopiestic solution of four salts, m_i
Na^+	10.7596	0.468012	0.485075
Mg^{2+}	1.2965	0.053343	0.055287
SO_4^{2-}	2.7124	0.028238	0.029267
Cl^-	18.3725	0.518223	0.537116

The salinity of the ideal isopiestic solution of four salts is $S = 33.141‰$.

As noted above, the values of the masses of the first three ions that correspond to the pure water mass L_s and occur in 1 kg of seawater are equal to the masses of these ions presented in [1]. The value of G_4 is changed so that the electric neutrality condition, which in this case has the form

$$N_{Na^+} + 2N_{Mg^{2+}} = 2N_{SO^{2-}} + N_{Cl^-}, \qquad (1)$$

is satisfied.

The use of the set of programs in [6] and the values of the instability constants of ion pairs in [7] shows that, for the indicated values of ion concentrations, the product of the Ca^{2+} and SO_4^{2-} concentrations does not exceed the solubility product.

As follows from the ion concentrations presented in [1], the content of Na^+ and Mg^{2+} in the solution far exceeds the content of Ca^{2+} and K^+. Therefore, it is expedient to determine the salt concentrations in two steps. At first, we assume that the seawater contains only four ions: Na^+, Mg^{2+}, Cl^-, and SO_4^{2-}, and, correspondingly, four salts: NaCl, Na_2SO_4, $MgCl_2$, and $MgSO_4$.

Using the values of the dissociation constants of sulfuric acid [7], we can show that, for the values of pH = 7.6–8.4 typical of seawater, the concentration of SO_4^{2-} ions far exceeds the concentration of HSO_4^- ions and that of neutral sulfuric acid. As will be seen from what follows, the influence of $NaSO_4^-$, $MgSO_4$ ion pairs on the properties of the NaCl–Na_2SO_4–$MgCl_2$–$MgSO_4$–H_2O system can be taken into account by using the

activity coefficients of binary solutions of the electrolytes under consideration, because the aforementioned ion pairs are present in binary solutions. Below, we will mark the quantities related to the salts NaCl, Na_2SO_4, $MgCl_2$, and $MgSO_4$ with the subscripts 1, 2, 3, and 4, respectively.

Let us write down the equations relating the salt and ion molalities:

$$\left.\begin{array}{r} m_1 + 2m_2 = m_{Na} \\ m_1 + 2m_3 = m_{Cl} \\ m_3 + m_4 = m_{Mg} \\ m_2 + m_4 = m_{SO_4} \end{array}\right\}. \qquad (2)$$

The values of the ion concentrations, except for the concentration of one ion, are set equal to the experimental values.

The set of equations (2) is linearly dependent. A linearly independent set contains three equations, which we choose to be as follows:

$$m_1 = m_{Cl} - 2m_{Mg} + 2m_4, \qquad (3)$$

$$m_2 = m_{Na} - m_{Cl} + 2m_{Mg} - 2m_4, \qquad (4)$$

$$m_3 = m_{Mg} - m_4. \qquad (5)$$

Obviously, the set of equations (3)–(5) does not make it possible to calculate the molalities of the salts.

It is necessary to add one more equation, which can be chosen in the form of the relationship referred to as the Zdanovski rule, which relates the molalities of the dissolved components in the mixed m_i and binary m_i^* isopiestic solutions [3]:

$$\sum_{i=1}^{r} \frac{m_i}{m_i^*} = 1, \qquad (6)$$

where r is the number of dissolved components. This relationship is applicable on the assumption that the seawater is an ideal isopiestic solution.

For the mixed solution of four salts under consideration, this relationship has the form

$$m_{Cl}\left(\frac{1}{m_1^*} - \frac{1}{2m_2^*}\right) + m_{Mg}\left(\frac{1}{m_2^*} - \frac{2}{m_1^*} + \frac{1}{m_3^*}\right)$$
$$+ \frac{m_{Na}}{2m_2^*} + m_4\left(\frac{2}{m_1^*} - \frac{1}{m_2^*} - \frac{1}{m_3^*} + \frac{1}{m_4^*}\right) = 1. \qquad (7)$$

Besides the variable m_4, Eq. (7) contains isopiestic concentrations of binary solutions that are functions of the only variable a_s. Therefore, it is necessary to add one more equation in the form of the expression for

density of an ideal isopiestic solution ρ_{mix} [8, 9]:

$$\rho_{mix} = \left(1 + 10^{-3}\sum_{i=1}^{r} m_i M_i\right)\left[\sum_{i=1}^{r}\frac{m_i}{m_i^*}\frac{1 + 10^{-3} m_i^* M_i}{\rho_i^*}\right]^{-1}, \quad (8)$$

where M_i is the molar mass of the ith dissolved component and ρ_i^* is the density of the isopiestic binary solution of the ith dissolved component.

Substituting the expression for m_4 following from Eq. (7) into Eq. (8), we bring Eq. (8) into the form

$$\rho_{mix} = \left\{1 + 10^{-3}\left[m_{Cl}\left(M_1 - \frac{M_2}{2}\right) + \frac{m_{Na}M_2}{2} + m_{Mg}(M_2 - 2M_1 + M_3)\right.\right.$$

$$\left.\left. + (2M_1 - M_2 - M_3 + M_4)\frac{1 - \dfrac{m_{Na}}{2m_2^*} - m_{Cl}\left(\dfrac{1}{m_1^*} - \dfrac{1}{2m_2^*}\right) - m_{Mg}\left(\dfrac{1}{m_2^*} - \dfrac{2}{m_1^*} + \dfrac{1}{m_3^*}\right)}{\dfrac{2}{m_1^*} - \dfrac{1}{m_2^*} - \dfrac{1}{m_3^*} + \dfrac{1}{m_4^*}}\right]\right\}$$

$$\times \left\{m_{Cl}\left(\frac{1 + 10^{-3} m_1^* M_1}{m_1^* \rho_1^*} - \frac{1 + 10^{-3} m_2^* M_2}{2m_2^* \rho_2^*}\right) + \frac{m_{Na}}{2m_2^*}\frac{1 + 10^{-3} m_2^* M_2}{\rho_2^*} + m_{Mg}\left(\frac{1 + 10^{-3} m_2^* M_2}{m_2^* \rho_2^*} - 2\frac{1 + 10^{-3} m_1^* M_1}{m_1^* \rho_1^*}\right.\right. \quad (9)$$

$$\left. + \frac{1 + 10^{-3} m_3^* M_3}{m_3^* M_3}\right) + \left(\frac{2}{m_1^*}\frac{1 + 10^{-3} m_1^* M_1}{\rho_1^*} - \frac{1 + 10^{-3} m_2^* M_2}{m_2^* \rho_2^*} - \frac{1 + 10^{-3} m_3^* M_3}{m_3^* \rho_3^*} + \frac{1 + 10^{-3} m_4^* M_4}{m_4^* \rho_4^*}\right)$$

$$\left. \times \frac{1 - \dfrac{m_{Na}}{2m_2^*} - m_{Cl}\left(\dfrac{1}{m_1^*} - \dfrac{1}{2m_2^*}\right) - m_{Mg}\left(\dfrac{1}{m_2^*} - \dfrac{2}{m_1^*} + \dfrac{1}{m_3^*}\right)}{\dfrac{2}{m_1^*} - \dfrac{1}{m_2^*} - \dfrac{1}{m_3^*} + \dfrac{1}{m_4^*}}\right\}^{-1}.$$

The calculation of the electrolyte concentrations in mixed and binary isopiestic solutions, as well as the calculation of the corresponding values of U_{mix}, is performed for a temperature of 25°C, for which the dependences of binary solution molalities on a_s are given in [3] and the dependencies of osmotic coefficients of binary solutions on the concentrations are presented in [10].

The right-hand side of the last relationship is a function of the only variable, which can be either a_s or the quantity

$$W = -10^3 M_s^{-1}\ln a_s, \quad (10)$$

where M_s is the molar mass of the solvent. Instead of the variable a_s, one can also use the molality of one of the four binary solutions m_1^*, which is in one-to-one correspondence with a_s. The value of W, for which the computed value of ρ_{mix} coincides with the experimental one, determines the value of a_s of the mixed solution, the values of molalities and densities of the isopiestic binary solutions, and the values of the salt concentrations in the mixed solution.

Dependences of the densities of binary solutions on their concentrations are taken from [1]. After the mola-

lities and densities of binary isopiestic solutions, as well as the molalities of the mixed solutions, are determined, we can use the formula for calculating the speed of sound in a mixed solution u_{mix} [12]:

$$u_{mix}^{-2} = \left(\sum_{i=1}^{r}\frac{m_i}{m_i^*}\frac{1 + 10^{-3} m_i^* M_i}{\rho_i^*}\right)^{-2}\left(1 + 10^{-3}\sum_{i=1}^{r} m_i M_i\right)$$

$$\times \left\{\sum_{k=1}^{r}\frac{m_k(1 + 10^{-3} m_k^* M_k)}{m_k^* \rho_k^{*2} u_k^{*2}} + T\sum_{t>l}\sum\frac{m_t}{m_t^*}\frac{m_l}{m_l^*} C_{pt}^* C_{pl}^*\right.$$

$$\times \left[\frac{\alpha_t^*}{C_{pt}^*}\frac{(1 + 10^{-3} m_t^* M_t)}{\rho_t^*} - \frac{\alpha_l^*}{C_{pl}^*}\frac{1 + 10^{-3} m_l^* M_l}{\rho_l^*}\right]^2 \quad (11)$$

$$\times \left.\left(\sum_{g=1}^{r}\frac{m_g C_{pg}^*}{m_g^*}\right)^{-1}\right\},$$

where C_{pi}^* are isobaric heat capacities of such a mass of the isopiestic binary solution of the ith dissolved component that contains 1 kg of the solvent. The concentration dependences of the densities and sound speeds for

Table 2. Masses of the Na^+, Mg^{2+}, K^+, Ca^{2+}, and SO_4^{2-} ions and the corresponding numbers of moles of these ions per 1 kg of seawater for $S = 35.043‰$. The mass of Cl^- and number of moles of Cl^- in 1 kg of seawater that are determined from the electric neutrality condition for the solution with six ions and the corresponding ion molalities

Ions	Masses of ions (in grams) per 1 kg of seawater, G_i, taken from [1] (except for G_{Cl})	Numbers of ion moles per 1 kg of seawater, N_i, taken from [1] (except for N_{Cl})	Molalities of ions in an ideal isopiestic solution of four salts, m_i
Na^+	10.7596	0.4880122	0.485075
Mg^{2+}	1.2965	0.0533429	0.055287
K^+	0.3991	0.010208	0.010580
Ca^{2+}	0.4119	0.010277	0.010652
SO_4^{2-}	2.7124	0.0282377	0.029267
Cl^-	19.4632	0.548915	0.569002

binary isopiestic solutions, u_j^*, are taken from [11]. The latter publication also contains the temperature dependences of the densities of the binary solutions of interest, which make it possible to compute the concentration dependences of expansion coefficients of the binary solutions α_j^*.

The values of the heat capacities of the binary solutions are taken from [7, 13].

According to [1], the value $S = 33.141‰$ corresponds to the value $\rho_{mix}^{exp} = 1021.971$ kg m^{-3}. From Eq. (9), it follows that $m_1^* = 0.541477$, $m_2^* = 0.480383$, $m_3^* = 0.365350$, $m_4^* = 0.978582$, $m_1 = 0.426562$, $m_2 = 0.029258$, $m_3 = 0.055281$, $m_4 = 0.000007$, $a_s = 0.98218$, and $\rho_{mix} = 1021.928$ kg m^{-3}. Using the value of the sound speed in water, which equals 1497.0 m s^{-1} at 25°C [14], and the values of the sound speed in the binary solutions of the four salts at 25°C [11], we determine the sound speed in seawater $u_{mix} = 1533.45$ m s^{-1}. The value of sound speed obtained from the experimental dependence $u_{mix}(S)$ is $u_{mix}^{exp} = 1533.14$ m s^{-1} for $S = 33.141‰$ [1].

As the next approximation, we take into account the presence of two more cations: Ca^{2+} and K^+. We neglect the presence of $CaSO_4$ on the basis of the value of its solubility product [7]. We consider the seawater to be an ideal isopiestic solution of a mixture of seven salts: $NaCl$, Na_2SO_4, $MgCl_2$, $MgSO_4$, KCl, K_2SO_4, and $CaCl_2$. The equations relating the ion and salt molalities have the form

$$\left. \begin{array}{r} m_1 + 2m_3 + m_5 + 2m_7 = m_{Cl} \\ m_1 + 2m_2 = m_{Na} \\ m_3 + m_4 = m_{Mg} \\ m_5 + 2m_6 = m_k \\ m_2 + m_4 + m_6 = m_{SO_4} \end{array} \right\}. \quad (12)$$

The subscripts 5, 6, and 7 refer to the properties of KCl, K_2SO_4, and $CaCl_2$, respectively. Evidently, we have $m_7 = m_{Ca}$. The value of m_{Cl}, as in the previous approximation, is changed so as to satisfy the electric neutrality condition, which can be represented as

$$N_{Na^+} + 2N_{Mg^{2+}} + N_{K^+} + 2N_{Ca^{2+}} = 2N_{SO_4^{2-}} + N_{Cl^-}. \quad (13)$$

The set of equations (12) contains six unknown quantities and is of rank four. Therefore, besides expression (8) for ρ_{mix}, we have to use one more relation that makes it possible to calculate a mixed solution property. For this purpose, we can use an equation connecting the isobaric heat capacity of such a mass of the mixed solution that contains 1 kg of solvent, C_{pmix}, and the isobaric heat capacities of such masses of the binary isopiestic solutions that contain 1 kg of solvent each, C_{pi}^* [8, 9]:

$$C_{pmix} = \sum_{i-1}^{r} \frac{m_i}{m_i^*} C_{pi}^*. \quad (14)$$

For the ideal isopiestic solution of the salt mixture under consideration, we have $S = 35.0474‰$. The values of the ion masses, the numbers of ion moles per L_s kg of pure water, and the values of molalities in the ideal isopiestic solution are presented in Table 2. Since the rank of the set of equations (12) equals four, the molalities of four salts can be expressed in terms of the molalities of two salts, which we choose to be m_3 and m_5.

In view of Eqs. (12), relationship (1) for the solution of the salt mixture under consideration takes the form

$$m_{Cl}\left(\frac{1}{m_1^*} - \frac{1}{2m_2^*}\right) + m_3\left(\frac{1}{m_3^*} - \frac{1}{m_4^*} - \frac{2}{m_1^*} + \frac{1}{m_2^*}\right) + \frac{m_{Na}}{2m_2^*} + \frac{m_k}{2m_6^*} + m_5\left(\frac{1}{m_5^*} - \frac{1}{m_6^*} - \frac{1}{m_1^*} + \frac{1}{2m_2^*}\right)$$

$$+ m_{Ca}\left(\frac{1}{m_7^*} - \frac{2}{m_1^*} + \frac{1}{m_2^*}\right) = 1 \quad (15)$$

and makes it possible to express m_5 and W. Because of the greater uncertainty than in the case of the seven-salt solution, the use of Eq. (10) is insufficient to determine the molalities of isopiestic solutions and the molalities of the mixed solution. It is necessary to use one more equation, which, for the solution of the seven-salt mixture, can be written as

$$
C_{p\mathrm{mix}} = m_{\mathrm{Cl}}\left(\frac{C_{p1}^*}{m_1^*} - \frac{C_{p2}^*}{2m_2^*}\right) + \frac{m_{\mathrm{Na}}}{2m_2^*}C_{p2} + m_3\left(\frac{C_{p3}^*}{m_3^*} - \frac{C_{p4}^*}{m_4^*} - \frac{2C_{p1}^*}{m_1^*} + \frac{C_{p2}^*}{m_2^*}\right) + \frac{m_{\mathrm{K}}}{2m_6^*}C_{p6}
$$
$$
+ m_5\left(\frac{C_{p5}^*}{m_5^*} - \frac{C_{p6}^*}{2m_6^*} - \frac{C_{p1}^*}{m_1^*} + \frac{C_{p2}^*}{2m_2^*}\right) + \frac{m_{\mathrm{Mg}}}{m_4^*}C_{p4}^* + m_{\mathrm{Ca}}\left(\frac{C_{p7}^*}{m_7^*} - \frac{2C_{p1}^*}{m_1^*} + \frac{C_{p2}^*}{m_2^*}\right). \tag{16}
$$

Determining m_3 from Eq. (15),

$$
m_3 = \frac{1 - m_{\mathrm{Cl}}\left(\dfrac{1}{m_7^*} - \dfrac{2}{m_1^*} + \dfrac{1}{m_2^*}\right) - m_5\left(\dfrac{1}{m_5^*} - \dfrac{1}{2m_6^*} - \dfrac{1}{m_1^*} + \dfrac{1}{2m_2^*}\right) - m_{\mathrm{Cl}}\left(\dfrac{1}{m_1^*}\dfrac{1}{2m_2^*}\right) - \dfrac{m_{\mathrm{Na}}}{2m_2^*} - \dfrac{m_{\mathrm{K}}}{2m_6^*} - \dfrac{m_{\mathrm{Mg}}}{m_4^*}}{\dfrac{1}{m_3^*} - \dfrac{1}{m_2^*} - \dfrac{2}{m_2^*} + \dfrac{1}{m_2^*}}, \tag{17}
$$

and using Eq. (16), we obtain

$$
C_{p\mathrm{mix}} = m_{\mathrm{Cl}}\left(\frac{C_{p1}^*}{m_1^*} - \frac{C_{p2}^*}{2m_2^*}\right) + \frac{m_{\mathrm{Na}}}{2m_2^*}C_{p2}^* + \frac{m_{\mathrm{Mg}}}{m_4^*}C_{p4}^* + m_5\left(\frac{C_{p5}^*}{m_5^*} - \frac{C_{p6}^*}{2m_6^*} - \frac{C_{p1}^*}{m_1^*} + \frac{C_{p2}^*}{2m_2^*}\right) + \frac{m_{\mathrm{K}}}{2m_6^*}C_{p6}^*
$$
$$
+ m_{\mathrm{Ca}}\left(\frac{C_{p7}^*}{m_7^*} - \frac{2C_{p1}^*}{m_1^*} + \frac{C_{p2}^*}{m_2^*}\right) + \left(\frac{C_{p3}^*}{m_3^*} - \frac{C_{p4}^*}{m_4^*} - \frac{2C_{p1}^*}{m_1^*} + \frac{C_{p2}^*}{m_2^*}\right)\left[1 - m_{\mathrm{Ca}}\left(\frac{1}{m_7^*} - \frac{2}{m_1^*} + \frac{1}{m_2^*}\right) - \frac{m_{\mathrm{Na}}}{2m_2^*} - \frac{m_{\mathrm{Mg}}}{m_4^*}\right. \tag{18}
$$
$$
\left. - m_5\left(\frac{1}{m_5^*} - \frac{1}{2m_6^*} - \frac{1}{m_1^*} + \frac{1}{2m_2^*}\right) - \frac{m_{\mathrm{K}}}{2m_6^*} - m_{\mathrm{Cl}}\left(\frac{1}{m_1^*} - \frac{1}{2m_2^*}\right)\right]\left[\frac{1}{m_3^*} - \frac{1}{m_2^*} - \frac{2}{m_1^*} + \frac{1}{m_2^*}\right]^{-1}.
$$

This formula allows us to express m_5 in terms of the properties of the binary isopiestic solutions:

$$
m_5 = \left\{\left(\frac{1}{m_3^*} - \frac{1}{m_2^*} - \frac{2}{m_1^*} + \frac{1}{m_2^*}\right)\left[C_{p\mathrm{mix}} - m_{\mathrm{Cl}}\left(\frac{C_{p1}^*}{m_1^*} - \frac{C_{p2}^*}{2m_2^*}\right) - \frac{m_{\mathrm{Na}}}{2m_2^*}C_{p2}^* - \frac{m_{\mathrm{Mg}}}{m_4^*}C_{p4}^* - \frac{m_{\mathrm{K}}}{m_6^*}C_{p6}^*\right.\right.
$$
$$
\left.- m_{\mathrm{Ca}}\left(\frac{C_{p7}^*}{m_7^*} - \frac{2C_{p1}^*}{m_1^*} + \frac{C_{p2}^*}{m_2^*}\right)\right] - \left(\frac{C_{p3}^*}{m_3^*} - \frac{C_{p4}^*}{m_4^*} - \frac{2C_{p1}^*}{m_1^*} + \frac{C_{p2}^*}{m_2^*}\right)\left[1 - m_{\mathrm{Ca}}\left(\frac{1}{m_7^*} - \frac{2}{m_1^*} + \frac{1}{m_2^*}\right)\right.
$$
$$
\left.\left. - m_{\mathrm{Cl}}\left(\frac{1}{m_1^*} - \frac{1}{2m_2^*}\right) - \frac{m_{\mathrm{Na}}}{2m_2^*} - \frac{m_{\mathrm{Mg}}}{m_4^*} - \frac{m_{\mathrm{K}}}{2m_6^*}\right]\right\}\left\{\left(\frac{C_{p5}^*}{m_5^*} - \frac{C_{p6}^*}{2m_6^*} - \frac{C_{p1}^*}{m_1^*} + \frac{C_{p2}^*}{2m_2^*}\right)\left(\frac{1}{m_3^*} - \frac{1}{m_2^*} - \frac{2}{m_1^*} + \frac{1}{m_2^*}\right)\right. \tag{19}
$$
$$
\left. - \left(\frac{C_{p5}^*}{m_5^*} - \frac{C_{p6}^*}{m_4^*} - \frac{2C_{p1}^*}{m_1^*} + \frac{C_{p2}^*}{m_2^*}\right)\left(\frac{1}{m_5^*} - \frac{1}{2m_6^*} - \frac{1}{m_1^*} + \frac{1}{2m_2^*}\right)\right\}^{-1}.
$$

The latter relationship is used in the formula for ρ_{mix} (9), which, for the solution under consideration, takes the form

$$
\rho_{\mathrm{mix}} = \left\{1 + 10^{-3}\left[m_{\mathrm{Cl}}\left(M_1 - \frac{M_2}{2}\right) + \frac{m_{\mathrm{Na}}M_2}{2} + m_3(M_3 - M_4 - 2M_1 + M_2) + \frac{m_{\mathrm{K}}M_6}{2}\right.\right.
$$
$$
\left.\left. + m_5(M_5 - M_6/2 - M_1 + M_2/2) + m_{\mathrm{Mg}}M_4 + m_{\mathrm{Ca}}(M_7 - 2M_1 + M_2)\right]\right\}\left\{m_{\mathrm{Cl}}\left(\frac{1 + 10^{-3}m_1^*M_1}{m_1^*\rho_1^*} - \frac{1 + 10^{-3}m_2^*M_2}{2m_2^*\rho_2^*}\right)\right.
$$
$$
\left. + \frac{m_{\mathrm{Na}}}{2m_2^*}\frac{1 + 10^{-3}m_2^*M_2}{\rho_1^*} + \frac{m_{\mathrm{Mg}}}{2m_4^*}\frac{1 + 10^{-3}m_4^*M_4}{\rho_4^*}\right. \tag{20}
$$

$$+ m_3\left(\frac{1 + 10^{-3}m_3^* M_3}{m_3^*\rho_3} - \frac{1 + 10^{-3}m_4^* M_4}{m_4^*\rho_4} - 2\frac{1 + 10^{-3}m_1^* M_1}{m_1^*\rho_1} + \frac{1 + 10^{-3}m_2^* M_2}{m_2^*\rho_2}\right)$$

$$+ m_{\text{Ca}}\left(\frac{1 + 10^{-3}m_7^* M_7}{m_7^*\rho_7} - 2\frac{1 + 10^{-3}m_1^* M_1}{m_1^*\rho_1} + \frac{1 + 10^{-3}m_2^* M_2}{m_2^*\rho_2}\right)^{-1}\Biggr\} .$$

One can readily see that the last two equations contain only two independent variables, namely, the quantity a_s or the quantity W determined by Eq. (13) and the molality of one of the electrolytes in the mixed solution; in our case, it is m_5. Using the concentration dependences of the densities of binary solutions and the dependences of the molalities of binary solutions on a_s, it is possible to determine a_s and the molalities of the mixed and binary solutions.

The values of α_i^* required for calculating u_{mix} by Eq. (14) can be found from the temperature dependences of the densities of binary solutions. The concentration dependences of the densities and the heat capacities of binary solutions and the speeds of sound in these solutions are taken from [7, 11, 13, 15, 16].

For the concentrations of 6 ions from Table 2 and for $S = 35.043‰$, the experimental values of the heat capacity and density of the mixed solution are $C_{p\text{mix}} = 4141.89$ J (kg of water)$^{-1}$ K^{-1} and $\rho_{\text{mix}}^{\text{exp}} = 1023.375$ kg m^{-3} [1].

The density value nearest to $\rho_{\text{mix}}^{\text{exp}}$, for which the set of equations (19), (20) has a solution, is $\rho_{\text{mix}} = 1023.285$ kg m^{-3}. The value $S = 35.043‰$ corresponds to the values $\rho_{\text{mix}}^{\text{exp}} = 1023.375$ kg m^{-3} and $C_{p\text{mix}} = 4141.34$ J (kg of water)$^{-1}$ K^{-1} [1]. From Eqs. (19), (20),

we obtain $a_s = 0.98133$, $m_1^* = 0.56727$, $m_2^* = 0.50611$, $m_3^* = 0.38122$, $m_4^* = 1.02709$, $m_5^* = 0.58285$, $m_6^* = 0.550597$, $m_7^* = 0.39061$, $m_1 = 0.45126$, $m_2 = 0.01065$, $m_3 = 0.04822$, $m_4 = 0.00707$, $m_5 = 0.00001$, $m_6 = 0.00528$, $m_7 = 0.1065$, $\rho_{\text{mix}} = 1023.315$ kg m^{-3}, $u_{\text{mix}} = 1536.0$ m s^{-1}, and $C_{p\text{mix}} = 4140.42$ J (kg of water)$^{-1}$ K^{-1}, while the experimental value of u_{mix} at $S = 35.043‰$ is 1535.04 m s^{-1}.

It is of interest to consider seawater as an ideal isopiestic solution of four salts on condition that the masses of the K$^+$ and Ca^{2+} ions are replaced by equal masses of the Na$^+$ and Mg^{2+} ions, respectively. Then, seawater is represented as an ideal isopiestic solution of four salts formed by two cations and two anions with a salinity that is closer to the salinity of seawater than the value of S corresponding to the solution of four salts considered above. As before, the value of the mass of chlorine ions in 1 kg of seawater should differ from the value given in [1] to satisfy the electric neutrality condition. The values of the ion masses and the numbers of ion moles per 1 kg of seawater are presented in Table 3.

The value 35.769‰ characterizing the solution composition given in Table 3 corresponds to the value of $\rho_{\text{mix}}^{\text{exp}}$ equal to 1023.958 kg m^{-3}.

From Eq. (9), we obtain $a_s = 0.98130$, $m_1^* = 0.56804$, $m_2^* = 0.50688$, $m_3^* = 0.38171$, $m_4^* = 1.02860$, $m_1 = 0.43767$, $m_2 = 0.02900$, $m_3 = 0.06567$, $m_4 = 0.00027$, $\rho_{\text{mix}} = 1023.122$ kg/m^3, $C_{p\text{mix}} = 4140.64$ J (kg of water)$^{-1}$ K^{-1}, and $u_{\text{mix}} = 1534.21$ m s^{-1}.

The experimental value of u_{mix} for $S = 35.769‰$ is equal to 1535.75 m s^{-1} [1].

Table 3. Mass of the SO_4^{2-} ion, the number of moles of SO_4^{2-} per 1 kg of seawater for $S = 35.043‰$, the masses of the Na$^+$ and Mg^{2+} cations that are changed to take into account the K$^+$ and Ca^{2+} ions, and the numbers of moles of Na$^+$ and Mg^{2+} in 1 kg of seawater. The mass of Cl$^-$ and the number of moles of Cl$^-$ in 1 kg of seawater that are determined from the electric neutrality condition for the solution with four ions and the corresponding ion molalities

Ions	Changed values of the masses of ions (in grams) per 1 kg of seawater, G_i	Changed values of the numbers of ion moles per 1 kg of seawater, N_i	Ion molality in the solution of four salts, m_i
Na$^+$	11.1587	0.485372	0.503377
Mg^{2+}	1.7084	0.070290	0.072898
SO_4^{2-}	2.7124	0.028238	0.029286
Cl$^-$	20.1896	0.569476	0.590601

REFERENCES

1. N. I. Popov, K. N. Fedorov, and V. M. Orlov, *Sea Water* (Nauka, Moscow, 1979).

2. *Chemistry of the Ocean,* Vol. 1: *Chemistry of the Ocean Waters*, Ed. by O. K. Bordovskiǐ and V. N. Ivangenov (Nauka, Moscow, 1979).

3. A. N. Kirgintsev, *Notes on the Thermodynamics of Water–Salt Systems* (Nauka, Novosibirsk, 1976).

4. D. A. Denisov, Akust. Zh. **33**, 772 (1987) [Sov. Phys. Acoust. **33**, 449 (1987)].

5. J. F. Hu, Bull. Chem. Soc. Jpn. **74**, 47 (2001).

6. K. Powell, D. Remimette, B. Byme, S. Gjobery, K. Popov, and L. Pettit, *Solution Equilibria. Principles*

and Applications. The How and Why of Equilibria in Solution (Roewyn Town, 2000).

7. *Handbook of a Chemist: Main Properties of Inorganic and Organic Compounds*, Ed. by B. P. Nikol'skiĭ *et al.*, 2nd ed. (Khimiya, Moscow, 1964), Vol. 3.

8. A. B. Zdanovskiĭ, Tr. Solyanoĭ Lab. Vses. Inst. Galurgii, Akad. Nauk SSSR, No. 6, 5 (1936).

9. Yu. G. Frolov and D. A. Denisov, Tr. Mosk. Khim.– Tekhnol. Inst. im. D. I. Mendeleeva, No. 111, 102 (1980).

10. R. A. Robinson and R. H. Stokes, *Electrolyte Solutions*, 2nd ed. (Butterworths, London, 1959; Inostrannaya Literatura, Moscow, 1963).

11. F. J. Millero, F. Vinokurova, M. Fernandes, and P. J. Hershey, J. Solution Chem. **16** (4), 269 (1987).

12. D. A. Denisov, Akust. Zh. **39**, 757 (1993) [Acoust. Phys. **39**, 399 (1993)].

13. V. A. Vasilev, *Calculation of the Density and Heat Capacity of Aqueous Solutions of Inorganic Compounds* (Mosk. Khim.–Tekhnol. Inst., Moscow, 1979).

14. *Physical Quantities: Handbook*, Ed. by I. S. Grigor'ev and E. Z. Meĭlikhov (Énergoatomizdat, Moscow, 1991).

15. *Technical Encyclopedia: Handbook on Physical, Chemical, and Technological Quantities* (Sovetskaya Éntsiklopediya, Moscow, 1933), Vol. 10.

16. P. Prozorov, Zh. Fiz. Khim. **14** (3), 384 (1940).

Translated by A. Svechnikov

Guided Waves in a Stratified Half-Space[1]

Bixing Zhang and Laiyu Lu

Institute of Acoustics, Chinese Academy of Sciences, Beijing, 100080, People's Republic of China
e-mail: zhbx@mail.ioa.ac.cn
Received January 8, 2002

Abstract—The dispersion and excitation mechanisms and the energy distribution of guided waves in a stratified half-space are studied. All possible guided waves excited by a symmetric point source in two or three-layer medium models and their relation to the medium parameters are analyzed in detail. The excitation and propagation characteristics, as well as the energy distribution along the depth direction, of all modes of the surface waves and trapped waves are numerically investigated and analyzed thoroughly not only in the case when the shear wave velocity increases from up to down layers but also when a low-velocity layer is contained in half-space, especially when the shear wave velocity decreases from up to down layers. It is found that there exist many guided wave modes in the case where the shear wave velocity of each layer increases from up to down layers. However, there is less than one guided wave mode in the case where the shear wave velocity of each layer decreases from up to down layers. The trapped waves exist and propagate along the low-velocity structure in the stratified half-space. It is also found that the characteristic of a mode is related to the source frequency. It is possible that a surface wave at one value of frequency is like a trapped wave at another value of frequency. Finally, the relation of the characteristics of all guided waves (surface waves and trapped waves) to the parameters of media is studied. © *2003 MAIK "Nauka/Interperiodica"*.

1. INTRODUCTION

The propagation of elastic waves in stratified half-space has been studied by many researchers. It is of great importance to theoretical and practical studies in many fields, such as geophysics, engineering survey, non-destructive testing (NDT), etc. It was found that guided waves propagating along the surface have characteristics such as strong amplitude, slow attenuation, and strong interference immunity. Therefore, detecting the material property of the medium and layered geometry in stratified half-space has attracted more and more attention. The method of Rayleigh wave exploration is a good method for detecting the media structure by the information of the guided waves [1–7].

Generally speaking, there exist infinite modes of the guided wave modes propagated along the stratified structure, which can be divided into two kinds in principle. One is a surface wave [8–10], whose energy concentrates near the free surface. The other is trapped wave [10–13], whose energy concentrates within an area under the free surface. The trapped wave sometimes cannot be detected at the free surface, because its energy is small. It is possibly the surface wave that is received by a detector located on the surface in NDT. However, there is no surface wave propagated along the free surface in some frequency ranges when there exist low-velocity layers or fractures below the surface. But trapped waves can be excited in this case and can be received by the detector. In fact, most of the energy of the trapped waves concentrates near the interface in the

low-velocity layers. Much information about the low-velocity layers is carried by the trapped waves. This shows that study of trapped waves is an important topic.

Much formation information can be obtained in geophysical survey thanks to the development of the cross-borehole and VSP (Vertical Seismic Profile) technology. If the receiver is in the borehole below the free surface, the surface waves are too small to be seen. The received signal in the borehole is related to the guided waves propagating along the low-velocity layer (oil, gas, and coal). So the position and characteristics of the low-velocity layer can be obtained by the borehole information. Johnson *et al.* [14] discovered evidence for mode conversion of Stoneley borehole waves (tube waves) to stratigraphically guided waves in data from cross-hole acoustic experiments conducted by the Department of Energy in Colorado. This shows that guided waves trapped in multilayered media are very likely to confirm the continuity of heterogeneous formation.

Although advanced works have been conducted by many researchers about the guided waves propagating along a stratified half-space, they are limited to surface waves. Parra [10] studied the dispersion characteristics of several modes of trapped waves in a stratified half-space containing a low-velocity and porous layer. However, the excitation mechanism was not considered further, and which layer the trapped waves propagated along was not illustrated in his paper. Guzhev [15] studied the energy distribution of Stoneley waves at the solid–liquid interface. Kaibichev [16] studied transverse waves in an inhomogeneous layer between two

---

[1] This article was submitted by the authors in English.

media. Bixing Zhang studied the dispersion characteristics and excitation mechanism of the surface waves [15, 16] and trapped waves [10–12] in an elastic stratified half-space, but not all guided waves are analyzed. Moreover, problems such as the relation of the excitation and propagation characteristics of the guided waves to the formation parameters, especially the relation of the guided waves to the structure of the low-velocity layer contained in a stratified half-space, must be studied further. The guided waves in a stratified half-space whose compressional and shear wave velocities increase from up to down layers have been studied in previous works. When the compressional and shear velocities decrease from up to down layers and the low-velocity layer is contained in the half-space, few authors studied the excitation and propagation mechanisms of all guided waves.

All possible guided waves (surface and trapped waves) are studied in this paper. The excitation and propagation characteristics, as well as the energy distribution along the depth direction, of all possible guided waves in the case when shear wave velocity decreases from up to down layers or a low-velocity layer is contained in a stratified half-space are investigated and analyzed thoroughly.

2. CONFIGURATION

A stratified half-space system that is composed of N homogeneous, isotropic, and elastic solid layers is considered. A cylindrical coordinate system (r, θ, z) is introduced. The positive direction of the z axis vertically points to the medium interior. $z = 0$ is the free surface. The jth layer is bounded by the planes $z = z_{j-1}$ and $z = z_j$. Only a P–SV wave is considered in this paper.

The symmetric point source [17] is located at the point $(0, 0, z_s)$ in the cylindrical coordinate system (r, θ, z) to excite elastic wave fields (guided waves, compressional waves, and shear waves). Only guided waves are studied in the frequency–wavenumber domain in this paper. The propagator matrix method [11, 17] is adopted to analyze the propagation of an elastic wave along the stratified direction. The related mathematical formulas can be found in previous papers [11, 17, 18]. The intensities of guided waves can be given by the residues of the corresponding poles of the dispersion function. All guided waves for any given frequency can be obtained by the bisection method, because the dispersion equation is a real equation for real horizontal wavenumber in elastic stratified half-space.

3. GUIDED WAVES IN A HALF-SPACE CONTAINING TWO LAYERS

In this case, there exist two layers in a stratified half-space. Dispersion and propagation characteristics of all guided waves are studied for the models shown in Table 1,

in which there are six parameter groups and the last column gives the velocity of the Rayleigh wave in the half-space where there is only the corresponding layer. The discussions about guided waves are conducted in two cases according to the parameters shown in Table 1. Although the guided waves in this case have been studied [19], we also analyzed it simply in different aspects. This is useful for the next parts.

3.1. $V_{S1} < V_{S2}$

V_{S1} and V_{S2} are the shear wave velocities of the first and second layers, respectively. The first, second, third, and fourth parameter groups in Table 1 are for this case. Infinite modes of the guided waves in these parameter groups can be excited. They can be called 1, 2, 3, 4, …, nth modes from low frequency to high frequency. Their dispersion characteristics are familiar to us [19]. It should be pointed out that the dispersion of guided waves in the fourth parameter group have some different characteristics from the first, second, and third parameter groups. Fig. 1a gives the dispersion of guided waves in the fourth parameter group (the dispersion curves in the first, second, and third parameter groups can be found in previous work [19]). In this case, the velocity of the Rayleigh wave in the case where there is only the first layer (denoted by $V_{1\infty}$) is greater than that where there is only the second layer (denoted by $V_{2\infty}$). It can be found that there exits not only normal dispersion (the phase velocity is greater than the group velocity) but also inverse dispersion (the phase velocity is less than the group velocity). The distance between different modes is greater than that in the first, second, and third parameter groups.

Figures 1b and 1c give the displacement intensity spectrums of guided waves at the free surface for the first and third parameter groups. It can be seen that the displacement of the first mode is greater than that of the higher modes. The intensity of the first mode is dominant and has a broad frequency band in the spectrum, while the intensities of the higher modes are relatively smaller and the frequency bands are narrow. There is a maximum in Airy phase (the point at which the group velocity is minimum) in the displacement spectrum for higher modes. Comparing Fig. 1b with Fig. 1c, it can be seen that the frequency band and the intensity of high modes have a significant difference when the model parameters are changed from the first group to the third group.

The relation of the displacement intensities to the depth is also analyzed for all modes in this paper. Figures 1d, 1e, and 1f show the displacement distribution of the guided waves along the depth direction for the first parameter groups. For better understanding, vertical lines showing positions of the layer-to-layer interfaces are introduced in the figures. It can be found that the displacement of the fundamental mode mainly concentrates in a small range near the free surface and

Table 1. The parameters of two-layer models

Note	Density ρ (kg/m^3)	P-wave velocity V_P (m/s)	S-wave velocity V_S (m/s)	Thickness h (m)	V_∞ (m/s)
1	2500	4000	2500	5	2269
	2800	5000	3000	∞	2743
2	2500	4000	2800	5	2458
	2800	5000	3000	∞	2743
3	2300	3500	2300	5	2063
	2200	6000	3800	∞	3439
4	4540	5990	2960	5	2763
	2800	5000	3000	∞	2743
5	2200	6000	3100	5	2884
	2800	5000	3000	∞	2743
6	2800	5000	3000	5	2743
	2500	4000	2500	∞	2269

attenuates quickly with depth. This can be seen as the surface wave (Fig. 1d). For the second mode (Fig. 1e) and the third mode (Fig. 1f), the maximum of the displacement appears at a given depth instead of at the free surface. In addition, the numbers of the maximum in the first layer will increase by one if the orders of modes increase by one. These higher modes can be seen as the trapped wave. For the other three parameter groups, the properties of the guided waves are similar to this parameter group.

The conclusion can be drawn that the first mode corresponds to the surface wave whose displacement is greatest at the free surface and attenuates exponentially with increasing depth. However, the displacements of the higher modes are relatively small at the free surface and mainly concentrate at a given depth below the free surface.

3.2. $V_{S1} > V_{S2}$

In this case, the S-wave velocity of the first layer is greater than that of the second layer. The fifth and sixth parameter groups in Table 1 are for this case. This is very common in practical applications and very important to study the mechanism of propagation and excitation of the guided waves.

For the fifth parameter groups, $V_{1\infty} < V_{S2}$, it can be found from Fig. 2a that there exists only one guided wave. The dispersion phenomenon exists in the low-frequency range. The limit of the phase velocity of this mode is $V_{2\infty}$ at low frequency and is $V_{1\infty}$ at high frequency. Figure 2b shows the displacement spectrum of this mode at the free surface, at which has a maximum at 1500 Hz. Figure 2c displays the displacement variation with depth. It can be seen that this guided wave is a surface wave whose displacement attenuates exponentially with depth.

For the sixth parameter group, $V_{1\infty} > V_{S2}$, Fig. 2d shows that there exists only one mode before 200 Hz, whose phase velocity limit at low frequency is $V_{2\infty}$. The guided waves whose phase velocity is real will not exist when the frequency is greater than 200 Hz in Fig. 2d. This is because the phase velocity of the guided waves must be less than the S-wave velocity of the last layer in a stratified half-space.

It must be pointed out that only the first layer plays a main role in the entire half-space when the frequency tends towards infinity. This case is equivalent to the half-space case where only the first layer exists. Therefore, the limit of the phase velocity should be $V_{1\infty}$ when the frequency tends towards infinity. For the sixth parameter group, although there is no mode whose phase velocity is greater than V_{S2}, we should think that the limit of the phase velocity at high frequency is $V_{1\infty}$ in Fig. 2d.

Fig. 2e and Fig. 2f give the relations of the displacement spectrum of this mode to the frequency at the free surface and to the depth, respectively, when frequency is 120 Hz. It can be found that this is also the surface wave whose energy is concentrated near the surface and attenuates exponentially with depth. It can be also seen from Fig. 2d that the frequency band of the guided wave whose phase velocity is real becomes narrower when the thickness of the first layer increases.

From the above discussions, it can be found that the propagation characteristics of the guided waves for the case $V_{S1} > V_{S2}$ are very different from the case $V_{S1} < V_{S2}$. For the case $V_{S1} > V_{S2}$ there is at most one mode of the guided wave, which is a surface wave, for a given frequency.

4. GUIDED WAVES IN A HALF-SPACE CONTAINING THREE LAYERS

Three cases are considered in this section: the S-wave velocity increasing from up to down layers, decreasing from up to down layers, and a half-space containing a low-velocity layer. Table 2 shows the corresponding parameters of the models composed of three layers.

4.1. $V_{S1} < V_{S2} < V_{S3}$

This means that the S-wave velocity of each layer increases from up to down layers. The seventh parameter group in Table 2 is for this case. Figure 3a displays the dispersion curves of this model. It can be seen that the limit of the phase velocity of the fundamental mode is $V_{3\infty}$ at low frequency and $V_{1\infty}$ at high frequency. The limit of phase velocity of the higher modes is V_{S3} at the cutoff frequency and V_{S1} at high frequency. It is normal dispersion for all modes. Figure 3b gives the displacement spectrum of all modes at the free surface. It can be seen that the displacement of the fundamental mode is dominant and has a broad frequency band. Figure 3c
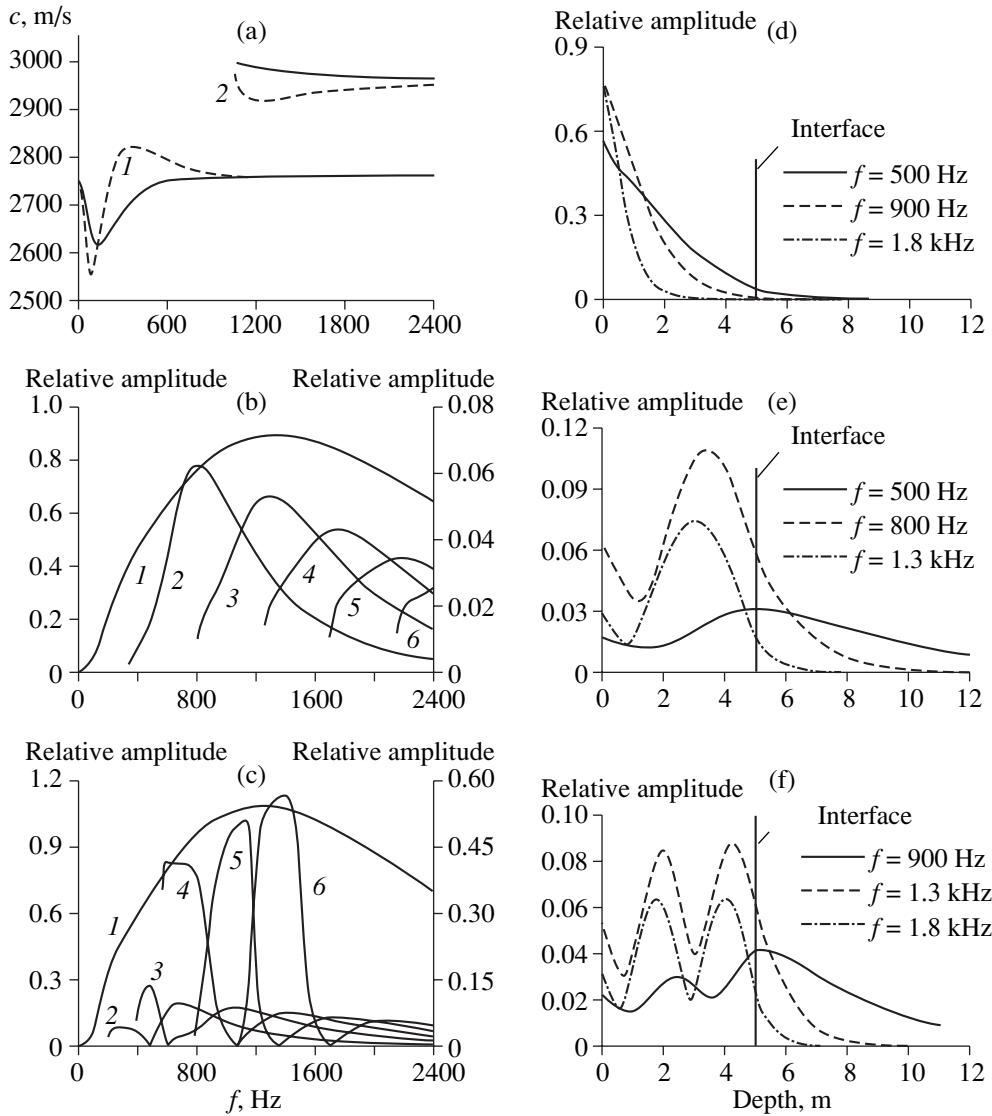
Fig. 1. The dispersion and displacement curves of guided waves in the first, third, and fourth parameter groups. (a) Is the dispersion curves in the fourth parameter group; the phase velocities and the group velocities are denoted by the solid line and the dashed lines, respectively. (b, c) Are the displacement spectrum at the free surface in the first and third parameter groups, respectively; the left and right ordinate axes are for the first and higher modes, respectively. (d, e, f) Are the displacement distribution with depth in the first parameter group.

gives the displacement distribution along the depth direction. It can be found that the fundamental mode is a surface wave whose displacement intensity mainly concentrates near the free surface. However, the modes with higher orders are trapped waves whose displacement intensities concentrate in the first layer. This case is similar to that in the first parameter group.

4.2. $V_{S1} > V_{S2} > V_{S3}$

In this case, the S-wave velocity of each layer decreases from up to down layers. The eighth and ninth parameter groups are for this case. For the eighth parameter group, $V_{1\infty} < V_{S3}$, the dispersion characteris-

tic of the guided wave is shown in Fig. 4a. Similar to the fifth parameter group (Fig. 2a), there exists only one surface wave mode. For the ninth parameter group, $V_{1\infty} > V_{S3}$, the dispersion characteristic of a guided wave is shown in Fig. 4b, which is similar to the sixth parameter group. There is only one surface wave mode in the low-frequency range. Figures 4c and 4d are the displacement distribution with the depth for the eighth and ninth parameter groups, respectively. Therefore, the characteristics of guided waves propagating along the stratified half-space in the case where the S-wave velocity decreases from up to down layers is very different from that in the case where the S-wave velocity increases from up to down layers. This conclusion is
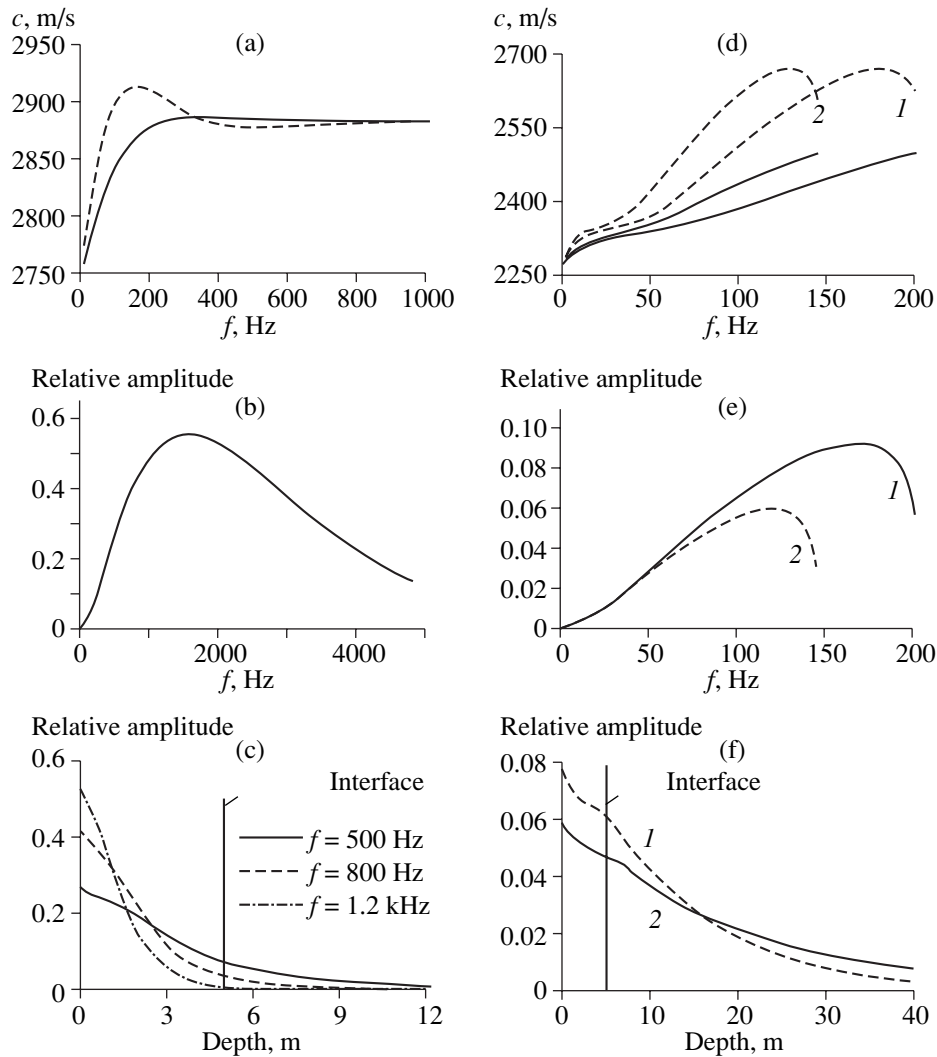
Fig. 2. The dispersion and displacement curves of guided waves in the fifth (a–c) and sixth (d–f) parameter groups. (a, d) Are the dispersion curves; the phase velocities and the group velocities are denoted by the solid line and the dashed lines, respectively; (b) and (e) are the displacement spectrum at the free surface; (c) and (f) are the displacement distribution with depth. 1—$h_1 = 5$ m; 2—$h_1 = 7$ m.

similar to that in the model containing two layers. So, it is proved that the effects of the number of layers on guided waves are insignificant in the case when shear wave velocity increases or decreases from up to down layers.

4.3. Medium Containing a Low-Velocity Layer

This case means that the S-wave velocity of the middle layer is less than the S-wave velocity of up and down layers. It is very common in practical applications, such as the oil layer in the Earth or fractures and pores in solid material. It is important to study how to detect the low-velocity layer. The propagation of guided waves in this case is complicated. Two cases are analyzed in the following.

4.3.1. $V_{S1} < V_{S3}$. The S-wave velocity of the first layer is less than that of the third layer in this case. The tenth parameter group in Table 2 is for this case. Figure 5 shows the characteristics of dispersion and propagation for this parameter group. It can be seen that the propagation of the guided waves is very different from the above discussions. The limit of the phase velocity of the fundamental mode is the S-wave velocity of the last layer at low frequency, while it is the S-wave velocity of low-velocity layer at high frequency. The dispersions of the modes with higher orders are normal dispersion. The dispersion of the fundamental mode is normal dispersion at low frequency and inversion dispersion at high frequency.

The phase velocity of the fourth mode is equal to $V_{1\infty}$ after the frequency exceeds 800 Hz (the order of the mode possessing these characteristics will be changed

Table 2. The parameters of three-layer models

Note	Density ρ (kg/m³)	P-wave velocity V_P (m/s)	S-wave velocity V_S (m/s)	Thickness h (m)	V_∞ (m/s)
7	2500	4000	2500	5	2269
	2800	5000	3000	2	2743
	3000	6000	3500	∞	3213
8	2200	6000	3100	5	2884
	2800	5000	3000	2	2743
	4540	5990	2960	∞	2763
9	3000	6000	3500	5	3213
	2800	5000	3000	2	2743
	2500	4000	2500	∞	2269
10	2500	4000	2500	5	2269
	1060	2350	1120	2	1048
	2800	5000	3000	∞	2743
11	2200	6000	3100	5	2884
	1060	2350	1120	2	1048
	2800	5000	3000	∞	2743
12	2800	5000	3000	5	2743
	1060	2350	1120	2	1048
	2500	4000	2500	∞	2269

Fig. 3. Dispersion curves (a), displacement spectrum (b) at free surface and displacement distribution (c) with depth in the seventh parameter group. In (b) and (c), left and right Y coordinates are for fundamental and high modes, respectively.

when h_2 is changed. The order of a mode increases when h_2 increases and decreases when h_2 decreases). The dispersion curves of the fifth mode and fourth mode intersect at 1060 Hz. Only the dispersion characteristics of the first, second, third, fourth, and fifth modes are given in Fig. 5a. In fact, there exist other higher modes whose dispersion characteristics are similar to that of the fifth mode. Their dispersion curves intersect that of the fourth mode and have a cutoff frequency at which the phase velocity is the S-wave velocity of the last layer. The limit of the phase velocity at high frequency is the S-wave velocity of the low-velocity layer. Figure 5b shows the displacement spectrum of each mode. It can be seen that the displacement intensity of the fourth mode is dominant and has a broad frequency band. The displacement of other modes concentrates in a narrow frequency band, especially for the fifth mode, whose energy distribution concentrates only in a very narrow frequency band, in which the phase velocity is very close to that of the fourth mode. Figs. 5c–5f are the relations of the displacement distributions of the first, third, forth, and fifth modes to depth, respectively. The displacement of the fundamental mode mainly concentrates between the first and second layer in the low-frequency range (less than 450 Hz). As the depth increases, it decays more slowly in the first layer than that in the second layer. When the frequency is greater than 450 Hz, the displacement concentrates gradually in the low-velocity layer and the
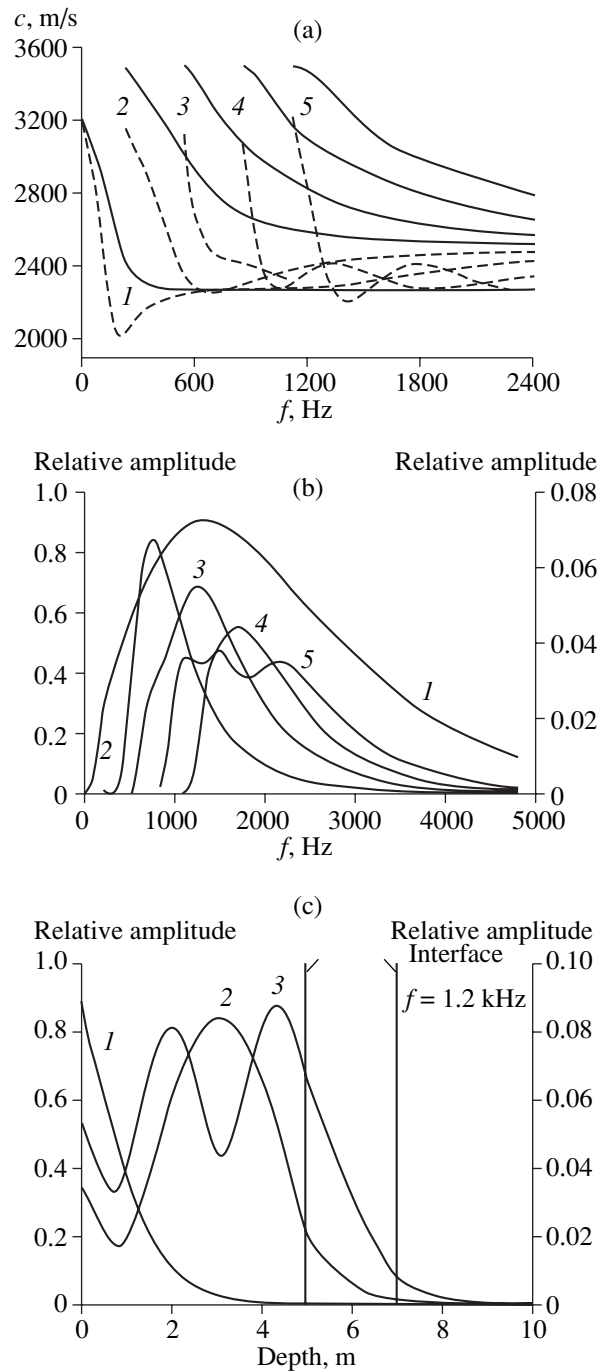
mode becomes trapped waves. Figure 5d shows that the displacement of the third guided wave mainly concentrates in the low-velocity layer before 450 Hz. The displacement of this mode distributes both in the first and second layers after 450 Hz, and it attenuates quickly in the first layer. If the frequency is in the range from 500 to 800 Hz, the guided wave is more like the surface
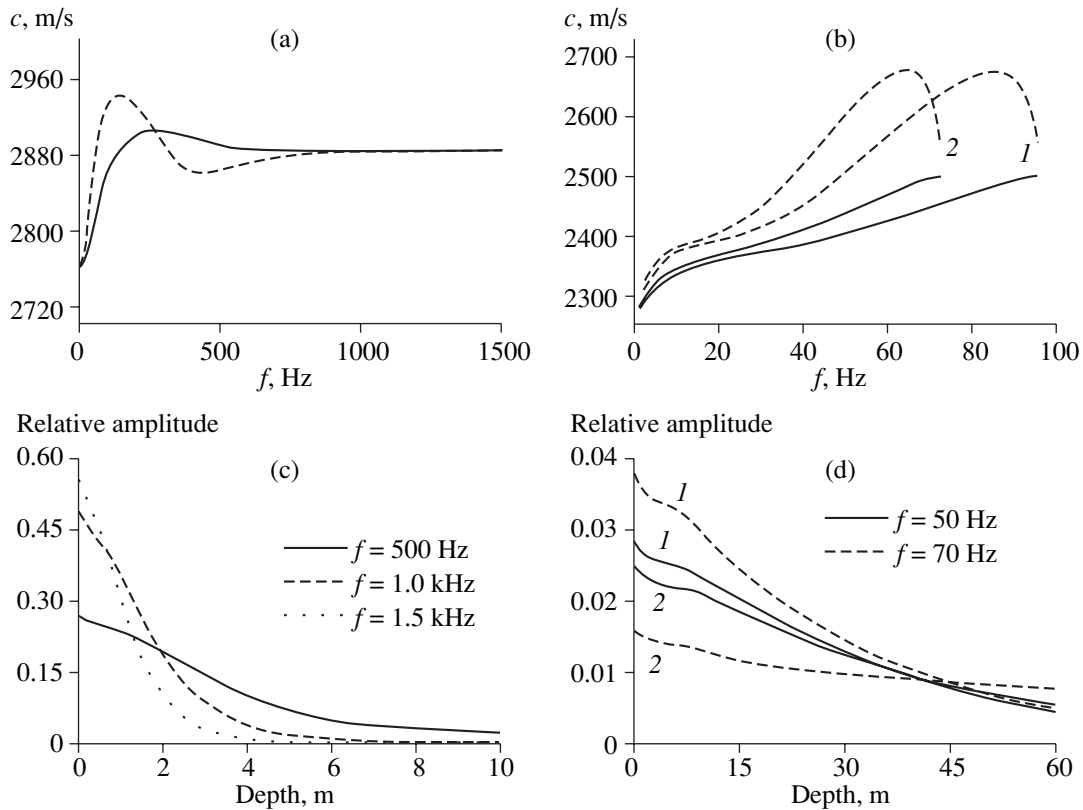
Fig. 4. Dispersion curves (a, b) and displacement distribution (c, d) with depth in the eighth (a, c) and ninth (b, d) parameter groups. *1*—$h_1 = 5$ m; *2*— $h_1 = 7$ m.

wave, since its displacement mainly concentrates in the first layer. The phase velocity in this frequency range (500–800 Hz) varies smoothly near $V_{1\infty}$ (see Fig. 5a). The guided wave becomes trapped wave when the frequency exceeds 800 Hz, and the displacement concentrates in the low-velocity layer. The fourth mode is the trapped wave whose energy concentrates in the low-velocity layer when the frequency is less than 800 Hz (Fig. 5e). However, the energy of this mode gradually moves to the first layer when the frequency is greater than 800 Hz (Fig. 5e). The closer the phase velocity to $V_{1\infty}$, the more this mode behaves as a surface wave. However, the properties of the fifth mode and the other modes with higher orders are very different from that of the above modes. The fifth mode is a trapped wave at any frequency (Fig. 5f), whose displacement is very small near the free surface and mainly concentrates in the low-velocity layer. The displacement variety with the frequency of the second mode is similar to that of the third mode.

From the above discussions, it can be found that there is no unified rule to explain which mode is a surface wave or which mode is a trapped wave. This is related to the source frequency. Some guided waves are surface waves at a given frequency, and they become trapped waves at another frequency. Sometimes the distribution of the displacement in the depth direction can

be found both near the free surface and in the low-velocity layer. In this case, the source frequency should be considered in order to judge whether the mode is a trapped wave or a surface wave. Nevertheless, it can be said that the higher modes, such as the fifth mode or modes with higher orders shown in Fig. 5, are trapped waves. For modes with low orders, the closer the phase velocity to $V_{1\infty}$, the more the mode is like a surface wave.

4.3.2. $V_{S1} > V_{S3}$. This means that the S-wave velocity of the first layer is greater than that of the third layer. The eleventh and twelfth parameter groups shown in Table 2 are for this case. For the eleventh parameter group ($V_{1\infty} < V_{S3}$), the dispersion curves of the guided waves propagating along the stratified layer are shown in Fig. 6a. It can be seen that the characteristics of dispersion curves are similar to that in the tenth parameter group. The limit of the phase velocity of the fundamental mode is V_{S3} at low frequency and V_{S2} at high frequency. The higher modes have cutoff frequencies at which the phase velocity is V_{S3}. The limits of the phase velocity of high modes at high frequency are the same as that of the fundamental mode, except for the seventh mode. The limit of the phase velocity of the seventh mode, which is the Rayleigh wave velocity in the case where there is only the first layer, is similar to that of the fourth mode shown in Fig. 5a. All modes are normal
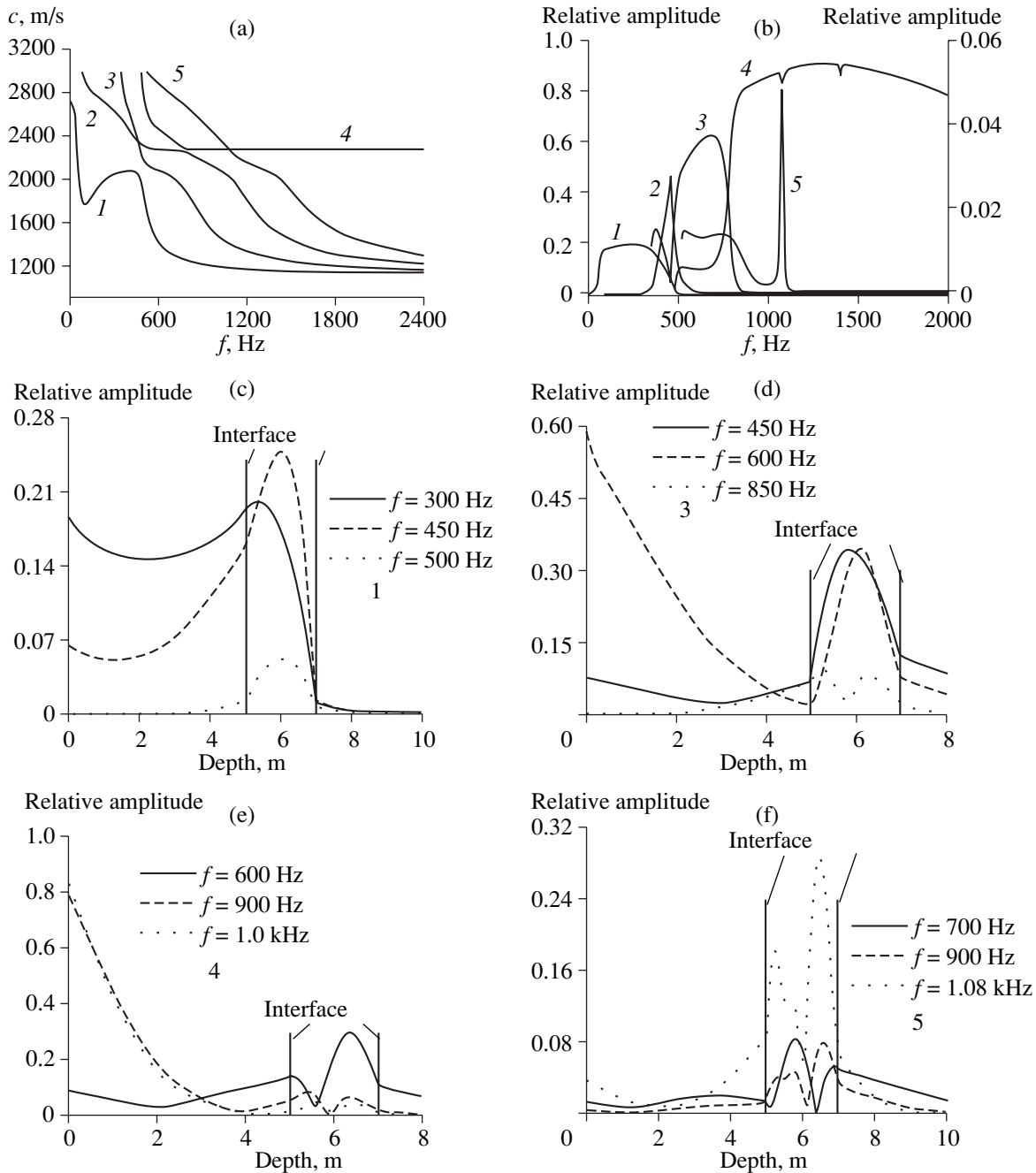
Fig. 5. Dispersion curves (a), displacement spectrum (b) at the free surface and displacement distribution (c–f) with depth in the tenth parameter group. In (b), right and left Y coordinates are for the fifth and the other modes, respectively.

dispersion except the fundamental mode, in which both normal and inverse dispersion can be found. Figure 6b shows the displacement spectrum of each mode at the free surface. It can be seen that the seventh mode has a broad frequency band, while the frequency bands of the other modes are narrow. Figures 6c, 6d, 6e, and 6f are the displacement distribution in the depth direction for the first, second, fifth, and seventh guided waves, respectively. It can be found from Fig. 6c that the displacement distribution of the first mode with depth is

similar to that of the first mode in the tenth parameter group. The displacement distribution can be found both in the first and the low-velocity layers. The displacement of this mode decays quickly in the low-velocity layer and slowly in the first layer. The mode gradually becomes a trapped wave with increasing frequency. The second mode shown in Fig. 6d is a trapped wave whose displacement concentrates in the low-velocity layer. The displacement distribution in the depth direction of the fifth mode is similar to that of the third mode
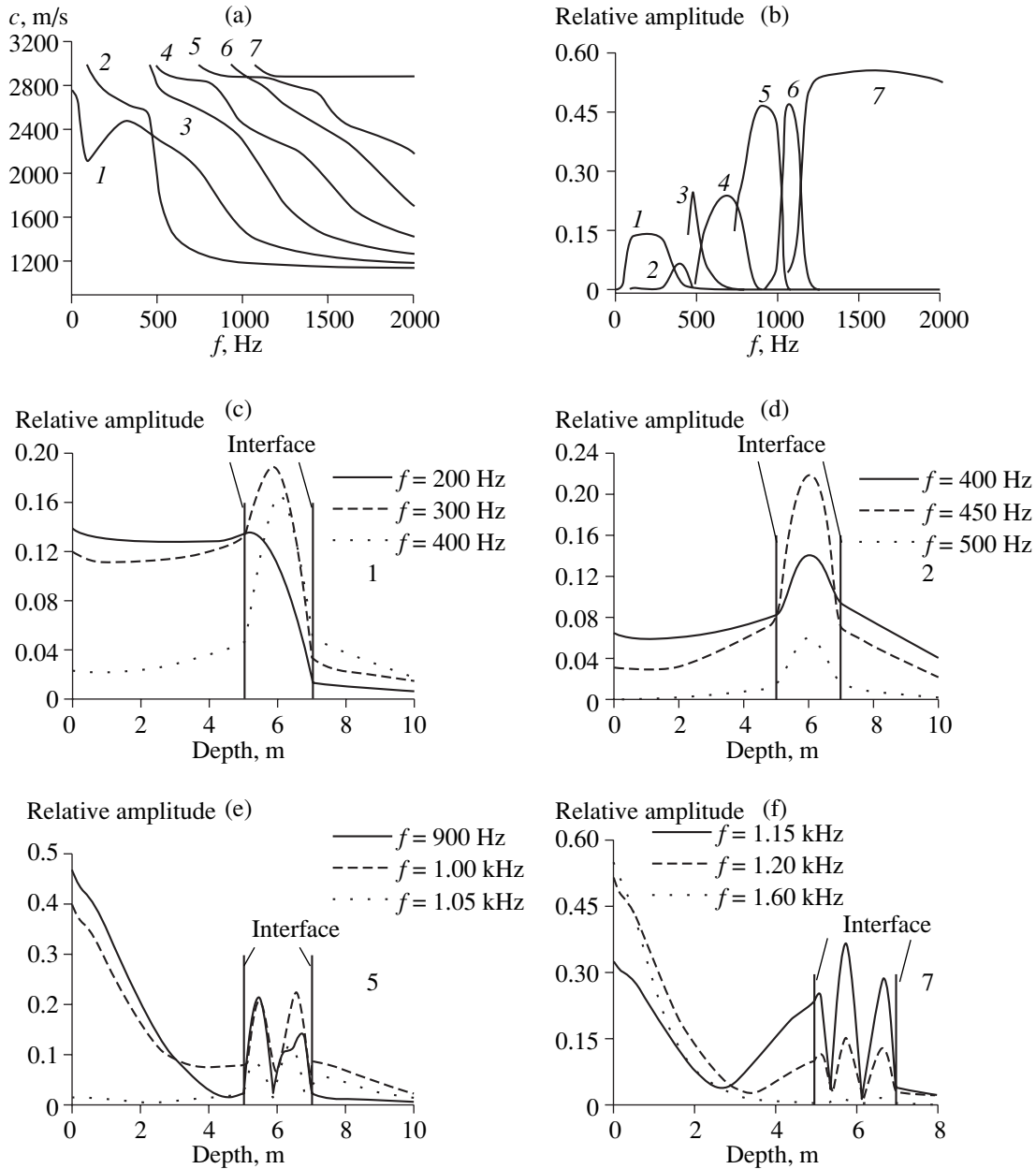
Fig. 6. Dispersion curves (a), displacement spectrum (b) at the free surface and displacement distribution (c– f) with depth in the eleventh parameter group.

in the tenth parameter group. In the frequency range in which the phase velocity is near $V_{1\infty}$, the mode whose displacement concentrates near the free surface and is small in the low-velocity layer is the surface wave. In the other frequency range, this mode is the trapped wave. The characteristic of the seventh mode shown in Fig. 6f is the same as the fourth mode in the tenth parameter group. The displacement distribution of this mode can be found both in the first layer and in the low-velocity layer at low frequency. This mode will become a surface wave when the frequency exceeds a given frequency value.

For the twelfth parameter group, $V_{1\infty} > V_{S3}$, the curves of dispersion and excitation of guided waves are shown in Fig. 7a. It can be seen that there is no guided wave whose phase velocity is greater than V_{S3}. That is to say that there is no mode whose characteristics are similar to the seventh mode in Fig. 6a. This is because the phase velocities of guided waves must be less than the S-wave velocity of the last layer. The limit of the phase velocity of the fundamental mode shown in Fig. 7a at low frequency is $V_{3\infty}$. The limits of phase velocity of all modes at high frequency are V_{S2}. The dispersion curves of the fundamental and second mode
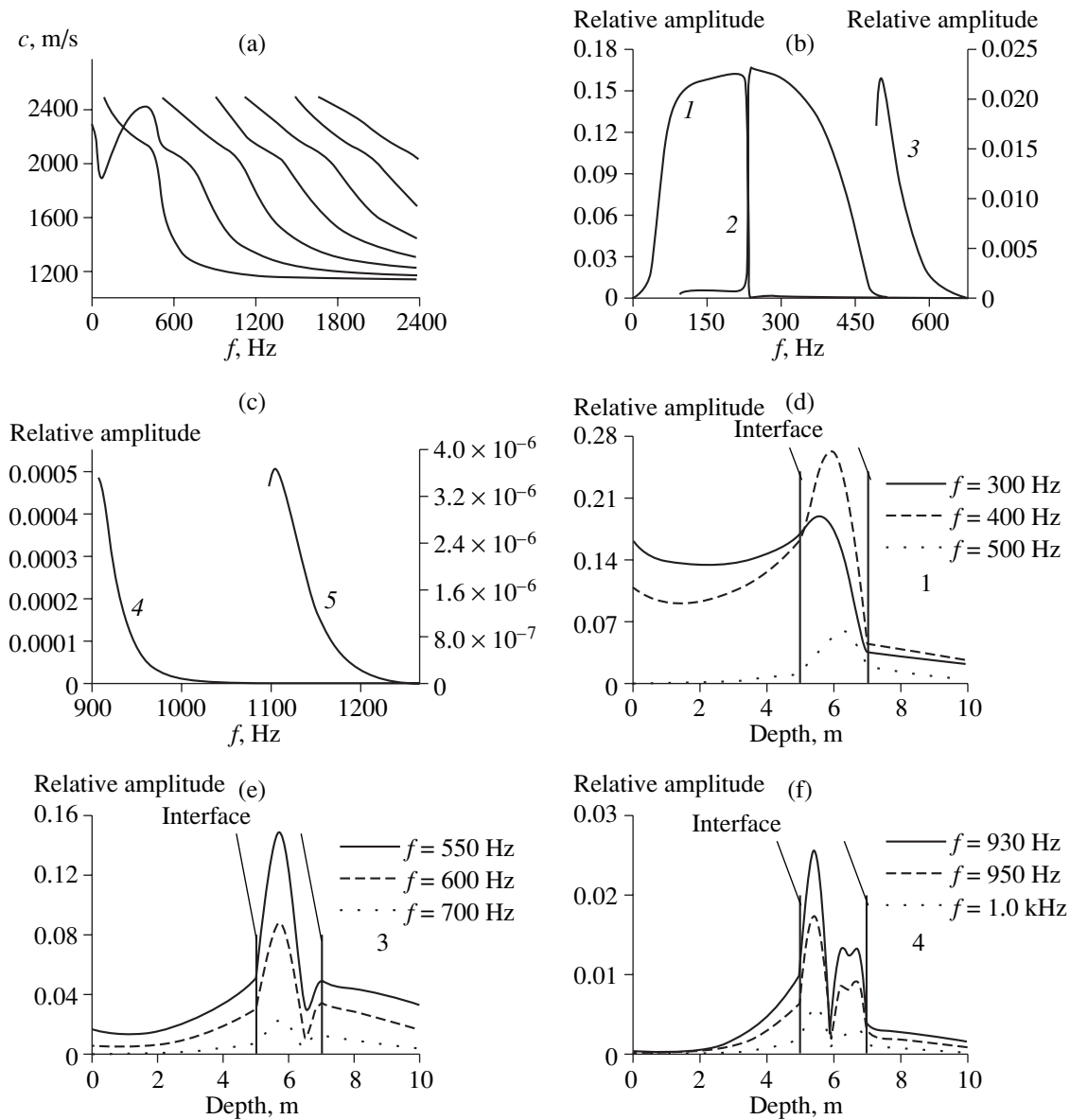
Fig. 7. Dispersion curves (a), displacement spectrum (b) at the free surface and displacement distribution (c–f) with depth in the twelfth parameter group. In (b), left Y coordinate is for the first and second modes; right Y coordinate is for the third mode. In (c), left and right Y coordinates are for the fourth and fifth modes, respectively.

have an intersection at low frequency. Similar to the eleventh parameter group, all modes with high orders are normal dispersion except for the fundamental mode, in which there is both normal and inverse dispersion. The displacement distribution in the depth direction at the free surface of each mode is shown in Figs. 7b and 7c. It can be seen that the fundamental mode and the second mode have a big displacement, which is located in the frequency range near the intersection. The displacement distribution with depth of the first, third, and fourth modes are shown in Figs. 7d, 7e, and 7f, respectively. Figure 7d shows that the displacement distribution with depth of the fundamental mode is similar to that in Fig. 6c. It can be seen from Figs. 7e

and 7f that the displacement distributions along the depth direction of the third and fourth modes are different from that of the tenth and eleventh parameter groups. In this case, the displacements of these two modes, which are trapped waves, concentrate in the low-velocity layer. The displacement distributions with depth of the second and fifth modes, which are also trapped waves, are similar to those of the third and fourth modes. It can be concluded in this case that all modes with high orders are trapped waves whose energy concentrates in the low-velocity layer and propagate along the low-velocity layer except the fundamental mode, which is the surface wave at low frequency.

From the above discussions about guided waves in a half-space containing a low-velocity layer, it can be found that the properties of the dispersion and the excitation are very complicated. The characteristics of the surface waves and trapped waves are related to not only the S-wave velocities of each layer but also the source frequency and the phase velocity of the Rayleigh wave in the case where there is only the first layer.

5. DISCUSSION

The mechanism of propagation and excitation of guided waves in a stratified half-space are studied in this paper. The propagation characteristics of all modes of the surface and trapped waves, especially in the medium containing a low-velocity layer and a stratified half-space in which the S-wave velocity decreases from up to down, are investigated. The relations of the guided waves to the medium parameters are analyzed through numerical simulations.

There exist infinite guided waves in the stratified half-space in which the S-wave velocity increases from up to down layers. The fundamental mode is a surface wave whose energy concentrates in a range near the free surface and attenuates exponentially along the depth direction. The modes with high orders are trapped waves whose energy concentrates in a range below the free surface.

In a stratified half-space in which the S-wave velocity decreases from up to down layers, if the $V_{1\infty}$ is less than the S-wave velocity of the last layer, there is only one mode that is a surface wave. If the $V_{1\infty}$ is greater than the S-wave velocity of the last layer, there is only one surface wave at low frequencies and no guided waves at high frequencies.

The propagation of guided waves is complicated in a medium containing a low-velocity layer. The guided waves have different characteristics at different frequencies. That is to say that the characteristic of a mode is related to the source frequency. It is possible that a surface wave at one value of frequency is like trapped wave at another value of frequency. Sometimes, it is neither a surface nor a trapped wave. It has a definite intensity distribution in the first layer and in the low-velocity layer.

REFERENCES

1. Bixing Zhang, Boxun Xiao, Wenjie Yang, *et al.*, Chin. J. Geophys. **43** (4), 591 (2000).
2. Bixing Zhang, Laiyu Lu, and Guangshu Bao, Chin. J. Geophys. **45** (2) (2002).
3. Xiaoping Guan, Jiazheng Huang, and Hongqiu Zhou, Chin. J. Geophys. **36**, 96 (1993).
4. Shoumin Yan, Prog. Geophys. **6**, 21 (1991).
5. S. Nazarian and K. H. Stokoe, Transp. Res. Rec. **1070**, 132 (1986).
6. G. A. McMechan and M. J. Yedlin, Geophysics **46**, 869 (1981).
7. Luca Malagnini, R. B. Herrmann, Alessia Mercuri, *et al.*, Bull. Seismol. Soc. Am. **87**, 1413 (1997).
8. F. Schwab and L. Knopoff, Bull. Seismol. Soc. Am. **61** (4), 893 (1971).
9. T. Kundu and A. K. Mal, Wave Motion **7**, 459 (1985).
10. J. O. Parra and Pei-cheng Xu, J. Acoust. Soc. Am. **95**, 91 (1994).
11. Bixing Zhang, Ming Yu, Cong-Qing Lan, *et al.*, J. Acoust. Soc. Am. **103**, 125 (1998).
12. Bixing Zhang, Ming Yu, Wei Xiong, *et al.*, Chin. J. Non-ferr. Met. **8**, 340 (1998).
13. Bixing Zhang, C. Q. Lan, *et al.*, Acta Acust. (China) **23** (2), 97 (1998).
14. P. A. Johnson and J. N. Albright, in *Proceedings of SEG 57th Annual International Meeting* (1987), p. 22.
15. S. N. Guzhev, J. Acoust. Soc. Am. **95**, 661 (1994).
16. I. A. Kaibichev and V. G. Shavrov, Acoust. Phys. **45** (1), 71 (1999).
17. Bixing Zhang, Ming Yu, Cong-Qing Lan, *et al.*, J. Acoust. Soc. Am. **100**, 3527 (1996).
18. Bixing Zhang, Ming Yu, and Cong-Qing Lan, Acta Acust. (China) **22** (3), 230 (1997).
19. G. W. Farnell and E. L. Adler, in *Physical Acoustics*, Ed. by W. P. Mason and R. N. Thurston (Academic, New York, 1972), Vol. 9, pp. 35–127.

Improvement of the Time Selection of Signals Received by Separate Rays in Sensing the Ocean with the Use of an M-Sequence

V. A. Zverev and A. A. Stromkov

Institute of Applied Physics, Russian Academy of Sciences,
ul. Ul'yanova 46, Nizhni Novgorod, 603600 Russia
e-mail: zverev@hydro.appl.sci-nnov.ru
Received April 24, 2002

Abstract—It is shown that the previously proposed method [7] of compressing narrowband signals can be used to improve the time resolution of the ray selection in sensing the ocean by broadband signals, in particular, by an M-sequence at the carrier. Data are presented that demonstrate the improvement of the ray selection in the experiments performed under the TETHIS II Program in the Mediterranean Sea and in experiments performed in the Baltic Sea. In all cases, a considerable increase in the resolution of rays is achieved. For the method to be successfully implemented, it is necessary to have a signal-to-noise ratio of 10 dB or higher. © *2003 MAIK "Nauka/Interperiodica".*

To select the signals received by separate rays in multipath sound channels, sensing methods based on M-sequences are successfully used. An M-sequence is a pseudorandom code sequence that consists of alternating zeros and unities. It has a self-correlation function with no side lobes and a spectrum adjoining the zero frequency. Therefore, to study the sound propagation in certain frequency bands, one uses signals with a harmonic carrier whose phase is modulated by an M-sequence (or "M-sequence at the carrier," see [1–4]). If the received signal produced by a source of the M-sequence is cross-correlated with the reference replica signal, the result is an estimate of the impulse response for the system under study (the replica differs from the transmitted signals when Doppler effects are present). This procedure is often called matched filtration, and the result of processing is referred to as the output of the matched filter [5]. If certain conditions are met (the differences in the propagation times for adjacent channels are greater than the width of the self-correlation function of the transmitted signal), the aforementioned processing procedure allows one to select in time the signals propagating along the rays. The resulting narrow pulse can be a narrowband one, which does not imply further compression. However, according to [6], conditions exist when this pulse can be additionally compressed. In a number of publications [6–10], a method is proposed for compressing such signals (which are not narrowband) by using the filters that extend the effective spectrum of the signal and adjust its phase. Such a procedure has no noise immunity [8, 10]. It requires a sufficiently high signal-to-noise ratio or a limitation of the final gain. In [10], a possibility is con-

sidered to optimize the gain and to improve the selection of multipath signals by using special filters.

In this paper, we present a study whose objective is to experimentally confirm the possibility (or impossibility) of using special methods [6, 7] of filtering to reduce the duration of the response obtained by compressing the signals of M-sequences in full-scale experiments. The problem was studied for the signals observed in the Baltic (experiment no. 1) and Mediterranean (experiment no. 2) seas. Experiment no. 2 was carried out under the TETHIS II International Program. This experiment was performed many years ago, and its data have been fully processed and published [2, 11]. It would be all the more interesting to apply the technique of compressing narrowband signals to these old data. Considering the possibility of additionally compressing the pulses recorded in former experiments (whose data have already been processed) is especially worthwhile, because, in planning and performing these experiments, no subsequent compression of the pulses was presupposed to improve the separation of the signals propagating along different rays in the multipath channel. There are many experiments of the kind, and successfully applying the technique to process (at least, partially) some old experimental data would allow one to hope for the same success in using the method of additional compression in time [6, 7] for processing the data of other former experimental studies.

The pulse obtained by correlating a single M-sequence at the carrier with the corresponding reference replica had the shape shown in Fig. 1 for all the experiments at hand. The signal shown occupies 14 time intervals of signal quantization. This fact means that the effective width of the spectrum, which is equal
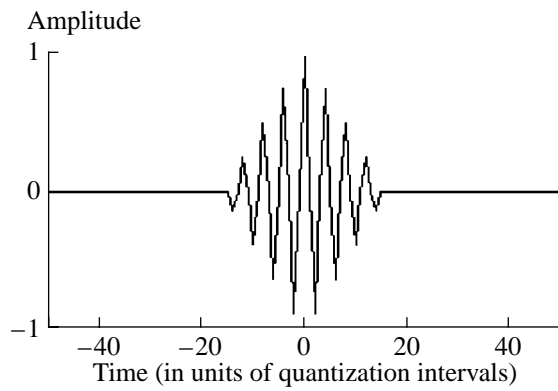
Amplitude

Fig. 1. Pulse shape obtained by a self-correlating M-sequence.

to the inverse value of the signal duration, is less than the actual spectrum width, and, according to [6, 7], the signal can be additionally compressed by a factor of up to 14. An additional compression of the signal is possible with the following algorithm [6, 7]:

$$S(\tau) = \Phi^{-1}[G(\omega)/U(\omega)], \qquad (1)$$

where $G(\omega)$ is the Fourier spectrum of the signal at the output of the matched filter, $U(\omega)$ is the Fourier spectrum of the replica self-correlation, and $\Phi^{-1}[z]$ denotes the procedure of the inverse Fourier transformation of z.

By applying Eq. (1), the experimental data were processed. To obtain satisfactory results with respect to the signal-to-noise ratio, we tentatively matched the frequency band for the transformation by Eq. (1) and set $G(\omega)$ equal to zero at higher and lower frequencies. The spectrum $U(\omega)$ has pronounced zeros. At these points and in their closest vicinities, we also set $G(\omega)$ equal to zero. As a result, we arrived at the additional signal compression that is clearly visible in the plots.

The result obtained illustrates one of the possibilities of signal compression. However, there is another possibility. The procedure of Eq. (1) is based on nothing but the fact that the spectrum corresponding to the correlation function of the M-sequence used is broader than its inverse duration. The second possibility of narrowing the output signal consists in updating the frequency response of the source–receiver channel. This problem was solved in the following way. The hypothesis was put forward that the frequency response of the channel can be well described as that of an oscillatory
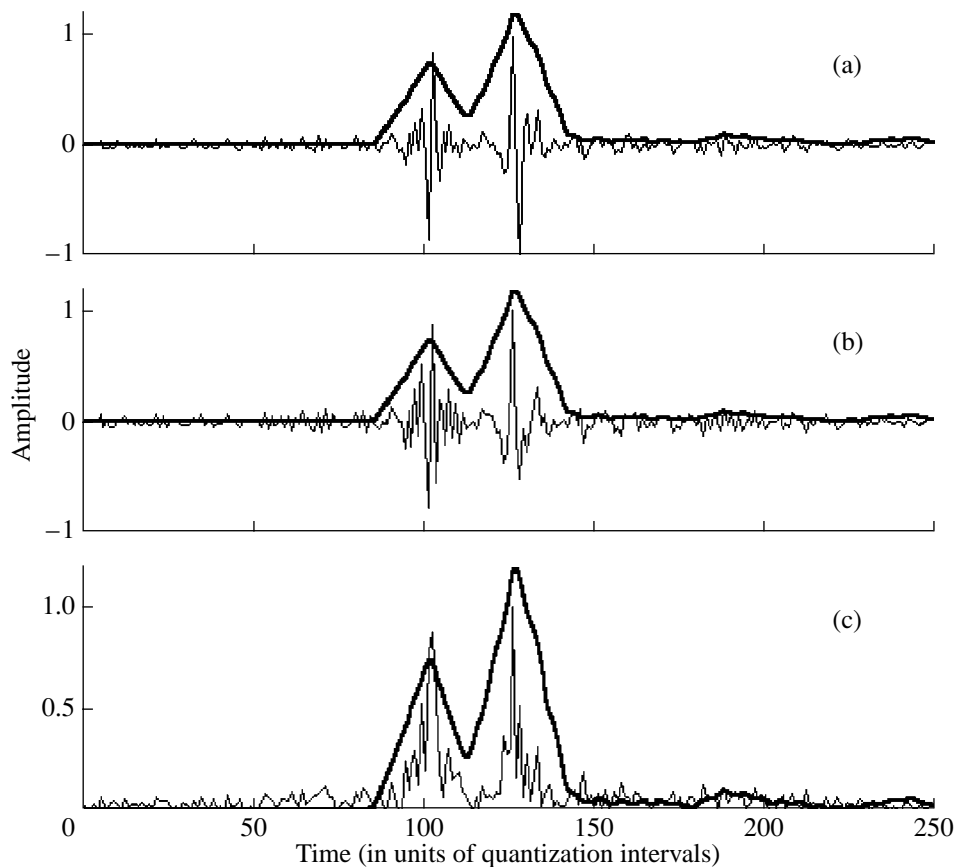

Fig. 2. Pulses received in the Baltic Sea experiment. The result of using the time compressing M-sequence before processing (the thick curve) and the signal compressed by additional processing (the thin curve). Additional processing was performed with the parameter J = (a) 10 (only first processing step) and (b) 0.6. (c) The lower plot shows the envelope of the signal presented in Fig. 2b.
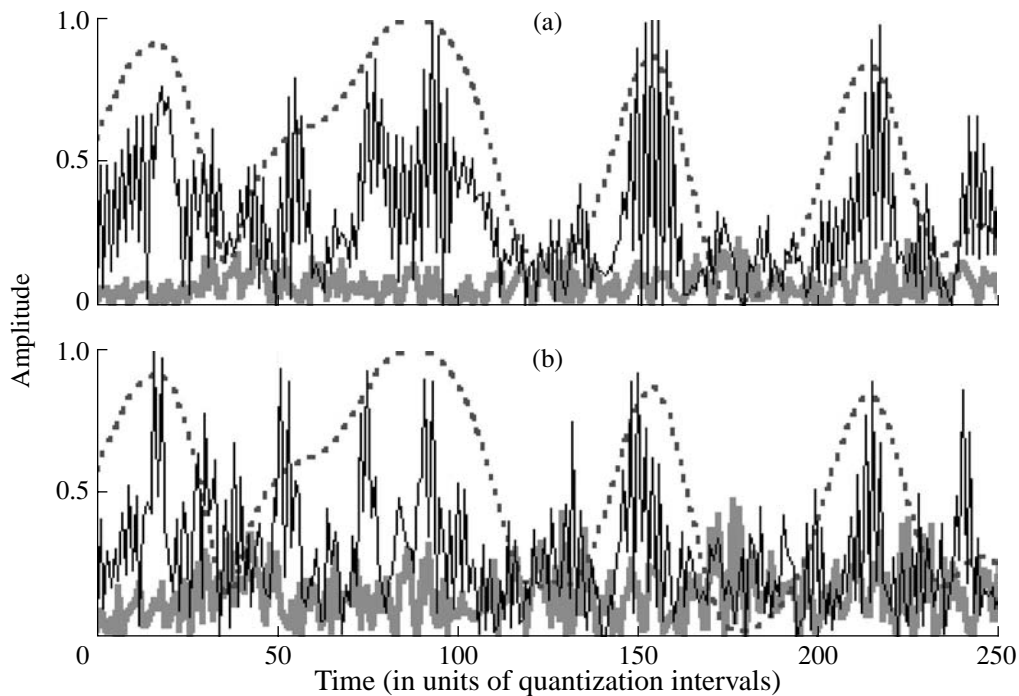
Fig. 3. Pulses received in the TETHIS II experiment. The result of using the time compressing M-sequence before processing (the dotted curve) and the signal compressed in additional processing (the thin curve). The thick curve indicates the noise (that is, the signal taken at a different time) that is caused by the additional processing. The latter was performed with the parameter $J =$ (a) 0.9 and (b) 0.3.

circuit with appropriate parameters. A signal in the form of the response of an oscillatory circuit tuned to the frequency of the intrapulse oscillations (seen in Fig. 1) was considered:

$$W(k) = \cos(0.5\pi k)\exp(-Jk). \quad (2)$$

Here, k is time in units of signal quantization (always positive), and J is the processing parameter that is tentatively matched. The additional processing procedure consists in the fact that the function $z(\omega)$, which is the Fourier spectrum of Eq. (2), is introduced into the denominator of Eq. (1). In doing so, the function $z(\omega)$ is squared. The latter manipulation allows one to take into account the nonuniformity of the frequency response for both source and receiver. The final processing procedure was performed according to the formula

$$S(\tau) = \Phi^{-1}\left(\frac{G(\omega)}{U(\omega)(z(\omega))^2}\right). \quad (3)$$

The result of compressing the signal of experiment no. 1 is shown in Fig. 2. In Fig. 2a, the signal processing was carried out by taking the parameter J of Eq. (2) equal to ten. With this value of J, Eq. (3) coincides with Eq. (1), because the exponent of Eq. (2) noticeably decreases within a single interval of quantization. The values of J that are higher than unity have nearly no effect on the form of the correcting function. The value

$J = 10$ means that, at the second step of this procedure, the frequency response was not updated at all. At the same time, the Fourier spectrum of Eq. (2) becomes uniform and leads to no changes in Eq. (3) in comparison with Eq. (1). In Fig. 2a, oscillations caused by the nonuniformity of the frequency response can be noticed. Figure 2b illustrates the signal processing with the value of J matched so as to eliminate the oscillations caused by the nonuniformity of the frequency response. Figure 2c displays the envelope of the additionally compressed signal shown in Fig. 2b.

Figure 3 illustrates the additional compression of the signal obtained in experiment no. 2. In this experiment, the signal-to-noise ratio was considerably lower than in experiment no. 1. The nonuniformity of the frequency response in the signal transmission and reception was higher. Therefore, the nonuniformity-caused oscillations last longer. In order to eliminate them completely, the values of J must be so small that the compressed signal will be nearly masked by the noise. In the case of long oscillations caused by the nonuniformity of the frequency response, it is more convenient to use the envelope of the compressed signal rather than its correlation function shown in Figs. 2a and 2b. In the experiment at hand, we failed to compensate the nonuniformity of the frequency response of the source–receiver channel.

In Fig. 3, the noise resulting from the signal compression is shown as an additional signal. This is the

same compressed signal additionally delayed for 4000 quantization intervals (the duration of the M-sequence is equal to 8176 quantization intervals). According to the results of compressing the M-sequence (without additional processing), there are no signals at such delays.

In Fig. 2, the noise level can be seen between the 0th and 40th quantization intervals: there are no signals in this range.

The study described above shows that, in principle, a considerable additional signal compression is possible with the use of such a perfect method as the cross-correlating M-sequence with the corresponding replica. However, for the additional signal compression to be successful, two conditions should be met. First, to fulfill the first step of compression, which does not imply updating the frequency response of the channel, a sufficiently great number of time quantization intervals should exist within the duration of the response for the compressed signal. The ultimate degree of the additional compression at the first step is equal to the number of these intervals. Second, one should have a sufficiently high signal-to-noise ratio (more than 10 dB). There is one more condition that is not so necessary: it is desirable to have a uniform frequency response of the entire channel, including the transmitting and receiving elements.

ACKNOWLEDGMENTS

REFERENCES

1. V. A. Zverev and A. A. Stromkov, *Detection of Signals Against Noise by Numerical Methods* (Inst. Prikl. Fiz., Ross. Akad. Nauk, Nizhni Novgorod, 2001).

2. D. I. Abrosimov, A. F. Erkin, A. Yu. Kazarova, *et al.*, Akust. Zh. **41**, 632 (1995) [Acoust. Phys. **41**, 556 (1995)].

3. A. L. Virovlyansky, A. A. Stromkov, and V. Artelnyi, in *Proceedings of the US–Russia Workshop on Experimental Underwater Acoustics* (Inst. of Appl. Phys., Russian Academy of Sciences, Nizhni Novgorod, 2000), p. 33.

4. A. A. Stromkov, L. Ya. Lyubavin, I. N. Didenkulov, *et al.*, in *Proceedings of Conference NATO ARW, Istambul, Turkey, 2001*, p. 110.

5. L. A. Vaĭnshteĭn and V. D. Zubakov, *Detection of Signals Against the Background of Random Noise* (Sovetskoe Radio, Moscow, 1960).

6. T. G. Birdsall and K. Metzger, J. Acoust. Soc. Am. **79**, 91 (1986).

7. V. A. Zverev, Izv. Vyssh. Uchebn. Zaved., Radiofiz. **43** (5), 406 (2000) [Radiophys. Quantum Electron. **43** (5), 366 (2000)].

8. V. A. Zverev, Izv. Vyssh. Uchebn. Zaved., Radiofiz. **44** (4) (2001).

9. V. A. Zverev, P. I. Korotin, and A. V. Tsiberev, Akust. Zh. **47**, 468 (2001) [Acoust. Phys. **47**, 419 (2001)].

10. J. E. Ehrenberg, T. E. Ewart, and R. D. Morris, J. Acoust. Soc. Am. **63**, 1861 (1978).

11. A. K. Morozov and A. A. Stromkov, in *Proceedings of the 4th European Conference on Underwater Acoustics, Rome, Italy, 1998*, p. 75.

Translated by E. Kopyl

Noise Field Anisotropy of Surface Sources in a Coastal Region with Arbitrary Bottom Relief and Sound Velocity Profile

N. N. Komissarova

Andreev Acoustics Institute, Russian Academy of Sciences, ul. Shvernika 4, Moscow, 117036 Russia
e-mail: bvp@akin.ru
Received March 27, 2002

Abstract—The noise field anisotropy of surface sources in a coastal region with an arbitrary three-dimensional bottom relief and an arbitrary sound velocity profile is investigated. The results of computations performed by a computer code in two stages are presented. The first stage consists in the computation of horizontal rays, i.e., the projections of the real rays multiply reflected from the bottom and sea surface onto the horizontal plane. The second stage summarizes the contributions of the noise sources lying within the surface elements that are cut out on the sea surface by a narrow ray tube launched from the point of observation in a given direction. The computations show that, in the coastal region, the noise field is essentially anisotropic, and this anisotropy occurs not only in the vertical plane, which is characteristic of the deep ocean, but in the horizontal plane as well. © 2003 MAIK "Nauka/Interperiodica".

A variety of numerical and analytical models of noise fields produced by surface sources have been developed for a stratified ocean. The computations of the noise field parameters for low frequencies were based on the modal representations [1–3], while for high frequencies, good results were obtained using the ray theory [4–7]. However, the stratified ocean model fails to explain some of the experimentally observed effects. A review [8] of experimental studies of noise field characteristics in the ocean shows that the noise field directivity (in the vertical and horizontal planes) observed at low frequencies in the deep ocean can be explained by the presence of surface and traffic noise in the regions of the continental shelf, slope, and underwater mounts, as well as by the features of sound propagation in these regions.

In this connection, noise field models were developed for a waveguide whose parameters depended on the spatial coordinates. The adiabatic approximation of the normal wave theory was used in [9] as the basis for calculating the noise field characteristics of the surface sources in the deep sea at low frequencies. The cited paper gives examples of the calculations for a medium modeling the presence of a mount, a slope, an oceanic front, and a distant storm. A similar approach was used in [10] for calculating the traffic noise in the coastal waters of the Mediterranean Sea, and a rather good agreement was obtained between experimental data and calculations. In [11], the ray approach was used and, under some simplifying assumptions, analytical expressions were obtained for the directivity of the noise field of the surface sources over a sloping bottom with various sound velocity profiles. In these studies, it is shown that the presence of the coastal slope leads to a situation when noise of the surface sources lying in

this region enters the underwater sound channel and propagates there over long distances with small attenuation. In this case, instead of a gap in the vertical characteristic of the noise directivity in the deep sea, which corresponds to the arrival angles of the water rays not reaching the surface, a wide smooth maximum (a "pedestal") appears. The ray approach also made it possible to explain the effect of such large inhomogeneities as underwater mounts, lenses, and internal waves on the vertical anisotropy of the noise field. These inhomogeneities are responsible for the insonification of the zone corresponding to the angles of the refractive minimum, which is observed in the experiments in various regions of the ocean [12, 13].

However, these works are limited by the Nx2D approximation, which allows for the changes in the parameters of the medium only along a straight line connecting the source and the receiver. However, it is known [14, 15] that a ray, due to multiple reflections from the bottom and surface, does not retain its initial direction in the horizontal plane but is turned up (bathymetric refraction); its horizontal trajectory is not only determined by the medium parameters but also depends on the grazing angle at the launch point. Thus, as was noted in [11], the Nx2D approximation is convenient but is not sufficiently correct under the conditions of a sloping bottom. The use of a rather simple model [16] of the coastal region allowed an exact three-dimensional ray calculation of the noise field directivity of the surface sources. The model of the medium was an isovelocity wedge overlying a half-space that was characterized by the reflection coefficient depending on the grazing angle of the incident wave. The method of image sources provided convenient formulas determining all the parameters of a ray in the three-dimensional

wedge and made it possible to calculate the dependences of the anisotropy characteristics on the azimuth and grazing angles for various bottom parameters. A limitation of this approach is the lack of allowance for such an important characteristic of the medium as the sound velocity profile. More information about various models of ocean noise can be found in the reviews [17, 18].

This paper is devoted to the calculation of the parameters of the noise field produced by surface sources in a three-dimensional waveguide with an arbitrary dependence of its depth on two horizontal coordinates and with a given (arbitrary) sound velocity profile. As a model of the medium, we consider a waveguide whose bottom topography is given by the dependence of the sea depth H on two horizontal coordinates x and y. It is assumed that $H(x, y)$ is an arbitrary, slowly varying function of the horizontal coordinates. The sound velocity depends on the vertical coordinate. The noise sources are uniformly distributed over the sea surface and have a directional pattern $D(\vartheta)$, where the angle ϑ is counted from the surface.

The approach frequently used in the calculations of noise fields in waveguides is as follows. From the reception point $P(x_P, y_P, z_P)$, we launch a narrow ray tube with a solid angle $d\Omega_P$, so that a ray with the launch angles ϑ_P (the grazing angle) and φ_P (the azimuth angle) is at the center of the tube. The ray is multiply reflected from the bottom and surface of the waveguide, and the corresponding ray tube cuts out surface elements S_i of area dS_i on the sea surface:

$$dS_i = \Delta S_i / \sin \overline{\vartheta}_i, \qquad (1)$$

where $\overline{\vartheta}_i$ is the ray grazing angle near the surface, which depends on the number i of the ray reflection; ΔS_i is the area of the tube cross section near the surface element S_i. The contribution of the ith surface element to the noise field that arrives at a point P from the direction given by the angles ϑ_P and φ_P is determined by the expression

$$dJ_i = WD(\overline{\vartheta}_i)I(S_i, P)\exp(-\delta\rho_i)dS_i, \qquad (2)$$

where W is the power density generated by the surface sources in a unit solid angle in the vertical direction, $D(\overline{\vartheta})$ is the directional pattern of the noise sources

$$D(\overline{\vartheta}) = \sin^2 \overline{\vartheta}, \qquad (3)$$

$I(S_i, P)$ is the sound field intensity produced at the reception point P (without considering the attenuation) by a point source located at the surface element S_i, δ is the sound attenuation coefficient in water, and ρ_i is the length of the ray path in the horizontal plane from the point P to S_i.

By virtue of the reciprocity principle, the field intensity generated at the point P by a point source located at the point S_i is equal to the field intensity generated at

the point S_i by a point source located at the point P; i.e., $I(S_i, P) = I(P, S_i)$. Therefore, the contribution of the ith surface element to the noise field received at the point P from the direction determined by the angles ϑ_P, φ_P is expressed as

$$dJ_i = WD(\overline{\vartheta}_i)I(P, S_i)\exp(-\delta\rho_i)\Delta S_i / \sin \overline{\vartheta}_i. \qquad (4)$$

Let us single out, as a separate factor, the energy losses at multiple bottom reflections of a ray launched from the point P in the direction defined by the angles ϑ_P, φ_P and arriving at the point S_i after performing i cycles. At an intermediate jth cycle, the ray can undergo a bottom reflection or have a turning point. In this case, the energy losses can be written as the product $\prod_{j=1}^{i} V_j^2$, where $V_j = V(\underline{\vartheta}_j)$ if at this cycle the ray is reflected from the bottom (under the angle $\underline{\vartheta}_j$) and $V_j = 1$ if at the jth cycle the ray has a lower turning point. The function $V(\vartheta)$ determines the dependence of the bottom reflection coefficient on the grazing angle. Now, Eq. (4) can be represented as

$$dJ_i = WD(\overline{\vartheta}_i)I_0(P, S_i)\exp(-\delta\rho_i)\Delta S_i \prod_{j=1}^{i} V_j^2 / \sin \overline{\vartheta}_i, \qquad (5)$$

where $I_0(P, S_i)$ is the sound intensity of the point source in a similar waveguide with perfectly reflecting boundaries.

By virtue of the conservation law for the energy flux in the ray tube, the zeroth approximation of geometric optics yields

$$I_0(P, S_i)\Delta S_i = \text{const} = I_0(P, S_P)\Delta S_P, \qquad (6)$$

where ΔS_i is the area of the cross section of the ray tube near the surface element S_i, S_P is a point on the ray at a unit distance R_P from the point P, $\Delta S_P = d\Omega_P R_P^2$ is the area of the cross section of the ray tube at a unit distance from the point P, and $I_0(P, S_P) = 1/R_P^2$. With allowance for Eqs. (3) and (6), Eq. (5) takes the form

$$dJ_i = d\Omega_P W\exp(-\delta\rho_i)\sin(\overline{\vartheta}_i)\prod_{j=1}^{i} V_j^2. \qquad (7)$$

Combining the contributions from all surface elements, we obtain the expression for the noise field arriving at the inside of the narrow ray tube from the direction given by the angles ϑ_P, φ_P. Thus, the noise field anisotropy, i.e., the intensity of noise arriving from the direction defined by the angles ϑ_P and φ_P in a unit solid angle, is determined by the formula

$$J(\vartheta_P, \varphi_P) = W\sum_{i=0}^{\infty} \sin(\overline{\vartheta}_i)\exp(-\delta\rho_i)\prod_{j=1}^{i} V_j^2. \qquad (8)$$

Formula (8) does not contain the ray tube divergence, which determines the area of the cross section

ΔS_i. This fact considerably simplifies the calculations for an inhomogeneous medium (as was noted in [5]). However, for our calculations, we need to know the grazing angles of a ray along its track near the surface $\bar{\vartheta}_i$ and the bottom $\underline{\vartheta}_j$. It is also necessary to know the length of the ray path ρ_i in the horizontal plane up to the points of reflection from the bottom and surface. All these parameters depend on the ray launch angles ϑ_P and φ_P at the point P.

Formula (8) serves as the basis for the numerical computation of the anisotropy of the noise field produced by the surface sources in a waveguide with an arbitrary dependence of its depth on two horizontal coordinates. The computation algorithm includes two stages. At the first stage, we calculate the horizontal rays, i.e., the projections of real rays multiply reflected from the bottom and the sea surface onto the horizontal plane. At this stage, for horizontal ray computations, we used the approximate method based on the results of earlier studies [19, 20]. Proceeding from the laws of the ray reflection from a sloping bottom, the following conclusions were made in [20]:

1. Along a horizontal ray, the invariant $I(q, H)$ retains its constant value (similar to the ray invariant introduced in [14, 15] for more simple models of the medium). For a ray multiply reflected from the bottom and surface, this invariant has the form

$$I(q, H(x, y)) = \int_0^{H(x, y)} \sqrt{n^2(z) - q^2}\, dz. \qquad (9)$$

Here, $n(z) = c(0)/c(z)$ is the refractive index of the medium and $c(z)$ is the sound velocity. When the ray, at a current point (x, y) of its horizontal projection (the sea depth is $H(x, y)$), has the upper or lower turning point, $\bar{z}$ or $\underline{z}$, the lower or upper integration limits in integral (9) are replaced by $\bar{z}$ or $\underline{z}$, respectively. The parameter q in integral (9) is (accurate to a constant) the projection of the wave vector on the horizontal plane. For a regular waveguide ($H(x, y) = $ const), $q = n(z)\cos\vartheta(z)$ and the value of this parameter is constant along the ray (Snell's law). In the case of an irregular waveguide, the parameter q changes when the ray is reflected from the sloping bottom, but it remains constant between ray reflections. If the bottom slope is small, the changes in q at the reflections are also small, and, as a result, q varies slowly along the horizontal ray trajectory. The equation

$$I(q, H) = I(q_P, H_P), \qquad (10)$$

where $H_P = H(x_P, y_P)$ and $q_P = n(z_P)\cos\vartheta_P$, determines the variation of $q(H)$ along the horizontal ray.

2. The horizontal ray trajectories obey the ray equations for a medium with a two-dimensional inhomogeneity, in which the effective refractive index n depends on two horizontal coordinates x and y. The refractive index is determined by the bottom relief and the sound velocity profile and can be represented as $\tilde{n}(x, y) = q(H(x, y))$. In the particular case of a medium with a constant sound velocity, we have $\tilde{n}(x, y) = \sqrt{1 - H_P^2 \sin^2\vartheta_P / H^2(x, y)}$. For a wedge-shaped region, where the depth H depends only on one horizontal coordinate, the effective refractive index depends only on this coordinate and the horizontal ray propagates as in a stratified medium.

This approach was realized in the computer code for horizontal ray calculations in coastal regions of the ocean [21, 22] and used as the basis for computing the characteristics of the noise field anisotropy. The code uses the piecewise linear approximation of the dependence of the squared refractive index $n(z)$ on the depth z. The bottom relief is given by isobaths. The bottom is approximated by adjacent triangles. The water medium above each triangle represents an element of a wedge-shaped region. A horizontal ray "propagates" in it as in a stratified medium with the effective refractive index $\tilde{n}(H)$. For each element of the wedge-shaped region, Eq. (10) is solved numerically. Then, the effective refractive index $\tilde{n}(H)$ is determined, and the horizontal ray is computed; i.e., the dependences $x(\rho)$ and $y(\rho)$ on the path length ρ of the horizontal ray are obtained. The code also allows the calculation of the parameter $q(\rho)$ and the depth $h(\rho)$ along the horizontal ray, as well as the number of half-cycles $N_C(\rho)$ covered by the real ray up to the current point (the half-cycle is the horizontal distance traveled by the real ray between the points of reflection from the bottom and the surface; in the following calculations, this parameter will allow us to determine the points of the ray exit to the bottom and the surface). Thus, we determined all the ray parameters necessary for computing the noise field anisotropy. In this case, it is unnecessary to determine the spatial trajectories of real rays, which is a time and memory consuming procedure. In the examples presented below, this computation stage takes only several minutes.

At the second stage of noise field calculations [by Eq. (8)], we sum up all the contributions of the noise sources located at the surface elements cut out on the sea surface by a narrow ray tube. The latter is launched from the point P in the direction determined by the angles ϑ_P and φ_P. The coordinates of the points of the real ray exit to the bottom, which are necessary for calculating the bottom reflection loss, are determined from the equation

$$N_C(\rho_i) - N_{C0} = 2i,$$

where N_{C0} is the half-cycle part covered by the ray from the point P to the first bottom reflection and i is the number of reflection ($i = 1, 2, 3, \ldots, i_{max}$, where i_{max} is the number of the last bottom reflection). Knowing the length of the horizontal ray arc ρ_i at the point of the bottom reflection of the real ray, we can determine the
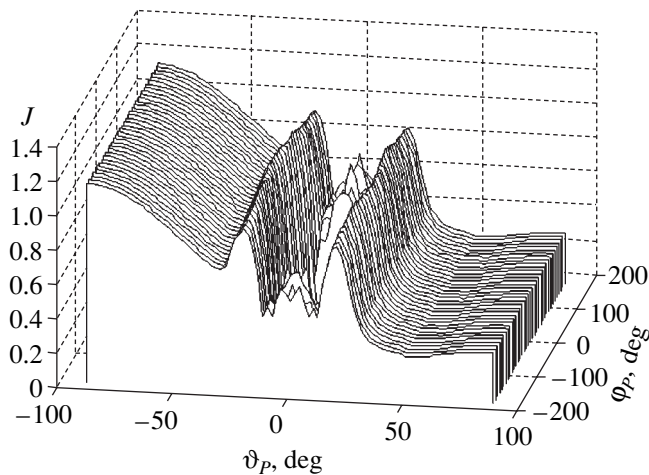
Fig. 1. Characteristic of anisotropy of the noise field of surface sources for a coastal region of the northern Pacific.

grazing angle $\underline{\vartheta}_i$ at this point from the relation $q(\rho_i) = n(h(\rho_i))\cos\overline{\vartheta}_i$. In a similar way, we determine the grazing angles of the real ray at its exit to the surface.

Figure 1 presents the results of computing the anisotropy of the noise field of surface sources for one of the coastal regions of the northern Pacific. The bottom topography of this region is shown in Fig. 2a. The sound velocity profile typical of the summer season is presented in Fig. 2b (curve *1*, the depth of the underwater sound channel axis is 35 m). The calculation was performed for the point of reception P with the coordinates $x_P = 16$ km, $y_P = 20$ km, and $z_P = 100$ m for the sea depth $H_P = 112$ m. The value of the attenuation coefficient was assumed to be 0.065 km^{-1}. The calculation was carried out for a sand bottom and a frequency of 1 kHz. The coefficient W involved in Eq. (8) was taken as unity.

In Fig. 1, the noise field anisotropy is plotted along the vertical axis, and the azimuth and grazing angles are plotted along the horizontal axes. The calculations were performed for the azimuth angles $\varphi_P = -180, -170, \ldots 0, \ldots 170$ degrees. The value $\varphi_P = 0$ corresponds to the positive direction of the x axis. The negative values of the grazing angle ϑ_P correspond to the noise reception from above, and the positive values, to the reception from below. As seen from Fig. 1, for grazing angles $|\vartheta_P| \leq 20°$, the intensity of the noise field noticeably depends on the azimuth angle.

This calculation illustrates the well-known effect of noise signal appearance in the underwater sound channel within the arrival angles of water rays not reaching the surface. The noise arriving within this angular interval may be of different origin, including that of the surface sources located in the region of the coastal slope. When a ray propagates down the slope, its grazing angle decreases with every bottom reflection. As a result, a ray with an initially large grazing angle can be transformed after passing the slope into a ray with a small grazing angle and appear in the group of water rays of the underwater sound channel. Such a mechanism underlies the energy transfer from noise generated in the region of the coastal slope to the noise arriving under small grazing angles.

To elucidate the features of the noise field anisotropy, we consider more simple models of a coastal zone. Figures 3 and 4 exhibit the calculated anisotropy characteristics of the noise field of surface sources for a coastal zone model in the form of a wedge with an angle of 3°. At a distance of 60 km from the edge of the wedge, the latter is assumed to pass into a regular waveguide with a depth of 3 km. The computations were performed for two sound velocity profiles relating to summer and winter conditions and for two bottom models. The main calculated quantity was the intensity $J(\vartheta_P, \varphi_P)$ of the noise field arriving at the reception point P within a unit solid angle from the direction determined by the grazing angle ϑ_P and the azimuth angle φ_P. The point of reception was located at the distance $x_P = 4$ km from the edge of the wedge, at the depth $z_P = 100$ m, and at the sea depth $H_P = 200$ m. In Figs. 3 and 4, the noise field anisotropy (in dB) is plotted along the vertical axis, and the azimuth and grazing angles are plotted along the horizontal axes. The computations were performed for 37 values of the azimuth angles $\varphi_P = 0, 5, 10, \ldots, 180$ degrees. The value $\varphi_P = 0$ corresponds to the reception from the side of the open sea, and $\varphi_P = 180°$, from the side of the coastal line. The negative values of the grazing angle ϑ_P correspond to the noise reception from above, and the positive values, the noise from below.

Figure 3a refers to the summer sound velocity profile showed in Fig. 2b (curve *1*). In the case of reception from the open sea ($\varphi_P = 0$), in the grazing angle interval $|\vartheta_P| < 12°$, which corresponds to arrival angles of water rays received at the point P but not reaching the surface, noise does not arrive at all (a refractive minimum). In the case of reception from the coast ($\varphi_P = 180°$), this angular interval is insonified by noise. The level of this insonification depends on the bottom reflection coefficient. Figure 3a shows the computation results for a sand bottom with a sound velocity of 1667 m/s and a density of 1.9 g/cm^3, and Fig. 3b corresponds to a muddy bottom with a sound velocity of 1530 m/s and a density of 1.44 g/cm^3. As one can see, the dependence of the anisotropy on the azimuth angle is much more pronounced for a sand bottom than for a muddy one.

Figure 4 refers to similar computations of the anisotropy characteristics for winter conditions, for (a) a sand bottom and (b) a muddy bottom (the sound velocity profile used in these calculations is presented in Fig. 2b, curve *2*). As can be seen from Fig. 4, the noise field anisotropy in the coastal zone is largely determined by the dependence of the sound velocity on depth and by the bottom reflection coefficient.
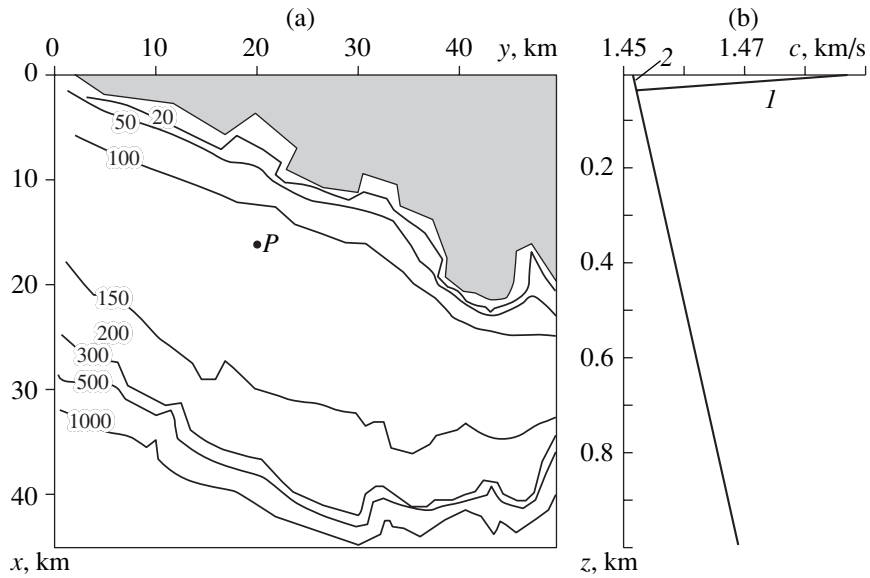
Fig. 2. (a) Bottom topography of the coastal region of the northern Pacific and (b) the sound velocity profiles for the (*1*) summer and (*2*) winter seasons.
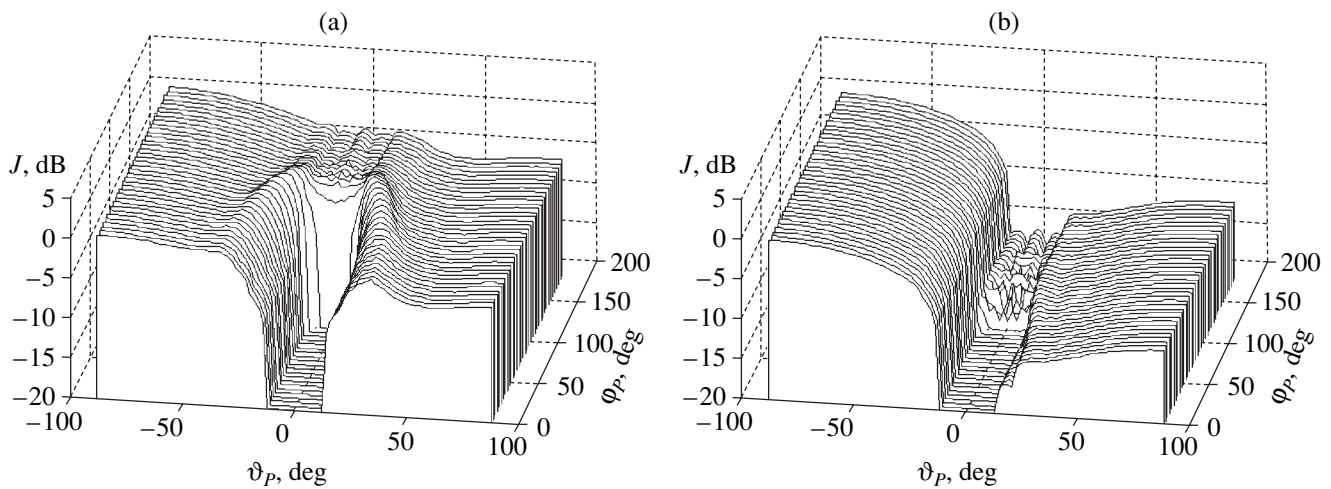

Fig. 3. Characteristic of anisotropy (in dB) of the noise field of surface sources for the coastal wedge in summer conditions: (a) a sand bottom and (b) a muddy bottom.

For these four cases, Fig. 5 shows the level of noise anisotropy $10\log J(\vartheta_P, \varphi_P)$ in the vertical plane normal to the coastal line. The right-hand part of each curve corresponds to reception from the open sea ($\varphi_P = 0°$), and the left-hand part, to reception from the coastal line ($\varphi_P = 180°$). The distance from the center of the plot to the dashed circumference corresponds to 10 dB. This plot clearly shows the noise signal appearing within the interval of the refractive minimum in the case of the reception from the coast with the summer sound velocity profile. The difference in the insonification level between the sand and muddy bottoms is 13–15 dB.

The computations for a wedge of 0.5° show that the result obtained for the winter conditions is practically

independent of the azimuth angle. The computation for the summer conditions show that, for azimuth angles $|\varphi_P| < 90°$, which correspond to reception from the open sea, the noise field anisotropy weakly depends on the azimuth angle and has a refractive minimum, while for azimuth angles corresponding to reception from the coast, the noise field anisotropy also weakly depends on the azimuth angle but has a different dependence on the angle ϑ_P. In the latter case, the refractive minimum is insonified by noise, and the insonification level is almost equal to that obtained for a wedge of 3°.

Similar computations are presented in Fig. 6 for one of the coastal regions of the Black Sea. The bottom topography is given by parallel isobaths; the depen-
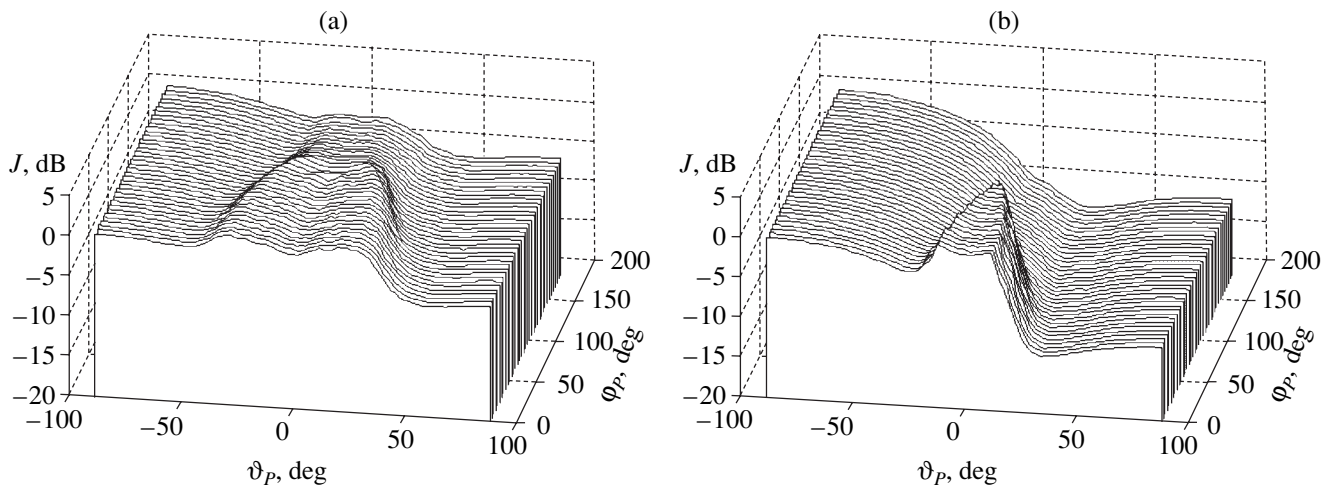
Fig. 4. Characteristic of anisotropy (in dB) of the noise field of surface sources for the coastal wedge in winter conditions: (a) a sand bottom and (b) a muddy bottom.
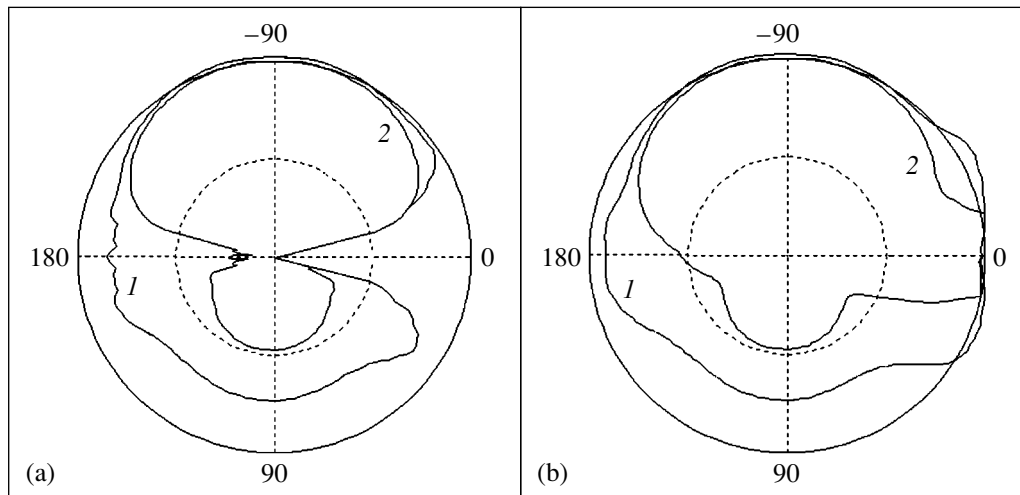

Fig. 5. Characteristic of anisotropy (in dB) of the noise field of surface sources in the vertical plane for the coastal wedge in (a) summer and (b) winter conditions: (*1*) a sand bottom and (*2*) a muddy bottom.

dence of the sea depth H on the distance x up to the coastal line is shown in Fig. 7a. The sound velocity profiles for summer and winter conditions typical of the test region are presented in Fig. 7b. The intensity $J(\vartheta_P, \varphi_P)$ of the noise field arriving at the point P in a unit solid angle from the direction determined by the angles ϑ_P and φ_P was computed. The point of reception was located at the distance $x_P = 14$ km from the coastal line at the depth $z_P = 100$ m and the sea depth $H_P = 200$ m. The attenuation coefficient was assumed to be 0.065 km^{-1}. The computation was performed for a sand bottom and a frequency of 1 kHz.

In summer conditions, for which the existence of an underwater sound channel with the axis at a depth of 75 m is typical, none of the rays launched from the point P toward the open sea ($0° < \varphi_P < 90°$) with graz-

ing angles $|\vartheta_P| < 15.4°$ can reach the surface. This situation corresponds to the dip in the plots. As $|\vartheta_p|$ increases, the noise field increases as well. A quite different picture is observed when the noise signal is received from the side of the coastal line ($90° < \varphi_P < 180°$). The noise signal also appears for reception from directions corresponding to angles $|\vartheta_P| < 15.4°$. This contribution is made by the rays propagating up the slope and turning because of multiple reflections from the bottom and the sea surface. In winter conditions, the underwater sound channel is retained at a depth of 100 m, but the sound velocity at the surface is smaller than in summer. Therefore, the refractive minimum for reception from the open sea persists, but it is much narrower than in summer. For reception from the coast, the refractive minimum is insonified, as in summer conditions.
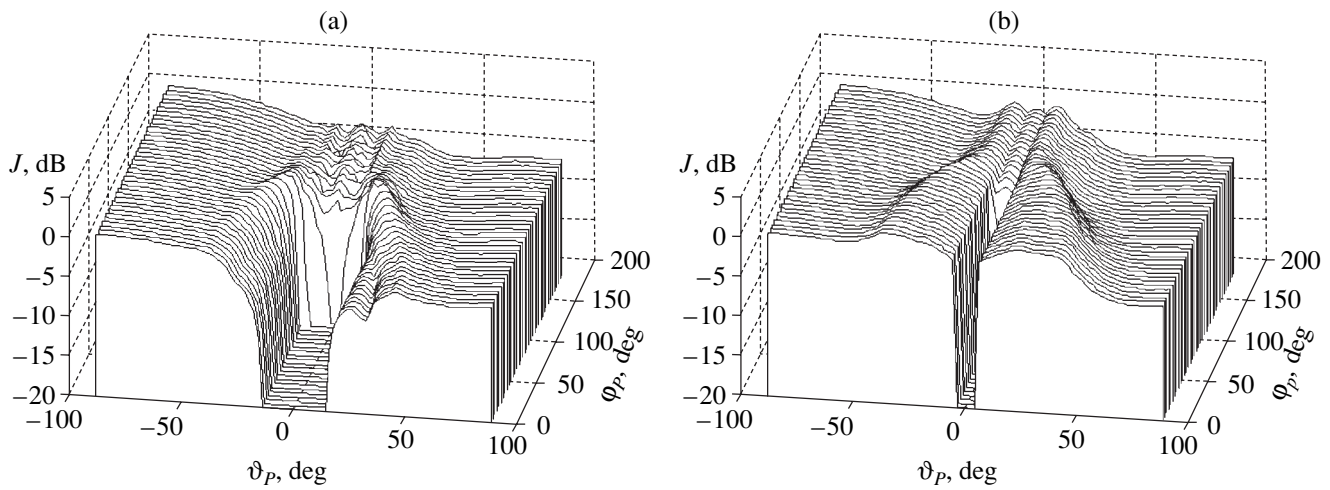
Fig. 6. Characteristic of anisotropy (in dB) of the noise field of surface sources for the coastal region of the Black Sea in (a) summer and (b) winter conditions.
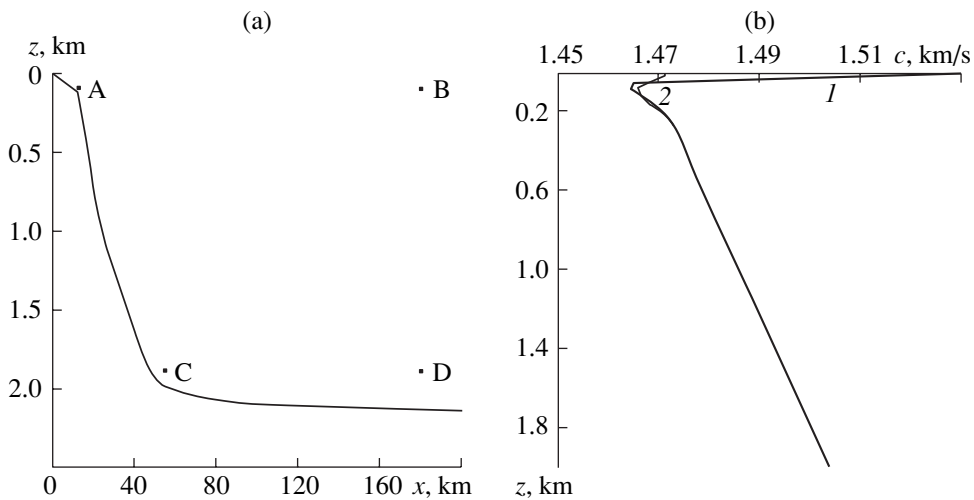

Fig. 7. (a) Bottom profile of the coastal region of the Black Sea and (b) the depth dependences of the sound velocity for (*1*) summer and (*2*) winter conditions.

Figure 8 shows the characteristics of the noise field anisotropy in the vertical plane normal to the isobaths in polar coordinates for four points, whose locations are shown in Fig. 7a. The right-hand parts of the plots correspond to reception from the open sea ($\varphi_P = 0°$), and the left-hand parts, to reception from the coastal line ($\varphi_P = 180°$). The scale factor along the radius vector (the distance between the center and the dashed circumference) is 10 dB. As can be seen from the plots, the appearance of the noise signal in the group of water rays manifests itself in different ways and depends on the locations of these points. Point A corresponds to reception in shallow water at the distance $x_P = 14$ km from the coast, and the level of the refractive minimum insonification is high when the reception is from the coast side (Fig. 8a). Point B corresponds to reception at the same depth $z_P = 100$ m as that of point A, but it is well off the coastal line ($x_P = 180$ km) and the sea depth is 2.1 km; for reception from the coast side, the level of the refractive minimum insonification is much lower (Fig. 8b) than in the case of point A; the characteristic of anisotropy is close to that in the deep sea. Points C and D correspond to reception near the bottom ($z_P = 1.95$ km); point C is located near the continental slope ($x_P = 55$ km), and point D is away from both the slope and the coast but at the same distance from it as point B ($x_P = 180$ km). The interval of arrival angles of the water rays reaching the surface (when the reception is from the open sea) is smaller than in cases A and B, which leads to a narrower refractive minimum (Figs. 8c, 8d). Point C is nearer to the coast, and the insonification of the refractive minimum (for reception from the coast) is higher than at the more distant point D.
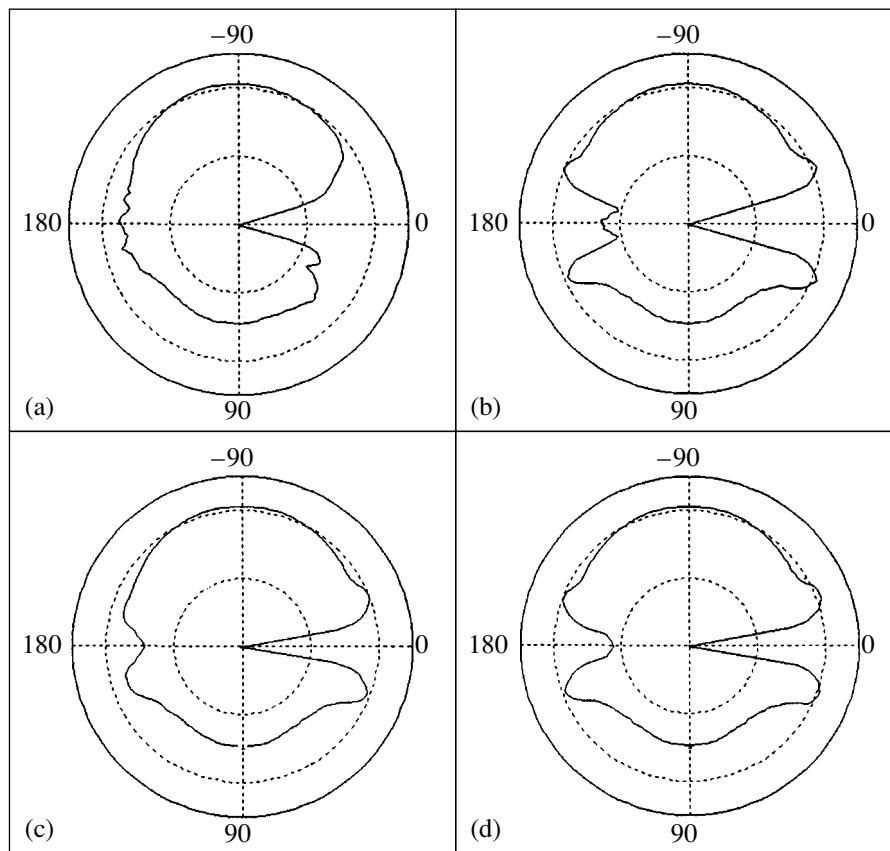
Fig. 8. Characteristic of anisotropy of the noise field in the vertical plane at four points A, B, C, and D shown in Fig. 7a for the Black Sea region.

Thus, the noise field of the surface sources in the coastal region is anisotropic in both vertical and horizontal directions and depends on the profile $c(z)$ and on the bottom structure. In the presence of the underwater sound channel, the features of sound propagation down the slope cause a noise insonification of the zone of the refractive minimum for reception from the side of the coast. The stronger the bottom reflection, the higher the level of insonification of the refractive minimum. As the distance from the coast and continental slope increases, the insonification of the zone of the refractive minimum decreases and the characteristic of anisotropy in the vertical plane approaches the angular dependence of the noise intensity in the deep sea. The smaller the bottom slope, the less the dependence of the noise field anisotropy on the azimuth angle.

The approach described above is based on the ray theory, which, naturally, imposes limitations on the frequency range for which this approach is valid. According to [23], the ray theory is valid for the shallow sea if the frequency and the waveguide depth are such that the two first modes are propagating modes. This suggests that, if the frequency satisfies the condition $f \gg c(0)/H_P$, Eq. (8) is valid. Another limitation of the ray theory is related to the existence of caustics in the vicinity of which this theory fails, but this limitation is unimpor-

tant in the case under study, because the focusing factor is not involved in Eq. (8).

REFERENCES

1. W. A. Kuperman and F. Ingenito, J. Acoust. Soc. Am. **67**, 1988 (1980).
2. R. M. Hamson, J. Acoust. Soc. Am. **78**, 1702 (1985).
3. T. C. Yang and Kwang Yoo, J. Acoust. Soc. Am. **101**, 2541 (1997).
4. A. V. Furduev, in *Ocean Acoustics* (Nauka, Moscow, 1974), pp. 615–691.
5. C. H. Harrison, J. Acoust. Soc. Am. **99**, 2055 (1996).
6. C. H. Harrison and D. G. Simons, J. Acoust. Soc. Am. **112**, 1377 (2002).
7. A. A. Aredov, N. N. Okhrimenko, and A. V. Furduev, Akust. Zh. **34**, 215 (1988) [Sov. Phys. Acoust. **34**, 128 (1988)].
8. W. M. Carey and R. A. Wagstaff, J. Acoust. Soc. Am. **80**, 1523 (1986).

9. J. S. Perkins, W. A. Kuperman, F. Ingenito, *et al.*, J. Acoust. Soc. Am. **93**, 739 (1993).

10. R. M. Hamson, J. Acoust. Soc. Am. **94**, 386 (1993).

11. C. H. Harrison, J. Acoust. Soc. Am. **102**, 2655 (1997).

12. A. A. Aredov, G. M. Dronov, N. N. Okhrimenko, and A. V. Furduev, Akust. Zh. **42**, 10 (1996) [Acoust. Phys. **42**, 5 (1996)].

13. A. A. Aredov, Sudostr. Prom., Ser. Akust., No. 3, 41 (1988).

14. D. E. Weston, Proc. Phys. Soc. London **78**, 46 (1961).

15. C. H. Harrison, J. Acoust. Soc. Am. **62**, 1382 (1977).

16. N. N. Komissarova, Akust. Zh. **33**, 43 (1987) [Sov. Phys. Acoust. **33**, 25 (1987)].

17. R. M. Hamson, Appl. Acoust. **51** (3), 251 (1997).

18. R. M. Kennedy and T. K. Szlyk, J. Acoust. Soc. Am. **89**, 673 (1991).

19. N. N. Komissarova, Akust. Zh. **41**, 617 (1995) [Acoust. Phys. **41**, 542 (1995)].

20. N. N. Komissarova, Akust. Zh. **41**, 902 (1995) [Acoust. Phys. **41**, 799 (1995)].

21. N. N. Komissarova, Akust. Zh. **44**, 68 (1998) [Acoust. Phys. **44**, 54 (1998)].

22. N. N. Komissarova, Akust. Zh. **44**, 801 (1998) [Acoust. Phys. **44**, 698 (1998)].

23. C. T. Tindle and G. B. Deane, J. Acoust. Soc. Am. **78**, 1366 (1985).

Translated by Yu. Lysanov

Wave Processes in Media with Hysteretic Nonlinearity: Part 2

V. E. Nazarov, A. V. Radostin, L. A. Ostrovsky, and I. A. Soustova

Institute of Applied Physics, Russian Academy of Sciences, ul. Ul'yanova 46, Nizhni Novgorod, 603950 Russia
e-mail: nazarov@hydro.appl.sci-nnov.ru
Received May 4, 2001

Abstract—Nonlinear processes caused by the propagation of low-frequency and high-frequency acoustic pulses in an unbounded medium and the propagation of continuous waves in a ring resonator are theoretically studied on the basis of two hysteretic equations of state for media with imperfect elasticity. The profiles and parameters of pulses, the resonance curve and the Q factor of the resonator, and the ratio of the nonlinear resonance frequency shift to the nonlinear damping decrement are determined. For nonlinear wave processes in such media, the distinctive features that allow one to choose an appropriate hysteretic equation of state for analytically describing the experimental data are revealed. © 2003 MAIK "Nauka/Interperiodica".

1. INTRODUCTION

This paper, which is a continuation of the previous paper [1], presents a theoretical study of nonlinear wave processes caused by low-frequency (LF) and high-frequency (HF) pulses propagating in an unbounded medium and by continuous waves in a ring resonator. The study is performed on the basis of phenomenological hysteretic equations of state with the use of the same designations as in the previous paper [1].

2. PROPAGATION OF UNIPOLAR STRAIN PULSES

We consider the propagation and evolution of unipolar (for definiteness, positive) disturbances in a medium with a hysteretic nonlinearity and assume that they are defined at the boundary $x = 0$ by the expression $\varepsilon(x = 0, \theta) = \varepsilon_0 \sin\theta$, $0 \leq \theta \leq \pi$. According to Eqs. (7) and (8) from [1], the propagation of such disturbances is characterized by two parameters: the amplitude and the duration $\theta_+^*(x)$. Integrating Eq. (6) [1] from 0 to θ_+^* with respect to θ, we obtain the following expressions for the first and second models of hysteresis:

$$\frac{\partial}{\partial x} \int_0^{\theta_+^*} \varepsilon(x, \theta)\,d\theta = -\frac{\beta_1 + \beta_2}{4}\varepsilon_m^2 < 0, \qquad (1)$$

$$\frac{\partial}{\partial x} \int_0^{\theta_+^*} \varepsilon(x, \theta)\,d\theta = 0. \qquad (2)$$

From Eq. (1) it follows that, in the first hysteresis model, the area $S(x)$ under the curve $\varepsilon = \varepsilon(x, \theta)$ decreases with increasing x and, consequently, the uni-

polar strain pulse is not conserved. It is also seen from Eq. (7) [1]: the points of the disturbance profile that correspond to $\varepsilon = 0$ move with the same velocity, so that the duration of the disturbance remains constant and its amplitude decreases due to the hysteresis loss; i.e., the area under the curve $\varepsilon = \varepsilon(\theta)$ also decreases. Thus, inelastic hysteresis is unsuitable for describing the propagation of unipolar disturbances.

For the second hysteresis model, from Eq. (2) we obtain $S(x) = 2\varepsilon_0 = \text{const}$; i.e., the unipolar strain pulse is conserved. The duration $\theta_+^*(x)$ of the disturbance (for $\gamma_{1,2} \geq 0$) is determined from Eq. (8) [1]: $\theta_+^*(x) = 4\mu_+\varepsilon_m^+ + 2\arcsin(\varepsilon_m^+/\varepsilon_0)$; the amplitude of the disturbance $\varepsilon_m^+(x)$ is determined by Eq. (17) [1]. At large distances from the source, the unipolar pulse becomes triangular (Fig. 1) with its amplitude and duration being equal to

$$\varepsilon_m^+(x) \approx \sqrt{\varepsilon_0/\mu_+} \sim (\varepsilon_0/x)^{1/2},$$

$$\theta_+^*(x) \approx 4\sqrt{\varepsilon_0\mu_+} \sim (\varepsilon_0 x)^{1/2}.$$

When $\gamma_2 < 0$ and $\gamma_1 + \gamma_2 \geq 0$ (similarly, the case of $\gamma_1 < 0$ can be considered), a discontinuity is formed at the trailing edge of the pulse at the point $\varepsilon = 0$ as the distance reaches the value $x_d = 2/|\gamma_2|\varepsilon_0 k$. The amplitude $\varepsilon_d^+(x)$ and phase $\theta_d^+(x)$ of the discontinuity are determined by the expressions

$$\varepsilon_d^+(x) = \frac{\sqrt{8|\gamma_2|\varepsilon_0 kx - 16}}{|\gamma_2|kx},$$

$$\theta_d^+(x) = 4\mu_+\varepsilon_m^+ + 2\arcsin(\varepsilon_m^+/\varepsilon_0)$$

$$- \arcsin(\varepsilon_d^+/\varepsilon_0) - \frac{\gamma_2}{2}\varepsilon_d^+ kx.$$

At the distance $x_2 = x_d(1 + |\gamma_2/\gamma_1|) > x_d$, the phase $\theta_m^+(x)$ catches up with the discontinuity phase $\theta_d^+(x)$, after which the disturbance amplitude decreases according to the law

$$\varepsilon_m^+(x) = \frac{\sqrt{8\gamma_1\varepsilon_0 kx - 16}}{\gamma_1 kx}.$$

At large distances ($x \gg 2/\gamma_1\varepsilon_0 k$), the amplitude and duration of the disturbance are determined by the expressions $\varepsilon_m^+ = \sqrt{8\varepsilon_0/\gamma_1 kx}$, $\theta_+^*(x) = \sqrt{2\gamma_1\varepsilon_0 kx}$.

3. SELF-DETECTION OF HIGH-FREQUENCY PULSES

In the propagation of an amplitude-modulated high-frequency (HF) acoustic wave in a medium with an even nonlinearity, a detection (or demodulation) of this wave takes place. As a result, a low-frequency (LF) wave is generated and propagates in the medium. This mechanism lies at the heart of the operation of parametric transmitting antennas [2–4]. The measurement of the characteristics of such a wave can be used for determining the nonlinear acoustic properties of a medium for diagnostic purposes. Here, we study the detection of HF acoustic pulses in a medium with a hysteretic nonlinearity.

We set the boundary condition at the source in the form $\varepsilon(x = 0, t) = \varepsilon_0 A(t)\sin\omega t$, where $A(t)$ is the envelope of the HF pulse of duration T and $\omega T \gg 1$. We seek the LF pulse $\varepsilon_2 = \varepsilon_2(x, \tau)$ arising from the detection of the propagating HF pulse $\varepsilon_1 = \varepsilon_1(x, \tau)$ by using the perturbation method. Setting $\varepsilon(x, \tau) = \varepsilon_1(x, \tau) + \varepsilon_2(x, \tau)$ and $|\varepsilon_2(x, \tau)| \ll |\varepsilon_1(x, \tau)|$, in Eq. (6) [1] we obtain the equation for the LF pulse:

$$\frac{\partial\varepsilon_2}{\partial x} = -\frac{1}{2C_0}\frac{\partial\langle f(\varepsilon_1, \dot{\varepsilon}_1)\rangle}{\partial\tau}, \tag{3}$$

where $\langle f(\varepsilon_1, \dot{\varepsilon}_1)\rangle = \frac{1}{2\pi}\int_0^{2\pi} f(\varepsilon_1, \dot{\varepsilon}_1)d\theta$. From Eqs. (7), (8) [1] (for $x \ll x_0$), we obtain

$$\langle f(\varepsilon_1, \dot{\varepsilon}_1)\rangle = a_0\varepsilon_0^2 A^2(\tau)\left(1 - \frac{d}{a_0}\varepsilon_0 A(\tau)kx\right), \tag{4}$$

where $a_0 = \dfrac{\beta_1 - \beta_2}{8}$, $d = \dfrac{4(\beta_1^2 - \beta_2^2)}{3\pi}$ for the first hysteresis model and

$$a_0 = \frac{1}{16}\left[\gamma_1 - \gamma_2 - \gamma_3 + \gamma_4 + \frac{4}{\pi}(\gamma_1 + \gamma_2 - \gamma_3 - \gamma_4)\right],$$

$$d = -\frac{1}{24\pi}[\gamma_1^2 + 11\gamma_2^2 - \gamma_3^2 - 11\gamma_4^2 + 12\gamma_1\gamma_2 - 12\gamma_3\gamma_4]$$
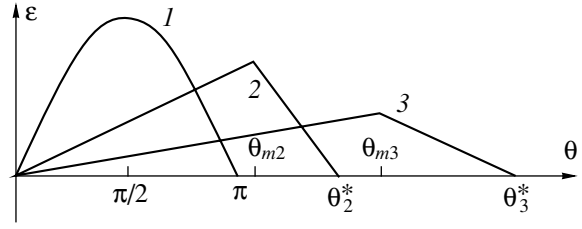
for the second one.

Fig. 1. Evolution of a unipolar pulse in a medium with an elastic hysteresis: (1) $x = 0$, (2) $x_1 > 0$, and (3) $x_2 > x_1$.

From Eqs. (3) and (4), we derive

$$\varepsilon_2(x, \tau) = -\frac{a_0\varepsilon_0^2 x}{2C_0}\frac{\partial}{\partial\tau}\left(A^2(\tau)\left[1 - \frac{d}{2a_0}\varepsilon_0 A(\tau)kx\right]\right). \tag{5}$$

From this expression it follows that, for $a_0 \neq 0$, practically regardless of the type of hysteresis, the form of the detected pulse is close to the first derivative of the square of the envelope with respect to time. Initially, its amplitude increases linearly with distance and then, due to the hysteresis loss of the HF pulse, the growth of the LF pulse slows down and its duration increases (Fig. 2). By measuring the amplitude and duration of the detected pulse at two different distances x from the source (or for two different amplitudes ε_0), it is possible to determine the nonlinearity parameters of the medium (a_0 and d). Here, we have a slight distinction between the detection processes in media with inelastic and elastic hysteresis properties: for $a_0 = 0$, in the first hysteresis model, the detection is absent [5], while in the second model, the detection takes place (if $d \neq 0$). In this case, the form of the LF pulse coincides with the first derivative of the cube of the envelope, and its amplitude is proportional to $\varepsilon_0^2 x^2$. The latter is connected with asymmetric distortion of the HF wave, which manifests itself as a change in the profiles of the positive and negative half-periods of the wave and in their durations (see Eqs. (17), (19) in [1]). (This kind of detection, however, is much weaker, as compared to the case of $a_0 \neq 0$.) Note that in media whose equations of state are described by a symmetric hysteresis ($\beta_1 = \beta_2$ [5] and $\gamma_1 = \gamma_2 = \gamma_3 = \gamma_4$), the detection of HF pulses of the form $A(t)\sin\omega t$ does not occur, because the effective parameters of the quadratic nonlinearity are also equal to zero ($a_0 = 0$, $d = 0$). In such media, according to Eqs. (12), (14) and (20), (22) [1], even harmonics also do not arise. It should be noted that, if the carrier of the modulated HF wave is anharmonic and has different durations of loading ($\dot{\varepsilon} > 0$) and relief ($\dot{\varepsilon} < 0$) stages, its propagation in a medium with a symmetric hysteresis is accompanied by the generation of an LF modulation wave [5].
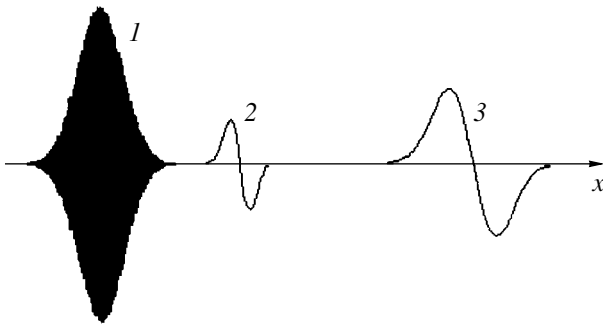
Fig. 2. Evolution of a detected pulse: (*1*) an HF pulse ($x = 0$) and (*2*, *3*) detected pulses at various distances from the source for $a_0 > 0$.
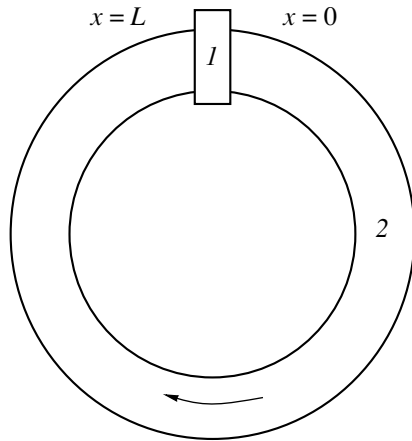

Fig. 3. Schematic diagram of a ring resonator: (*1*) source and (*2*) resonator.

4. TRAVELING WAVES IN A RING RESONATOR

Nonlinear effects manifest themselves more distinctly in resonators (compared to an unbounded medium), where, due to the high Q factor, the intensity of acoustic waves can be much higher. The excitation of a bar resonator gives rise to a standing wave formed as a sum of two waves traveling in opposite directions. Generally speaking, these waves can interact due to the odd nonlinearity of the medium. However, in a resonator with an even nonlinearity, the counter waves do not interact, so the problem of nonlinear oscillations in such a resonator presents no difficulties [4]. Since (in the general case) hysteretic nonlinearity contains both even and odd components, the counter waves propagating in a resonator with a hysteretic nonlinearity interact and the problem of the oscillations in bar resonators becomes more complicated. Here, we consider nonlinear oscillations in a ring resonator (Fig. 3) in which the wave travels in one direction [6]. (Basically, the traveling wave regime of a ring resonator can be provided, for example, by using two non-diametrically-opposite radiators that are excited by sinusoidal oscillations

shifted in phase. By choosing the appropriate phase shift between these oscillations, it is possible to excite a wave traveling clockwise and suppress the wave traveling counterclockwise, and vice versa.)

We determine the resonance curve, the amplitude of a steady-state wave, and the Q factor of such a ring resonator in two regimes: quasi-harmonic (or weakly nonlinear) and strongly nonlinear. In the latter case, a wave with a triangular profile is formed in the resonator for the first model of hysteresis and a wave with a pentagonal profile, for the second model (at $\gamma_1 = \gamma_4$, $\gamma_2 = \gamma_3$, when $\mu_+ = \mu_-$ and $\varepsilon_m^+ = \left|\varepsilon_m^-\right| = \varepsilon_m$ is the wave amplitude). The boundary condition for the strain at the source is set in the form $\varepsilon(x = 0, t) = \varepsilon_0 \sin \omega t$. It is obvious that, in steady-state operation, the following condition will be satisfied in the resonator:

$$\varepsilon_1(L) = \varepsilon_1(L)$$
$$\times \exp\{-ik_p L[1 + \Delta_p + \Delta_h(\varepsilon_m) - i\delta(\varepsilon_m)]\} + \varepsilon_0, \quad (6)$$

where $k_p = \omega_p/C_0$, $\omega_p = 2\pi p C_0/L$, L is the length of the resonator, p is the mode number, $\Delta\omega_p = \omega - \omega_p$, $\Delta_p = \Delta\omega_p/\omega_p$, $\Delta_h(\varepsilon_m) = \Delta C(\varepsilon_m)/C_0$, and the parameters $\delta(\varepsilon_m)$ and $\Delta C(\varepsilon_m)/C_0$ are determined by Eqs. (13), (15) for the first hysteresis model and (21), (23) for the second model [1]. From Eq. (6) we obtain the expression for the resonance curve

$$\varepsilon_m = \frac{\varepsilon_0}{2\pi p \zeta \sqrt{\delta^2(\varepsilon_m) + [\Delta_p + \Delta_h(\varepsilon_m)]^2}}, \quad (7)$$

where $\zeta = \varepsilon_1/\varepsilon_m$; in the quasi-harmonic regime, $\zeta = 1$, and in the strongly nonlinear regime, it is determined by Eqs. (16) and (24) [1], respectively. Note that the structure (i.e., formula (7)) of the resonance curve for a ring resonator coincides with the structure of the resonance curve for bar resonators [7–13]. As follows from Eq. (7), with an increase in the amplitude ε_0 of the generated wave, the resonance curves of these resonators shift and broaden asymmetrically. Unlike systems with a cubic elastic nonlinearity [14, 15], where a hysteresis of the resonance curve takes place, in this case such a situation may not exist. This is connected with the growth of the nonlinear loss and the broadening of the resonance curve preventing its inflection. Precisely this behavior of resonance curves was experimentally observed for bar resonators made of various materials [7–13] (Fig. 4).

We determine the Q factor $Q_p(\varepsilon_m)$ of the resonator as the ratio of the frequency ω_p to the width of the resonance curve at the level $1/\sqrt{2}$: $Q_p(\varepsilon_m) \cong 0.4/\delta(\varepsilon_m)$. It is of interest to trace the behavior of the Q factor $Q_p(\varepsilon_m)$ with the increase in the amplitude ε_0. In the quasi-harmonic regime, the wave power is proportional to ε_0^2 and the loss, being determined by the area of the hysteresis loop, is proportional to ε_0^3; therefore, we obtain

$Q_p(\varepsilon_0) \propto \varepsilon_0^{-1}$. In the strongly nonlinear regime, the wave power at the frequency ω_p is proportional to ε_m^2 and the loss, which is connected mainly with the generation of higher harmonics, is also proportional to ε_m^2; therefore, in this case, we have $Q_p(\varepsilon_0) \cong \text{const}$.

The nonlinear shift of the resonance frequency is determined by the expression $\Delta\omega_{p,h}(\varepsilon_m) = -\omega_p\Delta_h(\varepsilon_m) \sim \varepsilon_m$, and the dependences $\Delta\omega_{p,h} = \Delta\omega_{p,h}(\varepsilon_0)$ for a resonator with an inelastic hysteresis and a resonator with an elastic hysteresis are different, because ε_m depends on ε_0 in different ways. From Eq. (7) it follows that, at resonance, when $\Delta_p + \Delta_h(\varepsilon_m) = 0$, for resonators with an inelastic and an elastic hysteresis, we have the following dependences $\varepsilon_m = \varepsilon_m(\varepsilon_0)$:

$$\varepsilon_m = \frac{3}{2p(\beta_1 + \beta_2)}, \quad \varepsilon_m = \frac{12}{p(\gamma_1 + \gamma_2 + \gamma_3 + \gamma_4)}$$

in the quasi-sinusoidal regime and

$$\varepsilon_m = \left(\frac{\varepsilon_0}{p\zeta(\beta_1 + \beta_2)}\right)^{1/2}, \quad \varepsilon_m = \left(\frac{2\varepsilon_0^2}{\pi p\zeta(\gamma_1 + \gamma_2)}\right)^{1/3}$$

in the strongly nonlinear regime.

The independence of the amplitude ε_m from the initial amplitude ε_0 in the quasi-sinusoidal regime is connected with the neglect of the linear dissipative term in the equation of state (2) [1]. With consideration for this term, we naturally obtain $\varepsilon_m \sim \varepsilon_0$ [7–13], while the dependences $\varepsilon_m = \varepsilon_m(\varepsilon_0)$ for the strongly nonlinear regime will not change.

Now, we determine the parameter r equal to the ratio of the damping decrement δ to the relative change in the wave velocity $\Delta C/C_0$. This parameter is an important characteristic of the amplitude-dependent internal friction [16–20]. For resonators with an inelastic hysteresis and an elastic hysteresis, we have, respectively

$$r_1 = \frac{4}{3}\frac{\beta_1 + \beta_2}{\alpha}, \quad r_2 = \frac{4}{3}\left(1 + \frac{8}{3\pi}\frac{\gamma_1 - \gamma_2 + \gamma_3 - \gamma_4}{\gamma_1 + \gamma_2 + \gamma_3 + \gamma_4}\right)^{-1}$$

for the quasi-sinusoidal regime and

$$\varepsilon_1 = \frac{2(\beta_1 + \beta_2)}{\alpha}, \quad r_2 = \frac{4\pi\varepsilon_m}{\varepsilon_0} = \left(\frac{32\pi}{p(\gamma_1 + \gamma_2)\varepsilon_1}\right)^{1/2}$$

for the strongly nonlinear regime.

From these expressions, it is seen that the parameter r is constant only in the quasi-sinusoidal regime and, in the strongly nonlinear regime, it is amplitude-dependent. In addition, in the strongly nonlinear regime for an inelastic hysteresis, the parameter r does not depend on the mode of resonator excitation, while for an elastic hysteresis, we have $r \sim p^{-1/2}$. Apparently, one would expect that similar dependences of r on ε_1 and p will be
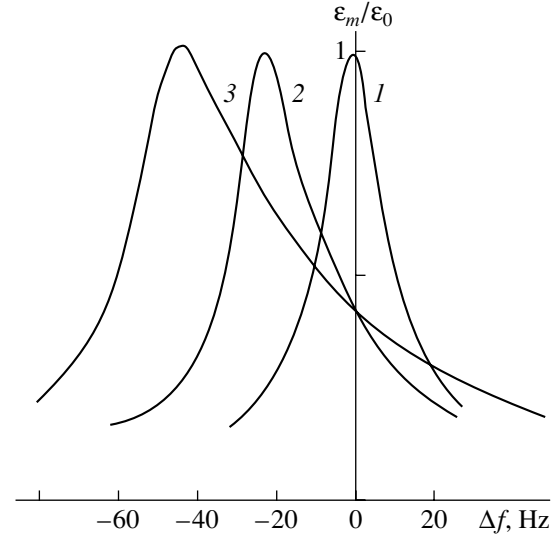

Fig. 4. Resonance curves for various excitation amplitudes of a bar resonator made of polycrystalline copper ($f_2 = 4350$ Hz) [8]: (1) $\varepsilon_0 = 4 \times 10^{-8}$, (2) 8.5×10^{-7}, and (3) 7×10^{-6}.

observed in bar resonators, in which the wave structure is a standing one.

5. GENERAL CONCLUSION

In this paper, we presented a description and comparison of two main phenomenological models of hysteretic equations of state for media with imperfect elasticity: the first model (an inelastic hysteresis) consists of two branches, and the second one (an elastic hysteresis) consists of four branches; all the branches of each hysteresis are approximated by quadratic functions of strain. Within the framework of these hysteretic equations, the study of nonlinear effects caused by the propagation of continuous and pulsed longitudinal acoustic waves in an unbounded medium and in a ring resonator is performed: the profiles and spectra of waves and the resonance curve and Q factor of the resonator are determined. To solve the nonlinear wave equations, we used the method of "sewing together" simple waves corresponding to each hysteresis branch at the points of intersection and superposition of these waves. It is shown that, when an initially harmonic wave propagates in a medium with an elastic hysteresis, the nonlinear loss and the appearance of discontinuities, which are caused by the nonanalyticity of the equation of state for zero stresses and strains, lead to the formation of a pentagonal asymptotic profile of each half-period of the wave, while in a medium with an inelastic hysteresis, where such a nonanalyticity is absent, a triangular wave profile is formed. The study described above showed that the propagation of elastic waves in media with different hysteretic equations of state is accompanied by nonlinear effects, the character of which depends on the type of hysteresis and may be different. For some

effects (such as a change in the wave velocity, the generation of higher harmonics, and the detection of high-frequency pulses), this difference is quantitative, and for other effects (such as the wave form, the dependence of the wave amplitude on the distance and on the initial amplitude, and the ratio of the damping decrement to the relative change in the wave velocity), it is qualitative. The latter distinction most clearly manifests itself in resonators excited in a strongly nonlinear regime, when the level of higher harmonics is comparable to the level of the fundamental frequency wave. Searching and revealing such distinctions in experimental studies of nonlinear acoustic effects will allow one to choose the appropriate hysteretic equation of state for a medium with an imperfect elasticity. On the other hand, the hysteretic equation of state chosen in this way and the hysteresis parameters determined from the comparison of analytical calculations of nonlinear wave processes with experimental results may provide a qualitative and quantitative basis for diagnostics of the type and quantity (i.e., volume concentration) of defects responsible for the acoustic (in the general sense) nonlinearity of a microinhomogeneous medium. In order to solve such diagnostic problems, it is necessary to reveal the physical mechanisms of nonlinearity of various media and create models of various nonlinear defects (dislocations, cracks, contacts, grains, etc.) and equations of state (not only hysteretic) describing the behavior of these defects in the field of an elastic wave. This "microscopic" approach to obtaining an equation of state requires knowledge of the defect structure of the medium and, as a rule, is more complicated compared to the phenomenological approach, in which the equation of state is postulated or reconstructed on the basis of the experimental amplitude and frequency dependences of various nonlinear effects. However, practice shows that both approaches can be successfully (and often independently) used and can complement each other in studies of nonlinear wave processes. In conclusion, we note that nonlinear acoustic methods of diagnostics for various media and materials may be rather diversified and can be based not only on the effects described here but also on other nonlinear effects. Depending on specific conditions, these methods may be simpler or more efficient. The examples of such effects are, apparently, the modulation of sound by sound, sound-by-sound damping, the generation of waves of combination frequencies (sum and difference frequencies), self-focusing, self-brightening, and so on. In media with different types of acoustic nonlinearity, all these effects will appear in different ways, and these differences may be used for determining the nonlinear equation of state of a medium for its diagnostics.

REFERENCES

1. V. E. Nazarov, A. V. Radostin, L. A. Ostrovskiĭ, and I. A. Soustova, Akust. Zh. **49**, 405 (2003) [Acoust. Phys. **49**, 344 (2003)].
2. L. K. Zarembo and V. A. Krasil'nikov, *Introduction to Nonlinear Acoustics* (Nauka, Moscow, 1966).
3. O. V. Rudenko and S. I. Soluyan, *Theoretical Foundations of Nonlinear Acoustics* (Nauka, Moscow, 1975; Consultants Bureau, New York, 1977).
4. K. A. Naugol'nykh and L. A. Ostrovskiĭ, *Nonlinear Wave Processes in Acoustics* (Nauka, Moscow, 1990).
5. V. Gusev, Acoust. Lett. **22** (2), 30 (1998).
6. V. E. Nazarov, L. A. Ostrovsky, I. A. Soustova, and A. V. Radostin, in *Nonlinear Acoustics at the Turn of the Millenium: Proceedings of ISNA-15, Goettingen, 1999*, Ed. by W. Lauterborn and T. Kurtz (Am. Inst. of Phys., Melville, N.Y., 2000), pp. 299–302.
7. V. E. Nazarov, L. A. Ostrovsky, I. A. Soustova, and A. M. Sutin, Phys. Earth Planet. Inter. **50** (1), 65 (1988).
8. V. E. Nazarov, L. A. Ostrovskiĭ, I. A. Soustova, and A. M. Sutin, Akust. Zh. **34**, 491 (1988) [Sov. Phys. Acoust. **34**, 285 (1988)].
9. S. V. Zimenkov and V. E. Nazarov, Fiz. Zemli, No. 1, 13 (1993).
10. V. E. Nazarov, Fiz. Met. Metalloved. **88** (4), 82 (1999).
11. V. E. Nazarov and A. B. Kolpakov, J. Acoust. Soc. Am. **107**, 1915 (2000).
12. R. A. Guyer and P. A. Johnson, Phys. Today, No. 4, 30 (1999).
13. J. A. TenCate and T. J. Shanklad, Geophys. Res. Lett. **23** (21), 3019 (1996).
14. N. N. Bogolyubov and Yu. A. Mitropol'skiĭ, *Asymptotic Methods in the Theory of Nonlinear Oscillations*, 4th ed. (Nauka, Moscow, 1974; Gordon and Breach, New York, 1962).
15. M. I. Rabinovich and D. I. Trubetskov, *Introduction to the Theory of Oscillations and Waves* (Nauka, Moscow, 1984).
16. A. Granato and K. Lucke, J. Appl. Phys. **27** (5), 583 (1956).
17. *Ultrasonic Methods for Studying Dislocations*, Ed. by L. G. Merkulov (Inostrannaya Literatura, Moscow, 1963).
18. G. S. Pisarenko, *Vibrations of Mechanical Systems with Allowance for an Imperfect Elasticity of Material* (Naukova Dumka, Kiev, 1970).
19. S. Asano, J. Phys. Soc. Jpn. **29** (4), 952 (1970).
20. A. B. Lebedev, Fiz. Tverd. Tela (St. Petersburg) **41**, 1214 (1999) [Phys. Solid State **41**, 1105 (1999)].

Translated by A. Svechnikov

Effect of Internal Waves on the Intensity and Interference Structure of the Sound Field in a Shelf Zone

A. N. Rutenko

Il'ichev Pacific Oceanological Institute, Far East Division, Russian Academy of Sciences,
Baltiiskaya ul. 43, Vladivostok, 690041 Russia
e-mail: rutenko@poi.dvo.ru

Received March 27, 2002

Abstract—Experimental data obtained by studying the effect of internal waves with known space–time parameters on the propagation of a 240-Hz tone signal and on the space–time interference structure of the sound field generated by a noiselike sound source are presented. © 2003 MAIK "Nauka/Interperiodica".

INTRODUCTION

Numerous experimental and theoretical studies show that internal waves (IW) strongly affect sound propagation in the irregular shallow-water waveguide that is characteristic of shelf zones of tidal seas with a seasonal thermocline [1–6]. The sound refraction and scattering by the IW-induced inhomogeneities of the sound speed field cause fluctuations in the frequency, spatial, and time characteristics of the sound field and lead to a transformation of its mode structure produced by a stationary sound source in the water layer of this waveguide. At the same time, in a shelf zone, the space–time characteristics of IWs have a number of important features governed by the tidal internal wave (TIW), which is generated by the interaction with the seafloor relief and the continental slope [7, 8]. A TIW generated at the edge of the shelf propagates towards the shelf in the form of a free-space gravity IW. Due to the interaction with the seafloor, it undergoes transformations accompanied by the generation of shorter internal waves and trains of quasi-harmonic and solitonlike IWs [8]. In experiments [9–11], the TIWs propagating in the given region of the Sea of Japan were shown to have a length of 10–16 km and a height of 9–20 m; the nonlinear IWs had a length of 60–350 m and could reach 20 m in height. In the theoretical studies [12, 13], it was established that the sound scattering from the spatial inhomogeneities generated by nonlinear IWs in the sound speed field can lead to a resonant interaction of the propagating acoustic modes and to abnormally high sound absorption at a certain resonant frequency. Such a phenomenon was observed in the experiments [12] carried out in the Yellow Sea.

This paper considers the data of in-sea experimental studies of the effect of a group of nonlinear IWs with known space–time parameters on the propagation of a tone signal with a frequency of 240 Hz and on the frequency–space–time interference structure of the sound field produced by a noiselike sound source. The mea-

surements were carried out in October, 2001, on the shelf of the Sea of Japan.

REGION OF STUDIES AND EXPERIMENTAL LAYOUT

Figure 1 shows the map of the region under study with the indicated positions of measuring devices and the path on which the measurements were carried out. The 240-Hz tone and noiselike signals were transmitted by a piezoceramic sound projector bottom-moored at a depth of 36 m, near the steep coast (point 1) [14]. At a distance of about 3.5 km from point 1, three radiosonic buoys were fixed in positions forming a triangle with sides of 160, 210, and 230 m. The buoys were equipped with bottom hydrophones and distributed temperature sensors measuring the variations about the mean temperature within the 30-m water layers covered by them. Synchronous reception of the radiotelemetering signals was performed at the Schultz Point (at the Sea Experimental Station of the Pacific Oceanological Institute). Such an experimental layout allowed us, for the first time, to quantitatively study the effect of IWs with known space–time parameters on the frequency–space–time interference structure of the sound field in the shelf zone.

In the region under study, an irregular semidiurnal tide was observed with a height of up to 30 cm. At the same time, set-down and pileup phenomena governed by wind-driven water flows and nonlinear surface waves substantially contributed to the displacements of the sea surface. The storm winds from the south and southeast can cause an elevation of the sea level of up to 50 cm. In this case, the seasonal thermocline is expelled from the shallow-water part of the shelf, and the water layer becomes nearly homogeneous in temperature. The measurements of the vertical temperature profiles showed that, during the acoustic and hydrophysical measurements, the water temperature was
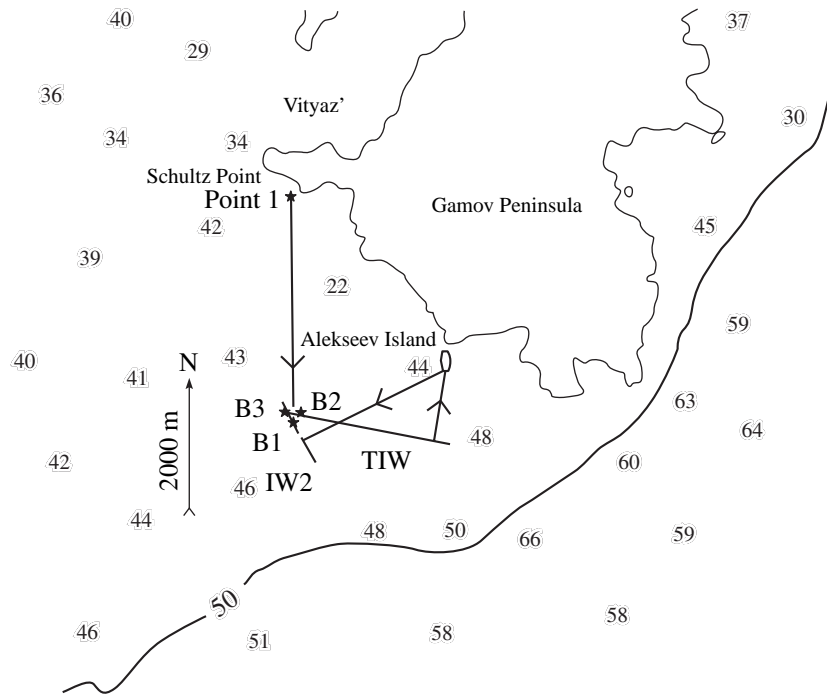
Fig. 1. Map of the experimental site indicating the positions of the measuring devices, the acoustic path, and the crests and propagation directions for the tidal internal wave (TIW) and the group of short nonlinear internal waves (IW2), which were observed in the acoustic experiment. The self-contained radiosonic buoys with the distributed temperature sensors are labeled as B1, B2, and B3. The sound transmitter is at point 1. The arrow is directed north, and its length corresponds to a distance of 2 km.

14.6°C near the surface and 12.2°C at a depth of 42 m. After a 30-hour-long northwest wind (storm waves with white caps), which stopped in the evening of October 17, we observed a relatively short-lived (10-hour-long) intrusion of cold water into the experimental site (this observation was performed at night, on October 18). Such a phenomenon is known [15] to be accompanied by intense nonlinear IWs. Thus, the data of the acoustic-hydrophysical measurements presented below offer a unique opportunity to study the parameters of the IWs generated by the destroyed TIW and their effect on the sound propagation along a fixed path 3.5 km in length.

DATA OF ACOUSTIC-HYDROPHYSICAL MEASUREMENTS

Figure 2 shows the spectrum of the voltage produced at the transmitter by a high-precision sine-wave generator (240 Hz) and a noise generator. The figure also presents the spectrum of the signal received by a hydrophone of the radiosonic buoy near the bottom, at point B1 (see map in Fig. 1). Figure 2 illustrates the frequency-dependent interference structure of the sound field produced by the broadband noiselike signal in the waveguide with a water layer that is nearly uniform in temperature.

Figure 3 shows a fragment of the destroyed TIW that causes the intrusion of near-bottom cold water and the formation of nonlinear IWs. Remember that the distributed temperature sensor measures the variations about the mean temperature in the water layer covered by it. Therefore, the plot of $\eta(t)$ provides information on the amplitude and period of the propagating IWs. The values of $\eta(t)$ were synchronously measured at three points, so that the plots allow one to estimate the propagation direction and the phase velocity of the TIW and some of the most pronounced IWs. The data presented show that the IWs are formed by the propagating spatial formations consisting of cold water, up to 6 m in height, with sharp crests and relatively broad feet. According to the analysis of the plots presented in Fig. 3a, the TIW and the nonlinear IW1 had the front and propagation direction shown in Fig. 1 (TIW). Their phase velocities were $V_{TIW} = 0.42$ m/s and $V_{IW1} = 0.4$ m/s. Figure 1 shows that these waves traveled approximately from south to north, this direction corresponding to the model of TIW formation at the edge of the shelf. The propagation direction of the IW2 ($V_{IW2} = 0.23$ m/s) allows one to assume that this group of nonlinear IWs was generated as a result of the reflection of the TIW from the steep coast of Alekseev Island. Figure 1 shows the TIW and IW2 propagation trajectories corresponding to the TIW reflection from this island. If, before the reflection, the TIW propagated with the mean phase
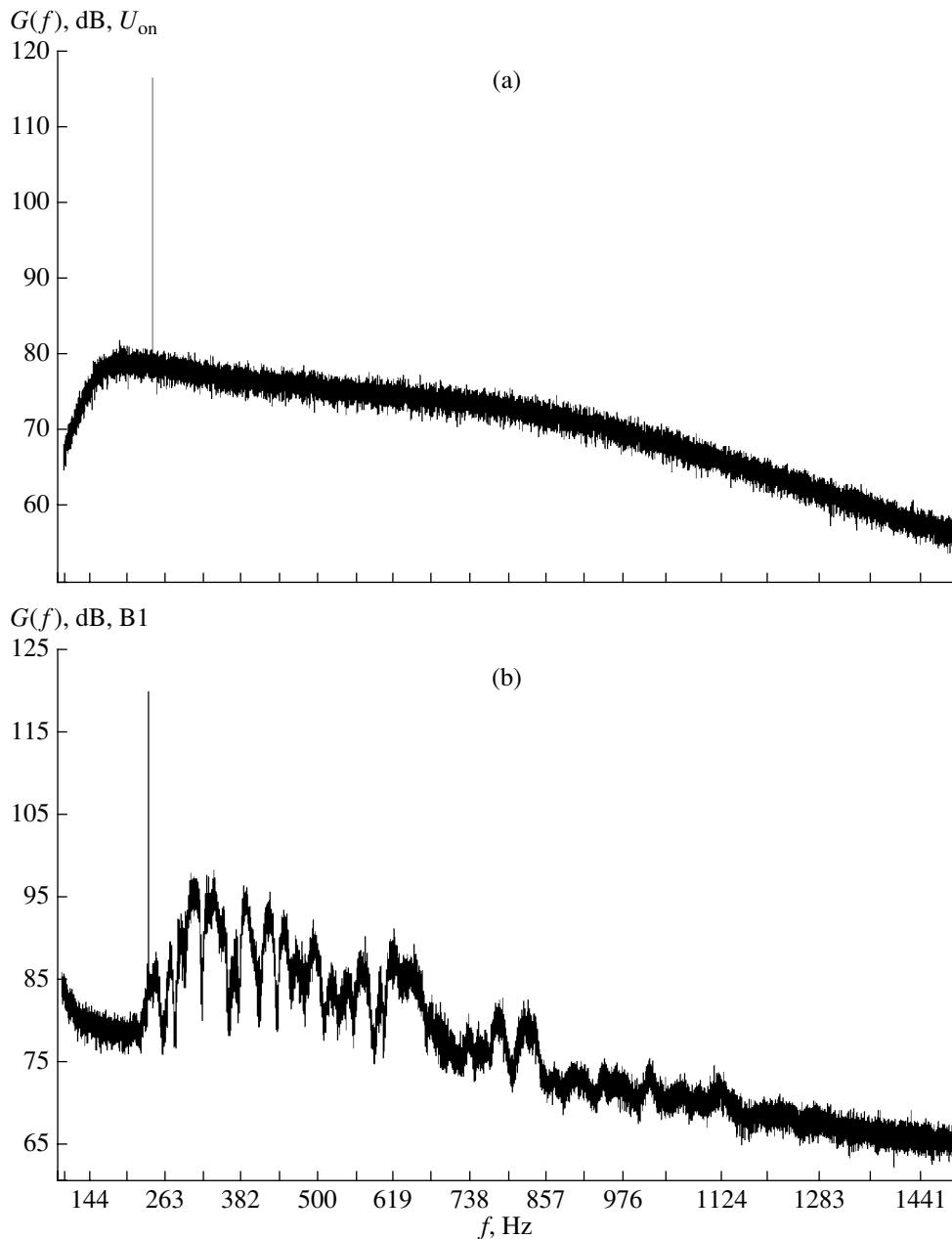
Fig. 2. Spectra $G(f)$ of (a) the voltage U_{on} produced at the transmitter by the sine-wave generator (240 Hz) and (b) the noise generator and $G(f)$ of the sound field synchronously measured by the hydrophone of the radiosonic buoy B1 (Fig. 1).

velocity $V_{TIW} = 0.4$ m/s, it would arrive at the Alekseev Island within 41 min (see Fig. 1). As a result of breaking and reflection of the TIW from the nearly vertical wall of the island (with a depth drop of more than 40 m), the IW2 was formed, which propagated with $V_{IW2} = 0.23$ m/s. Hence, the IW2 should arrive at point B2 four hours later than the TIW, and this value approximately agrees with the data presented in Fig. 3a (4 h 20 min).

Let us now consider the data of the acoustic measurements. These data are presented in Fig. 3b as plots of intensity $I(t)$ of the tone sound field with a frequency of 240 Hz. The effects of the IWs are most pronounced when they approach the transmitter. On the other hand, this is precisely the time when the IWs propagated in the region under test, including the IW2 generated due to the reflection of the TIW from the steep coast of the Gamov Peninsula. The crests of such IWs are oriented nearly parallel to the acoustic path (see Fig. 1). It is known that the effect of such IWs on the sound propagation is maximal, and, in this case, the periods of the intensity variations should correspond to those of the IWs. This is precisely what we can see in Fig. 3b, in the plots of $I(t)$ after 7:00.
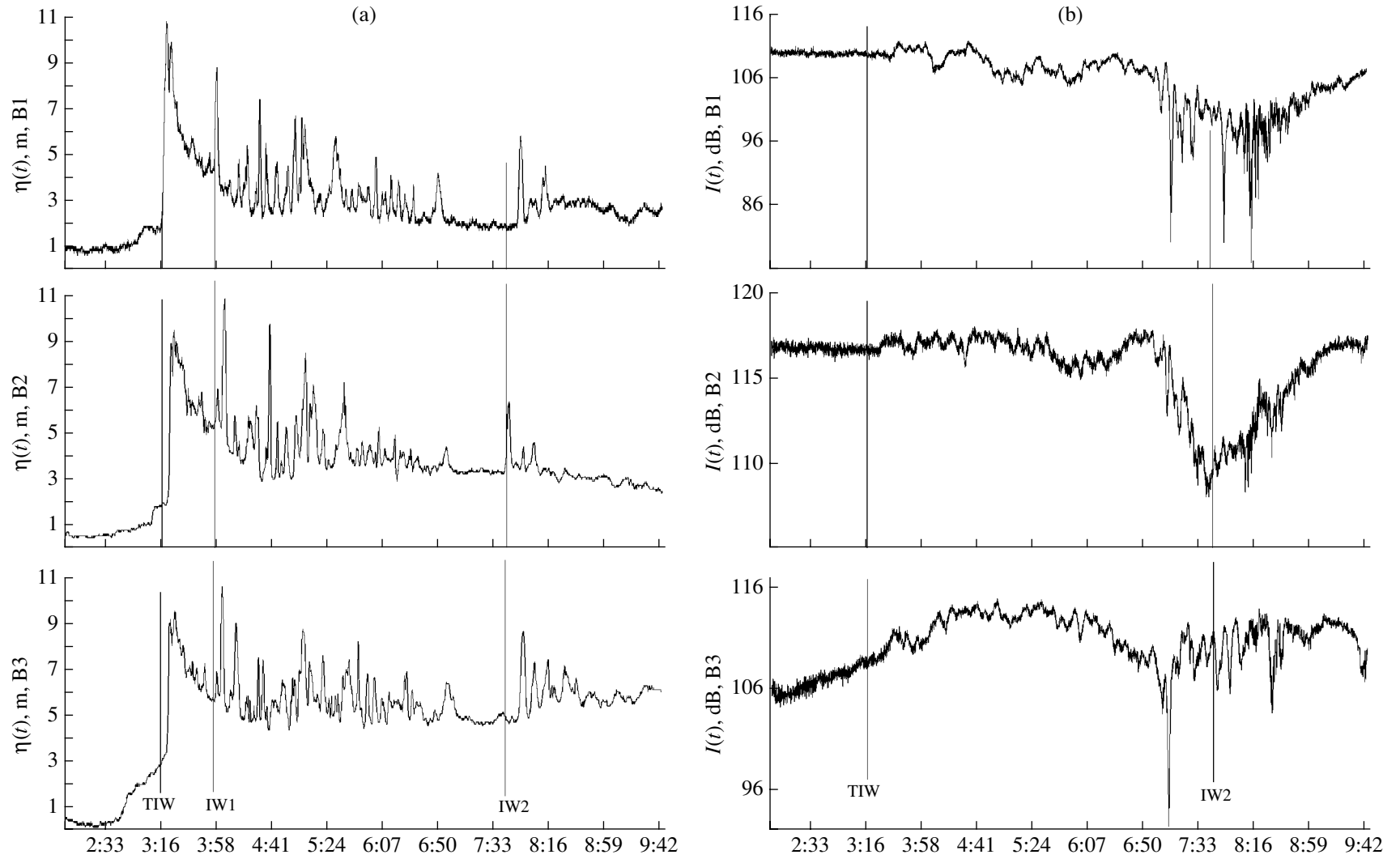
Fig. 3. (a) Profiles $\eta(t)$ of the internal waves and (b) the intensity $I(t)$ of the sound field generated by the 240-Hz tone signal transmitted from point 1. The data are obtained from synchronous measurements by the radiosonic buoys at the three spatially separated points (Fig. 1) at night, on October 18, 2001.
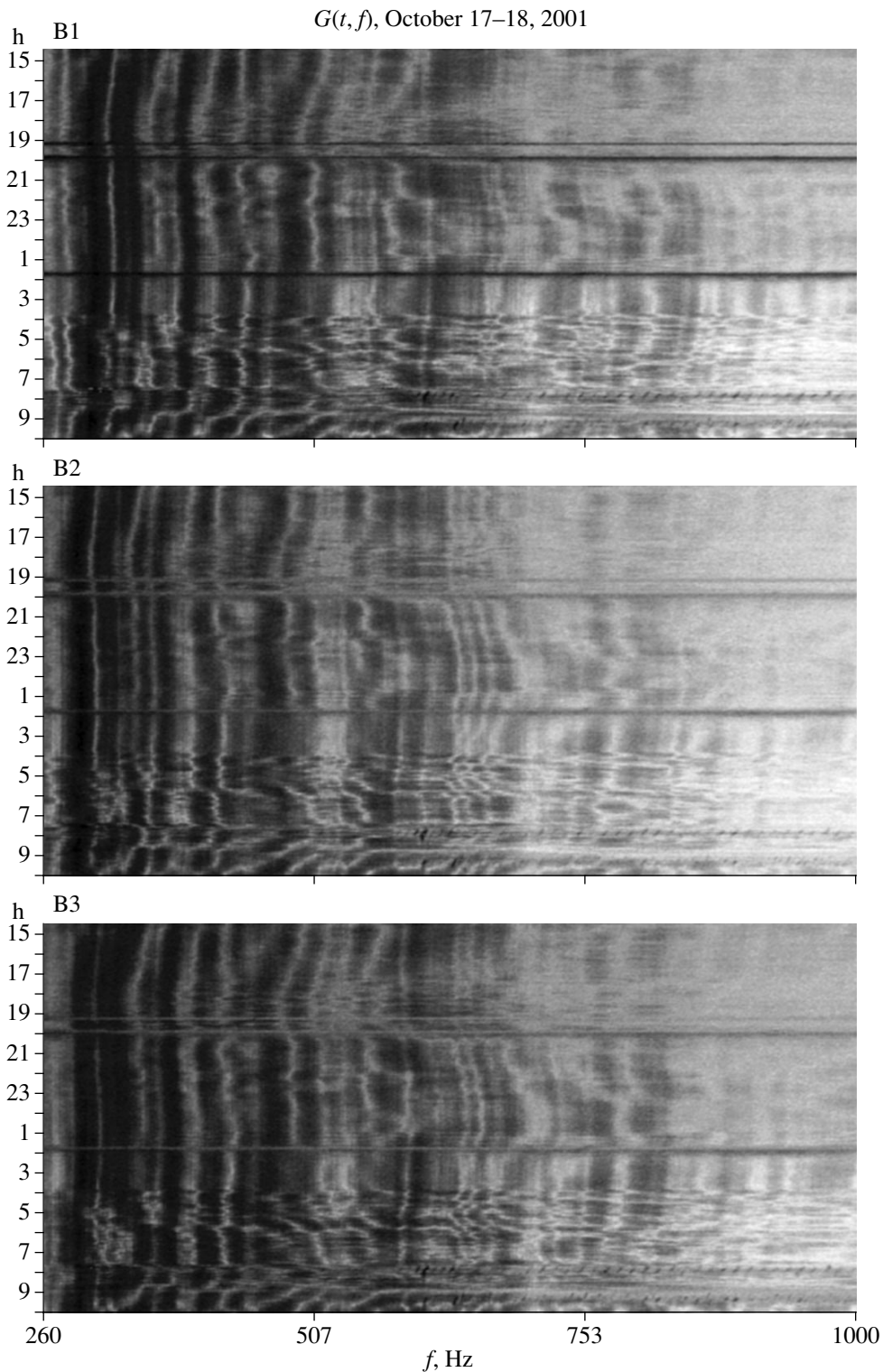
Fig. 4. Sonograms of the spectra $G(f, t)$ of the noiselike sound field transmitted from point 1 and synchronously measured at the three spatially separated points (Fig. 1).

The effect of IWs on the frequency–space–time interference structure of the sound field is illustrated by the sonograms $G(f, t)$ of the noiselike signals (Fig. 4). According to these data, prior to the arrival of the TIW and short IWs at the path, the frequency–time interference structure was rather stable in the frequency band 260–1000 Hz. However, after 4:00, this stability was broken by the IWs.

The analysis of the experimental data allows one to argue that the relatively short IWs generated by the TIW, which breaks in shallow water, considerably affects the sound propagation in the shelf zone. The propagating sound waves are scattered by the IW-induced inhomogeneities of the sound speed field. Such scattering processes lead to strong fluctuations of the sound field and to high propagation losses. Figure 3b shows that, at the time when the short IWs pass through the near-transmitter part of the path, the sound intensity measured at 240 Hz (see the plots of $J(t)$ for the points B1 and B2) decreases by more than 6 dB. Presumably, this decrease is caused by energy transfer from the modes of low numbers to those of high numbers [12, 13], which propagate with higher losses due to their absorption in the seafloor.

ACKNOWLEDGMENTS

REFERENCES

1. D. Tielbuger, S. Funette, and S. Wolf, J. Acoust. Soc. Am. **101**, 789 (1997).
2. A. N. Rutenko, Akust. Zh. **46**, 259 (2000) [Acoust. Phys. **46**, 207 (2000)].
3. A. N. Rutenko, in *Acoustics of the Ocean: Proceedings of the VIII School–Seminar of Academician L.M. Brekhovskikh* (GEOS, Moscow, 2000), pp. 151–155.
4. B. G. Katsnel'son and S. A. Pereselkov, Akust. Zh. **46**, 779 (2000) [Acoust. Phys. **46**, 684 (2000)].
5. B. G. Katsnel'son, S. A. Pereselkov, V. G. Petnikov, *et al.*, Akust. Zh. **47**, 494 (2001) [Acoust. Phys. **47**, 424 (2001)].
6. R. Oba and S. Finette, J. Acoust. Soc. Am. **111**, 769 (2002).
7. V. I. Il'ichev and V. V. Navrotskiĭ, Dokl. Akad. Nauk SSSR **294**, 216 (1987).
8. P. E. Holloway, E. Pelinovsky, T. Talipova, and B. Barnes, J. Phys. Oceanogr. **27**, 871 (1997).
9. A. N. Serebryanyĭ, Okeanologiya (Moscow) **25**, 744 (1985).
10. A. N. Serebryanyĭ, Okeanologiya (Moscow) **35**, 497 (1995).
11. L. F. Bondar', L. K. Bugaeva, and A. N. Rutenko, Akust. Zh. **46**, 613 (2000) [Acoust. Phys. **46**, 534 (2000)].
12. J. X. Zhou, X. Z. Zhang, and P. H. Rogers, J. Acoust. Soc. Am. **90**, 2042 (1991).
13. B. G. Katsnel'son and S. A. Pereselkov, Akust. Zh. **44**, 786 (1998) [Acoust. Phys. **44**, 684 (1998)].
14. V. A. Akulichev, V. V. Bezotvetnykh, S. I. Kamenev, *et al.*, Dokl. Akad. Nauk **381**, 243 (2001).
15. A. N. Rutenko, Morsk. Gidrofiz. Zh., No. 3, 58 (1989).

Translated by E. Kopyl

Space–Time and Frequency–Phase Stability of the Acoustic Field in the Underwater Sound Channel

N. V. Studenichnik[†]

Andreev Acoustics Institute, Russian Academy of Sciences, ul. Shvernika 4, Moscow, 117036 Russia
e-mail: vadov@akin.ru
Received May 20, 2002

Abstract—The space–time and frequency–phase stability of the acoustic field is studied for the case of long-range propagation in the underwater sound channel. The possibility of splitting the field components produced by the Doppler effect in the total interference structure of a monochromatic signal is revealed for different ranges, parameters of the channel inhomogeneities, and frequencies. The experiments are performed in summertime in the northwestern part of the Pacific Ocean, near the Kamchatka Peninsula, on a path of 2100 km. Highly stable sound sources with resonant frequencies of 230 and 380 Hz are used for the measurements. The sources are towed at a depth of 70 m with a speed of 5–6 knots. To receive the signal near the channel axis, a bottom-moored (at a depth of 200 m) stationary system is used. The width of the sound beams is studied, and the broadening limits of the frequency spectra are estimated for the coherent and incoherent field components in the case of super-long-range sound propagation. The phase velocities of the split components are determined. © 2003 MAIK "Nauka/Interperiodica".

In 1980, the Andreev Acoustics Institute, in cooperation with the Institute of Applied Physics of the USSR Academy of Sciences and the USSR Navy Hydrographic Service and with the participation of the MORFIZPRIBOR Central Research Institute and other organizations, carried out complex studies of the acoustic-oceanographic characteristics in the northwestern part of the Pacific Ocean [1]. The studies were carried out in summertime near the southern extremity of the Kamchatka Peninsula. The experimental layout provided for experimental data to be obtained on numerous key parameters of the sound field, for sound and infrasound frequency bands for long-range and super-long-range propagation along paths with complex bottom reliefs and varying environmental conditions. Among the stated tasks, including studies of the field's fine structure, the decays of sound intensity in range, the coefficients of spatial attenuation, the bottom reflectivity, the field correlation characteristics, and the effects of frontal zones and coastal wedge, a problem of special interest was the study of the space–time and frequency–phase stability of the sound field components in the interference structure produced by a monochromatic sound source in an inhomogeneous waveguide. This interest was caused by the fact that there were no such data at that time. Therefore, the feasibility of extracting individual components from complex interference structures seemed to be problematic. To solve this problem, we used tone signals that were highly stable in frequency and broadband signals generated by underwater explosions. This paper presents the data

obtained with the tone signals only. The path, 2100 km in length, was oriented perpendicularly to the coastline of the Kamchatka Peninsula, along the arc of the great circle, in the southeast direction. The bottom relief was represented by a small shallow-water fraction of the shelf (3–4 km in length), a continental slope of 10°–15°, and a deepwater part with 200-m to 5000- to 7000-m depths. At distances of 800–1000 km, the path crossed the Emperor Mounts with depths of 2000–3000 m.

The northwestern part of the Pacific Ocean is one of most complex ocean regions from the viewpoint of the variability of hydrophysical conditions and the spatial distribution of different water masses. A specific feature of the region consists in the substantial instability of the deepwater layers because of the influence of water dynamics, the interaction between the permanent subarctic waters of the cold Oyashio Current and the sub-tropical warm waters of the Kuroshio Current, the migration of the frontal zones, and the instability of the eddies. Thus, in this region, a specific thermal structure of coastal waters is formed with a stable region of cold waters (less than 1°C) at depths within 50–100 m and a region of relatively warm waters (up to 3–4°C) at 300–400 m. The detailed hydrographic studies of the region revealed four main fronts: the Kamchatka front (the northern Oyashio Current, 50–150 km from the coastline), the Oyashio front (the Oyashio Countercurrent, 800–850 km), the northern polar front (1100–1300 km), and the Kuroshio front (2000–2100 km). The first three fronts do not considerably change the sound speed profile. All of them are governed by water masses of polar and moderate latitudes. In such structures, the axis of
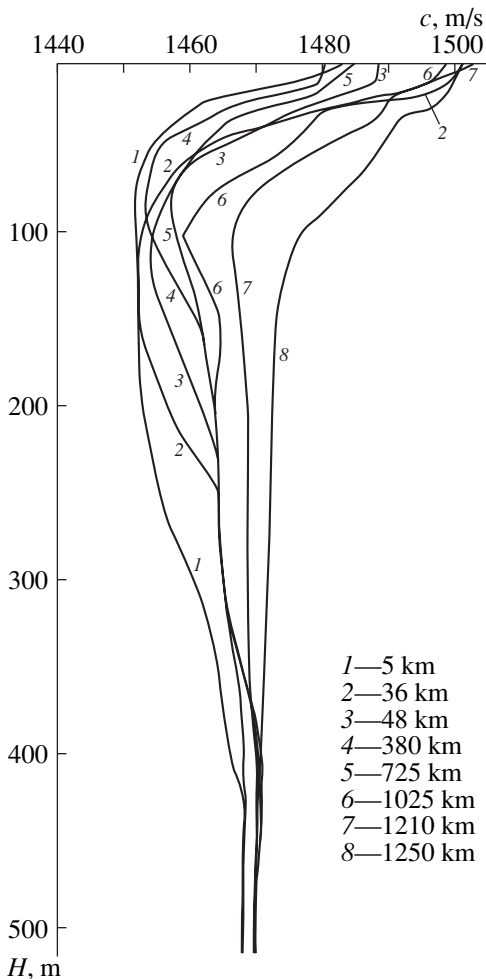

[†] Deceased.

Fig. 1. Samples of the sound speed profiles along the propagation path in the near-surface layers up to a depth of 500 m.

the sound channel is at depths from 70 to 200 m, up to a distance of 2000 km. At the axis, the sound speed varies within 1446–1474 m/s. The only exception is the path fraction behind the Emperor Mounts, at distances of 1100–1300 km (the northern polar front): here, a thick water layer of nearly constant sound speed exists, which covers depths from 70–100 to 800–1000 m. In this layer, a slightly noticeable minimum of the sound speed, 1474 m/s, corresponds to horizons of 400–500 m. A transition to tropical structures with a deeper (1000 m) axis of the sound channel occurs near the deepwater Kuroshio front at distances of 2000–2100 km. There, the sound speed at the channel axis increases up to 1480 m/s and even higher, i.e., to a value that is 25–35 m/s higher than the sound speed at the axis of the coastal sound channel. At depths of 50–100 m, the difference in the sound speed values reaches 50–55 m/s. Figure 1 shows examples of the sound speed profiles for the near-surface water layers (up to a depth of 500 m) on the path. The meteorological conditions during the experimentation were auspicious: the wind

speed was no higher than 10–12 m/s, and the sea state was Beaufort 3–4.

The acoustic experiments with tone signals were carried out on July 17–25. The studies were based on the much tested method of continuously towing several transmitting systems along the path. The transmitters used in the experiments had resonant frequencies of 100, 230, 380, and 1000 Hz. They were mounted on a single frame along with the reference hydrophone and a depth meter. At a towing speed of 5–6 knots, the transmission depth was maintained within 65–75 m. The maximal distance of continuous towing was 300 km. Quartz oscillators with a frequency stability of 10^{-6} were used as the master drivers. We chose a transmission mode that was close to continuous: the signal duration was 280 s and the pause duration was 10 s. All four transmitters were driven by the same controller that allowed us to continuously monitor the operation of the sound sources and their depths. The method of end-to-end calibration of the hydrophone circuit allowed one to estimate the power transmitted by any source and to maintain it at a desired level. The signals were received by a directional array, which was bottom-moored in the shelf zone at a depth of 200 m. The distance between the source and the receiver was measured by a satellite navigation system and monitored by estimating the propagation times of the sound signals. A more detailed description of the experimental layout, the scope of measurements, the environmental characteristics, and the results obtained can be found in the previous paper [1].

At a frequency of 1000 Hz, a stable signal reception took place up to a distance of 1200 km, with an 8 to 10-dB excess over the noise level. At frequencies of 100, 230, and 380 Hz, the excess was 10–25 dB for distances up to 2100 km. The analysis of the recorded signals showed that, in the envelopes of the signal amplitude, relatively ordered interference structures are observed at all distances up to 1200–2100 km, even for the evidently inhomogeneous waveguide at hand. Figure 2 presents 690-s samples of the recorded signals with frequencies of 1000, 380, and 230 Hz for distances of 1000–2050 km. The average spatial interference period (with a modulation depth of 30 dB) is 100–150 m at 1000 Hz, 350–600 m at 380 Hz, 400–1000 m at 230 Hz, and 500–1000 m at 100 Hz. These features indicate a high stability of the phase fronts and the conservation of coherence in the signal components (for certain characteristic angles), this coherence providing the regular phase summation of the components (the characteristic angles are those at the points where the rays cross the channel axis). Otherwise (in the case of the summation of irregular components), the aforementioned frequency stability of the signals would be broken, and the resultant sound field would take the form of a noise-like process with a constant mean level. The latter fact is well known and has been confirmed by us in the experiments performed later, in winter, at the same frequencies and on the same path, with a strong surface channel (from the surface to the bottom) and
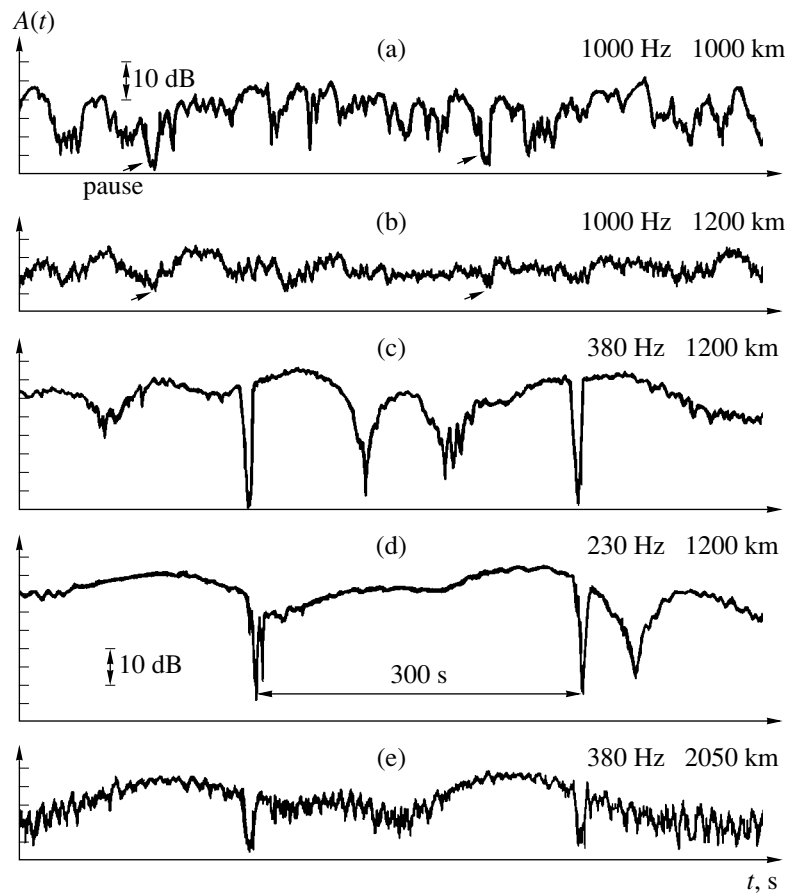
Fig. 2. Fragments of the tone signal records at the frequencies 230, 380 and 1000 Hz for distances within 1000–2050 km. The amplitudes are shown on a logarithmic scale.

sea states varying from Beaufort 2–3 to 6–7 along the path. The envelope characteristics obtained in these experiments at long ranges exhibited no frequency dependence, and the modulation effects observed in the summertime experiments were fully excluded. The coherence of the total field decreased to 0.2 at distances of 700–1000 km. Another feature was observed in the envelopes of the signals propagating in the summertime sound channel. It consists in the fact that, at long ranges (1000–2100 km) and low signal-to-noise ratios (15–20 dB), the regular short-period envelope variations in the multiray signal is accompanied by high-frequency interference variations of the signal amplitude (Fig. 2e, for instance), with a period of 5–11 s and a modulation depth of 8–10 dB. This period is frequency independent. The nature and mechanisms of these interference phenomena are not quite evident. However, it seems that they can be attributed to the effects of small- and large-scale inhomogeneities of the surface roughness. If so, the envelope period would be close to that of the low-frequency ocean swell (0.1 Hz) and to the period of the vessel's roll.

To study the space–time characteristics of the sound field and to quantitatively estimate the frequency–phase stability of its components, we used the recorded sig-

nals of 230 and 380 Hz, received at distances of 1000, 1200, 1500, and 2000 km. The records were computer processed by S.I. Dvornikov. Signal samples of 5 and 17.5 min (300 and 1050 s) were entered into the computer, which corresponded to a change of 750 and 2625 m in the distance between the source and the receiver at a towing speed of 2.5 m/s. The frequency resolution of the analysis was 0.003 and 0.00095 Hz, respectively. In the experiments, 5-min signals alternated with 20-s no-signal periods. Hence, in long samples, there were pauses in the analyzed records that enriched the signal spectrum by high-frequency components and decreased the resolution of the processing method. To estimate the effects of pauses, we modeled monochromatic signals of the frequencies at hand with 20-s gaps. Simultaneously, we estimated the influence of the tape recorder's detonation on the response of the system. The resultant resolution, in view of both the pauses and the detonation, proved to be no higher than 0.001 Hz at 230 and 1000 Hz for samples of 1050 s.

Figures 3 and 4 present (a) fragments of the records for the 230- and 380-Hz signals received at the distance of 1000 km, (b) their spectra, and (c) the autocorrelation functions obtained by the signal processing. The vertical lines in Figs. 3b and 4b correspond to the
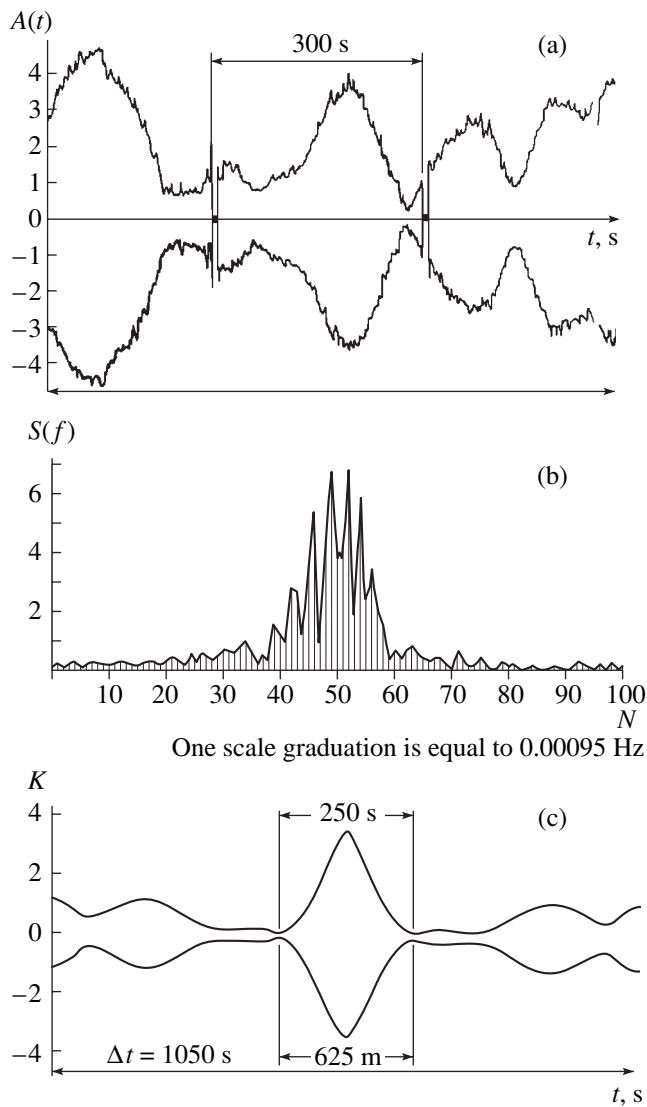
Fig. 3. Fragment of the tone signal record at a frequency of 230 Hz for a distance of 1000 km: (a) the signal envelope; (b) the frequency spectrum; and (c) the envelope of the autocorrelation function. The source moves away with a speed of 2.5 m/s; N is the number of the Doppler filter; the filter passband is 0.00095 Hz; $N = 1$ corresponds to 229.66 Hz, and $N = 100$ corresponds to 229.565 Hz.

0.00095-Hz resolution of the method. The interference period is 2–3 min and 1–2 min at the frequencies 230 and 380 Hz, respectively. The time of autocorrelation proved to be close to the interference period of the envelope. The frequency broadening of the split signal quartet was 25 and 40 mHz at the frequencies 230 and 380 Hz, respectively (this broadening is caused by the Doppler shifts of the coherent signal components at different characteristic angles). The total broadening of the spectrum, including the incoherent (nonsplit) components, reaches 50 and 60 mHz, respectively. At both frequencies in the frequency spectrum, eight to nine well-resolved maxima are noticeable that correspond to

individual components (quartets) of the signal. As we will show later, the phase velocities of these components vary within the range 1457–1540 m/s. To resolve the quartets themselves, one should have a resolution that is an order of magnitude higher for the chosen positions of the transmitter and receiver. With the 5-min samples and a resolution of 0.003 Hz, the splitting of the components at both frequencies becomes worse and even hardly noticeable.

In Fig. 5, the frequency spectra are shown for the 230- and 380-Hz signals received at a distance of 2000 km (the samples have a duration of 17.5 min). As in Figs. 3 and 4, eight to nine well-resolved maxima are present in the records. The coherent signal components correspond to the numbers $N = 60$–80 of the Doppler filters. At higher filter numbers, there is a spectrum of incoherent near-axis signal quartets with the characteristic angles $\pm 0°$–$9°$. Lower filter numbers, $N = 10$–40, correspond to incoherent components with the angles $\pm 14°$–$20°$. Their low level is caused by the loss of coherence, high absorption, surface scattering along the path, and bottom reflections in the case of the steep propagation within the coastal wedge. The lack of splitting in the near-axis components with the angles $\pm 0°$–$9°$ is caused by a strong prereverberation (with the related loss of coherence), by low relative delays of these components, and by weak and chaotic dependence of their arrival times on the characteristic angles.

The results obtained exhibit the frequency–amplitude and space–time structure of the sound field, along with the phase stability of the field components, for different ranges of the characteristic angles in the course of the long-range propagation of monochromatic signals in an inhomogeneous waveguide. These results also show the relatively high efficiency of the chosen processing method. Moreover, the experimental data are evidence for a high space–time stability of the phase characteristics of the sound field and for the conservation of coherence of the field components in a certain, although rather narrow ($\pm 9°$–$13°$), range of the characteristic angles at the frequencies at hand (for summertime conditions), even in a waveguide that is inhomogeneous along the path.

In more detail, the space–time and intensity structure of the long-range-propagating sound field can be seen from a record of the explosion-generated signal. Such a record is presented in Fig. 6a. Here, the amplitude–time structure of the sound field is more evident and needs no additional explanation. The record is obtained at the same time and on the same path at a distance of 1000 km, with source and receiver depths of 100 and 200 m, respectively, within the frequency band 100–2000 Hz. The signals of large characteristic angles are first to arrive; they are substantially attenuated when propagating into the coastal wedge. These signals are ahead of the near-surface components by 10–12 s. After that, the time-split coherent components (9 quartets) arrive, with characteristic angles of $\pm 9°$–$13°$. They
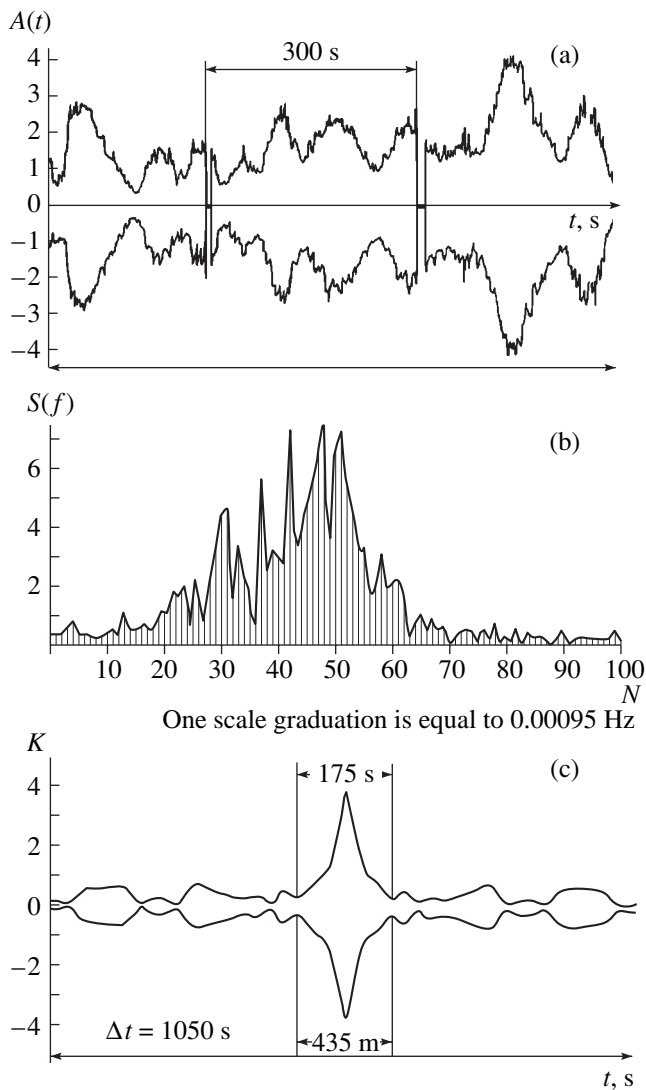
$A(t)$

300 s   (a)

t, s

$S(f)$

(b)

10 20 30 40 50 60 70 80 90 100
N

One scale graduation is equal to 0.00095 Hz

K

175 s   (c)

$\Delta t = 1050$ s   435 m

t, s

Fig. 4. Same as in Fig. 3, for a frequency of 380 Hz; $N = 1$ corresponds to 379.4 Hz, and $N = 100$ corresponds to 379.305 Hz.

$S(f)$

(a)

2000 km
230 Hz

(b)

2000 km
380 Hz

10 20 30 40 50 60 70 80 90 100 N
f

One scale graduation is equal to 0.00095 Hz

Fig. 5. Frequency spectra of the signals at a distance of 2000 km for frequencies of (a) 230 and (b) 380 Hz. The frequency resolution is 0.00095 Hz.

occupy a time interval that is shorter than 3 s. The near-axis incoherent components are last to arrive. They overlap in time, have characteristic angles of ±0°–9°, and last in total for more than 7 s. Note that, according to numerous spectrograms of the 230-Hz and 380-Hz signals received at distances of 1000–2100 km, the number of the split components (8–9) and their angular spectra were close to each other and to those shown in Figs. 3b, 4b, and 5b. The only exception is the 380-Hz signal received at 2000 km: the angular range of its components is somewhat broadened because of the steeper propagation trajectories (the filter numbers $N = 10$–30). The amplitudes of these (not fully resolved) components are lower than the maximal values by as little as 7–13 dB. The aforementioned data on the frequency splitting of the sound field components were
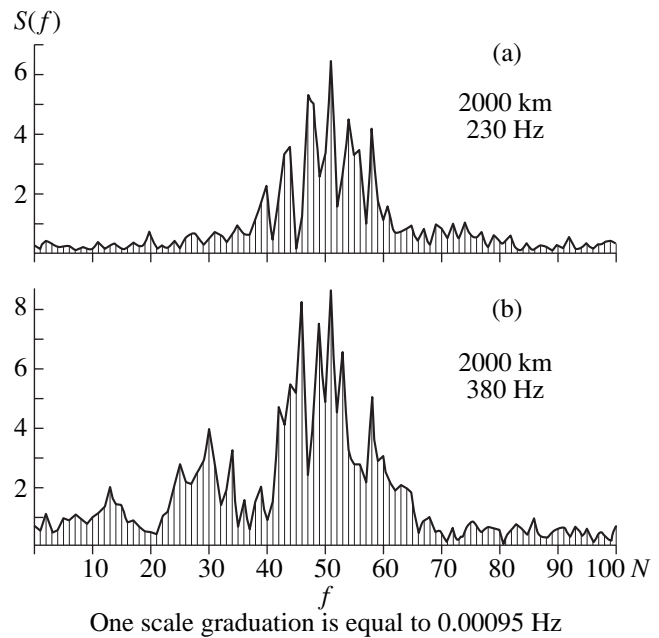
published in [1] and partially reported at the XII Session of the Russian Acoustical Society [2].

Figure 6b shows the calculated space–time characteristics of the sound field in the waveguide with the propagation conditions changing along the path. The calculations are performed with the computer code of Vagin [3], in view of the bottom relief, for a source depth of 100 m and characteristic angles ranging from –8° to +13° (these angles correspond to the rays that do not touch the bottom when entering the coastal wedge). Four sound speed profiles corresponding to the distances 0, 37, 75, and 430 km were used in the calculations. At these distances, the sound speed at the channel axis changed from 1450 to 1460 m/s. The depth of the axis was within 70–100 m. The waveguide parameters were approximated by a linear dependence on distance. The distance (in km) is represented by the abscissa axis, and the advance time of the signals, by the ordinate axis (relative to the time of the propagation along the channel axis at the velocity $c = 1450$ m/s), depending on the departure angle at the source. Curves *1–5* correspond to the numbers of ray cycles for large departure angles. The dashed curves approximate the most probable advance times at the given departure angles. The individual dots, with the indication of the departure angle, illustrate the spread of the advance times and their offsets from the mean values. According to Fig. 6, the mean horizontal velocity of propagation strongly depends on the angular range of the signal components. Thus, in the near-axis range, the arrival times of the rays at different distances prove to be not strictly related to the departure angles. The largest changes correspond
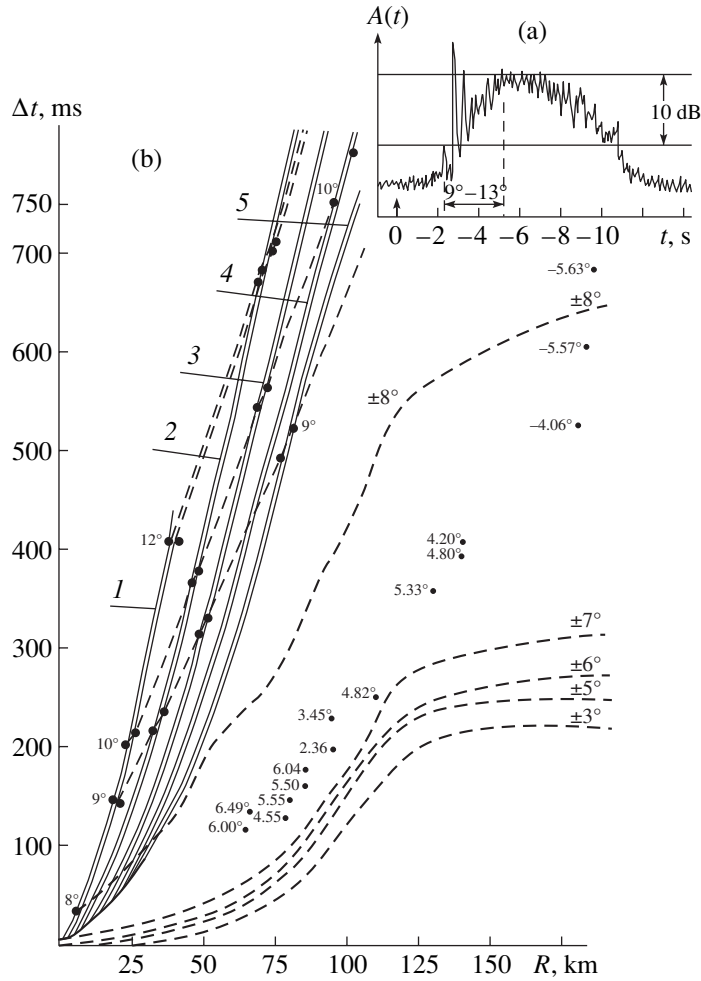
Fig. 6. Shape of the broadband explosion-generated signal received at a distance of 1000 km. The explosion and reception depths are 100 and 200 m, respectively. The reception band is 100–2000 Hz. (a) The signal amplitude (on a logarithmic scale) and (b) the space–time field characteristics calculated for the varying conditions on the path.

to the characteristic angles $\pm(0$–$9°)$. Within this range, the rays that leave the source at lower angles can arrive at the source earlier than those with greater departure angles, and vice versa. Their arrival times can reach several tens and hundreds of milliseconds, which demonstrate the potentialities of using the phase methods for the sound field calculations (the method of normal waves, for instance). Thus, at a distance of 175 km, the ray that departed at $-5.63°$ arrives before the rays that departed at $8°$, and its arrival time differs from the mean value by 420 ms. The observed field features, which are governed by large-scale inhomogeneities (rather than small-scale ones forming the prereverberation), lead not only to a strong volume prereverberation [4] but also to angular and time splitting, the diffusion of whole beams of rays, and fully chaotic time and angular structures of the sound field in the oceanic waveguide. These phenomena destroy the coherence and phase stability of the near-axis signal components at frequencies down to several tens and units of hertz (if one stays within the framework of ray considerations). At charac-

teristic angles outside the range of $\pm(8°$–$9°)$, a sharp increase in the mean horizontal velocities occurs, the angular and time dependences become more ordered, and the effect of the inhomogeneities decreases. The steep rays cross the inhomogeneities, which exist mainly in the near-surface water layers, at high angles. Most of the trajectories of such rays correspond to the deepwater ocean layers with small changes in the sound speed profile. Within this rather narrow angular range, a definite order in the arrival times exists for signal components, and phase stability persists. As the angles increase, the waveguide boundaries begin to affect the propagation. Therefore, the signal level substantially decreases, and the coherence becomes lost. In multiple reflections from the boundaries, the prereverberation components increase in their amplitudes, and the coherent components decay. The aforementioned mechanisms form a complex structure of the sound field in an inhomogeneous waveguide. Such a structure is implemented in natural conditions and observed in ocean experiments.

Let us determine the phase velocities of the split components. As the receiver moves away from the bottom-moored receiver with the speed V (2.5 m/s), the frequency of the field components is governed by the Doppler effect:

$$f_n(\alpha) = f_0[1 - V/C(\alpha)],$$

where f_0 is the transmitted frequency, $C(\alpha)$ is the phase velocity of individual components (signal quartets) in the space–time field structure (these components being discrete in their arrival times and angles), α is the characteristic angle of the components, and n is the ordinal number. Hence, the Doppler frequency shift of the nth and mth individual components is

$$\Delta f = f_n(\alpha) - f_m(\alpha) = f_0 V[1/C_m(\alpha) - 1/C_n(\alpha)],$$

so that we have

$$\Delta f/f_0 = V[C_n(\alpha) - C_m(\alpha)]/[C_m(\alpha)C_n(\alpha)].$$

From the frequency shift Δf, one can find the phase velocities of the components:

$$C_m(\alpha) = C_n(\alpha)f_0 V/[f_0 V + (f_m - f_n)C_n(\alpha)].$$

The phase velocity of the near-axis components, as determined from the measured frequency spectrum, is 1457 m/s. From this value, we can obtain the phase velocities of individual components of the signal that is refracted and partially bottom and surface reflected (in entering the shelf). Note that the specified phase velocity of the near-axis component is somewhat conventional, because the sound speed at the channel axis changes from 1450 to 1465 m/s along the path. However, this approximation weakly (and linearly) influences the phase velocities of other permitted signal components with higher characteristic angles.

For a frequency of 230 Hz and a distance of 1000 km, the frequency shift of the components Δf_n leads to a change of 1464–1540 m/s in the phase velocities. The phase velocity values are summarized in Table 1.

For a frequency of 380 Hz and a distance of 1010 km, the frequency shift of the components leads to a change of 1463–1509 m/s in the phase velocities (Table 2).

The analysis performed in this paper shows how intricate the sound field structure can be in natural inhomogeneous waveguides and how important it is to identify the factors that govern the formation of this struc-

ture, including the frequency–phase stability of the coherent and incoherent components of the propagating sound field. These data are most important for predicting the sound fields by the phase methods of data processing (normal-wave techniques or others).

The coherence of the sound field in underwater waveguides has been intensively studied earlier and is being studied nowadays (see [5, 6], for instance). However, all these studies analyze the integral effects of all factors and field components, both in the vertical and horizontal planes, without angular and time selection and, especially, without frequency-angular resolution of the components. Thus, in [5], the total coherence of the sound field is studied in a deep ocean and a shallow sea. It is shown that, in the deep ocean, at 400 Hz, the deterministic signal model (with a weak volume scattering) holds up to a distance of 500 km. This conclusion agrees well with our prereverberation studies performed in the Atlantic, Pacific, and Indian oceans at frequencies of several hundreds of hertz on paths of up to 1500 km. In [6], the field structure is studied for the anisotropic environment of a shallow sea with a near-bottom sound channel. The propagation losses, the horizontal refraction, and the coherence of the signals are studied at frequencies of 200 and 400 Hz for distances of 10 km in the longitudinal and 1 km in the transverse directions.

From experimental studies of the fine structure of the sound field, we obtained data on the frequency splitting of a monochromatic signal propagating in an underwater waveguide that is inhomogeneous along the path. It is shown that, at the frequencies 230 and 380 Hz, the components of the total sound field generated by a tone source retain their stable phase characteristics up to a distance of 2000 km for characteristic angles ±(9°–13°). Such a stability allows one to split individual groups (quartets) of rays and determine their phase velocities.

For characteristic angles of ±(0°–9°), it is impossible to split the components because of both strong prereverberation and full loss of coherence. The phase velocities of the split components range from 1464 to 1540 m/s at the frequency 230 Hz and from 1463 to 1509 m/s at the frequency 380 Hz. The broadening of the spectra of regular components is 0.02 and 0.035 Hz at the frequencies 230 and 380 Hz; the total broadening (including the irregular components) reaches 0.06 and 0.07 Hz, respectively.

Table 1

Δf, mHz	2	4	6	9	14	16	21
C, m/s	1464	1471	1482	1493	1508	1520	1540

Table 2

Δf, mHz	3	6	10	15	22	24
C, m/s	1463	1470	1480	1492	1502	1509

REFERENCES

1. N. V. Studenichnik, Akust. Zh. **46**, 850 (2000) [Acoust. Phys. **46**, 749 (2000)].

2. N. V. Studenichnik, in *Acoustics of the Ocean: Proceedings of IX School–Seminar of Academician L.M. Brekhovskikh Combined with XII Session of the Russian Acoustical Society* (GEOS, Moscow, 2002), pp. 179–182.

3. A. V. Vagin and N. E. Mal'tsev, Vopr. Sudostr., Ser. Akust., No. 9, 61 (1977).

4. N. V. Studenichnik, Akust. Zh. **48**, 123 (2002) [Acoust. Phys. **48**, 110 (2002)].

5. W. M. Carey, J. Acoust. Soc. Am. **104**, 831 (1998).

6. R. Oba and S. Finette, J. Acoust. Soc. Am. **111**, 769 (2002).

Translated by E. Kopyl

Noise as an Indicator of Cavitation in a Centrifugal Pump[1]

M. Chudina

University of Ljubljana, Faculty of Mechanical Engineering, Askerceva 6, 1000 Ljubljana, Slovenia
e-mail: mirko.cudina@fs.uni-lj.si
Received March 5, 2002

Abstract—One of the sources of instability in a centrifugal pump is cavitation within the pump. Cavitation of a centrifugal pump is the result of insufficient net positive suction head (NPSH) and can occur within the entire range of operating conditions. Cavitation may cause three different and undesirable effects: (1) a drop in head-capacity and efficiency curves, (2) damage to the impeller by pitting and erosion, and (3) structure vibration and resulting noise. Therefore, the cavitation process must be prevented by all means. To prevent the onset of cavitation we have to detect the beginning of the cavitation process in the pump. To detect the beginning of the cavitation process, the emitted noise can be used, among other possibilities. Specifically, a noise spectra structure can be used to detect the beginning of cavitation and its development. Experiments have shown that there is a discrete frequency tone, at 147 Hz, which is strongly dependent on the cavitation process and its development. Therefore, noise spectra can also be used to determine the NPSH required or the critical value, representing the upper limit of the permissible pump operation without cavitation. © 2003 MAIK "Nauka/Interperiodica".

1. INTRODUCTION

The noise generated by a centrifugal pump depends on its geometry (size and form) and on the operating conditions (speed and load). Another factor that increases noise is pump instability. Pump instability may be caused by stall, surge, and cavitation in the pump.

Stall and surge can occur when the pump is operating below the design flow rate or BEP ($Q < Q_{des}$), whereas cavitation can occur within the entire operating regime. Cavitation can occur without stall and surge, and vice versa [1, 2]. Cavitation occurs more easily at higher flow rates ($Q > Q_{des}$) due to the increased velocity of flow and the pressure drop; therefore this type of instability can be avoided by pushing the operating point toward lower flow rates. But at lower flow rates the stall and surge can cause pump operation instability, especially with pumps with unstable characteristics, when the surge point appears at the flow rate, which is higher than zero ($Q > 0$). The surge as a type of noise generation mechanism is beyond the scope of this paper since the pump discussed has a stable operating characteristic.

Cavitation occurs when the absolute static pressure at some point within a pump falls below the saturated vapor pressure of the fluid at the prevailing temperature conditions; the fluid starts to flash and vaporization occurs. Vaporization of the flowing fluid is connected with the onset of bubbles. The bubbles are caught up by the flowing liquid and collapse within the impeller when they reach a region of higher pressure, where they condense. This process is accompanied by a violent collapse or implosion of the bubbles (the time of collapse $t \leq 0.003$ s) and a tremendous increase in pressure, which has the character of water hammer blows [3]. This process of cavitation and bombardment of the pump surface by the bursting bubbles causes three different, undesirable, effects: (a) deterioration of the hydraulic performance of the pump (total delivery head, capacity, and efficiency), (b) possible pitting and material erosion of the impeller blades and shrouds (and volute casing) in the vicinity of the collapsing bubbles, and (c) vibration of the pump walls excited by the pressure and flow pulsations, and resultant noise. Therefore, cavitation in the pump, as an unacceptable phenomenon, should be avoided by all means. To do this we have to know the moment of cavitation inception within the pump and when it is fully developed, especially for pumps working in industrial environments. Cavitation within water pumps (and water turbines) has been the subject of much research, numerous studies, and almost all books that describe centrifugal pumps [3–9]. According to the available literature, there are two different ways to detect the onset of cavitation in a centrifugal pump: numerical or analytical modeling and engineering methods.

Numerical and analytical modeling is often used to predict the onset of cavitation of a single bubble [4, 7–10] and rarely within a pump. There are some well-known models that can be used in describing the phenomena and behavior of cavitation cores [4, 7–9, 11, 12]. However, there is not an exact algorithm to calculate the noise due to cavitation at the different operating conditions of a centrifugal pump. It is well known that the noise due to cavitation increases approximately linearly with the flow rate (or flow velocity with nearly a power of two), the number of bubbles, the maximum

---

[1] This article was submitted by the authors in English.

equivalent volume of the cavitation bubbles and their concentration per unit volume [3]. Due to the chaotic rise of the bubbles in number and size (volume), however, there is no possibility of predicting an exact value of the emitted noise.

The exact value of cavitation noise can be obtained by one of the available engineering methods. There are different engineering methods in practice:

(a) Determination of the net positive suction head (NPSH) at a constant speed and flow rate is the most popular engineering method. According to ISO 3555 standards [13], the NPSH value is determined by a 3% drop in the total delivery head and represents the required or critical value at which cavitation is fully developed. The method needs a special test stand prescribed by standards and a set of measurement results to determine the NPSH required value at different flow rates. It is also used to guarantee tests, but it is not suitable for cavitation monitoring in on-site operations.

(b) Visualization of the flow by an in-pump impeller eye is the second most popular engineering method. Using a transparent model casing and stroboscopic light, in which the cavitating flow is calmed down, visualization and photographic evidence of cavitation is possible. The procedure for testing is similar to the one before, but measuring is based on NPSH(4 mm) data or 4-mm-long vapor cavities, which correspond to a 3% drop in total delivery head or the state of fully developed cavitation (NPSH required). The method is suitable for a single bubble and for high-powered pumps, as well as for localization of the cavitation vortex cores within the pump or water turbine [5, 8, 9, 14–16]. However, it is less appropriate for small pumps and for flow rates far from the BEP, i.e., at low flow rates and at the free delivery. Instead of stroboscopic light, computer-aided camera visualization and digitalization of the pictures can be used. It can also be used to guarantee tests.

(c) Paint erosion testing is based on painting the impeller blades and shrouds and observation of the cavitation erosion by the evident removal of the paint. Its application is good in combination with the NPSH (4 mm) test, which shows whether the cavitation process occurs within the pump or not. This method is complicated by difficulties in choosing the proper paint adhesivity and sensitivity [8]. The same method can be used for metal erosion after a long time of operation and for comparison with the painted erosion at the same percentage of design flow rate.

(d) A method that is based on measurement of the static pressure within the flow or on the volute-casing wall. With this method the onset of the cavitation cores is determined indirectly by comparison of the measured static pressure and the vapor pressure at the given temperature of the flow or by the spectral analysis of the vortex patterns and pressure signal using so-called wavelet analysis [17]. The method is impractical since the local static pressure can be changed by the random changing of the integral pump parameters (caused by changing the operation point) and by flow instability (caused by the onset of stall and surge).

(e) Measuring the vibration of the structure by mounting a transducer in the pump inlet near the impeller blades or as close as possible to the place of implosion bubbles. The method is similar to the previous one but simpler and, unfortunately, less accurate. The measured signal may be contaminated and corrupted by background noise, such as that of aerodynamical, mechanical, and electromagnetic origins, which attenuate or amplify the measured signal [6, 7, 17]. According to the literature used, the cavitation noise is broadband in nature and pronounced mainly in the high frequency range—in ultrasound. Therefore, many researchers measured the acoustic signal in the frequency range up to 1 MHz. They used two different sensors: for low frequency noise (up to 80 kHz), an accelerometer was used, and for the higher frequency range (up to 1 MHz), an AE sensor had to be used [7]. Many authors excluded the low frequency range up to 10 kHz by using a high pass filter [7], so that there is little data about cavitation noise from centrifugal pumps in the audible frequency range below 20 kHz.

(f) A method based on sound pressure measurement. This is a rarely used engineering method, although it is simple and logical. The appearance of cavitation is clearly heard by normal listening; therefore, using acoustic signals has been a dream of many researchers. The significance of sound in monitoring pump operations, as well as the phenomena of cavitation, its appearance and development, has been known for a long time. Nevertheless, relatively few original studies have been published in which sound waves are regarded as a source of information for monitoring the onset of cavitation and its development in centrifugal pumps [18–20]. Citation of these works can be found in many books [5–9]. Common to all these studies are measurements of noise emission in ultrasound up to 1 MHz. As a transducer, a hydrophone or an AE sensor appropriate for a high frequency range was used. All of them detected pronounced noise peaks at the high frequency range above 40 kHz and up to 500 kHz.

In detecting cavitation noise, the researchers were concerned with the following important questions: where to measure, which sensor to use, which signal treatment to use (in the frequency or time domain), and, finally, which acoustic or vibratory parameter to calculate in order to quantify the degree of erosive cavitation. Many researchers prefer to use a hydrophone mounted as closely as possible to the place of appearance of cavitation and to present results in the frequency domain [6, 7, 9].

Using an acoustic signal to control the cavitation in a centrifugal pump has not yet been applied in the industrial environment. This is partly due to the presence of surrounding noise, not a result of the pumping process, which can obstruct analysis and the application of measured signals. Therefore, the surrounding

noise might be considered one of the most significant obstacles for measuring cavitation noise and applying acoustic monitoring techniques in commercial use. Acoustic techniques can be used to detect the onset of cavitation, but not as an unambiguous means of measuring cavitation erosion intensity [8]. This means that a deeper understanding of the relation between the cavitation process and sound generation is needed to overcome obstacles of a purely statistical approach to using acoustic signals for on-line monitoring.

The scope of this study is to promote the use of audible sound (up to 20 kHz), as well as the use of microphones, as sensors. Microphones are particularly useful because measurement of sound signals is easy and simple; we just need a hand-held sound level meter or microphone and a computer equipped with a sound card.

Since the structure of a particular noise spectrum, as well as the total noise level, depends on the operating conditions and the cavitation phenomenon within the pump, detailed analysis of noise spectra of the pumping process was used to detect the onset and development of the cavitation phenomenon. We tried to find the correlation between the cavitation noise and its spectra and the corresponding NPSH required value, at design and off-design operating conditions. In assessing cavitation noise, two parameters were pursued in this paper: discrete frequency amplitudes in the generated broadband noise and their frequencies. The total sound pressure level was also observed. Only audible sound was measured and discussed in this paper. Both our earlier research work [21–23] and the present study are aimed at establishing an experimental base to implement acoustic monitoring of the cavitation process in industrial environments.

2. NOISE SOURCES OF A PUMPING SET AT DESIGN AND OFF-DESIGN OPERATION AND WITHOUT CAVITATION

A pumping set (Fig. 1) consisting of a centrifugal pump *1*, electric motor *2*, and cooling fan *3* generates a noise caused by different noise-generating mechanisms (aerodynamical, hydrodynamical, mechanical, and electromagnetic) and has a broadband noise spectrum with pronounced discrete frequency tones. The discrete frequency tones are called "tonal noise," also known as rotational noise, and the broadband noise is called "turbulent noise," also known as nonrotational noise [21–23].

The tonal noise is mainly created by the interaction of the unsteady flow with the (pump and fan) rotor blades and the interaction of the rotor blades with nearby stationary objects (e.g., the volute tongue, Fig. 2a, and the ribs on the electric motor casing, Fig. 1). These two noise-generating mechanisms create discrete frequency tones at the rotational frequency, RF, and/or blade passage frequency of the pump, the fan, and the electric motor rotor gaps when passing the stationary part of stator or electric motor channels, and

their higher harmonics, BPF = inz_f (i is the number of harmonics, n is the revolutions per second, and z_f is the number of rotor blades of the fan or number of impeller blades of the pump, or the number of the rotor slots–channels of the electric motor). In many cases the first three harmonics of the RF and the BPF are predominant. The tonal noise is independent of the load of the pumping set and has a constant value within entire operating regimes.

The turbulent noise of the pumping set is provoked by pressure fluctuations caused by turbulence and flow friction, by internal recirculation, by laminar and turbulent boundary layer vortex shedding, by flow separation and vortices produced by boundary layer interaction between a high-velocity and low-velocity region in the main fluid field, and by vortices in the radial and axial clearances between the semiopen rotor of the centrifugal pump and cooling fan, respectively, and the adjacent stationary part of the casing [21–23].

At the design point of operation, the blade interaction with the vortices in the radial and axial clearances (Fig. 2), which are created due to the viscous friction of the pumping fluid (water in the pump and air in the cooling fan) and pressure difference between the pressure and suction sides of the rotor blades, represents one of the main sources of turbulent noise. Turbulent noise is strongly dependent on the operating point; at the design point of operation it has its minimum value.

At the off-design operation, an additional turbulent noise is created; so that the total emitted noise steadily increases towards a zero flow rate and towards free delivery. With a constant speed of the driving electric motor, the cooling fan operates at a constant speed and constant load. Therefore, the aerodynamical and mechanical noise corresponds to the design point of operation, and their emitted acoustical energy and spectra are unchanged by changing operating conditions [21, 22]. On the other hand, the hydrodynamical noise caused by the centrifugal pump and the electromagnetic noise caused by the electric motor depends on the pump load.

When the pump operates at higher flow rates ($Q > Q_{des}$), the flow hits on the suction side of the blade, causing a declination of the flow at the pressure side of the blade (Fig. 3a). The pump is subject to the effect of laminar and turbulent boundary layer vortex sheddings on the pressure side of the blade that increase towards the trailing edge of the blade. The blade channel is still fully occupied and only the flow turbulence is increased. Because of this, additional hydraulic noise is generated that increases towards the higher flow rate, and especially towards the free delivery (Fig. 6).

At partial flow rates ($Q < Q_{des}$), additional hydraulic noise is created by rotating stalls (and surge at unstable pump characteristics) and by destabilizing forces that develop through the angular rotation of liquid in the internal running (radial and axial) clearances. The rotating stalls are created due to internal recirculation in
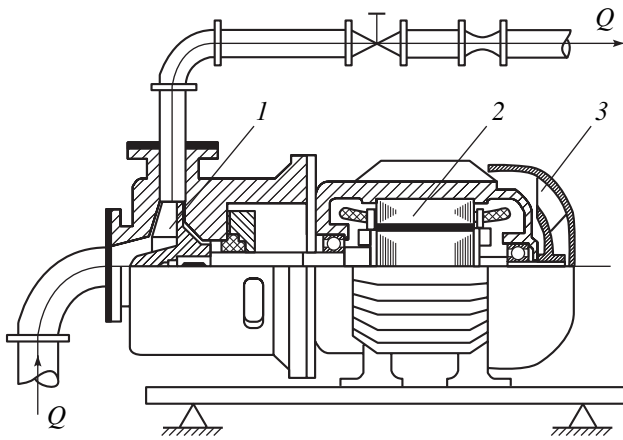
Fig. 1. Pumping set.

the suction and discharge areas of the pump impeller. Rotating stall at the impeller inlet (A, Fig. 3a) occurs due to the large inlet width and sharp 90° turn of the nozzle and due to the velocity and pressure differences in the rotor inlet cross section owing to insufficient flow (Fig. 3b). At the same time, an additional separation of the flow occurs at the suction sides of the blades towards the impeller outlet (Fig. 3c).

When the flow rate is reduced further, a sudden decrease in static pressure occurs within the rotating stalls and the inlet stall will spread over the entire suction cross section. The same process happens with the stall in the impeller discharge on the suction side of the blades [21]. The stalled regions are present in all the blade passages and rotate at 60–80% of the impeller speed [3]. By further throttling, the stall cells A and B in Fig. 3a grow from shroud to hub and progressively fill the entire flow passage leading to partial blockage of

the flow. Stall A spreads partially into blade channels causing an unsteady load on the blades. When stall cells A and B join into one before a zero flow rate, an unstable characteristic of the pump with surge phenomenon and an additional intensive turbulent noise occur.

Electromagnetic noise is generated in the electric motor as a consequence of changes in Laplace, Maxwell, and Coulomb forces and the phenomenon of magnetostriction: the vibration in size of ferromagnetic material when subjected to a changing electromagnetic field [24, 25]. At off-design points of operation, the electromagnetic noise increases by increasing the load of the pump, because the intensity of the current and the phase angle increase due to copper and iron losses.

Within the design point of operation, the hydrodynamical and aerodynamical noises due to the RF and BPF and their higher harmonics are the dominant noise sources. At off-design operations the turbulent noise can achieve and even exceed the tonal noise.

3. NOISE SOURCES OF THE PUMPING SET WITH CAVITATION

When cavitation occurs within the pump, an additional noise generation mechanism appears—so-called cavitation noise. Cavitation is chaotic in nature and, thus, part of turbulent noise. There are two types of hydrodynamically induced cavitation noise. One type is associated with low flow rate and the internal recirculation of local flow causing the formation of stalls with high velocities at their core and a significant lowering of the static pressure at that location. The low-pressure zone attains the value of the vapor pressure first at the impeller inlet (see number of bubbles in suction nozzle in Fig. 2b). When discharge recirculation is established, the vortices associated with it produce low pressure regions with the potential for cavitation erosion, as well
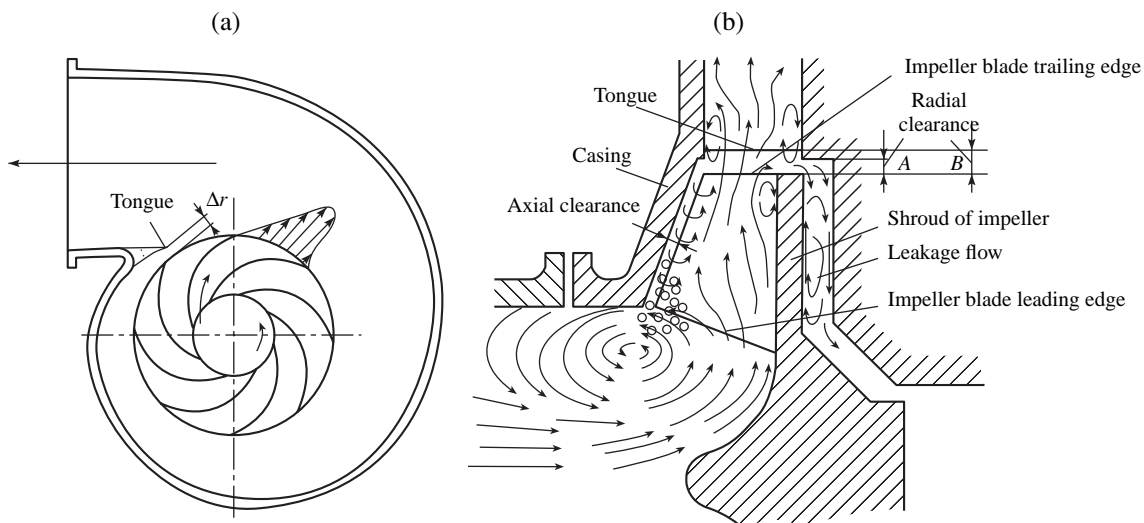

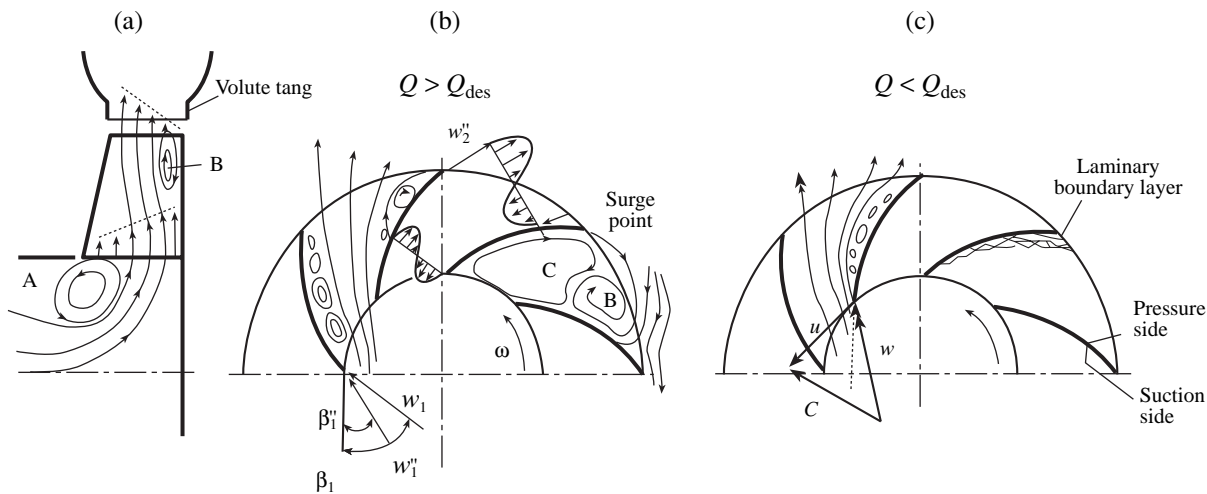**Fig. 2.** Tonal and turbulent noise generating mechanisms.

Fig. 3. Turbulent noise generating mechanisms at off-design operation.

as random pressure pulsations that act both within the impeller, between its shrouds, and in the space between the impeller and the adjacent volute casing. The internal recirculation of discharge occurs at low flow rates causing a noise with a random frequency. In the fully developed stage of cavitation, the low-pressure zone expands rapidly across the entire passage (Fig. 2b). This type of cavitation does not cause fluctuations in the overall mass of flow through the pump; it is known as noise due to unsteady rotational cavitation at the impeller inlet and sometimes at discharge and is usually of minor intensity.

The other type of cavitation noise is associated with insufficient suction head of the pump. This type of cavitation causes overall pressure and mass flow oscillations throughout the entire pump and is known as autooscillation or surge. In this case, cavitation can cause hydraulic surging and erosion of the impeller like that caused by rotating stall and surge, although it takes place in a different area of the impeller.

A sudden decrease in static pressure below vapor pressure, $p_{st} < p_v$, leads to intense cavitation accompanied by a great increase in pressure pulsation and noise. Cavitation noise, which has a characteristic crackling or hissing noise, is produced by the pulsation waves of bubbles (monopole noise source) and by the collapse (implosion) of the vapor bubbles at the moment when they enter the region of high pressure. At the beginning of the cavitation process (in the region of cavitation incipiency) bubbles are too small and too few, therefore they collapse within and into the surrounding liquid, causing microshocks. At fully developed cavitation, bubbles collapse in close proximity to the impeller walls (blades, shrouds) acting like impulses (impact waves) to the metal itself and eroding it. Since the implosion of the bubbles appears randomly and chaotically, they cause a turbulent noise in a wide frequency spectrum or at a specific frequency, so that the onset of

cavitation can cause a change either in the total noise level or just in a particular frequency band.

In order to find the correlation between the onset of the cavitation and corresponding noise levels and their spectra at design and off-design operating conditions, the total noise level, noise spectra, and the available values of net positive suction head (NPSH) were measured simultaneously.

The NPSH required value is a head that is required above the liquid vapor pressure at the place of the lowest static pressure, e.g., at the suction nozzle. The NPSH is defined by the well-known formula

$$\text{NPSH} = \sigma H, \tag{1}$$

where σ is the Thomas cavitation coefficient, which is a measure of the resistance of the flow to cavitation. The lower the coefficient σ is, the more likely cavitation is to occur. σ is defined by the quotient of the static pressure and the flow speed w or corresponding dynamic pressure:

$$\sigma = \frac{p_{st} - p_v}{0.5\rho w^2}, \tag{2}$$

where p_{st} is the local static pressure (usually ambient static pressure), p_v is the vapor pressure corresponding to the local temperature of the pumping liquid, ρ is the density of the liquid, and w is the local flow (usually relative) velocity in the pump.

The NPSH required is determined by a test in which the total head is measured at a constant speed, flow rate, and test water temperature, under varying NPSH conditions (Fig. 4). Lowering the NPSH value to the point where the available NPSH is insufficient causes a cavitation sufficient to degrade the performance of the pump, and the total delivery head deteriorates. The exact value of NPSH required for a centrifugal pump and the incipiency of cavitation is difficult to determine. Therefore, for a particular speed and flow rate
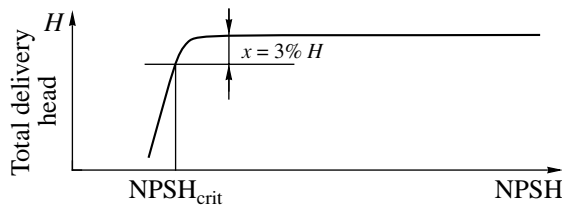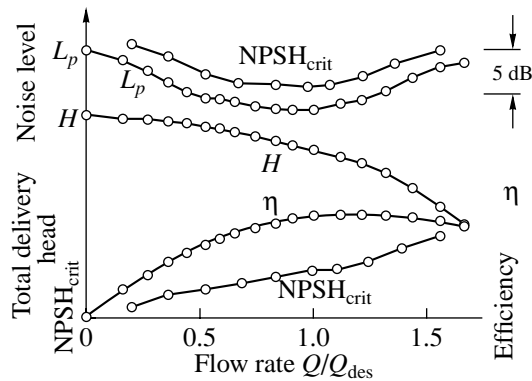
Fig. 4. Determination of the NPSH required.

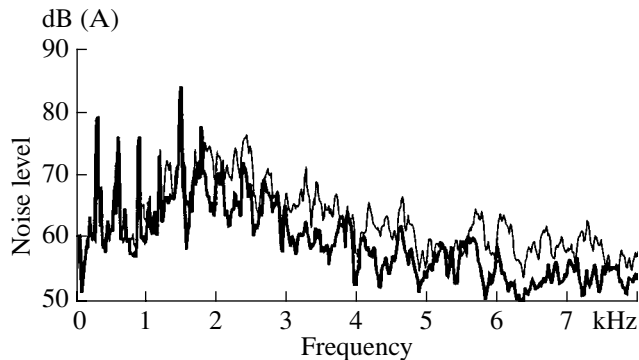**Fig. 5.** Performance and noise characteristics of the pumping set.

Fig. 6. Noise spectra at design point (thick curve) and at off-design operations (thin curve).

the pump has 6 semiopen blades and the cooling fan has 7 rotor blades. The performance and cavitation characteristics, as well as the noise characteristics, were measured on a special test stand in a closed loop, according to the valid ISO 3555 standard (quality level B) [13, 26]. The pump took fluid from a closed vessel in which the pressure level was varied by changing the air pressure above the liquid level. To detect the onset of the cavitation of the pump, the total delivery head is measured at a constant speed (48.5 s^{-1}) and constant flow rate, with varying NPSH available conditions. At the same time, the spectra and total emitted level of noise were measured by a microphone placed at a distance of 0.5 m and perpendicular to the pump–motor axis. A B&K FFT analyzer (Type 2032) was used for the spectral analysis. Since the NPSH values vary with flow rates, the procedure was repeated for different flow rates.

5. EXPERIMENTAL RESULTS AND DISCUSSION

5.1. Noise Analyses of Pumping Set without Cavitation

Measurements have shown that, at the design point of operation, the total noise level of the electric motor is nearly 13 dB (A) lower than that of the complete pumping set, and that the noise level of the electric motor with the cooling fan is nearly 4 dB (A) lower than that of the complete pumping set [21, 22]. This means that the noise generated by the centrifugal pump accounts for the majority of the total noise level.

Figure 5 shows the total emitted noise of the pumping set at design and at off-design operation. At off-design operation, the total noise level increases due to the turbulent noise by nearly 5 dB (A).

Figure 6 shows noise spectra of the pumping set at the design point (thick curve) and nondesign point of operation—at free delivery (thin curve).

Both spectra in Fig. 6 are broadband with pronounced discrete frequency tones at the RF and BPF of the pump and of the cooling fan and their higher harmonics. In off-design operating conditions, the broadband turbulent noise especially increases within the higher frequency range. The discrete frequency tones, at the RF and BPF, should be the same as those at the design point of operation, but their level is changed too, primarily because of the different effects of the turbulent noise, which contribute more or less also at the RF and BPF (see Fig. 7).

At off-design operation, noise levels of the first to the sixth harmonic of the BPF of the pump start to increase steeply towards the free delivery due to laminar and turbulent boundary layer vortex shedding and towards a zero flow rate. This is due to the internal recirculation and the appearance of rotating stall and intensification of the vortices in the axial and radial

being tested, the NPSH that produces an approximately 3% drop in total delivery head is stated to be the NPSH required at which cavitation takes place (see Fig. 4) [13].

In this study, the NPSH available value was used as a basis for determining the significant noise signal, which could be used to detect the beginning of the cavitation phenomenon and its development.

4. TEST PROCEDURE

A pumping set used in a nuclear power plant and consisting of a centrifugal pump and a driving electric motor and cooling fan with a common shaft was used in the experiments (see Fig. 1) [21–23]. The impeller of
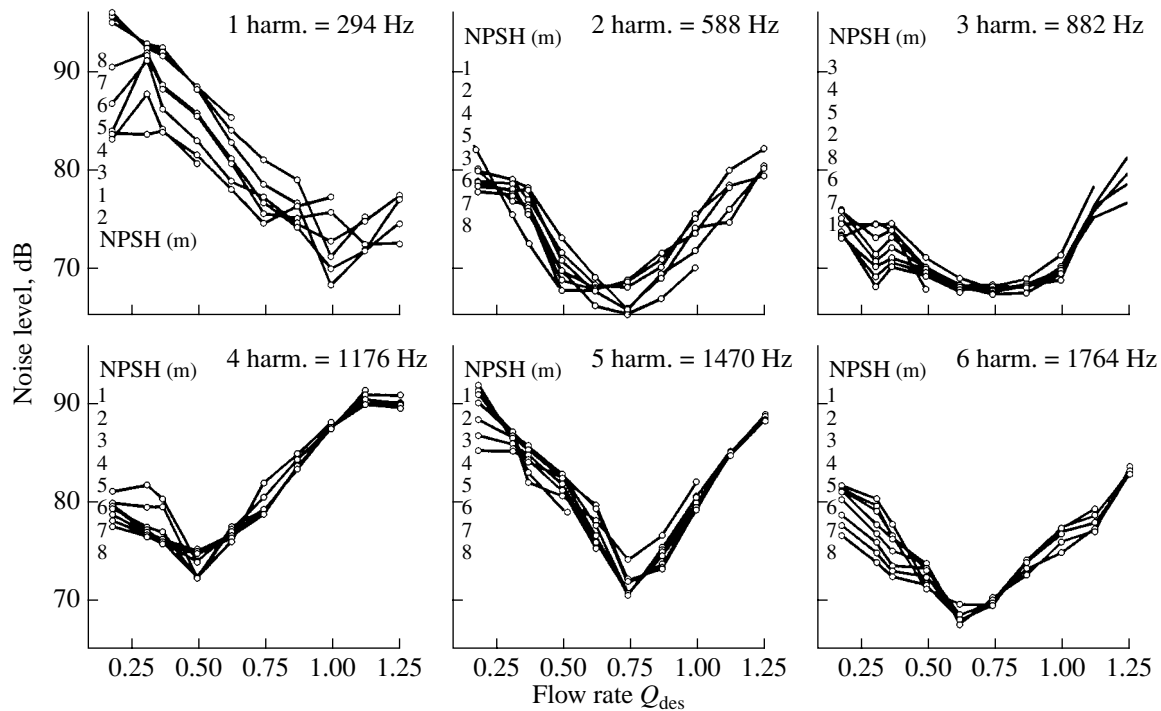
Fig. 7. Effect of blade loading on tonal noise.

clearances between the impeller and volute casing of the pump.

From Fig. 7, we can see that the discrete frequency tones have their minimum at different flow rates. The two most pronounced harmonics are influenced by one noise generating mechanism only. The first harmonic of the BPF (at 294 Hz) has its minimum at the design flow rate (Q_{des}) or best efficiency point (BEP) and is affected first of all by the onset of rotating stall caused by throttling the pump. The fourth harmonic of the BPF (at 1174 Hz) has its minimum at approximately half the BEP and is affected mainly by the laminar and turbulent boundary layer vortex shedding that appears at higher flow rates. The remaining four smaller, less pronounced harmonics, the second, third, fifth, and sixth (at 588, 882, 1470, and 1764 Hz), have their minimum approximately in the middle of the minima of the first and fourth harmonic and are affected by more noise generating mechanisms. Their minima lie near the minimum of the total noise level (see also Fig. 6). The measured results presented in this section are the basic noise data on which the cavitation noise was supplemented.

5.2. Noise Analyses of Pumping Set with Cavitation

Figure 8 shows the measured total delivery head and the corresponding total noise level versus NPSH value at a constant flow rate and speed of rotation. At higher values of NPSH, the values of the delivery head *H* and the noise level remain substantially constant. Lowering the NPSH value to the point where the available NPSH is insufficient causes enough cavitation to degrade the delivery head. The 3% drop in total delivery head (see Fig. 4) signified the required or critical value of NPSH at which cavitation is fully developed for a centrifugal pump.

Figure 8b shows the corresponding total noise level that is measured simultaneously with the NPSH value. In Figs. 8a and 8b, the empty squares indicate the points of cavitation inception and the black dots indicate the beginning of instability known as autooscillation and the points at which the NPSH required or NPSH critical value (NPSH$_{crit}$) is defined. The black points, thus, indicate the state of fully developed cavitation in the pump.

From Fig. 8b, it can be seen that the emitted noise increases slightly when the cavitation process develops. When the NPSH required value is achieved, the emitted noise begins to increase steeply with higher flow rates. Around the design flow rate it fluctuates slightly, and at lower flow rates, the emitted noise starts to decrease steeply. This process of noise reduction at lower flow rates can be explained by the onset of rotating stall. When cavitation is fully developed at lower flow rates and the flow is partially or fully blocked, the generated noise decreases since the volume of the vapor bubbles increases so that some of them begin to cushion the collapsing impulses of others [6]. The role of rotating stall is also diminished since the noise due to internal recirculation of the vapor bubbles is small. At higher flow rates there are no such effects.
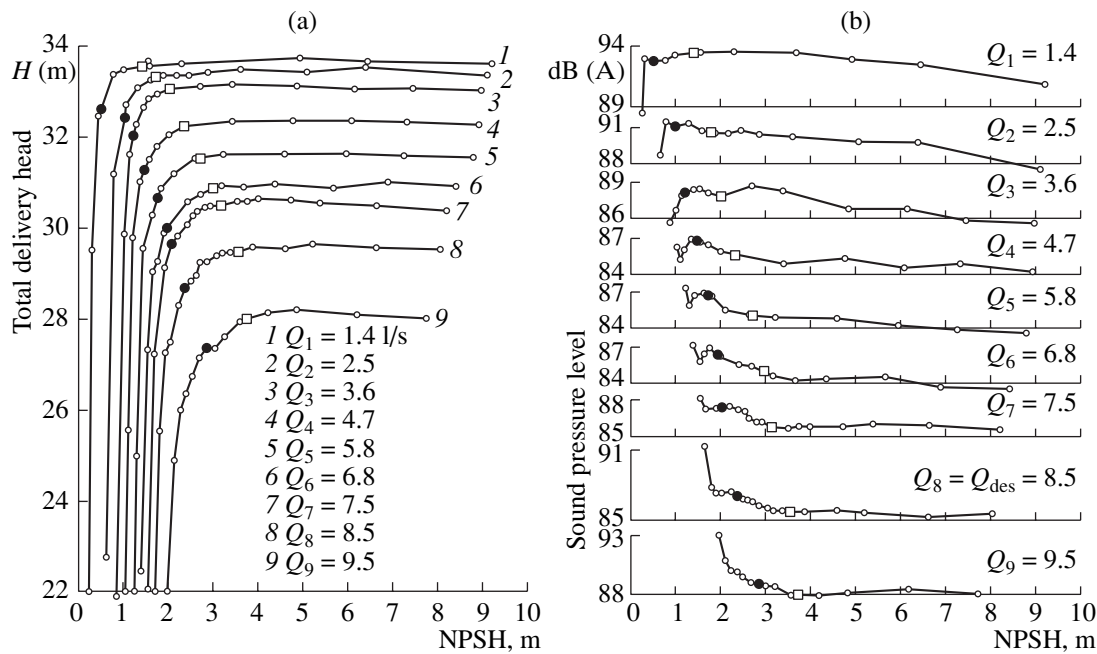
Fig. 8. NPSH and corresponding noise characteristic at constant flow rate and speed of rotation.

The total noise level of the pumping set with cavitation in the pump is also depicted in Fig. 5 (curve $L_p(\text{NPSH}_{\text{crit}})$). This curve corresponds to the level of the black dots in Fig. 8. The differences between the total noise level before cavitation inception (L_p) and after it was fully developed ($L_p(\text{NPSH}_{\text{crit}})$) are approximately 3 dB(A). This means that the energy of the emitted noise caused by fully developed cavitation in the pump is nearly twice as high as that without cavitation in the pump. These differences are great enough to use the total level of noise as a signal to detect the onset of cavitation and to prevent a further process of cavitation in the pump by means of initiating an alarm, shutdown, or control signal via an electrical control system. Nevertheless, changing the operating point of the pump can

diminish this difference or even abolish it; therefore, it cannot be used to prevent the onset of cavitation within the pump by changeable operating conditions. Because of this, additional analyses have been done.

In Fig. 9, noise spectra of the pumping set at the design operation are presented, both before incipient cavitation in the pump (thick curve) and after cavitation was fully developed (thin curve). From this figure, we can see that mainly broadband turbulent noise is increased, especially within the high frequency range. From a set of such noise spectra, we could not get any useful information about the onset of cavitation in the pump, since the alterations of the pronounced noise peaks at the BPF and its higher harmonics are almost not visible.

The discrete frequency peaks of the BPF and its higher harmonics versus flow rate at different NPSH values are also presented as a parameter in Fig. 7. The smaller NPSH values correspond to stronger cavitation in the pump. It can be seen that cavitation in the pump has almost no effect on the noise peaks of the BPF and its higher harmonics at higher flow rates, where laminar boundary layer vortex shedding or turbulence noise prevail. However, it has an effect on the noise peaks at lower flow rates, especially at the first harmonic of the BPF, where rotating stall prevails. The noise level of the first BPF peak decreases when the cavitation process develops, whereas the peaks of its higher harmonics slightly increase. This could be explained by the fact that the effect of rotating stall decreases when the NPSH available value decreases and the number and volume of cavitating bubbles increases. On the other hand, the cavitation noise increases through the devel-
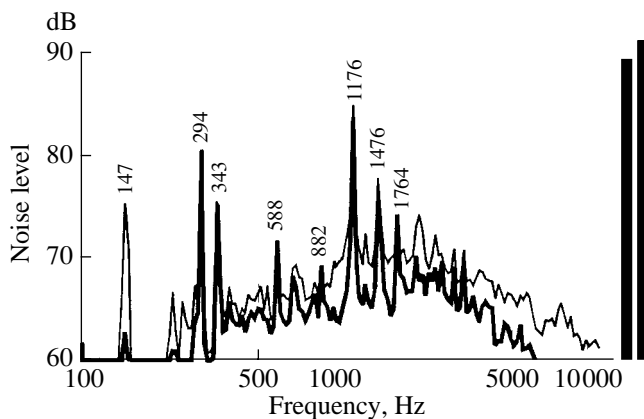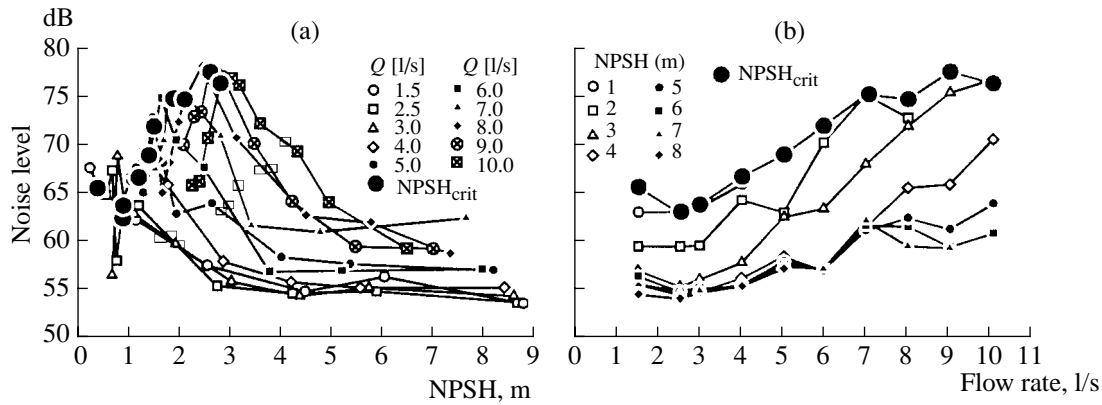

Fig. 9. Noise spectra before cavitation inception (the thick line) and after it was fully developed (the thin line).

Fig. 10. Effect of cavitation process on discrete frequency tone at 147 Hz.

opment of the cavitation so that it overlaps the lower level of the higher harmonics of the BPF. Since the differences in levels for the pronounced peaks in Fig. 7 are negligibly small, these peaks could not be used in the identification and development of the cavitation process.

From comparison of the noise spectra before cavitation inception and after it was fully developed, we can see a great difference in the noise peak at the discrete frequency of 147 Hz, which was not noticed before, in Fig. 6. This frequency is exact half the BPF (BPF/2). Detailed analyses have shown that the peak at the discrete frequency of 147 Hz could well be used to detect the cavitation process in the pump.

Figure 10 shows the noise level of the peak at the frequency of 147 Hz versus NPSH available value at different flow rates, and vice versa. We can see that the noise level of the peak increases by decreasing the NPSH available value and by increasing the flow rate. The level of the peak starts to increase steeply through development of the cavitation process until it reaches a maximum or critical value (black dots in Fig. 10a), when the cavitation process is fully developed, and then it starts to decrease rapidly. Thus, the black dots represent the NPSH critical value corresponding to a 3% drop in the total delivery head.

Differences between the noise levels before cavitation inception (the minimum value) and after it was fully developed (black dots) are between 12 and 20 dB for different flow rates (see Fig. 10a).

Figure 11 shows comparison between the total noise level (L_{ptot}), the noise level at 147 Hz ($L_{p147\,Hz}$), and the total delivery head (H) for a particular flow rate versus NPSH available values.

From Fig. 11 we can also see that the incipiency of cavitation occurs much sooner than is reflected in the curve of the total noise level (L_{ptot}) or in the total delivery head (H). According to Li [7], cavitation noise appears sooner than the drop of total delivery head due to the additional "thermodynamic" effect causing an

additional adiabatic evaporation of liquid and unsteady cavitation oscillations and noise. Figure 11 is also in agreement with the findings of other authors [18–20] and the statements of those who cited them [6–9], but it is not in agreement with the real time and frequency domain. In McNulty's work [18, 19], the noise due to cavitation starts to rise much sooner before the total delivery head starts to fall and falls before the NPSH required was achieved. Besides, their noise curve is at the one-third octave frequency of 40 kHz and coincides with the beginning of the cavitation damage. Gopalakrishnan's findings [20] are similar to those of McNulty, but his pronounced frequencies bands appear between 20 to 120 kHz.

An explanation for differences with our statements could be found in the different range of broadband frequency spectra observed. In [18–20] the high frequency spectra were observed, above 20 kHz (ultrasound), whereas the low frequency part of the spectra were excluded by a high pass filter. In our case, only audible sound was observed, up to 20 kHz. The other reason could be found in the transducer used and its mounting:
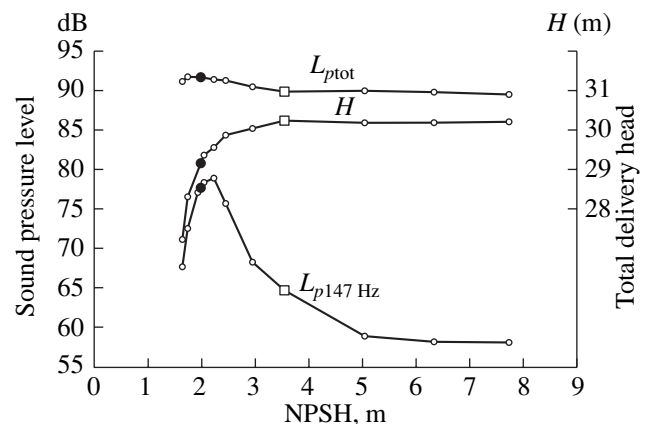

Fig. 11. Comparison between total noise level (L_{ptot}), noise level at 147 Hz ($L_{p147\,Hz}$), and the total delivery head (H) for different NPSH available values.

they used a hydrophone mounted near the suction flange, whereas in our case, a microphone was placed at a distance of 0.5 m and perpendicular to the motor–pump axes.

The differences in noise level of the peak at 147 Hz are great enough to use the noise signal to detect the onset of the cavitation process in the pump at a particular flow rate, and also in the case when the actual value of the flow rate is not known. For a reasonable flow rate in on-site operation covering 50–120% of the design flow rate (Q_{des}), these differences are 15–20 dB (see Figs. 10, 11) and are satisfactory, although the lower values above 12 dB are great enough too. The lower value of the differences (towards 12 dB) correspond to the lower flow rates, where the pumps rarely operate and where the danger of the onset of cavitation is much smaller due to the lower value of NPSH required.

The discrete frequency tone at 147 Hz can, thus, be separated from the total noise of cavitating pumps and used to control the operation of the pump and to prevent the onset of the cavitation process in the pump. It is also suitable for on-site operation in an industrial environmental where a background noise is present. As an alternative method, this noise signal can also be used to determine the NPSH-required value by determining the first positive slope on the noise level curve situated in the black dots in Fig. 10a. In comparison with other methods, this method using sound signals to detect cavitation phenomena is cheap, easy, and user friendly. There is no need to bore a hole in the pump wall to mount a sensor, which can also have an effect on the vibration and the structure.

6. PHYSICAL INTERPRETATION OF THE FREQUENCY 147 HZ

Cavitation noise is a result of the implosion of vapor bubbles or by vapor fill in zones (cavitation field). The implosion energy depends on the driving pressure difference, the number and volume of the vapor bubbles. The number and volume of the bubbles are chaotic in nature and cannot be predicted exactly, although it is well known that they increase when the cavitation process develops or the NPSH available value decreases. The cavitation phenomenon causes pressure fluctuation in the liquid and, consequently, vibrations in the structure and noise in the surrounding air. Noise in the surrounding air, which is measured by a microphone, is much more affected by background noise than that measured by a hydrophone in the water. On the other hand, the dampening of the pump's wall significantly reduces the noise in the air. High frequency noise, especially, is strongly attenuated. The noise in ultrasound is affected even more, although high-level ultrasound cannot be measured by microphone. Therefore, the noise level, as well as the noise spectrum of cavitation noise, is different when measured in water and in the air, and these two cannot simply be compared to each other. In both cases, the spectra are broadband in

nature, but their total level and frequency distribution are different. Our measurements, made by microphone in the air and presented in the previous section, show that development of the cavitation process especially affects the discrete frequency tone at 147 Hz, whereas the measurements made by McNulty, Pearsall, and Gopalakrishnan [18–20, 28] using a hydrophone mounted at the inlet flange show strong pressure pulsations and high noise level in the range of ultrasound, above 20 kHz and up to 160 kHz. According to their findings, high frequency noise increased during the cavitation process to a maximum and then decreased before the point where the delivery head dropped off. Similar characteristics were obtained for low frequency noise although their amplitudes are much lower. The low frequencies below 1 kHz were excluded due to the high level of shaft and blade passage frequency noise. According to McNulty, Pearsall, and Gopalakrishnan's findings, cavitation inception occurs long before the pump performance is affected and at a much higher NPSH value than has often been supposed. The ratio of the cavitation index from inception to that of breakdown for medium specific pumps ranges from a low of 2.5 to over 10 [18]. The peak noise corresponds to the point where erosion danger is most severe. Unfortunately, the authors did not present the whole noise spectra they talked about, so that we cannot get a complete picture about the frequency spectra discussed, which were presented in one-third octave or in much broader frequency bands.

Measurements made by Pearsall on a Kaplan turbine (presented by Young in [9]) show that the low frequency noise (at 250 Hz) increased steeply as the cavitation developed, i.e., in the period when the total delivery head dropped off. However, no attention was paid to this, although the maximum level reaches the maximum level of high frequency noise above 4 kHz, which starts to increase long before the drop of the delivery head.

Our measurements have shown a relatively small rise in the noise level due to cavitation noise in the frequency range above 1 kHz and a little more in the high frequency range above 4 kHz, whereas at the discrete frequency tone of 147 Hz, the noise level rises progressively until it reaches the NPSH critical value, when it starts to drop rapidly. The differences between our results and the results obtained by McNulty *et al.* [18–20] can be explained as follows.

In general, the spectra of cavitation noise change in frequency and amplitude owing to the changing number and intensity of implosion of bubbles. The intensity of implosion of bubbles depends on the driving pressure difference and volume of the bubbles. The implosion of small bubbles causes high frequency noise and large bubbles causes low frequency noise [9, 27]. It is obvious that the discrete frequency tone at 147 Hz does not follow these rules, since the frequency remains the same as the NPSH decreases, although the number and

volume of the vapor bubbles should be changed (usually they increase). The discrete frequency at 147 Hz can be a by-product of a nonlinear interaction with the blade-passing component and is, according to Tsujimoto et al. [29], the result of so-called rotating cavitation.

The main feature of rotating cavitation is that the cavitated region rotates faster than the impeller but slower than rotating stall in gas handling turbo machines [30]. Tsujimoto has shown that rotating cavitation is a local 2D flow instability caused by a positive mass flow gain factor of the cavitation and that the pressure fluctuations are in phase at all circumferential locations. A similar explanation was given by Gülich [28]. According to him, the low frequency noise is a result of oscillation of large voluminous cavitation zones, which represent compressibility and lead to instability of the system; this is also called cavitation surge. This instability should not be confused with performance instability since it can also appear at stable performance characteristics.

According to Gülich [28], the large voluminous cavitation zones are formed in the region of lowest static pressure, i.e., in the suction nozzle. At sufficiently low NPSH available values, a cloud of vapor bubbles is formed, which partially blocks the flow cross section. As pressure is reduced further, there are so many bubbles in the stream and they are so large that a ring-shaped bubble field is formed; the suction passages become vapor locked and choke the flow. Lowering the pressure beyond this region extends the cloud of bubbles from the impeller eye upstream into the suction pipe, causing an intermittent flow of liquid, followed by vapor, then again by water, and so on—a very unstable and violent process, with high vibrations and noise, until the pump essentially is running dry. Blockage of the flow changes the angle of attack of inflow velocity, which causes sinking of the bubble field downstream into the impeller blade channel where it split, and it collapses in a region of higher pressure. In the suction nozzle, blockage disappeared and the angle of attack of inflow velocity is changed so that a new ring-shaped bubble field is formed and a new cycle is repeated. Formation of a new bubble field is finished in a period of one revolution (the lifetime of a bubble) so that the implosion of the bubble field occurs each second revolution. Since the implosion of the bubble field occurs in each blade channel of the impeller, the number of sound impulses is equal to half of BPF (BPF/2 = 147 Hz).

Presently, it is not clear whether sound waves generated by the BPF of the pump impeller have an effect on the formation of bubble fields. According to Young [9], it may cause an oscillation of the bubbles and formation of the bubble field, which then radiates sound as an acoustic emission at the driving frequency (BPF) or at another frequency, since the bubble field has a resonance frequency and nonlinear equations govern its motion. If the driving frequency is a multiple n of the resonant frequency, the bubble field may be excited at this resonance, which can also be a subharmonic, for example BPF/2 as in our case.

According to Gülich [28], the bubble field oscillation causes low frequency noise (below 1 kHz) and contributes mainly to material erosion due to cavitation. Therefore, low frequency noise measured by a microphone in the surrounding air is very important and can undoubtedly be used to detect the onset and development of the cavitation phenomenon. The changes in amplitude of high frequency noise above 4 kHz in Fig. 9 are much smaller than at 147 Hz; furthermore, they change randomly, and therefore they cannot be used to detect cavitation phenomenon in the range of audible sound.

The measurements of McNulty et al. [18–20] made with a hydrophone in water show pronounced noise spectra at high frequency noise in ultrasound above 20 kHz and up to 160 kHz. The high frequency noise in ultrasound is pronounced in a very broadband frequency spectrum and without pronounced discrete frequency tones—the result of the implosion of numerous small bubbles with different volumes. According to their explanation, the increase of the high frequency noise starts to rise far before the total delivery head starts to drop off and in the region of the beginning of intensive material erosion. The high frequency noise is very likely the result of the implosion of numerous small bubbles of air dissolved in water (gaseous cavitation), which is dangerous due to the enormous number of bubbles (approximately 2% in drinking water with a radius up to $(2–5) \times 10^{-3}$ mm and above [9]) causing material erosion, although they have no effect on the total delivery head. When the static pressure decreases below the vapor pressure, vaporous cavitation occurs. The presence of a vapor phase in bubbles first reduces the bubbles' surface tension and the noise level drops, which sometimes also leads to an increase in the total delivery head (a well known phenomenon with some water turbines). With further development of vaporous cavitation, the number and volume of cavitating bubbles and cavitation noise starts to increase rapidly. When a cloud of bubbles is densely gathered, a bubble field is formed, which is ring shaped in a suction nozzle [28]. After the critical value is reached (at an approximately 3% drop of the total delivery head, i.e., NPSH 3%), the noise level starts to decrease rapidly. The reason for this is the two-phase flow with a large part of vapor and compressibility, which causes absorption of sound energy and a reduction in sound velocity [27]. A so-called cavitation surge appears, after which the delivery head as well as the noise level start to decrease rapidly. This process of vaporous cavitation is perfectly accompanied by a discrete frequency at 147 Hz. We could not get such an exact indication by measuring in water using a hydrophone and in ultrasound. The results of McNulty et al. showing that the cavitation inception started much before a 3% drop of delivery head are a useful indicator for detecting the beginning of material erosion (although the main process of mate-

rial erosion happens during vaporous cavitation [27]), but it cannot be used for an exact prediction of the momentum valid criterion of NPSH 3%. The discrete frequency tone at 147 Hz can, on the other hand, be used as an alternative method of determining the NPSH critical value or NPSH 3%.

7. CONCLUSIONS

The emitted noise of a pumping set depends on the speed and load of the pump and on the instability in the pump. Instability in the pump can be stall, surge, and cavitation. Cavitation as a source of instability causes vibration, cavitation noise, pitting, and material erosion and deterioration of pump performance. The cavitation is a consequence of an insufficient NPSH required value. Therefore, the NPSH required must be maintained to prevent the cavitation erosion and noise. The NPSH has to be established experimentally on a special test stand. Instead of this noise, a discrete frequency tone at 147 Hz (1/2 BPF) can be used. The differences in noise level of the discrete frequency tone at 147 Hz before the incipiency of cavitation and after it was fully developed is between 12 and 20 dB. This is great enough to use the signal of the noise to detect the onset of the cavitation process and to prevent the further development of the cavitation process even in an industrial environment where background noise is present. The differences in noise levels are great enough to use the signal at the frequency of 147 Hz to determine NPSH and to control the operation of the pump by means of initiating an alarm, shutdown, or control signal via an electrical control system.

REFERENCES

1. E. M. Greitzer, J. Fluids Eng. **103** (6), 193 (1981).
2. L. Mongeau *et al.*, J. Sound Vibr. **163** (1), 1 (1993).
3. I. Karassik and T. McGuire, *Centrifugal Pumps*, 2nd ed. (Pergamon, New York, 1997).
4. T. G. Leighton, *The Acoustic Bubble* (Academic, London, 1994).
5. D. Japikse, D. W. Marscher, and R. B. Furst, *Centrifugal Pump, Design and Performance* (ETI, Vermont, 1997).
6. L. Nelik, *Centrifugal and Rotary Pumps: Fundamentals with Applications* (CRC Press, Boca Raton, 1999).
7. S. C. Li, *Cavitation of Hydraulic Machinery* (Imperial College Press, London, 2000).
8. E. Grist, *Cavitation and the Centrifugal Pump: a Guide for Pump Users* (Taylor and Francis, Philadelphia, PA, 1999).
9. F. R. Young, *Cavitation* (McGraw-Hill, London, 1989).
10. N. Bidin, R. A. Hassan, and M. M. Sanagi, in *Proceedings of Second International Conference on Pumps and Fans* (Beijing, 1995).
11. T. Uchiyama, Appl. Math. Modell. **22**, 235 (1998).
12. M. Fanelli, *Some Present Trends in Hydraulic Machinery Research, Hydraulic Machinery and Cavitation* (Kluwer Academic, London, 1996).
13. ISO 3555. Centrifugal, Mixed Flow and Axial Pumps—Code for Acceptance Tests—Class B (1977).
14. Y. Nakayama, K. Aoki, and H. Ohta, Proc. ASME **22**, 101 (1985).
15. H. Ohki, Y. Yoshinaga, and Y. Tsutsumi, in *Proceedings of the 3rd International Symposium on Flow Visualization, Ann Arbor, Michigan, USA* (1983).
16. R. Palgrave and P. Cooper, in *Proceedings of the Third International Pump Symposium, Turbomachinery Lab., Texas A&M Univ., Texas* (1986).
17. D. E. Newland, *Random Vibrations, Spectral and Wavelet Analysis* (Addison-Wesley, Harlow, 1993).
18. P. J. McNulty and I. S. Pearsall, J. Fluids Eng. **104** (March), 99 (1982).
19. P. J. McNulty, *Measurement Techniques and Analysis of Fluid-Borne Noise in Pumps* (Natl. Eng. Lab., Glasgow, 1981), NTIS: N82-22504.
20. S. Gopalakrishnan, in *Proceedings of 2nd International Pump Symposium, Turbomachinery Lab., Texas A&M Univ., College Station* (1985), p. 3.
21. M. Cudina, J. Mech. Eng. **45** (4), 134 (1999).
22. M. Cudina, in *Proceedings of the 7th International Congress on Sound and Vibration, Garmishpartenkirchen* (2000), pp. 543–550.
23. M. Cudina, in *Proceedings of the First Congress of Slovenian Acoustical Society* (Portoroz, 1998), p. 125.
24. P. L. Timar, A. Fazekas, J. Kiss, A. Miklos, and S. J. Yang, *Noise and Vibration of Electrical Machines* (Akad. Kiado, Budapest, 1989).
25. J. Delcambre and J. Wood, in *Proceedings of the Inter-Noise 88, Avignon, France* (1988), p. 845.
26. S. Lazarkiewicz and T. A. Troskolansky, in *Impeller Pumps* (Pergamon Press, Oxford, 1965), Chap. 15, pp. 365–396.
27. I. S. Pearsal, *Cavitation* (Mills and Boon, London, 1972).
28. J. F. Gulich, *Kreiselpumpen, Ein Handbuch fur Entwicklung, Anlagenplanung und Betrieb* (Springer, Berlin, 1999).
29. Y. Tsujimoto, Y. Yoshida, Y. Maekawa, *et al.*, J. Fluids Eng. **119**, 775 (1997).
30. M. Cudina, Proc. Inst. Mech. Eng., Part C: J. Mech. Eng. Sci. **215** (1/2), 57 (2001).

SHORT COMMUNICATIONS

Sound Propagation through a Corrugated Pipe

A. D. Lapin

Andreev Acoustics Institute, Russian Academy of Sciences, ul. Shvernika 4, Moscow, 117036 Russia
e-mail: mironov@akin.ru

An airflow through a pipe with a corrugated wall is accompanied by the generation of pure-tone or multitone sound [1–3]. To understand the physical process responsible for the sound generation, it is necessary to estimate the effect of the corrugation parameters (i.e., parameters of the periodic roughness of the wall) on the velocity of the sound propagation through the pipe. Assume that a corrugated wall is characterized by the effective acoustic compliance Y with $\operatorname{Im} Y < 0$. Then, the sound velocity in a pipe of radius R is determined by the formula [4]

$$\gamma = \frac{c}{\sqrt{1 + \dfrac{2\rho c}{kR}|Y|}},$$

where ρ and c are the density of the medium and the sound velocity in it and k is the wave number. For example, for a pipe with small, closely spaced, axisymmetric, rectangular grooves, we obtain

$$Y = -\frac{i}{\rho c}\frac{ka}{2}\frac{b}{L},$$

where a and b are the depth and width of a groove, respectively, and L is the spatial period of corrugation. Then, the velocity of sound is expressed as

$$\gamma = \frac{c}{\sqrt{1 + \dfrac{a}{R}\dfrac{b}{L}}} \approx c\left[1 - \frac{a}{2R}\frac{b}{L}\right]. \tag{1}$$

This velocity linearly decreases with increasing groove depth.

In the general case, the effective compliance of a corrugated surface cannot be determined by simple physical methods, and, therefore, the deceleration of a sound wave should be calculated using the general theory of wave propagation in periodic structures [5, 6]. Below, this calculation is performed for a pipe with a small sinusoidal roughness.

Consider a pipe with a rigid wall described by the following equation in the cylindrical coordinate system: $r = R + a\cos(qz + qz + \varepsilon)$, where $kR < 1$, $ka \ll 1$, $qa \ll 1$, and $2\pi/q$ is the roughness period. The sound pressure p satisfies the Helmholtz equation in the

medium filling the pipe, and, at the pipe wall, it satisfies the boundary condition

$$\frac{dp}{dr} - \frac{dp}{dz}\frac{du}{dz} = 0 \quad \text{for} \quad r = R + u(z),$$

where $u(z) = a\cos(qz + \varepsilon)$. This exact boundary condition can be considered with respect to the cylindrical surface $r = R$. Then, as a first approximation in $k|u|$ and $\left|\dfrac{du}{dz}\right|$, we obtain

$$\left[\frac{dp}{dr}\right]_{r=R} + \left[\frac{d^2p}{dr^2}\right]_{r=R} u(z) - \left[\frac{dp}{dz}\right]_{r=R}\frac{du}{dz} = 0. \tag{2}$$

In a pipe without roughness, the zeroth mode has the form $p = \exp(ikz)$. For a pipe with a small sinusoidal roughness, we seek the zeroth mode in the form

$$p(r, z) = F(r, z)\exp[i(k+\alpha)z],$$

where $|\alpha| \ll k$ and $F(r, z)$ is a function periodic along the z axis with the period $2\pi/q$. Representing this function as a Fourier series and satisfying the Helmholtz equation, we arrive at the expression

$$p(r, z) = \sum_{n=-\infty}^{n=+\infty} A_n I_0(\varsigma_n r)\exp(i\xi_n z), \tag{3}$$

where

$$\xi_n = (k + \alpha + nq), \quad \left(\varsigma_n = \sqrt{(k+\alpha+nq)^2 - k^2}\right),$$

and $I_0(X) \equiv J_0(iX)$ is a Bessel cylindrical function of an imaginary argument.

To satisfy the boundary condition at the pipe wall, we substitute Eq. (3) into Eq. (2) and equate the multipliers of the harmonics $\exp(i\xi_n z)$ to zero. Then, we obtain a set of homogeneous algebraic equations for the amplitudes A_n. Equating the determinant of this set of equations to zero, we obtain a dispersion equation for the coefficient α. If in Eq. (3) we take into account only the three terms corresponding to $n = 0, 1$, and -1, we obtain a third-order determinant, and the dispersion

equation takes the form $|d_{ij}| = 0$, where

$$d_{11} = \varsigma_0 I_0'(\varsigma_0 R),$$

$$d_{12} = [I_0''(\varsigma_1 R)\varsigma_1^2 - q\xi_1 I_0(\varsigma_1 R)]u_{-1},$$

$$d_{13} = [\varsigma_{-1}^2 I_0''(\varsigma_{-1}R) + q\xi_{-1} I_0(\varsigma_{-1}R)]u_1,$$

$$d_{21} = [\varsigma_0^2 I_0''(\varsigma_0 R) + q\xi_0 I_0(\varsigma_0 R)]u_1,$$

$$d_{22} = \varsigma_1 I_0(\varsigma_1 R), \quad d_{23} = d_{32} = 0,$$

$$d_{31} = [\varsigma_0^2 I_0''(\varsigma_0 R) - q\xi_0 I_0(\varsigma_0 R)]u_{-1},$$

$$d_{33} = \varsigma_{-1} I_0''(\varsigma_{-1}R), \quad u_1 = \frac{a}{2}\exp(i\varepsilon),$$

$$u_{-1} = \frac{a}{2}\exp(-i\varepsilon),$$

the prime denotes differentiation with respect to the argument, i is the row number, and j is the column number. This dispersion equation has the solution

$$\alpha \approx \frac{a^2}{4kR}\left\{ \frac{(-qk)}{\varsigma_{-1}}\left[\varsigma_{-1}^2 + \frac{q\xi_{-1}}{1 - \frac{1}{(\xi_{-1}R)}\frac{I_1(\varsigma_{-1}R)}{I_0(\varsigma_{-1}R)}} \right] \right.$$

$$\left. + \frac{(qk)}{\varsigma_1}\left[(\varsigma_1^2 - q\xi_1) - \frac{\varsigma_1^2}{(\varsigma_1 R)}\frac{I_1(\varsigma_1 R)}{I_0(\varsigma_1 R)} \right] \right\}_{\alpha = 0}. \tag{4}$$

The velocity of sound in a corrugated pipe is

$$\gamma = \frac{\omega}{(k + \alpha)} \approx c(1 - \alpha/k).$$

When $\varsigma_{\pm 1}R \gg 1$, from expression (4) we obtain

$$\alpha \approx \frac{k(qa)^2}{4R}\left[\frac{1}{\varsigma_{-1}^0} + \frac{1}{\varsigma_{+1}^0} \right], \quad \varsigma_{\pm 1}^0 = \sqrt{(k \pm q)^2 - k^2}.$$

For $q \gg k$, we have $\varsigma_{+1}^0 \approx \varsigma_{-1}^0 \approx k$, and, hence, $\alpha \approx \frac{kqa^2}{2R}$.

Then, the velocity of sound in a corrugated pipe is expressed as

$$\gamma \approx c\left[1 - \frac{a}{2R}(qa) \right]. \tag{5}$$

This velocity decreases with increasing roughness amplitude according to a square law. The difference in the amplitude dependences in formulas (1) and (5) is determined by the difference in the corrugation slopes.

REFERENCES

1. A. M. Petrie and I. D. Huntley, J. Sound Vibr. **70** (1), 1 (1980).

2. Y. Nakamura and N. Fukamachi, Fluid Dyn. Res., No. 7, 255 (1991).

3. L. H. Cadwell, Am. J. Phys. **62** (3), 224 (1994).

4. M. A. Isakovich, *General Acoustics* (Nauka, Moscow, 1973).

5. L. Brillouin, *Wave Propagation in Periodic Structures* (Dover, New York, 1953; L. Brillouin and M. Parodi, Inostrannaya Literatura, Moscow, 1959).

6. Ch. Elachi, Proc. IEEE **64** (12), 1666 (1976).

Translated by E. Golyamina

Modeling of Vowels

D. I. Yakushev and O. P. Sklyarov

St. Petersburg Ear, Nose, Throat, and Speech Research Institute, ul. Bronnitskaya 9, St. Petersburg, 198013 Russia
e-mail: skljarov@admiral.ru
Received April 12, 2001

Attempts to construct mathematical models of vowels in the time domain rather than in the frequency domain were performed years ago [6, 7]. The results of these studies were confirmed in subsequent publications [1, 5]. Similar studies were carried out in recent years [3, 4]. These models are based on the linear approximation, and the pitch periods in them are approximated by dependences in the form of a sum of decaying sinusoids that contains no parameters of the sound wave rise. Alternatively, attempts were made to describe the voice source spectrum by a nonlinear model [8].

In this paper, we propose a model that contains not only the formant structure of vowels but also describes the rise and fall of the sound wave at every pitch period, which is achieved through the introduction of a square-law time dependence.

In the modeling, we used the following axiomatics:

(i) Vowels have a periodic structure of pitch rise and fall. The corresponding rise–fall period is called the pitch period.

Note that the pitch period is not a period in the strict mathematical sense, because it does not satisfy the condition $f(t + T) = f(t)$.

(ii) Vowels have a formant structure.

In addition, the model was constructed using the following assumptions:

(i) As a result of many experiments with different kinds of mathematical dependences, we accepted the curve $t^2 \exp(-bt)$ as a model of the pitch rise and fall within one pitch period. This curve provides the closest agreement of the model with the original in both objective and subjective sense. Attempts to use other dependences for describing the pitch rise process resulted in less suitable models.

(ii) A formant represents a single frequency; i.e., it is a single sinusoid characterized by frequency, amplitude, and phase: $a \sin(2\pi f t + \varphi)$. When the rise–fall pitch characteristic is superimposed on this frequency, the formant manifests itself as a sound amplification in the signal spectrum region corresponding to this frequency.

With these assumptions, we constructed an empirical model of vowels within pitch periods:

$$p(t) = t^2 \exp(-bt) \sum_{i=1}^{n} a_i \sin(2\pi f_i t + \varphi_i), \qquad (1)$$

where t is time within the pitch period T; $t = 0$ corresponds to the onset of signal generation; b is the coefficient characterizing the stress (the voice intensity): the greater b, the stronger the stress is; n is the number of formant frequencies (determined for every individual vowel); and a_i, f_i, and φ_i are the amplitude, frequency, and phase of the ith formant.

The coefficients a_i, f_i, and φ_i, where i varies from 1 to n, are calculated for each pitch period separately. The parameters n and b are common to all pitch periods.

The method allows one to perform the analysis of the signal, i.e., to determine the parameters of the model, as well as its synthesis, i.e., the sound reproduction from the model.

The degree of similarity between the model and the original is characterized by the quantity $Q = (1 - D_{res}/D)$, where D_{res} is the residual variance of the signal and D is the initial one [2]. The quantity Q may vary from zero to unity (the latter occurs in the case of a total coincidence). Investigations showed that the parameter chosen for characterizing the degree of similarity fits well the results of the auditory comparison between model and original. For some of the pitch periods, this parameter was as high as $Q > 0.995$.

To test the computational algorithm, we modeled several tens of vowel phonemes produced by several speakers. For different speakers, at different phonemes, we obtained a degree of similarity of the model and the original that was higher than 0.9. This result demonstrates the suitability of the proposed model for vowel studies.

When the degree of similarity between model and original is sufficiently high, the proposed method allows one

(i) to divide the signal into pitch periods and construct a model for each individual pitch period,

(ii) to analyze the formant frequency composition of a given signal,

Pitch frequency F_0, formant frequencies f_i, and formant amplitudes a_i in model (1) for the vowel [U] (the formant phases are zero: $\varphi_i = 0$)

Voice intensity b					2.11				
Pitch peri-od number	F_0 (Hz)	f_1 (Hz)	f_2 (Hz)	f_3 (Hz)	f_4 (Hz)	a_1	a_2	a_3	a_4	Q
1	114	232	457	864	3210	6.9	3.5	0.2	0.0	0.99
2	114	230	454	855	3287	7.0	3.3	0.2	0.0	0.98
3	114	229	453	858	3288	7.3	3.4	0.2	0.0	0.99
4	114	229	452	854	3309	7.7	3.7	0.3	0.0	0.99
5	112	228	452	846	3273	8.1	3.6	0.3	0.0	0.98
6	112	227	450	843	3269	8.2	3.6	0.3	0.0	0.98
7	114	227	450	847	3291	8.3	3.6	0.3	0.0	0.98
8	114	229	455	848	3302	8.3	3.5	0.3	0.0	0.98
9	114	229	454	852	3303	8.5	3.7	0.3	0.0	0.99
10	115	230	458	855	3288	8.4	3.5	0.3	0.0	0.98
11	115	232	462	863	3335	8.4	3.8	0.3	0.0	0.98
12	115	232	458	862	3332	8.2	4.0	0.3	0.0	0.98
13	115	235	463	871	3327	8.5	4.3	0.3	0.0	0.98
14	115	234	460	866	3343	9.0	4.5	0.3	0.0	0.98
15	115	232	461	869	3246	9.2	4.8	0.4	0.0	0.98
16	114	231	456	859	3325	9.4	4.9	0.4	0.0	0.98
17	115	230	455	861	3238	9.6	5.0	0.4	0.1	0.98
18	115	232	458	864	3239	9.8	5.0	0.4	0.1	0.98
19	115	232	458	862	3243	9.9	5.0	0.4	0.0	0.98
20	116	233	459	867	3258	9.8	4.8	0.4	0.1	0.98
21	116	235	464	876	3249	9.8	4.8	0.4	0.0	0.99
22	115	234	462	870	3236	9.3	4.8	0.4	0.1	0.98
23	115	233	459	868	3239	8.9	5.1	0.4	0.1	0.98
24	116	234	460	871	3263	8.7	5.0	0.4	0.1	0.98
25	116	234	462	873	3265	8.6	4.9	0.4	0.1	0.98
26	119	238	464	707	3291	8.7	4.9	1.2	0.1	1.00
27	119	240	468	711	3274	8.7	4.8	1.2	0.0	1.00
28	119	242	471	710	3398	8.8	4.8	1.1	0.1	1.00
29	120	243	475	712	3259	8.9	4.7	1.0	0.0	0.99
30	120	243	479	722	3260	9.6	4.7	0.9	0.0	0.99

(iii) to compare the amplitude characteristics of separate formant frequencies,

(iv) to obtain numerical characteristics of stress, and

(v) to reveal the relation between the changes that occur in the rise–fall characteristics of a sound wave or in the formant frequencies it contains and the changes in the auditory estimation of the corresponding synthesized vowel.

In particular, the proposed method was used to analyze the vowels produced by a speaker with a nasal speech defect.

For example, the model obtained for the vowel [U] (without environment) is represented by the table.

Analyzing the results of the vowel modeling, we arrive at the following conclusions:

(i) A high degree of similarity between the model and the experiment is obtained for all pitch periods: $Q > 0.98$.

(ii) A vowel realization is characterized by the rise of the pitch frequency (F_0).

(iii) The first two formants indicate the quality of the vowel [U].

(iv) The presence of the third formant in the frequency band from 700 to 900 Hz points to the nasalization of the vowel, which is typical of vowels produced by speakers with a nasal speech defect.

(v) The amplitudes of the first two formants determining the vowel quality exceed the amplitudes of the two other formants by an order of magnitude or more.

Thus, the experimental studies confirmed the validity of the proposed method of modeling in vowel analysis. In addition, the proposed model offers promise for sound synthesis. Experiments with the frequency composition of formants, their amplitudes, and the stress characteristics may be useful for the quantitative description of other auditory characteristics of vowels (clear or hoarse sound, etc.).

The proposed model includes both the formant vowel structure and the pitch rise and fall characteristic for every pitch period. The similarity between the model and the original can be estimated by both the mathematical methods and the organs of sense (hearing). The objective and subjective estimates of the similarity between the model and the original practically coincide and testify to the adequate representation of the vowel phonation processes by the model. In addition, the proposed model can be used to study the effect of the changes in the rise and fall parameters and the changes in the formant frequencies on the auditory characteristics of sound.

REFERENCES

1. A. Sh. Akbulatov, S. P. Baronin, V. I. Kulya, *et al.*, *Vocoder Telephony. Methods and Problems*, Ed. by A. A. Pirogov (Svyaz', Moscow, 1974), pp. 475–477, 480–481.

2. G. Korn and T. Korn, *Mathematical Handbook for Scientists and Engineers*, 2nd ed. (McGraw-Hill, New York, 1968; Nauka, Moscow, 1984).

3. V. Kouznetsov, in *Proceedings of XI Session of the Russian Acoustical Society* (GEOS, Moscow, 2001), p. 439.

4. V. I. Vorobev and A. G. Davydov, in *Proceedings of XI Session of the Russian Acoustical Society* (GEOS, Moscow, 2001), p. 457.

5. R. D. Leĭtes and V. N. Sobolev, *Digital Simulation of Synthetic Telephony Systems* (Svyaz', Moscow, 1969), pp. 54–55, 58–59.

6. H. J. Manley, J. Acoust. Soc. Am. **35**, 464 (1963).

7. E. N. Pinson, J. Acoust. Soc. Am. **35**, 1264 (1963).

8. O. P. Sklyarov, Akust. Zh. **43**, 675 (1997) [Acoust. Phys. **43**, 583 (1997)].

Translated by E. Golyamina

===== **CHRONICLE** =====

Konstantin Aleksandrovich Naugol'nykh
(On His 70th Birthday)
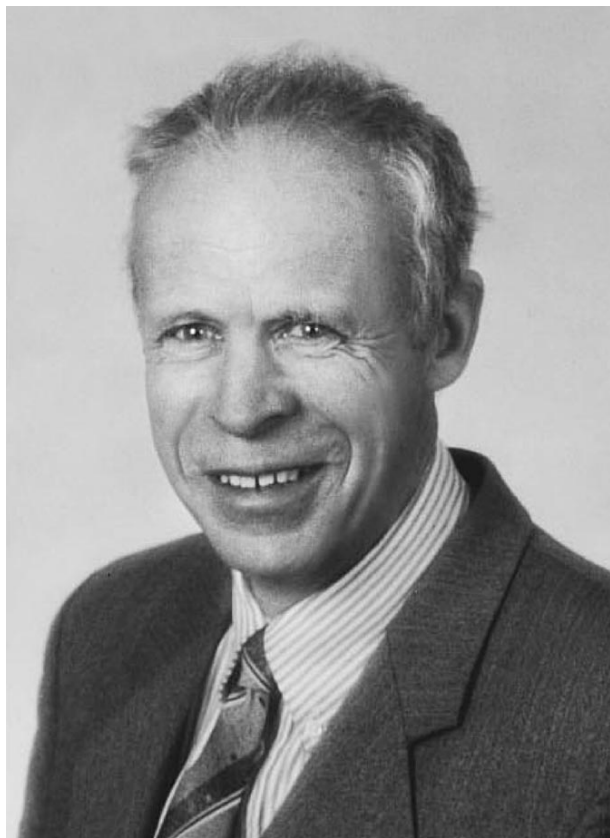
October 7, 2002, marked the 70th birthday of Doctor of Physics and Mathematics Professor Konstantin Aleksandrovich Naugol'nykh, a leading scientist of the Andreev Acoustics Institute and a well-known specialist in nonlinear acoustics.

Naugol'nykh carried out his first research projects when he was a student at the Faculty of Physics and Mathematics of Perm State University. There, his work was supervised by professors G.A. Ostroumov, M.G. Shaposhnikov, and V.S. Sorokin. After his graduation from the university in 1955, he came to Moscow to take a postgraduate course at the Acoustics Institute, and this institute became his permanent place of work. Naugol'nykh's scientific interests were formed under the influence of the prominent Soviet physicist Academician N.N. Andreev. Under his supervision, Naugol'nykh prepared his candidate's dissertation, which he successfully defended in 1959. The dissertation was concerned with the theoretical aspects of the propagation of finite-amplitude acoustic waves. This area of research was new at that time and attracted the interest of young researchers from the Acoustics Institute and Moscow State University, as well as scientists representing the Gorki scientific school. Naugol'nykh, together with S.I. Soluyan and V.V. Khokhlov, considered the detection of a modulated acoustic wave in a nonlinear medium. This study provided the basis for the investigation of the ultimate operation conditions of a parametric sound radiator. Naugol'nykh became acquainted with research in parametric sound radiation when he visited Brown University, Providence, where he worked on probation in cooperation with R. Beyer and P. Westerwelt. In the early 1960s, research into parametric radiation in acoustics was at its initial stage, and, for Naugol'nykh, it was rather interesting to participate in its development.

In the following years, Naugol'nykh turned his attention to nonlinear acoustohydrodynamic phenomena. In this area of research, the main problem was that of radiation and propagation of an intense acoustic pulse generated by an electric discharge. Naugol'nykh derived an effective analytical solution to the Taylor problem of the radiation of a finite-amplitude spherical wave. The results of the studies concerned with this subject were summarized in the monograph *Electric Discharges in Water*, which was written by Naugol'nykh together with N.A. Roĭ in 1971. Today, this book is still widely used by specialists in acoustics. The studies carried out by Naugol'nykh revealed the common physical nature of the sound radiations caused by electric and optical breakdowns in liquid and by cavitation. The theory of the acoustic phenomena accompanying such intense hydrodynamic processes, which was developed by Naugol'nykh, made it possible to describe numerous experiments and has found application in industry. The results of studying these and other nonlinear acoustohydrodynamic phenomena formed the basis of the doctoral dissertation defended by Naugol'nykh in 1971. His studies of acoustohydrodynamic phenomena also provided the basis for his long-term cooperation with Professor S.A. Rybak.

From the early 1970s, Naugol'nykh, together with L.M. Lyamshev, was involved in the research into laser generation of sound in liquid. At that time, these studies were started at the Acoustics Institute (L.M. Lyamshev, K.A. Naugol'nykh, S.V. Egerev, I.B. Esipov, and others), the Physical Institute (later, the General Physics Institute) of the Academy of Sciences of the USSR (F.V. Bunkin, V.G. Mikhalevich, A.I. Bozhkov, and oth-

ers), and at Moscow State University (S.A. Akhmanov, O.V. Rudenko, A.A. Karabutov, and others). The development of research in this new area, which lies at the boundary between laser optics and acoustics, brought interesting results, which were experimentally tested in full-scale conditions. Naugol'nykh headed the first combined expedition of scientists from the Acoustics Institute and the Physical Institute of the Academy of Sciences of the USSR, as well as a number of other full-scale investigations, which were carried out to verify the main principles of sound generation in the sea by laser radiation.

The technological developments of the late 1980s opened up new possibilities for the application of parametric radiators in the ocean. Naugol'nykh made a substantial contribution to the development of this unconventional acoustic means and pioneered the practical application of parametric radiators in long-range propagation tasks under complicated hydrological conditions of the ocean. Throughout the whole period of Naugol'nykh's scientific activity at the Acoustics Institute, including his postgraduate studies, research into wave processes in the ocean, work at the Moscow Institute of Physics and Technology, and full-scale experimental studies in the ocean, he enjoyed the advice and support of Academician L.M. Bre-khovskikh. In 1990, together with L.A. Ostrovskiĭ, Naugol'nykh published the monograph *Nonlinear Wave Processes in Acoustics*, which soon was translated into English by Cambridge University Press. The scientific style of Naugol'nykh is characterized by clear and obvious representation of the results. He taught his students to follow this rule in their studies. In 1985, Naugol'nykh, together with several of his colleagues and coauthors, received a USSR State Award for a series of theoretical and experimental investigations.

Today, Naugol'nykh is working on the problems of acoustic monitoring of the ocean at the Environmental Technology Laboratory, ETL/NOAA, Boulder, CO, thus promoting the development of cooperation between specialists in the USA and Russia working in this area of research.

Naugol'nykh participates in the work of the editorial board of *Acoustical Physics* and the Bureau of the Scientific Council on Acoustics of the Russian Academy of Sciences. He is a member of the Russian Acoustical Society and a member of the Acoustical Society of America. He is also a member of the International Organizing Committee for Symposia on Nonlinear Acoustics. As the vice-president of the Russian Acoustical Society, Naugol'nykh represents Russian acousticians in the commissions of the Acoustical Society of America.

Celebrating his 70th birthday, the prominent Russian acoustician Konstantin Aleksandrovich Naugol'nykh is full of creative ideas and plans. We wish him good health and new scientific achievements.

Translated by E. Golyamina

=== **CHRONICLE** ===

In Memory of Vladimir Mikhaĭlovich Kudryashov
(December 11, 1930–February 26, 2003)

On February 26, 2003, Vladimir Mikhaĭlovich Kudryashov—Candidate of Physics and Mathematics, senior researcher, and a well-known specialist in acoustics—passed away.

Kudryashov was born on December 11, 1930, in Borisov, into the family of a military officer. His studies at school were interrupted by World War II. Together with his father, he was in the army near Brest and, as a "son of the regiment," took part in action in 1941–1943.

He was awarded the Medal for Courage and the Medal for Services in Battle. In 1943, Kudryashov returned to school and, after graduation, continued his education at the Faculty of Physics of Moscow State University. In 1959, Kudryashov became a postgraduate student at the Acoustics Institute, and in 1972, he defended his candidate's dissertation. In 1963, Kudryashov became a junior researcher at the Acoustics Institute, and at this institute he worked to the end his life. Kudryashov made a substantial contribution to the theory of sound propagation in the Arctic. He developed algorithms and programs for computing the sound fields in the arctic waveguide with the use of a two-scale model of the ice cover roughness. This model allowed him to calculate the sound field characteristics with a high accuracy and to obtain a good agreement with experimental data. The significance of the programs developed by Kudryashov was recognized by both Russian and foreign scientists.

To the last day of his life, Kudryashov worked as a leading researcher at the Acoustics Institute. His list of publications includes 92 scientific papers and more than 100 reports and publications in the proceedings of the Acoustics Institute and many scientific conferences. The wide scope of Kudryashov's scientific interests allowed him to work simultaneously in different areas of research. In recent years, he substantially contributed to the acoustic monitoring of the climate in the Arctic Ocean by developing an entirely new and promising branch of ocean acoustics: acoustic halinometry.

All those who knew Kudryashov acknowledged his benevolence, kindness, and generosity. His personality was characterized by intelligence, culture, education, devotion to science, and love of poetry.

The shining memory of Vladimir Mikhaĭlovich Kudryashov will forever remain in the hearts of his friends and colleagues.

Translated by E. Golyamina

===== **CHRONICLE** =====

In Memory of Vladimir Aleksandrovich Krasil'nikov
(On His 90th Birthday)
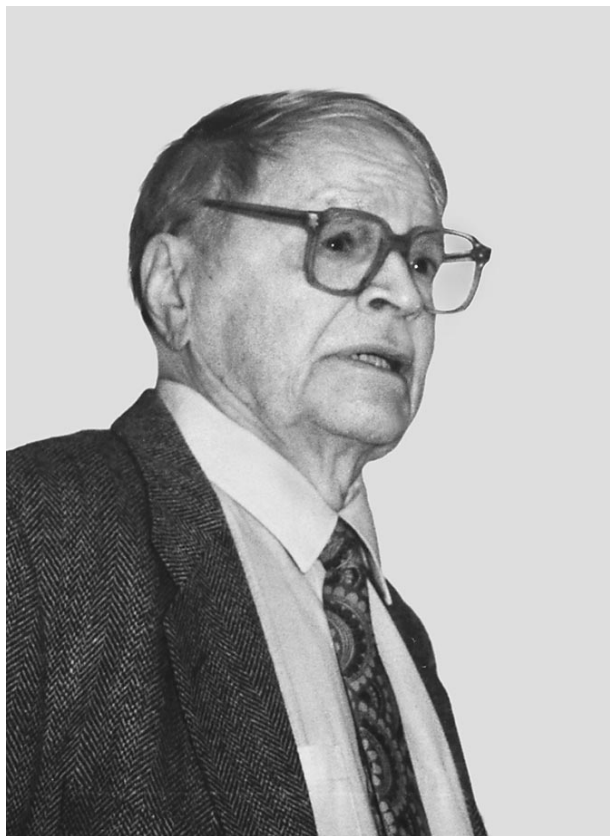
September 14, 2002, marked the 90th birthday of Vladimir Aleksandrovich Krasil'nikov—a prominent scientist, one of the founders of nonlinear acoustics and the physics of waves propagating in turbulent media, a winner of the State Award and the Lomonosov Prize, ex-head of the Acoustics Department of the Faculty of Physics of Moscow State University, and an Honorary Professor of Moscow State University. Two scientific events were dedicated to this anniversary: the 16th International Symposium on Nonlinear Acoustics, which was held at the Faculty of Physics of Moscow State University on August 19–23, 2002, and the Anniversary Session of the Acoustics Department of the Faculty of Physics of Moscow State University. Unfortunately, Krasil'nikov did not live till these days. In March 2000, his life ended as a result of a tragic accident. Possibly, if it were not for the fatal encounter with a careless driver on the pedestrian crossing of Volgina street, Krasil'nikov himself would be able to receive the congratulations on this anniversary.

In the last years of his life, Krasil'nikov made an impression that time had no power over him. He never mentioned his health problems or any difficulties of everyday life. He always looked fit and full of energy. He expressed keen interest in new scientific achievements and in the work carried out at the Acoustics Department. One could remember his good-humored teasing (sometimes about himself) and his fatherly attitude toward students and young scientists. To the last days of his life, Krasil'nikov retained his creative abilities in science and his keenness of mind. He continued writing scientific papers. In particular, two of his reviews appeared in 1998 and 1999 in *Acoustical Physics*: on the sound propagation in a turbulent medium and on nonlinear acoustics. He continued lecturing at the Acoustics Department and took active part in the work of the editorial board of *Acoustical Physics*. He also participated in scientific conferences. In 1998 and 1999, despite his age, Krasil'nikov flew to United States, where he was invited to give papers at the Meeting of the Acoustical Society of America and at the International Congress on Acoustics. After one of his trips, he told a funny story about a young Russian border guard who could not believe that the year of birth indicated in his passport was really 1912 and that there was no mistake in the document. At the Anniversary Session of the Faculty of Physics of Moscow State University devoted to his 85th birthday, which was held in one of the grand physical auditoriums, Krasil'nikov made a speech that was bright and charming and full of jokes. Although Krasil'nikov physically was no giant and never raised his voice in everyday life, he was able to talk without a microphone at any meeting in any large hall so that the audience could hear every word. This "acoustic ability" (which was used by him on rare occasions) was developed by Krasil'nikov at the time of his childhood near Volga: there, a strong voice was necessary to communicate between people in a boat and those on the bank of the great river.

Krasil'nikov was born and grew up in Simbirsk (now Ul'yanovsk). His first research projects were carried out in Moscow at Moscow State University, while he was a student. At that time, the Faculty of Physics was located in the central part of Moscow, in a small building made of red brick and situated behind the Intourist hotel (in Tverskaya street), which has now been demolished. Today, this building belongs to the Institute of Radio Engineering and Electronics of the Russian Academy of Sciences, where Krasil'nikov is

well known as a specialist in acoustics: some research projects carried out at this institute are concerned with acoustics of solids and acoustoelectronics. As a graduate student, Krasil'nikov was supervised by Academician M.A. Leontovich (who, in his turn, was one of the first students of L.I. Mandel'shtam). After his graduation from the university in 1935, Krasil'nikov worked for two years at Gorki (now Nizhni Novgorod) State University. Then, he returned to Moscow and started working at the newly founded Institute of Theoretical Geophysics of the Academy of Sciences of the USSR. In 1939, according to the proposal put forward by S.É. Khaĭkin (professor of Moscow State University and, simultaneously, head of a laboratory of the Institute of Theoretical Geophysics), Krasil'nikov began experimental studies of sound propagation through a turbulent atmosphere. The results of these studies served as a basis for his candidate's dissertation, which was entitled "Sound Propagation through a Turbulent Atmosphere" (1942).

During World War II, Krasil'nikov was involved in the development of radar equipment and also in artillery engineering. In addition, he developed the equipment for acoustic detection and ranging of airplanes. Later, remembering this period of his life, Krasil'nikov characterized his work as rather hard and pressing: sometimes, it was necessary to test the new equipment on the planes by making a series of flights over two or three days without sleep and almost without food. In 1944, Krasil'nikov was invited to work as a part-timer at the Acoustics Department, which was newly established at the Faculty of Physics of Moscow State University by S.N. Rzhevkin.

In 1950, Krasil'nikov left the Institute of Theoretical Geophysics, and the Faculty of Physics of Moscow State University became his main place of work. In 1953, he defended his doctoral dissertation entitled "The Effect of the Refractive Index Fluctuations in Atmosphere on the Propagation of Acoustic and Electromagnetic Waves." In 1955, he received the title of Professor. Soon, Doctor of Science Professor Krasil'nikov was offered a part-time job at the Laboratory of Anisotropic Structures of the Academy of Sciences of the USSR, where experiments on cancer treatment with intense ultrasound were carried out. The scientists and engineers working at this laboratory designed focusing ultrasonic transducers with a record high radiation intensity. Unfortunately, these unique medical-physical experiments were interrupted by the early death (in 1957) of the leader and head of the laboratory A.K. Burov. However, these studies attracted Krasil'nikov's attention to the physics of nonlinear acoustic waves, and this area of research became the main subject of investigation for Krasil'nikov.

For years, Krasil'nikov was on the editorial board of the *Moscow University Physics Bulletin*, and in 1975–1980, he was the editor-in-chief of this journal. From 1969 to 1980, Krasil'nikov was a part-time head of the Ultrasound Department of the Acoustics Institute of the Academy of Sciences of the USSR. From 1969 to the end of his life, Krasil'nikov was a member of the editorial board of *Acoustical Physics*.

In 1975, two important events occurred in Krasil'nikov's career: first, he organized the 6th International Symposium on Nonlinear Acoustics, which was held at Moscow State University, and, second, he became the head of the Acoustics Department. Although the Organizing Committee of the symposium was chaired by Head of Moscow State University Academician R.V. Khokhlov, obviously the major part of the work was performed by Krasil'nikov, who was deputy chair of the committee. As the head of the Acoustics Department, Krasil'nikov worked until 1987, after which he remained a professor.

It so happened that, on the day of Krasil'nikov's death, he became the winner of the main prize of the Russian Academy of Sciences in Radio-Wave Physics, namely, the Mandel'shtam prize. Earlier, in the application for the prize, Krasil'nikov summarized his scientific achievements as follows:

(1) The first experiments on sound propagation in a turbulent atmosphere (1939–1953) and the phase and amplitude fluctuations of the signal. The results are interpreted using the Kolmogorov–Obukhov statistical theory of locally isotropic turbulence (which was published in 1941) and substantiate this theory within its limits of applicability. Quantitatively, the experiments also justify the Kolmogorov–Obukhov two-thirds power law.

(2) The theory of the sound amplitude fluctuations agrees well with the aforementioned experiments only for small distances between the source and the receiver. As this distance increases, diffraction effects come into play. These effects were taken into account by other authors, and the results obtained by them coincide with the experimental results.

(3) The first explanation based on the two-thirds power law was given for the twinkling of stars (fluctuations of intensity and angle of arrival).

(4) The first explanation of the amplitude fluctuations (fading) and phase fluctuations (bearing fluctuations) in the propagation of ultrashort radio waves through a turbulent atmosphere: the phenomenon is explained by the fluctuations of the refractive index.

(5) The first direct experimental observation of harmonics in a plane ultrasonic wave propagating in a low-viscosity fluid, the formation of a sawtooth wave (a weak periodic shock wave), and the nonlinear attenuation of ultrasonic and hypersonic waves. Before these experiments were carried out, it was believed that, at low intensities (which were used in the experiments), the nonlinear properties of the fluid should not manifest themselves. However, for dispersionless fluids with a weak sound absorption, it was found that the wave propagation is accompanied by the accumulation of wave distortions.

(6) The first direct observation of harmonics that appear in a plane longitudinal acoustic wave propagating in a solid (even in the case of low sound intensities) because of the nonlinearity of the Hooke law in the isotropic body.

(7) Observation of the scattering of sound by sound in solids as a result of the nonlinear interaction of longitudinal and shear waves. A direct verification of the selection rules for phonon–phonon interactions by using the interaction of coherent phonons as an example; i.e., a direct proof of the concepts proposed by L.D. Landau and Yu.B. Rumer (hypersound) and by A.I. Akhiezer (ultrasound), which served as the basis for the theory of sound absorption in solids.

(8) Observation of "forbidden" nonlinear interactions in solids. In isotropic solids and in some crystals, according to the nonlinear (five-constant) elasticity theory, the second harmonic should not manifest itself. Experiments showed that this harmonic is present. It strongly depends on external conditions (the pressure applied to the solid and the temperature) because of the structural inhomogeneity (dislocations in crystals, residual stresses, microcracks, and the grain structure of a solid medium). This was the first experimental observation of structural nonlinearity (unlike physical and geometric nonlinearities known previously; this term is now in common use). Structural nonlinearity, in addition to the dependence on the external conditions, is rather large (giant nonlinearity), especially in strongly inhomogeneous solids. Recent experiments (carried out in the 1990s) revealed a correlation between the acoustic nonlinearity and the strength characteristics of a body. This property offers the possibility of determining the strength characteristics of materials by measuring their nonlinearity under small loads. Currently, structural nonlinearity is of considerable interest for applications in materials science, physics of the Earth, and seismology.

Krasil'nikov is the author of more than 200 papers published in leading Russian and foreign journals: *Doklady Physics, Journal of Experimental and Theoretical Physics, Physics–Uspekhi, Physics of the Solid State, Acoustical Physics, Moscow University Physics Bulletin, Nature, Journal of the Acoustical Society of America*, etc. The books written by Krasil'nikov are widely known among the scientific community:

(1) *Sonic and Ultrasonic Waves in Air, Fluids, and Solids* (Nauka, Moscow, 1960). This book survived three editions and was translated into several languages.

(2) *Introduction to Nonlinear Acoustics* (coauthored with L.K. Zarembo; Nauka, Moscow, 1966). This was the world's first monograph on nonlinear acoustics, which played an important role in the development of this area of research. The author of the present essay (a former postgraduate student of Krasil'nikov), tried to buy this book for his own library on acoustics and finally found it only in a secondhand bookstore in Dushanbe (attempts to find the book in Moscow bookstores failed).

(3) *Introduction to Physical Acoustics* (coauthored with V.V. Krylov; Nauka, Moscow, 1984). This book is a manual. It offers a concise, clear, and comprehensive description of a wide range of problems studied by contemporary physical acoustics. The appearance of this book met the expectations of professionals involved in the education process, and the book was sold out within a few days. Krasil'nikov planned to prepare a new extended edition of this book but met with serious difficulties related to the changes in the Russian publishing industry of that time.

An interesting fact illustrating the influence of Krasil'nikov's scientific activity on the development of research into nonlinear wave phenomena can be revealed by considering the publications on solitons of that time. This area of research was booming in the 1960s, and one of the key studies that stimulated this process was the paper by N.J. Zabusky and M.D. Kruskal "Interaction of 'Solitons' in a Collisionless Plasma and the Recurrence of Initial States" (Phys. Rev. Lett., Vol. 15, No. 6, pp. 240–243 (1965)). If one looks more closely at the occupations of these authors of that period, one finds out that, immediately before publishing the aforementioned paper, Zabusky prepared another paper, which was concerned with the numerical modeling of the experiment carried out by Gedroits and Krasil'nikov in 1963: N.J. Zabusky, "Interpretation of the 'Stabilization Distance' as Evidence of Weak Shock Formation in Low-Loss Longitudinal Nonlinear Wave Propagation," J. Phys. Chem. Solids, Vol. 26, No. 6, pp. 955–958 (1965). The abstract of this paper includes the following passage: "Waves of moderate intensity propagating in a lossy medium generate a second harmonic, which reaches a maximum amplitude at the 'stabilization distance' because of the losses. This is used to explain the results of Gedroits and Krasil'nikov for experiments in a magnesium-aluminum alloy." This fact shows that Krasil'nikov's studies stimulated the interest in nonlinear waves even in such a prominent scientist as Zabusky, who was one of the founders of "soliton science."

Krasil'nikov's work in science and education for many years resulted in the formation of the well-known scientific school of Krasil'nikov in nonlinear acoustics. His former students include thirty candidates of science, eight of which have become doctors of science and professors. Some of his former students received State Awards and other prizes from the government and the Academy of Sciences. As a supervisor, Krasil'nikov displayed a composed and tactful attitude toward young scientists. He had a talent for awaking creative abilities in surrounding people. On the other hand, Krasil'nikov said that, for him, the advantage of working at the university is the chance to communicate with talented young people and to select the most gifted students to work with. For Krasil'nikov, the aim of his work was

scientific achievements rather than career or political purposes. He formed a fascinating creative scientific atmosphere at the Acoustics Department and, in particular, at its seminars.

The shining memory of Vladimir Aleksandrovich Krasil'nikov, a true scientist and a wonderful person, will forever remain in the hearts of those who were lucky to work and communicate with him and to study under his supervision.

V.G. Mozhaev

*Acoustics Department of the Faculty
of Physics of Moscow State University*

PUBLICATIONS ON VLADIMIR ALEKSANDROVICH KRASIL'NIKOV

1. *V. A. Krasil'nikov (On His 50th Birthday)*, Akust. Zh. **9**, 130 (1963) [Acoust. Phys. **9,** 104 (1963)].

2. *V. A. Krasil'nikov (On His 60th Birthday)*, Akust. Zh. **18**, 632 (1972) [Acoust. Phys. **18**, 513 (1972)].

3. V. B. Braginskiĭ, L. K. Zarembo, B. S. Ishikhanov, A. P. Sukhorukov, and V. S. Fursov, *Vladimir Aleksandrovich Krasil'nikov (On His Seventieth Birthday)*, Vestn. Mosk. Univ., Ser. 3: Fiz. Astron., **24** (2), 100 (1983).

4. *Vladimir Aleksandrovich Krasil'nikov: On His 75th Birthday*, Akust. Zh. **34**, 375 (1988) [Acoust. Phys. **34**, 223 (1988)].

5. *Krasil'nikov, Vladimir Aleksandrovich: On His 80th Birthday*, Akust. Zh. **38**, 1124 (1992) [Acoust. Phys. **38**, 616 (1992)].

6. V. B. Braginskiĭ, V. A. Burov, L. K. Zarembo, N. I. Koroteev, V. V. Krylov, V. I. Pavlov, O. V. Rudenko, I. Yu. Solodov, and A. P. Sukhorukov, *Vladimir Aleksandrovich Krasil'nikov (On His 80th Birthday)*, Vestn. Mosk. Univ., Ser. 3: Fiz. Astron., **33** (5), 94 (1992).

7. *Vladimir Aleksandrovich Krasil'nikov (On His 85th Birthday)*, Akust. Zh. **43**, 860 (1997) [Acoust. Phys. **43**, 751 (1997)].

8. *Vladimir Aleksandrovich Krasil'nikov (On His 85th Birthday)*, Vestn. Mosk. Univ., Ser. 3: Fiz. Astron., No. 5, 66 (1997).

9. *Vladimir Aleksandrovich Krasil'nikov (September 14, 1912–March 17, 2000)*, Akust. Zh. **46**, 716 (2000) [Acoust. Phys. **46**, 627 (2000)].

10. *In Memory of Vladimir Aleksandrovich Krasil'nikov (September 14, 1912–March 17, 2000)*, Vestn. Mosk. Univ., Ser. 3: Fiz. Astron., No. 4, 71 (2000).

11. *Mandel'shtam Prize of 2000—to V.A. Krasil'nikov,* Vestn. Ross. Akad. Nauk, **70** (8), 765 (2000).

12. *Scientific School by Professor V.A. Krasil'nikov,* Izv. Ross. Akad. Nauk, Ser. Fiz., **64**, 2322 (2000).

Translated by E. Golyamina